National Library of Canada

Acquisitions and Bibliographic Services Branch

395 Wellington Street
Ottawa, Ontario
K1A 0N4

Bibliothèque nationale du Canada

Direction des acquisitions et des services bibliographiques

395, rue Wellington
Ottawa (Ontario)
K1A 0N4

Your file Votre référence

Our file Notre référence

NOTICE

The quality of this microform is heavily dependent upon the quality of the original thesis submitted for microfilming. Every effort has been made to ensure the highest quality of reproduction possible.

If pages are missing, contact the university which granted the degree.

Some pages may have indistinct print especially if the original pages were typed with a poor typewriter ribbon or if the university sent us an inferior photocopy.

AVIS

La qualité de cette microforme dépend grandement de la qualité de la thèse soumise au microfilmage. Nous avons tout fait pour assurer une qualité supérieure de reproduction.

S'il manque des pages, veuillez communiquer avec l'université qui a conféré le grade.

La qualité d'impression de certaines pages peut laisser à désirer, surtout si les pages originales ont été dactylographiées à l'aide d'un ruban usé ou si l'université nous a fait parvenir une photocopie de qualité inférieure.

Canada

TLM ANALYSIS OF MICROWAVE AND MILLIMETRE WAVE STRUCTURES

WITH EMBEDDED NONLINEAR DEVICES

By

Jorgen Staal Nielsen

A Doctoral Dissertation
Submitted to the School of Graduate Studies and Research
of the University of Ottawa
in partial fulfilment of the requirements
for the Degree of

Doctor of Philosophy

in Electrical Engineering

Ottawa-Carleton Institute
for Electrical Engineering
Department of Electrical Engineering
University of Ottawa

ISBN 0-315-80021-6

Canada

UNIVERSITÉ D'OTTAWA
UNIVERSITY OF OTTAWA

I hereby declare that I am the sole author of this thesis. I authorize the University of Ottawa to lend this thesis to other institutions or individuals for the purpose of scholarly research.

Jorgen S. Nielsen

I further authorize the University of Ottawa to reproduce this thesis by photocopying or by other means, in total or in part, at the request of other institutions or individuals for the purpose of scholarly research.

Jorgen S. Nielsen

In the beginning God created the heavens and the earth. The earth was without form or void and darkness was upon the face of the deep; and the spirit of God was moving over the face of the waters. And God said, let there be light.....

Genesis 1:1-3

The created universe, is characterized by vastness, magnificence and beauty. It is also characterized by wild and wonderful phenomenon, some elegantly simple, some totally beyond comprehension by human minds.

The depth of the universe gives purpose and excitement to its study. It also humbles us as we realize the small fraction of His creation that we are able to understand, let alone, adequately simulate.

ACKNOWLEDGEMENTS

I wish to express my acknowledgements to my thesis supervisor, Dr. Wolfgang Hoefer, for his guidance and encouragement throughout the course of this thesis. His clear teaching of numerical methods was appreciated.

I also wish to acknowledge the support from Lockheed Canada Inc. in terms of financial support as well as the "time off" provided to pursue this goal. In particular I wish to express my gratitude towards Paul Pulsifer and Lee Gartley of Lockheed for their personal encouragement.

Finally, I am grateful for the unfailing support provided by my wife, Ileana, who in her way, made this task so much easier and so much more enjoyable. I acknowledge her consistent encouragement and means of putting things into perspective.

ABSTRACT

A methodology has been developed such that electromagnetic structures with embedded non-linear devices can be accurately analyzed by the three-dimensional (3D) condensed node TLM algorithm. The method is based on incorporating a variable time step differential equation integration scheme, simulating the electrical behaviour of the devices, into the 3D TLM electromagnetic field simulation algorithm. The scheme can accommodate existing piece-wise linear SPICE device models of arbitrary complexity without non-physical instabilities or other spurious behaviour.

A set of new 3D TLM node structures have been developed to complement the condensed node to better model the field at sharp conductor strip edges. These node structures provide substantial improvement in the accuracy of modelling strip-like transmission-line structures with a coarse mesh. They also provide a direct interface to the device model resulting in a more accurate simulation of the driving point impedance as seen by the device.

A propagation analysis of the TLM condensed node was performed resulting in a derivation of the general dispersion relation. The superior dispersion characteristics of the condensed node relative to other TLM and FD-TD formulations was demonstrated based on the dispersion equation. Further exploration of the dispersion equation led to the discovery and characterization of spurious modes supported by the condensed node mesh. A derivation of the recursion equations of the equivalent FD-TD scheme representing the condensed node was then performed to establish the origin of the spurious modes and methods of suppressing them.

CONTENTS

3. SIMULATION OF CONDUCTOR STRIPS

4. EMBEDDED NONLINEAR DEVICES IN THE TLM MESH

5. APPLICATIONS

LIST OF VARIABLES

C_{link}	capacitance per unit length of link lines
C_s	capacitance of capacitive stub
d	distance between nodes
d_s	length of dielectric stub
B	magnetic field density vector
D	electric field density vector
E	electric field vector
G_l	conductance of loss stub
H	magnetic field vector
$h_{LP}(t)$	low pass filter impulse response
I	identity matrix
i,j,k	node position indices node located at x=id,y=jd,z=kd
$\mathbf{J_b}$	Jacobian matrix used in PWL algorithm
$J_1(t)$	equivalent current to port 1
$J_2(t)$	equivalent current to port 2
k_o	propagation constant along link lines
k_x,k_y,k_z	component propagation constants in the **x**, **y** and **z**
L_{link}	inductance per unit length of link lines
N_{mesh}	number of segments in low pass filter
N_x	number of nodes in the x-direction
N_y	number of nodes in the y-direction
N_z	number of nodes in the z-direction
p	port index of node
P	transition matrix
q	time interval index
s	stability factor in FD-TD method
S	scattering matrix of the TLM node

$\mathbf{S_{hy}}$	scattering matrix of the y directed half-node
$\mathbf{T}$	transmission matrix
$\mathbf{T_{dh}}$	transformation matrix from half-node to device
$\mathbf{T_{hd}}$	transformation matrix from device to half-node
$\mathbf{u_3, u_2, u_1, u_0}$	state variable vectors used in DDES
V_d	voltage across device
$\mathbf{V^i}$	incident voltage vector to the TLM node
$\mathbf{V^r}$	reflected voltage vector from the TLM node
V^i_{as1}	incident antisymmetric voltage from port 1
V^i_{as2}	incident antisymmetric voltage from port 2
V^r_{as1}	reflected antisymmetric voltage to port 1
V^r_{as2}	reflected antisymmetric voltage to port 2
V^i_{s1}	incident symmetric voltage from port 1
V^i_{s2}	incident symmetric voltage from port 2
V^r_{s1}	reflected symmetric voltage to port 1
V^r_{s2}	reflected symmetric voltage to port 2
v_{link}	EM velocity of link lines
v_{mesh}	EM velocity of TLM mesh at low frequency
v_s	EM velocity of stub
Y_o	characteristic admittance of ling lines
Z_g	characteristic impedance of simulated waveguide mode
Z_o	characteristic impedance of link lines
Δt	update time interval for the TLM mesh
Δt_e	variable update time interval used in the DDES
ϵ_s	relative dielectric constant of capacitive stub
ϵ_{r1}	relative dielectric constant of medium above conductor
ϵ_{r2}	relative dielectric constant of medium below conductor
μ	medium permeability

LIST OF ACRONYMS

CAD	Computer Aided Design
DDES	Device Differential Equation Solver
det	Matrix determinant
DFT	Discrete Fourier Transform
EM	Electro-Magnetic
FD-TD	Finite Difference Time Domain
FE-TD	Finite Element Time Domain
FIR	Finite Impulse Response
HB	Harmonic Balance
IIR	Infinite Impulse Response
LRCG	Inductor Resistor Capacitor Conductance circuit
MIC	Microwave Integrated Circuit
MMIC	Monolithic Microwave Integrated Circuit
NR	Newton-Raphson method
PWL	Piece-Wise Linear
SPICE	Trade name of PWL nonlinear circuit simulation algorithm
TLM	Transmission Line Matrix method
TMDS	TLM Microstrip Device Simulator
1D	One-Dimensional
2D	Two-Dimensional
3D	Three-Dimensional

CHAPTER 1

INTRODUCTION

1.1 MOTIVATION

The motivation behind this thesis was to develop a numerical analysis tool capable of performing transient analysis of electromagnetic structures containing distributed devices that may be strongly nonlinear. The electromagnetic structures may be waveguides, planar transmission line circuits, MMIC devices or detailed models of distributed devices such as FET's, laser diodes, high speed photo-detectors etc. The resulting numerical method is an amalgamation of the Transmission Line Matrix (TLM) method and a Piece-Wise Linear (PWL) algorithm. The TLM method simulates the hyperbolic Maxwell's equations while the PWL algorithm integrates the nonlinear differential equations modelling the embedded devices. This new method is therefore referred to as the TLM-PWL method.

Historically, frequency domain methods such as Method of Moments [1][2], Finite Element [3], Mode Matching [4] and Transverse Resonance [5] have been used to analyze electromagnetic structures, the advantage being that since the structures were assumed to be linear, the excitation could be monochromatic. Eliminating one degree of freedom by assuming time harmonic fields, reduced the problem such that it could be solved by computer without excessive memory or CPU requirements. If the response to a non-harmonic excitation is required, the

structure can be solved for an appropriate set of frequencies, and the temporal response obtained by linear superposition of the component harmonic responses.

In the presence of nonlinearities, superposition of harmonic solutions is no longer valid, and time domain methods must be used. The Harmonic Balance (HB) method can be employed to determine the steady state solution by balancing the response of the linear and non-linear portions through the connecting ports [6][7]. The HB method is well suited to determining steady state periodic solutions when there are only a small number of relevant spectral components. In the case where the input waveform consists of a large number of relevant harmonics, such as digital signals, or when the circuit is highly non-linear, HB is less practical.

In problems involving highly nonlinear devices such as a transistor switch, the most efficient method of obtaining a transient solution is a PWL simulation [8][9]. A PWL simulator is based on LCR (inductor, capacitor, resistor) networks, controlled voltage and current sources and time delay units to model devices that can be approximated as linear and time invariant over a small time interval. Significant effort has been expended on PWL device models as they have become a standard circuit design CAD tool. PWL has been adopted into many SPICE programs developed by universities and industry for simulation of analog and digital circuits.

Unfortunately, it is difficult to model dispersive propagation delays with lumped element models. Therefore PWL methods are less applicable to MIC circuits where dispersion of interconnecting transmission lines or guided wave structures is significant. Considerable effort has been expended to overcome this problem by modelling sections of dispersive transmission lines by lumped LRCG networks [10][11]. Another method, recently incorporated into BNR's SCAMPER algorithm

is to model transmission lines by a truncated impulse response [12][13].

If the simulation problem is limited to solving MIC type problems where mutual coupling effects between circuit elements can be ignored then it is adequate to model interconnecting transmission lines with truncated impulse responses of the transmission line interconnects. The problem is then reduced to determining impulse responses of canonical structures. These impulse responses can be determined by TLM, Finite Difference Time Domain (FD-TD) or a Fourier transform of frequency domain Green's function methods.

In a circuit where the nonlinear devices are spatially distributed and densely packaged, the coupling between the devices and the surrounding electromagnetic structure becomes cumbersome to describe by a finite number of impulse responses. In these cases, it is more appropriate to simulate the surrounding electromagnetic structure with a numerical time domain method and embed the device directly into the mesh used by the method. Applicable time domain methods are TLM, FD-TD, the Method of Lines or the Finite Element Time Domain (FE-TD) method.

In 1966, K. Yee published the 3D FD-TD algorithm which was the first attempt at a practical transient response electromagnetic simulator applicable to general structures [14]. It was not extensively used due to the CPU and memory requirements which were deemed excessive in relation to the current computer capability. During the 1970's P. Johns and his co-workers developed a two-dimensional (2D) TLM method suitable for problems with field homogeneity in one direction [15][16]. Further development of the method was performed by Saguet [17], Mariki [18] and Hoefer [19]. Due to the advance in computer technology, practical problems could now be effectively solved using the TLM algorithm. 3D versions of the TLM method were developed by Akhtarzad [20] and

Johns [21] and Saguet [17]. A comprehensive review of the 2D and 3D TLM methods was given by Hoefer [22][23].

While the origins of the FE-TD, FD-TD and TLM methods are different, they are very closely related methods. For example it can be shown that the expanded TLM node is a special case of Yee's 3D FD-TD node [24]. Yee's node, can in turn, be considered as a special case of a point matched FE-TD method [25]. The TLM condensed node can also be rewritten in terms of finite difference recursive relations between electric and magnetic fields [26]. It can be demonstrated that any TLM procedure can be written as an equivalent FD-TD formulation.

An advantage of the TLM formulation is that the nodes can be represented as a passive network of transmission lines and scattering nodes. Hence at each iteration, energy is conserved resulting in a numerically stable and robust method. FD-TD and FE-TD formulations do not necessarily conserve energy and are therefore generally less numerically robust.

The concept of incorporating nonlinear devices into the TLM mesh was originally demonstrated by Johns and O'Brien [27] where stubs were used to connect the elements to the mesh nodes. Kosmopoulos et. al [28], and Voelker and Lomax [29] used stubs with voltage-dependent characteristic admittances to model the nonlinear devices. Russer et al. [30], used stubs terminated with a reflection coefficient that was computed by an iterative formula. This iterative formula represented a time-discrete integration of the differential equations modelling the nonlinear device. The admittance of the stubs was matched to the driving point admittance of the node, leading to an explicit integration of the device nonlinear differential equations. In these approaches, the update time interval for the device differential equations is slaved to the update interval of the TLM mesh. Hence the TLM mesh must be chosen sufficiently fine such that

the update interval is short enough to ensure appropriate accuracy and stability in solving the device differential equations. Since the stiffness of the differential equations describing a typical device varies with time, there will be periods where the update interval is excessively small resulting in an inefficient algorithm. Likewise there may be periods where the interval is too long resulting in an inaccurate solution that may become unstable.

A natural evolution of the above methods is to merge the TLM method with a variable time step PWL algorithm. A TLM mesh will model the linear portion of the electromagnetic structure. The nonlinear devices will be embedded into the mesh at appropriate locations and interfaced with the TLM nodes. The PWL algorithm with a variable time step will solve the required parameters for the nonlinear devices. The purpose of this thesis is to develop this combined TLM-PWL method and apply it to practical microwave and millimetre-wave circuit problems.

While the methods developed can be applied to the FE-TD and FD-TD scheme, the interconnecting transmission lines in the TLM method offer a natural means for interfacing lumped devices. Because of the time discretized scattering process in the TLM method, simulation of embedded nonlinear devices can be facilitated by an explicit PWL differential equation solver rather than having to resort to an implicit method. This results in a much more computationally efficient algorithm. For this reason the TLM method was pursued rather than building on FD-TD or FE-TD formulations. The 3D condensed TLM node was selected for the implementation of this method. 3D analysis is necessary since for most circuit problems all 6 field components are relevant and must be simulated.

1.2 ORIGINAL CONTRIBUTIONS

The original contributions to the advancement of the TLM method, that have resulted from this research work, are listed below:

1. Development of general analytical dispersion relationships for the TLM nodes. This resulted in the first complete formulation of space and frequency dispersion characteristics of 2D and 3D TLM nodes. Prior to this, the dispersion was only known along specific axes. (Chapter 2, Appendix B)

2. Discovery and characterization of propagating and evanescent spurious solutions of the 3D condensed TLM node. (Chapters 2 and 5)

3. Conception and implementation of new specialized nodes for modelling conductor strips in the 3D condensed node mesh. (Chapter 3)

4. Development of a method of embedding lumped and distributed nonlinear device circuit models into the 3D condensed node mesh. (Chapters 3 and 4)

5. Implementation of a TLM-PWL routine with a variable step size for solving arbitrary nonlinear circuits. (Chapters 4 and 5)

1.3 OUTLINE OF THESIS

This thesis is organized into six chapters which are described below:

Chapter 1 contains this introduction and outline.

Chapter 2 reviews the FD-TD method and the various TLM node structures with a detailed description of the condensed node. A FD-TD equivalence of the condensed node is given to determine the relationship to Maxwell's equations. The dispersion equations for the various node structures are derived such that propagation attributes of the various TLM nodes can be established. This results in a demonstration of the superior dispersion characteristics of the condensed node as well as the supported spurious modes.

Chapter 3 presents a set of new 3D TLM node structures developed specifically for accurate modelling of conductor strips denoted as "conductor strip nodes". Numerical examples of these nodes are given, demonstrating the improved simulation accuracy of planar transmission line structures. A method of interfacing lumped and distributed devices with the conductor strip node structures is developed.

In Chapter 4, a description of the method used to interface the TLM and the PWL algorithm is given. Various idealized nonlinear circuit examples are presented to demonstrate the concepts.

Chapter 5 focuses on applications of the TLM-PWL algorithm to simulating practical microwave and millimetre-wave circuits. A comparison of experimental measurements of a stripline microwave switch circuit with the numerical solution of the TLM-PWL algorithm is included to demonstrate the accuracy of the TLM-PWL simulation.

Chapter 6 contains an overall conclusion with a discussion of further research.

CHAPTER 2

THE TLM CONDENSED NODE METHOD OF FIELD ANALYSIS

In this Chapter a review of the FD-TD and the TLM methods will be given. This will provide the foundation for the development of the new 3D TLM node structures for modelling of conductor strips described in Chapter 3, and the interface with the PWL algorithm that models the embedded nonlinear devices described in Chapter 4.

TLM and FD-TD simulations are based on temporal and spatial sampling of the electromagnetic fields. This process introduces distortion in the form of numerical dispersion and anisotropy, spurious parasitic solutions and in some cases, numerical instabilities. Temporal and spatial sampling also affects the driving point impedance as seen by a lumped device that is embedded into the mesh. Consequently, a detailed investigation of the distortions caused by sampling was performed. This is summarized in this chapter.

In Section 2.4 the general dispersion relation of the various TLM node structures are derived. This analysis demonstrates that the condensed node has better dispersion characteristics than the expanded TLM node and the leap-frog FD-TD method. In Section 2.5, the attributes of the spurious modes supported by the condensed node mesh are described. Knowing these attributes is important in developing methods for minimizing the distortion from spurious modes. Further applications of the dispersion analysis are discussed in Section 2.6. In Section 2.7 the equivalent FD-TD recursive equations of the condensed node scattering process are derived. The reason for this derivation is not so much to establish

a FD-TD algorithm based on the condensed node but rather to establish the relation between the condensed node formulation and the time dependent Maxwell's equations. The equivalent FD-TD formulation also presents definite clues as to the origin of spurious modes in the condensed node mesh. Section 2.8 is an overall review of the chapter content.

2.1 FINITE DIFFERENCE TIME DOMAIN METHOD

The electromagnetic fields in a linear isotropic source-free medium are represented by Maxwell's equations given as

$$\frac{\partial \boldsymbol{B}}{\partial t} + \nabla \times \boldsymbol{E} = 0 \tag{2-1a}$$

$$\frac{\partial \boldsymbol{D}}{\partial t} - \nabla \times \boldsymbol{H} = 0 \tag{2-1b}$$

$$\boldsymbol{B} = \mu \boldsymbol{H} \tag{2-1c}$$

$$\boldsymbol{D} = \epsilon \boldsymbol{E} \quad . \tag{2-1d}$$

The TLM and FD-TD methods involve discretizing the medium into numerous small elemental volumes with dimensions much smaller than the spatial wavelengths of the simulated fields. The medium is approximated as being homogeneous throughout each elemental volume. However, it can vary arbitrarily from one elemental volume to the next.

Assuming a Cartesian coordinate system, Maxwell's curl equations can be written as a set of component scalar equations as

$$-\frac{\partial B_x}{\partial t} = \frac{\partial E_z}{\partial y} - \frac{\partial E_y}{\partial z} \qquad (2\text{-}2a)$$

$$-\frac{\partial B_y}{\partial t} = \frac{\partial E_x}{\partial z} - \frac{\partial E_z}{\partial x} \qquad (2\text{-}2b)$$

$$\frac{\partial B_z}{\partial t} = \frac{\partial E_x}{\partial y} - \frac{\partial E_y}{\partial x} \qquad (2\text{-}2c)$$

$$\frac{\partial D_x}{\partial t} = \frac{\partial H_z}{\partial y} - \frac{\partial H_y}{\partial z} \qquad (2\text{-}2d)$$

$$\frac{\partial D_y}{\partial t} = \frac{\partial H_x}{\partial z} - \frac{\partial H_z}{\partial x} \qquad (2\text{-}2e)$$

$$\frac{\partial D_z}{\partial t} = \frac{\partial H_y}{\partial x} - \frac{\partial H_x}{\partial y} \,. \qquad (2\text{-}2f)$$

In the FD-TD method, the time and spatial curl operators of these equations are approximated by finite difference expressions resulting in a corresponding set of coupled equations that can be solved recursively to obtain the time domain solution of the electromagnetic field component. The most commonly used approximation is the leap-frog scheme originally introduced by K.Yee [14]. The elemental cubic volume of Yee's scheme is shown in Fig. 2-1 indicating the distributed locations where the six field components are evaluated. The purpose of this staggered distribution is such that the curl spatial derivatives can be approximated by a second order central difference approximation. As an example, Eq. 2-2d is updated as

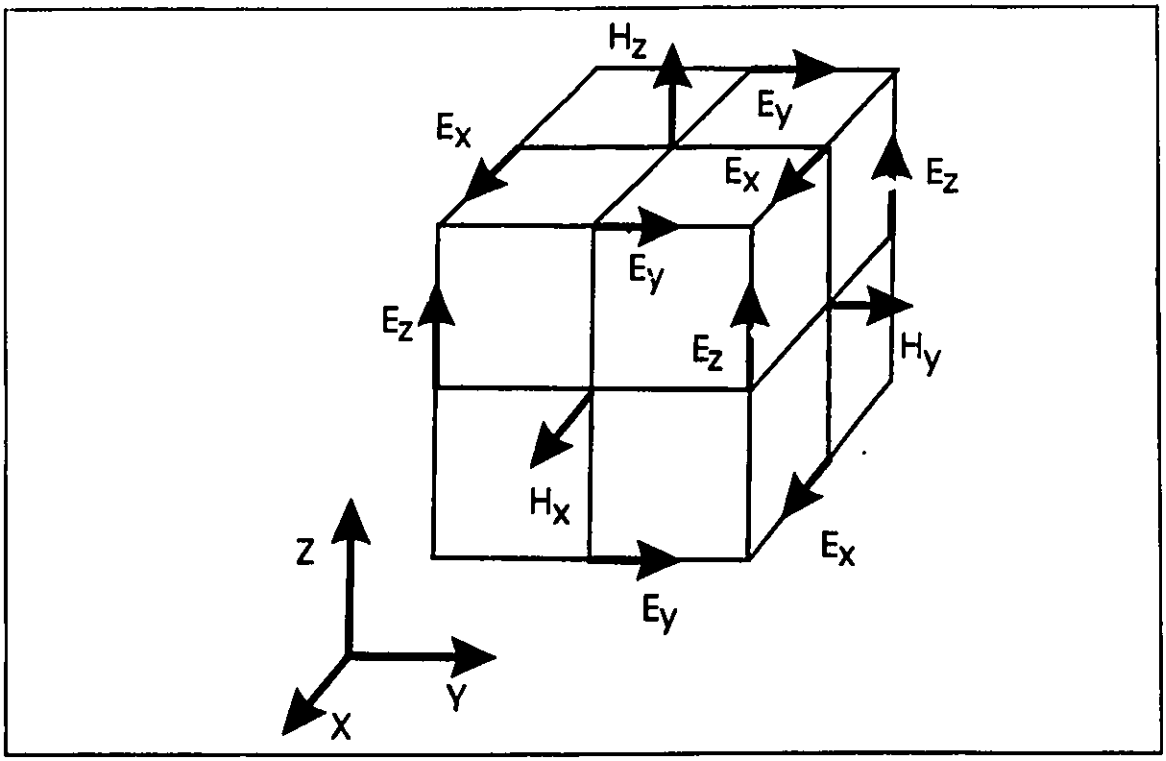

Fig. 2-1 Elemental cell of Yee's leap-frog FD-TD scheme indicating the position where the field components are computed

$$
\begin{aligned}
{}_{q+1}E_x(i,j,k) \;=\; & {}_{q}E_x(i,j,k) \\
+ \frac{\Delta t}{d\,\epsilon_x(i,j,k)} \Big[& {}_{q+\frac{1}{2}}H_z\left(i+\tfrac{1}{2},j+\tfrac{1}{2},k\right) - {}_{q+\frac{1}{2}}H_z\left(i+\tfrac{1}{2},j-\tfrac{1}{2},k\right) \\
& + {}_{q+\frac{1}{2}}H_y\left(i+\tfrac{1}{2},j,k+\tfrac{1}{2}\right) - {}_{n+\frac{1}{2}}H_y\left(i+\tfrac{1}{2},j,k-\tfrac{1}{2}\right) \Big]
\end{aligned}
\qquad (2\text{-}3)
$$

where the index "q" represents the time sample such that $t=q\Delta t$, where Δt is the time interval. Throughout this thesis, the indices i,j,k will be used to denote the node located at $x=i\cdot d$, $y=j\cdot d$ and $z=k\cdot d$ where d is the dimension of the cubic cell. It has been assumed that the permittivity is a diagonal tensor such that

$$\begin{pmatrix} \epsilon_x & 0 & 0 \\ 0 & \epsilon_y & 0 \\ 0 & 0 & \epsilon_z \end{pmatrix} \begin{pmatrix} E_x \\ E_y \\ E_z \end{pmatrix} = \begin{pmatrix} D_x \\ D_y \\ D_z \end{pmatrix} \qquad (2\text{-}4)$$

which defines ϵ_x in Eq. 2-3.

Yee's scheme is convergent such that the smaller the cube dimensions are, relative to the field wavelength, the better the approximation of the spatial curl operators will be, and consequently the better the simulation fidelity. A detailed review of Yee's FD-TD scheme is given by Kim [31].

2.2 TLM METHOD

While the FD-TD method has its origin in finite difference approximations of the time derivative and curl operators in Maxwell's equations, the TLM method originates from an application of Huygens' principle to an array of scattering points [23]. To demonstrate the basic principle, consider a 2D array of node points with an internode spacing of "d" shown in Fig. 2-2. In the array, the incident and scattered impulses propagate along a rectangular mesh of interconnecting transmission lines. At each intersection or node, the transmission lines are connected in either a series or shunt fashion. When an impulse impinges on the node, its energy is scattered equally in four directions according to Huygens' principle. Using this principle as well as imposing energy conservation and continuity of tangential fields during the scattering event, a scattering matrix of the node can be derived.

In the TLM method it is assumed that the interconnecting transmission lines

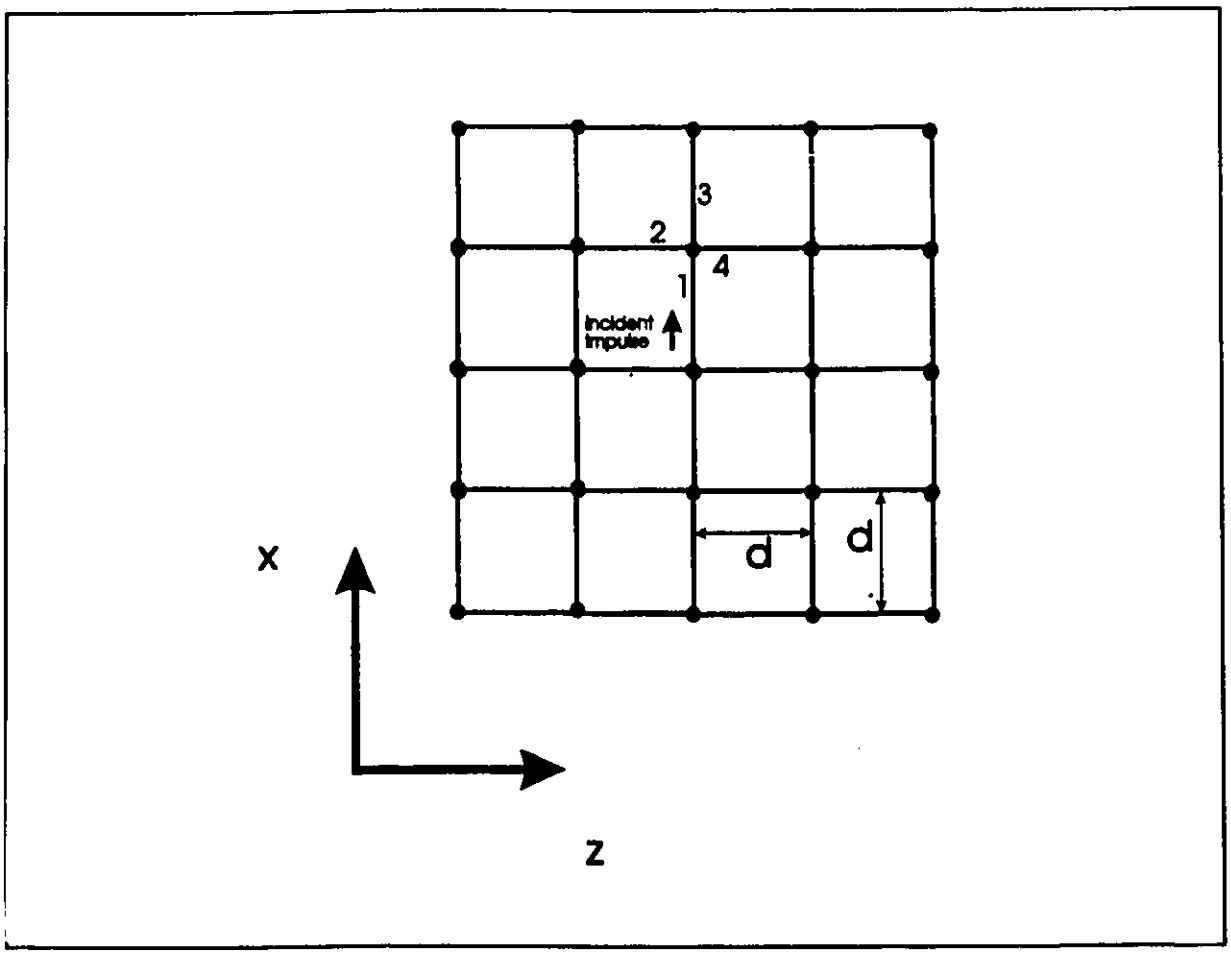

Fig. 2-2 A 2D node array simulating Huygens' principle

are dispersionless with a constant delay from one node to the next, denoted by Δt. Hence, the method consists of determining all the scattered impulses at every time interval Δt. The equivalent electric and magnetic field quantities at each node are approximated by suitable additions of the incident and reflected impulses. There are two node types for the 2D TLM method, the shunt and series nodes, which will be briefly reviewed in Sections 2.2.1 and 2.2.2. Various forms of 3D TLM meshes exist that are based on the same principle discussed above. The expanded and condensed node types will be reviewed in Sections 2.2.3 and 2.2.4, respectively. Other 3D node types have been reviewed by Hoefer [22][23].

2.2.1 2D TLM Shunt Node

The 2D shunt node sketched in Fig. 2-3a can represent 3 field components, namely E_y, H_x and H_z. The shunt node consists of an intersection of two transmission lines of characteristic impedance Z_o. $\mathbf{V}^i$ and $\mathbf{V}^r$ are defined as the vectors of incident and reflected voltages, respectively, given as

$$\mathbf{V}^i = \begin{pmatrix} V^i_1 \\ V^i_2 \\ V^i_3 \\ V^i_4 \end{pmatrix} \qquad \mathbf{V}^r = \begin{pmatrix} V^r_1 \\ V^r_2 \\ V^r_3 \\ V^r_4 \end{pmatrix} . \tag{2-5}$$

The subscript numbers refer to the ports of the shunt node given in Fig. 2-3a. $\mathbf{V}^i$ and $\mathbf{V}^r$ are related through a scattering matrix, $\mathbf{S}$, as

$$\mathbf{V}^r = \mathbf{S}\ \mathbf{V}^i , \tag{2-6}$$

$\mathbf{S}$ is derived from Fig. 2-3 as

$$\mathbf{S} = \frac{1}{2}\begin{pmatrix} -1 & 1 & 1 & 1 \\ 1 & -1 & 1 & 1 \\ 1 & 1 & -1 & 1 \\ 1 & 1 & 1 & -1 \end{pmatrix} \tag{2-7}$$

If the transmission lines are approximated by lumped inductors and capacitors as illustrated in Fig. 2-3b, then a pair of coupled differential equations result with resemble Maxwell's equations. These are

$$\frac{\partial V_y}{\partial x} = -L_{link}\frac{\partial I_x}{\partial t} \tag{2-8a}$$

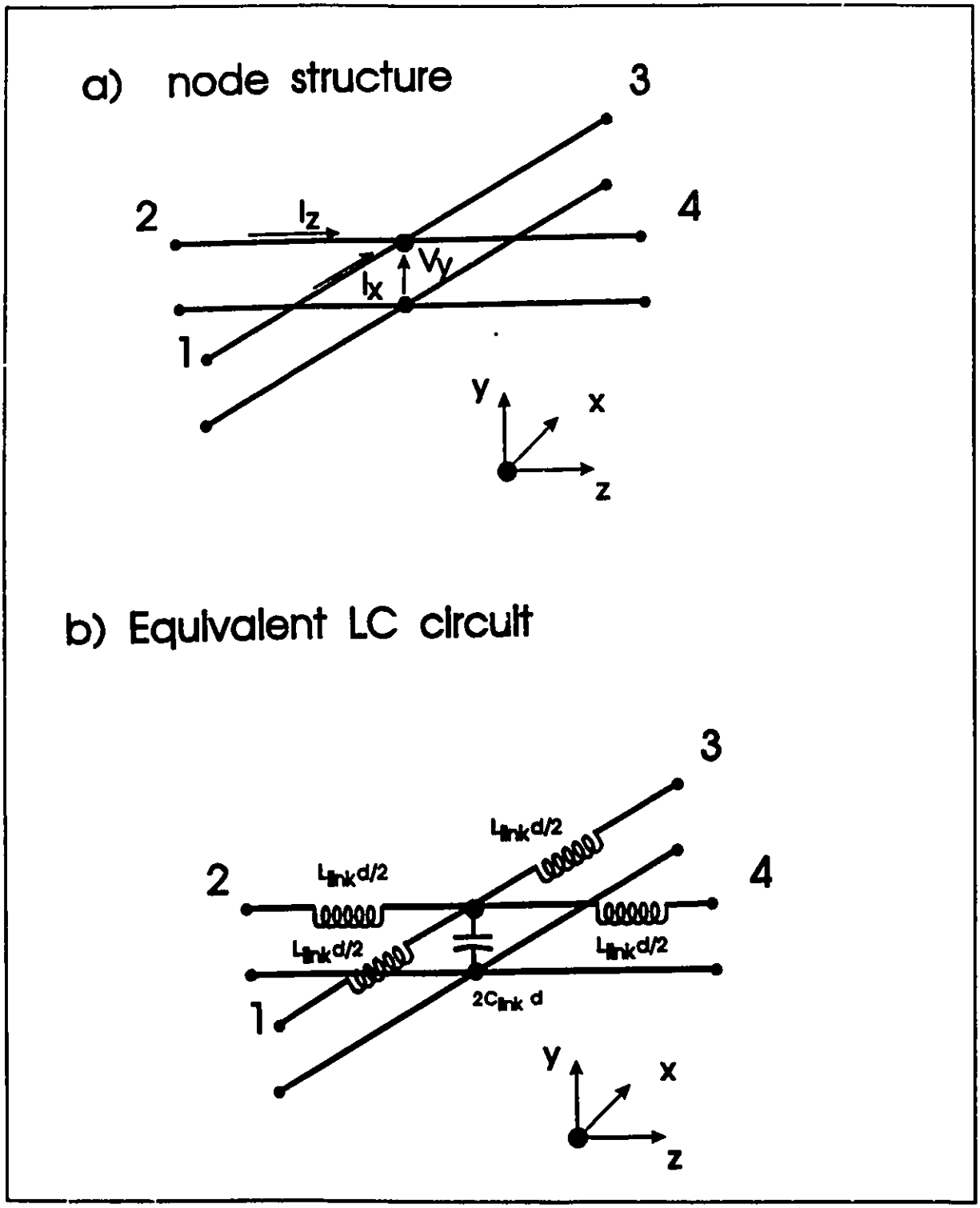

Fig. 2-3 2D TLM shunt node structure

$$\frac{\partial V_y}{\partial z} = -L_{link} \frac{\partial I_z}{\partial t} \qquad (2\text{-}8b)$$

$$\frac{\partial I_z}{\partial z} + \frac{\partial I_x}{\partial x} = -2C_{link} \frac{\partial V_y}{\partial t} \qquad (2\text{-}8c)$$

where V_y, I_x and I_z are indicated in Fig. 2-3b. L_{link} and C_{link} are defined as the inductance and capacitance of the link line per unit length. It is readily observed that if the following equivalences are made

$$E_y = -\frac{V_y}{d}, \quad H_z = -\frac{I_x}{d}, \quad H_x = \frac{I_z}{d}, \qquad (2\text{-}9)$$
$$\mu = L_{link} \quad [H/M], \qquad \epsilon_y = 2C_{link} \quad [F/M]$$

then Eq. 2-8 reduces to Maxwell's equations for the TE case where

$$E_x = 0, \quad E_z = 0, \quad H_y = 0, \quad \frac{\partial}{\partial y} = 0 \; . \qquad (2\text{-}10)$$

2.2.2 2D TLM Series Node

The 2D series node is sketched in Fig. 2-4a and can represent three field components of TM modes, namely E_x, E_z and H_y. The series node consists of a series connection of two transmission lines of impedance Z_o. The scattering matrix of this node is

$$\mathcal{S} = \frac{1}{2}\begin{pmatrix} 1 & 1 & 1 & -1 \\ 1 & 1 & -1 & 1 \\ 1 & -1 & 1 & 1 \\ -1 & 1 & 1 & 1 \end{pmatrix} \tag{2-11}$$

If the transmission lines are again approximated by lumped inductors and capacitors as illustrated in Fig. 2-4b then a pair of coupled differential equations emerges as

$$\frac{\partial I_y}{\partial x} = -C_{link} \frac{\partial V_z}{\partial t} \tag{2-12a}$$

$$\frac{\partial I_y}{\partial z} = -C_{link} \frac{\partial V_x}{\partial t} \tag{2-12b}$$

$$\frac{\partial V_x}{\partial z} + \frac{\partial V_z}{\partial x} = -2L_{link} \frac{\partial I_y}{\partial t} \tag{2-12c}$$

where I_y, V_x and V_z are indicated in Fig. 2-4b. If the following equivalences are made

$$H_y = \frac{I_y}{d}, \quad E_x = -\frac{V_x}{d}, \quad E_z = \frac{V_z}{d} \tag{2-13}$$

$$\mu = 2L_{link}\ [H/M]; \qquad e_{x,z} = C_{link}\ [F/M]$$

then Eq. 2-12 reduces to Maxwell's equations for the TM case with

$$H_x = 0, \quad H_z = 0, \quad E_y = 0, \quad \frac{\partial}{\partial y} = 0 \tag{2-14}$$

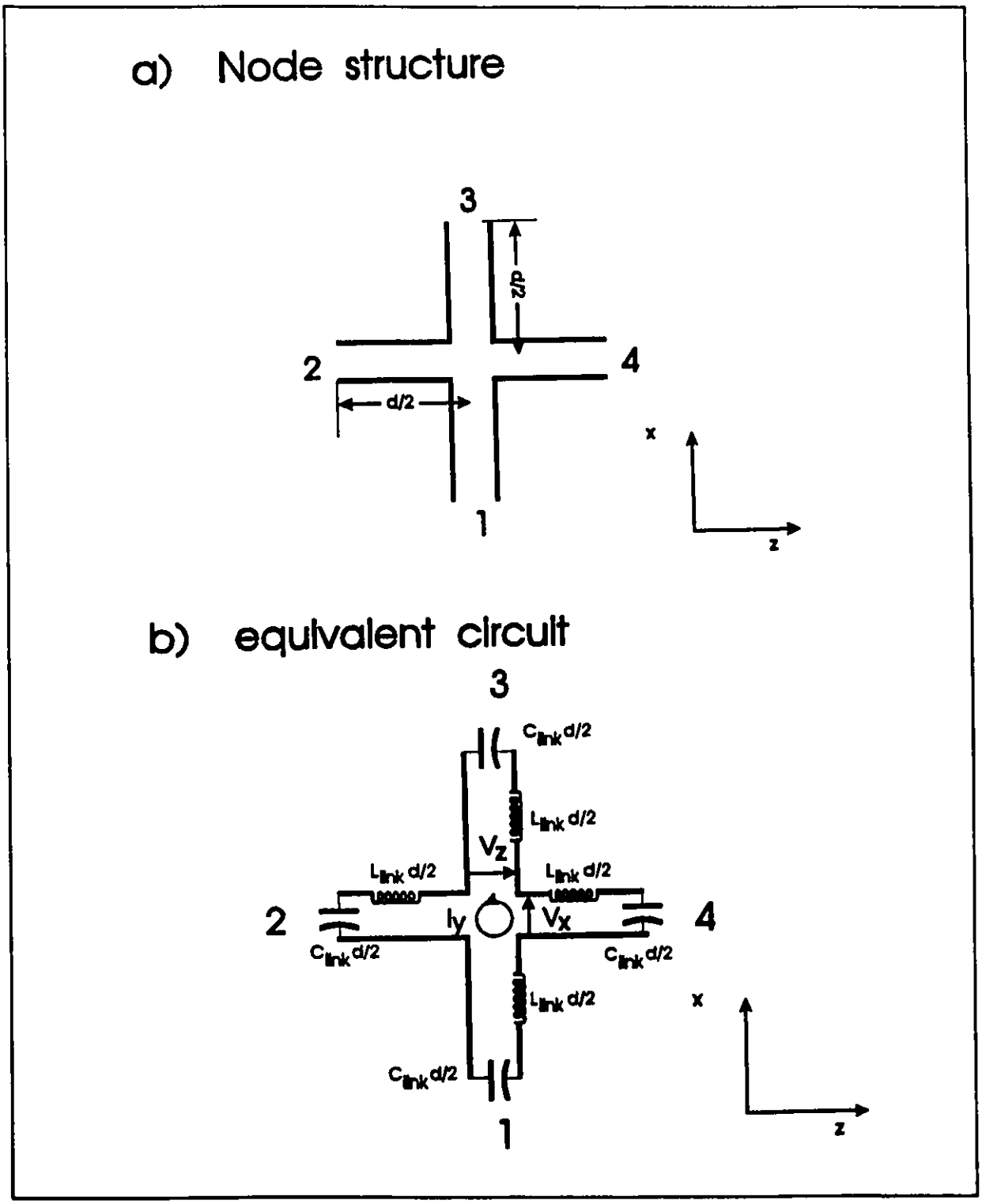

Fig. 2-4 TLM series node structure

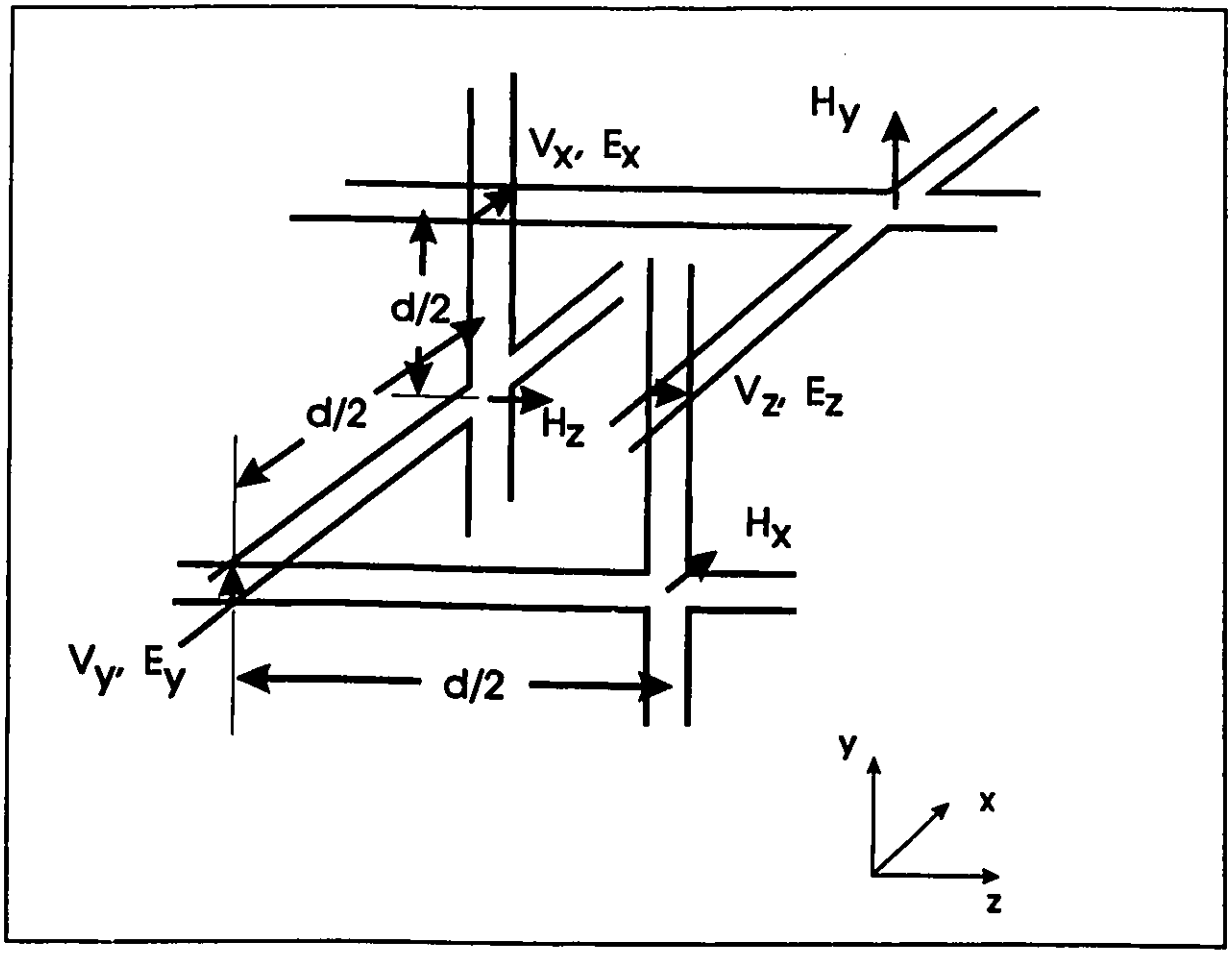

Fig. 2-5 3D TLM expanded node structure

2.2.3 Expanded 3D TLM Node

Akhtarzad and Johns [20] arranged the series and shunt nodes described above in an interlaced arrangement resulting in the 3D expanded node as illustrated in Fig. 2-5. The term "expanded" was used since the evaluated field components were not collocated. Each cell of the expanded node consists of three shunt nodes, representing the E_x, E_y and E_z fields, and three series nodes representing the H_x, H_y and H_z fields. Notice that the spacing between the series and shunt

nodes is d/2 such that the overall cell size is d.

The incident voltages converging on the shunt nodes are scattered at interval time steps and the incident voltages converging on the series nodes are scattered half a time step later. Hence the E and H fields are not updated at the same time but at half time step intervals as in Yee's FD-TD scheme. A detailed description of the expanded node is given in [23].

2.2.4 Condensed Node Structure

One disadvantage of the expanded node is that the six field components are not collocated, nor are they updated at the same time. This makes it difficult to impose arbitrary mixed boundaries. This motivated P. Johns to develop a different 3D TLM node structure denoted as the "condensed node" which consisted of one central scattering centre in each cube of medium rather than a set of series and shunt nodes as in the expanded node [21]. The node lattice is a cubic structure as shown in Fig. 2-6a and the node structure is shown in Fig. 2-6b.

The condensed node consists of twelve ports that connect to adjacent nodes. There is no practical transmission line equivalent circuit of the node itself. The incident voltage and reflected voltage in port "p" of the condensed node is denoted by V^i_p and V^r_p, respectively, as before. $\mathbf{V}^i$ and $\mathbf{V}^r$, the vector representations of the incident and reflected voltages, are related through the node scattering matrix, $\mathbf{S}$, given by Johns [21]

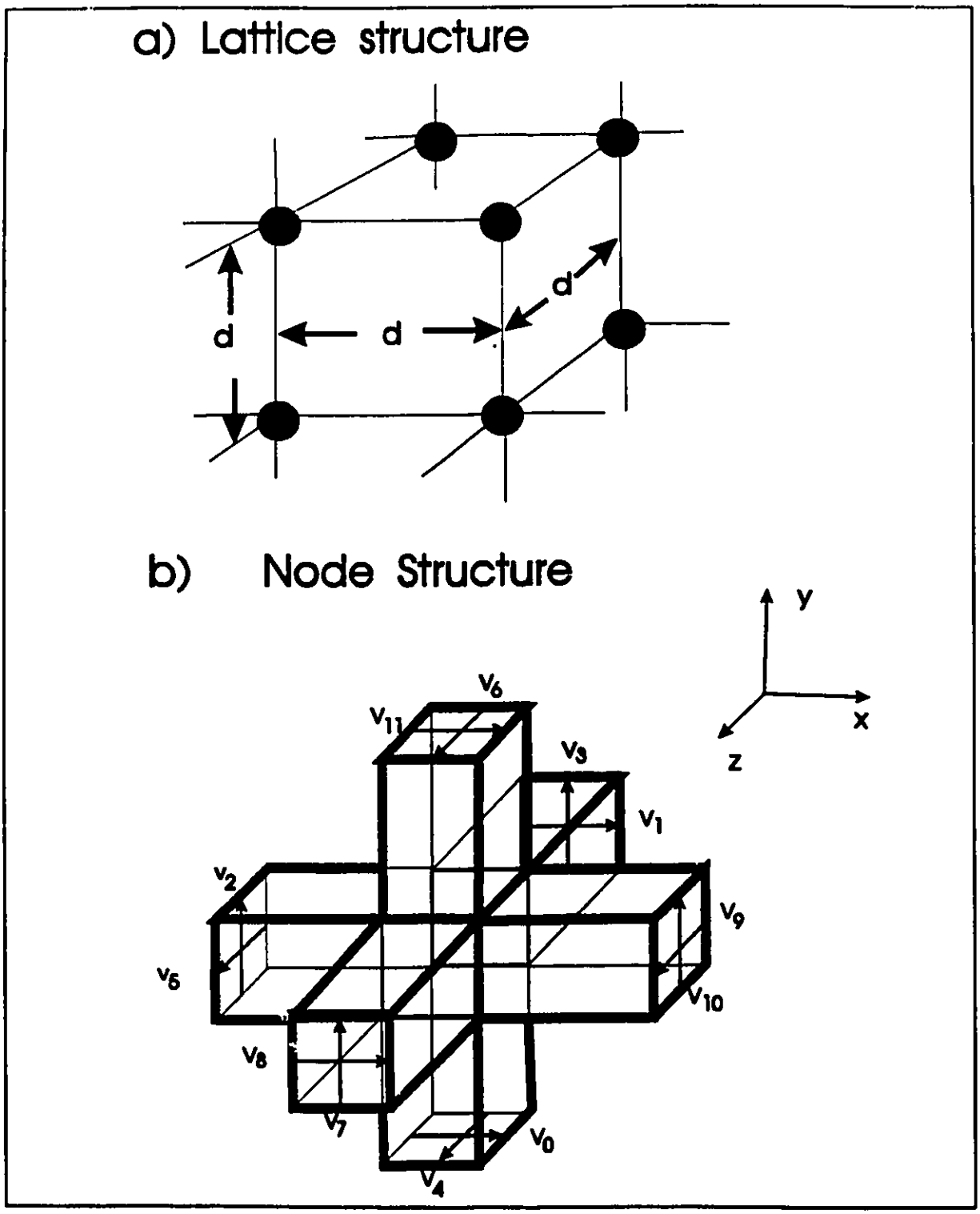

Fig.2-6 3D TLM condensed node structure

$$S=\frac{1}{2}\begin{pmatrix} 0 & 1 & 1 & 0 & 0 & 0 & 0 & 0 & 1 & 0 & -1 & 0 \\ 1 & 0 & 0 & 0 & 0 & 1 & 0 & 0 & 0 & -1 & 0 & 1 \\ 1 & 0 & 0 & 1 & 0 & 0 & 0 & 1 & 0 & 0 & 0 & -1 \\ 0 & 0 & 1 & 0 & 1 & 0 & -1 & 0 & 0 & 0 & 1 & 0 \\ 0 & 0 & 0 & 1 & 0 & 1 & 0 & -1 & 0 & 1 & 0 & 0 \\ 0 & 1 & 0 & 0 & 1 & 0 & 1 & 0 & -1 & 0 & 0 & 0 \\ 0 & 0 & 0 & -1 & 0 & 1 & 0 & 1 & 0 & 1 & 0 & 0 \\ 0 & 0 & 1 & 0 & -1 & 0 & 1 & 0 & 0 & 0 & 1 & 0 \\ 1 & 0 & 0 & 0 & 0 & -1 & 0 & 0 & 0 & 1 & 0 & 1 \\ 0 & -1 & 0 & 0 & 1 & 0 & 1 & 0 & 1 & 0 & 0 & 0 \\ -1 & 0 & 0 & 1 & 0 & 0 & 0 & 1 & 0 & 0 & 0 & 1 \\ 0 & 1 & -1 & 0 & 0 & 0 & 0 & 0 & 1 & 0 & 1 & 0 \end{pmatrix} \qquad (2\text{-}15)$$

The other half of the recursion equations relating the new incident voltages to the reflected voltages from the surrounding nodes are given by

$$\begin{aligned}
{}_{q+1}V^{i}_{i,j,k,0} &= {}_{q}V^{r}_{i,j-1,k,11} \\
{}_{q+1}V^{i}_{i,j,k,1} &= {}_{q}V^{r}_{i,j,k-1,8} \\
{}_{q+1}V^{i}_{i,j,k,2} &= {}_{q}V^{r}_{i-1,j,k,10} \\
{}_{q+1}V^{i}_{i,j,k,3} &= {}_{q}V^{r}_{i,j,k-1,7} \\
{}_{q+1}V^{i}_{i,j,k,4} &= {}_{q}V^{r}_{i,j-1,k,6} \\
{}_{q+1}V^{i}_{i,j,k,5} &= {}_{q}V^{r}_{i-1,j,k,9} \\
{}_{q+1}V^{i}_{i,j,k,6} &= {}_{q}V^{r}_{i,j+1,k,4} \qquad (2\text{-}16) \\
{}_{q+1}V^{i}_{i,j,k,7} &= {}_{q}V^{r}_{i,j,k+1,3} \\
{}_{q+1}V^{i}_{i,j,k,8} &= {}_{q}V^{r}_{i,j,k+1,1} \\
{}_{q+1}V^{i}_{i,j,k,9} &= {}_{q}V^{r}_{i+1,j,k,5} \\
{}_{q+1}V^{i}_{i,j,k,10} &= {}_{q}V^{r}_{i+1,j,k,2} \\
{}_{q+1}V^{i}_{i,j,k,11} &= {}_{q}V^{r}_{i,j+1,k,0} \ .
\end{aligned}$$

Here q denotes the time interval index such that the new incident voltages at

$(q+1)\Delta t$ are evaluated in terms of the reflected voltages from the previously derived reflected voltages evaluated at $q\Delta t$. Note that the ports are numbered from 0 to 11 rather than the commonly used ordering, from 1 to 12, proposed by Johns [21]. This was done to make the port numbering compatible with the numbering scheme used in the computer programs developed.

For the analysis in this thesis it is most convenient if the node update timing is such that at $t=q\Delta t$, the reflected signals, ${}_qV^r_p$, cross the half-way point between nodes resulting in the incident signals ${}_{q+1}V^i_p$. This causes less confusion since devices embedded into the mesh will be interfaced at the half-way points.

In modelling an electromagnetic structure containing homogeneous material of ϵ_o and μ_o with a condensed node structure, the impedance and the phase velocity of the link lines must be specified. Two approaches can be taken. The first approach is to assume that the capacitance and inductance per unit length of the link transmission lines, C_{link} and L_{link} respectively, are given by

$$\begin{aligned} C_{link} &= \epsilon_o \quad [F/M] \\ L_{link} &= \mu_o \quad [H/M] \ . \end{aligned} \tag{2-17}$$

It follows then that the propagation velocity of the link lines, denoted by V_{link}, is given by

$$V_{link} = \frac{1}{\sqrt{\epsilon_o \mu_o}} \ . \tag{2-18}$$

It will be shown in Section 2.5 that the phase velocity of a low frequency (much less than $1/\Delta t$) plane wave propagating in the condensed node mesh, denoted by

V_{mesh}, will be approximately given by

$$V_{mesh} \approx \frac{V_{link}}{2} = \frac{1}{2\sqrt{\epsilon_o \mu_o}} . \qquad (2\text{-}19)$$

Consequently, all the physical dimensions of the structure must be reduced by a factor of 2. Furthermore when modelling spatially distributed elements, compensation of this factor of 2 must be made. This can be confusing and easily result in error.

The other approach, which will be followed here, is to increase the phase velocity on the link lines by a factor of 2 such that

$$C_{link} = \epsilon_o / 2$$
$$L_{link} = \mu_o / 2 . \qquad (2\text{-}20)$$

Now the phase velocity of a plane wave propagating within the mesh will be approximately equal to the physical velocity. Hence the physical dimensions of the object are maintained in the model. Now Δt is reduced by a factor 2 such that

$$\Delta t = \frac{d}{2} \sqrt{\epsilon_o \mu_o} . \qquad (2\text{-}21)$$

Required boundary walls are generally added halfway between tne nodes. Provided that the boundary reflection is frequency independent, a simple reflection coefficient can be assigned to the boundary. This is illustrated in Fig. 2-7 for port "p" terminated by a wall with a reflection coefficient R_b. Hence

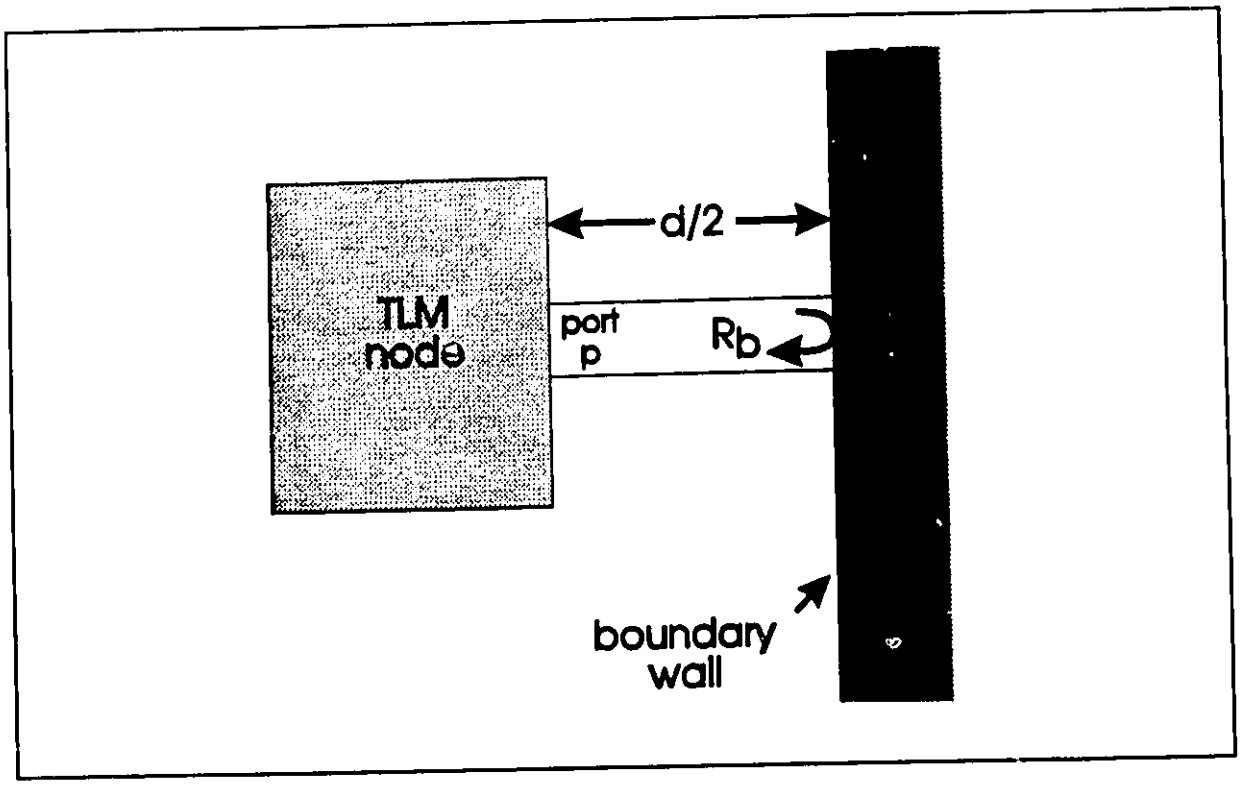

Fig. 2-7 Implementation of a dispersionless boundary in a TLM mesh

$$ {}_{q+1}V^{i}_{p} = R_b \, {}_{q}V^{r}_{p} \qquad (2\text{-}22) $$

If the boundary is an electric wall, R_b=-1 and if the boundary is a magnetic wall R_b=1 as expected. It was determined that while this method is sufficient for modelling infinite boundaries without edges, it is not accurate for modelling conductor strip boundaries with edges. Hence a set of modified condensed nodes were developed specifically to model conductor strips. In these nodes, the boundary is placed in the middle of the node such that the strip edge couples more strongly with the surrounding nodes. This will be developed in detail in Chapter 3.

It is more complicated to implement an absorbing boundary wall. For narrow band applications or cases where the incident field is a plane wave impinging on

the boundary at a fixed angle of incidence, R_b can be set to a specific value. For wide bandwidth applications or cases where the incidence angle must be arbitrary, a dispersive boundary reflection is required. Such absorbing boundaries can be simulated using a Johns wall [32]. Unfortunately, these are very numerically intensive. Presently. absorbing boundaries based on spline interpolations of the field components adjacent to the boundary are being developed, which will be more numerically efficient, but as yet, pose problems of instability [33].

2.3 DIELECTRIC MATERIAL MODELLING USING STUBS

By adding capacitive, inductive and loss stubs to the condensed node, it is possible to model dielectric and magnetic material that can be lossy. Three capacitive and three inductive stubs were originally incorporated into the condensed node by Johns [21] to model the diagonal permittivity and permeability tensor components. Series and shunt loss stubs were added later by Naylor and Dessai [34]. Magnetic materials were not considered since the focus was primarily on development of methodologies for embedding nonlinear devices rather than methods of modelling an arbitrary medium. Consequently, only the capacitive and loss stubs will be reviewed.

Consider a cube of homogeneous dielectric material of relative permittivity ϵ_r. If the cube dimension is "d" then the intrinsic capacitance is $\epsilon_r\epsilon_o d$. Considering the condensed node, there are four link lines shunting the electric field for each polarization. The capacitance represented by these four link lines of length d/2 and an added capacitive stub with a capacitance denoted

by C_{stub} must be equivalent to $\epsilon_r\epsilon_o d$. Consequently

$$C_{stub} = \epsilon_r \epsilon_o d - 4 C_{link} \frac{d}{2} \quad . \tag{2-23}$$

Using Eq. 2-20

$$C_{stub} = \epsilon_o d (\epsilon_r - 1) \quad . \tag{2-24}$$

C_{stub} must be equal to the capacitance of the open stub at low frequencies. The admittance of this stub, normalized by the admittance Y_o of the link lines, is denoted by Y_s. Y_s is determined by constraining the velocity along the stub line to V_{link} and setting the length of the stub to d/2. This ensures time synchronism of the overall node. Consequently,

$$C_{stub} = \frac{Y_s Y_o}{V_{link}} \frac{d}{2} \quad . \tag{2-25}$$

Using Eq. 2-24 in Eq. 2-25 we obtain the required value of Y_s as

$$Y_s = 4 (\epsilon_r - 1) \cdot \tag{2-26}$$

Losses in the dielectric can be simulated by a shunt conductance. In the condensed node, this conductance is represented by an infinitely long stub with a normalized admittance of G_1. Three shunt loss stubs are included in the condensed node, one for each polarization. Details of relating G_1 to the dielectric loss tangent are described by Hoefer [23].

The scattering matrix for the condensed node with dielectric stubs is a 15 by 15 matrix which is given in the table below. Ports 12, 13 and 14 are attached to the x, y and z polarized dielectric stubs respectively.

Table 2-1 Scattering matrix of condensed node with dielectric and loss stubs (taken from [34])

row no.	column no.														
	0	1	2	3	4	5	6	7	8	9	10	11	12	13	14
0	a	b	d						b		-d	c	g		
1	b	a				d			c	-d		b	g		
2	d		a	b				b			c	-d		g	
3			b	a	d		-d	c			b			g	
4				d	a	b	c	-d		b					g
5		d			b	a	b		-d	c					g
6				-d	c	b	a	d		b					g
7			b	c	-d		d	a			b			g	
8	b	c				-d			a	d		b	g		
9		-d			b	c	b		d	a					g
10	-d		c	b				b			a	d		g	
11	c	b	-d						b		d	a	g		
12	b	b							b			b	h		
13			b	b				b			b			h	
14					b	b	b			b					h

The constants used in the above table are given below:

$$a = -\frac{G_1 + Y_s}{2\ (G_1 + Y_s + 4)} \qquad (2\text{-}27a)$$

$$b = \frac{2}{G_1 + Y_s + 4} \qquad (2\text{-}27b)$$

$$c = -\frac{G_1 + Y_s}{2\ (G_1 + Y_s + 4)} \qquad (2\text{-}27c)$$

$$d = \frac{1}{2} \qquad (2\text{-}27d)$$

$$h = -\frac{G_1 - Y_s + 4}{G_1 + Y_s + 4} \qquad (2\text{-}27e)$$

$$g = Y_s\, b \quad . \qquad (2\text{-}27f)$$

In addition to modelling dielectric and magnetic material, stubs can be used to represent lumped LRC components. Using Eq. 2-25, a lumped capacitor denoted by C_{lump}, can be represented by a capacitive stub with a normalized characteristic admittance of

$$Y_s = \frac{4\ C_{lump}}{d\ e_o} \quad . \qquad (2\text{-}28)$$

A lumped shunt conductance of admittance G_{lump} can be modelled by a loss stub of infinite length with a normalized admittance G_1 given by

$$G_1 = G_{lump} \,/\, Y_o \quad . \qquad (2\text{-}29)$$

Shorted stubs can be used to model lumped inductors. Consider modelling an inductance L_{lump} with a shorted stub of length d/2 and phase velocity of V_{link}.

The condition

$$j\,\omega\,L_{lump} = \frac{j}{Y_s\,Y_o}\tan\left(\frac{d\,\omega}{2\,V_{link}}\right) \qquad (2\text{-}30)$$

must be satisfied. For frequencies much lower than $1/\Delta t$, Eq. 2-30 reduces to

$$Y_s \approx \frac{d}{2\,Y_o\,V_{link}\,L_{lump}} = \frac{d\,L_{link}}{2\,L_{lump}}\,, \qquad (2\text{-}31)$$

2.4 GENERAL DISPERSION RELATION OF THE TLM NODE STRUCTURES

In this section the general dispersion relations for the various TLM node structures will be derived. These will be used to quantify the numerical dispersion and anisotropy of each node. A comparison of the dispersion relations demonstrates the superior dispersion characteristics of the condensed node relative to the other TLM nodes and Yee's FD-TD algorithm. Previously, the dispersion relation for the condensed node has only been considered in special cases such as propagation along the three coordinate axes and along the diagonals [23].

The dispersion relation derived for the condensed node was based on applying Floquet's theorem to an infinite 3D periodic TLM mesh [35] [36]. This resulted in an eigenmatrix equation whose characteristic is the desired dispersion relationship. By solving for the corresponding eigenvectors, the field structure of each supported eigenmode in the TLM mesh can be determined and compared with theoretical mode attributes.

A bounded TLM node lattice supports a finite number of modes which forms an orthogonal set of basis functions as a Hilbert space. Hence the limitation in simulation fidelity can be determined by the errors involved in having a finite number of supported modes in the TLM mesh as well as by the numerical distortion in each of these modes.

The knowledge of the propagation constant and characteristic impedance for each mode leads to an accurate method of extracting scattering parameters from waveguide circuits. This is presented in Appendix C. Having an analytical dispersion relation also facilitates the investigation of instabilities in the TLM mesh containing embedded active devices.

2.4.1 Dispersion Relation of the 2D Shunt Node

The 2D shunt node is sketched in Fig. 2-8. The node is connected to its four neighbours by link lines of length "d", which is the node spacing as before. Each of the link lines is identified by an index "p". The terminology that will be used in this derivation is as follows. "Adjacent" nodes refers to the four peripheral nodes at a distance "d" from the "centre" node. V_c denotes the total voltage amplitude at the centre of the node and V_p denotes the voltage of line "p" at the centre of the adjacent node attached to line "p". The dispersion relation is based on determining the interdependence between node voltages V_c and V_p.

V_p is composed of incident and reflected voltages such that

$$V_p = V^i_p + V^r_p \qquad (2\text{-}32)$$

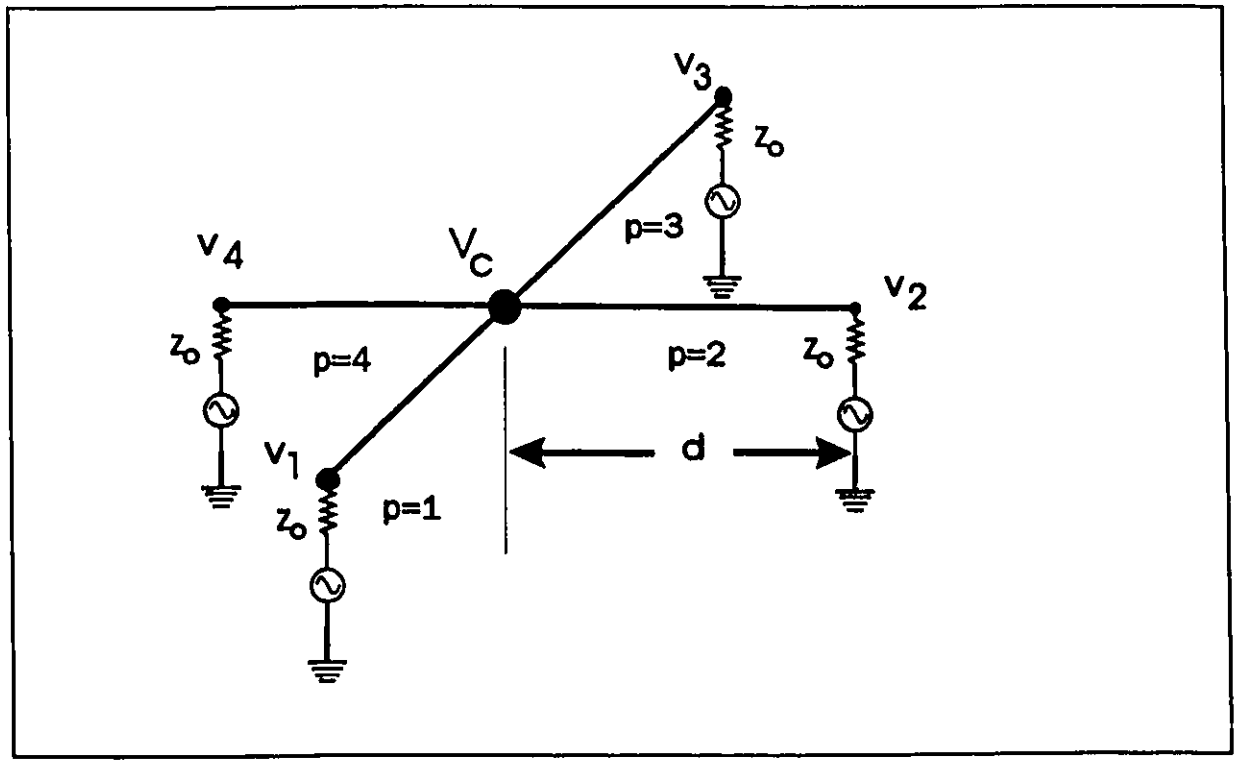

Fig. 2-8 Geometry of the TLM 2D shunt node for the calculation of the dispersion relation

where V^i_p and V^r_p are the incident and reflected voltages to and from the adjacent node attached to the p^{th} link line. In addition we define V^{i*}_p and V^{r*}_p as the incident and reflected voltages at the centre node on line "p". The scattering matrix of the shunt node itself, excluding the four interconnecting lines, was given by Eq. 2-7. The dispersion relation is developed at a single excitation frequency such that V^{i*}_p can be related to V^r_p as

$$V^{i*}_p = T_o \; V^r_p \qquad (2\text{-}33)$$

where T_o is given as

$$T_o = e^{-jk_o d} \tag{2-34}$$

where k_o is the propagation constant along the link lines at the excitation frequency. Likewise

$$V^i_p = T_o \; V^{r*}_p \; . \tag{2-35}$$

Now we define $\mathbf{V}^{i*}$, $\mathbf{V}^{r*}$, $\mathbf{V}^i$ and $\mathbf{V}^r$ as vector forms of V^{i*}_p, V^{r*}_p, V^i_p and V^r_p respectively. In addition a 4x4 matrix, $\mathbf{T}$ is defined as

$$\mathbf{T} = T_o \; \mathbf{I} \tag{2-36}$$

where $\mathbf{I}$ represents a 4x4 identity matrix. Consequently

$$\mathbf{V}^i = \mathbf{T} \, \mathbf{V}^{i*} \tag{2-37a}$$

$$\mathbf{V}^r = \mathbf{T} \, \mathbf{V}^{r*} \; , \tag{2-37b}$$

In view of Eq. 2-6, V_c can be expressed as

$$V_c = V^{i*}_p + V^{r*}_p = \frac{1}{2} \sum_{p=1}^{4} V^{i*}_p \; . \tag{2-38}$$

Also

$$\boldsymbol{V} = \boldsymbol{V}^i + \boldsymbol{V}^r = (\boldsymbol{T}^{-1} + \boldsymbol{T}\,\boldsymbol{S}) \; \boldsymbol{V}^{i*} \tag{2-39}$$

where $\mathbf{V}$ is defined as the vector of the adjacent node voltages, V_p. Combining

Eq. 2-38 and Eq. 2-39 with a little algebra, we obtain an equation relating V_c to V_p as follows:

$$V_c \left(\frac{2 \sin(2k_o d)}{\sin(k_o d)} \right) = V_1 + V_2 + V_3 + V_4 \qquad (2\text{-}40)$$

Solutions to Eq. 2-40 can be obtained by applying Floquet's theorem since the TLM shunt node is arranged in a uniform array of similar nodes forming a 2D periodic structure. In this application, Floquet's theorem is equivalent to postulating a field solution of the form

$$V_{i,j,k} = A_o \, e^{-j k_x d i} \, e^{-j k_y d j} \, e^{-j k_z d k} \qquad (2\text{-}41)$$

where k_x, k_y and k_z are unknown components of the mesh propagation vector, and A_o is an arbitrary constant. Hence, given the link line propagation constant k_o, we are looking for the family of plane wave eigensolutions of the form given by Eq. 2-41 that satisfies the relation given in Eq. 2-40. In this case a 2D mesh is considered in the xz plane, and therefore k_y=0. Assuming that a solution of the form given by Eq. 2-41 exists with k_y=0, we can write

$$V_1 = V_c \, e^{jk_x d} \qquad (2\text{-}42a)$$

$$V_2 = V_c \, e^{jk_x d} \qquad (2\text{-}42b)$$

$$V_3 = V_c\, e^{-jk_x d} \qquad (2\text{-}42c)$$

$$V_4 = V_c\, e^{-jk_x d} \quad . \qquad (2\text{-}42d)$$

Substituting Eq. 2-42 back into Eq. 2-40 results in the desired dispersion relation

$$\frac{\sin(2k_o d)}{\sin(k_o d)} = \cos(k_x d) + \cos(k_z d) \quad . \qquad (2\text{-}43)$$

Eq. 2-43 can be compared with the two known dispersion relations of the shunt TLM mesh in the direction along the x or z axis and along the diagonal x=y [23]. Consider first the case where $k_x d = 0$ which represents propagation along the z axis. Eq. 2-43 becomes

$$\frac{\sin(2k_o d)}{\sin(k_o d)} - 1 = \cos(k_z d) \qquad (2\text{-}44)$$

which can be written in a different form as

$$\cos(k_z d) = \cos(k_o d) - \tan(k_o d/2)\, \sin(k_o d) \qquad (2\text{-}45)$$

which appears in the literature [23].

Consider next the case when the propagation is along the diagonal line x=z by setting $k_x d = k_z d$. Using Eq. 2-43 we obtain

$$\cos(k_o d) = \cos(k_z d)$$

or $k_x d = k_z d = k_o d$. Consequently, the effective propagation constant is non-dispersive and is given by $\sqrt{2}\, k_o$ which is in agreement with the literature [23].

Note also that the general dispersion relation given by Eq. 2-43 is periodic in terms of $k_o d$ with a period of 2π. This also represents the periodicity with respect to the input frequency with a period of $1/\Delta t$.

In using Floquet's theorem, monochromatic excitation of the mesh is implied. The resulting dispersion relation is then valid for time harmonic fields but not necessarily for time sampled fields as is encountered in TLM processing. However, since the interconnecting transmission lines in the TLM mesh are assumed to be dispersionless, and the mesh is uniformly periodic, it can be shown that the dispersion relation of the mesh is exactly the same for a time harmonic signal as for a time sampled signal. This is shown in Appendix A.

2.4.2 Dispersion Relation of the 2D Series Node

The derivation of the dispersion relation for the series node is very similar to the derivation above for the shunt node. In this case the current at the centre of the series node is related to the currents at the centre of the four adjacent nodes as illustrated in Fig. 2-9. The currents into the node at the node centre are denoted as $J^{\cdot}_p$, where again "p" denotes the line number. $\mathbf{J}^{\cdot}$ is the vector of these currents. Likewise, at the centre of the adjacent nodes, the currents are denoted as J_p, and $\mathbf{J}$ is the vector array of these currents. I_c is the value of the current flowing around the centre series node in the

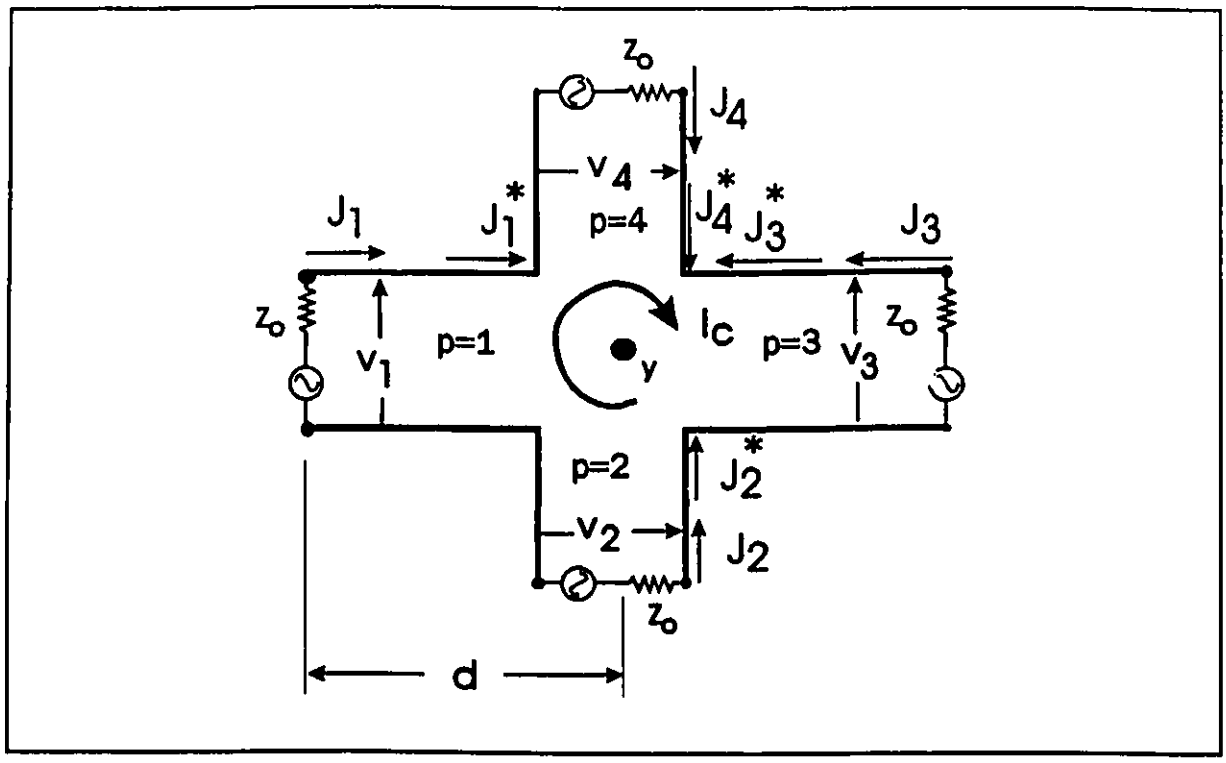

Fig. 2-9 Geometry of the 2D series TLM node used in the calculation of the dispersion relation

direction indicated in Fig. 2-9.

J^* and J can be written in terms of the incident and reflected voltages as

$$J^* = Y_o \, (V^{i*} - V^{r*}) \tag{2-46a}$$

$$J = Y_o \, (V^i - V^r) \, , \tag{2-46b}$$

Using the scattering matrix for the series node, given by Eq. 2-10,

$$J = Y_o \, (T^{-1} - T \, S) \, V^{i*} \tag{2-47}$$

where T was given in Eq. 2-36. Consequently

$$(\boldsymbol{T}^{-1} - \boldsymbol{T}\,\boldsymbol{S})^{-1}\,\boldsymbol{J} = Y_o\,\boldsymbol{V}^{i\bullet}\,, \tag{2-48}$$

The current I_c can be written in terms of $\mathbf{V}^{i\bullet}$ using Eq. 2-46a as

$$I_c = Y_o\,(V^{i\bullet}{}_1 - V^{r\bullet}{}_1)\,. \tag{2-49}$$

Using Eq. 2-48 and Eq. 2-49 gives

$$I_c = \frac{\sin(k_o d)}{2\,\sin(2k_o d)}\,(J_1 - J_2 - J_3 + J_4)\,. \tag{2-50}$$

The TLM shunt node is arranged in a uniform array of similar nodes forming a 2D periodic structure. Applying Floquet's theorem as for the shunt node in Section 2.4.1, an eigensolution to Eq. 2-50 is postulated based on the assumption that

$$J_1 = J_c\,e^{jk_x d} \tag{2-51a}$$

$$J_2 = J_c\,e^{jk_x d} \tag{2-51b}$$

$$J_3 = J_c\,e^{-jk_x d} \tag{2-51c}$$

$$J_4 = J_c\,e^{-jk_x d} \tag{2-51d}$$

resulting in the dispersion relation

$$\frac{\sin(2k_o d)}{\sin(k_o d)} = \cos(k_x d) + \cos(k_z d) . \qquad (2\text{-}52)$$

Eq. 2-52 is the desired dispersion relation for the 2D series node mesh. It is exactly the same as the dispersion relation of the shunt node.

2.4.3 Dispersion Relation of the 3D Expanded Node

The structure of the 3D TLM expanded node was given in Fig. 2-5 as an interlaced arrangement of series and shunt nodes. The dispersion relation was derived using a similar procedure to the derivations for the shunt and series nodes above. Since the algebra is somewhat tedious, details of the derivation are presented in Appendix B. In its final form, the eigenmatrix equation for the expanded node is given by

$$\mathbf{A} \begin{pmatrix} V_x \\ V_y \\ V_z \end{pmatrix} = 0 \qquad (2\text{-}53)$$

where the voltages V_x, V_y and V_z are indicated in Fig. 2-5. The eigenmatrix **A** is a 3 by 3 matrix with entities a_{ij} given by

$$a_{11} = C_o^2 \, (12 + 2\, C_y + 2\, C_z) - 1$$

$$a_{12} = 4\, C_o^2 \, T_x^{*} \, T_y^{*} \, S_x \, S_y$$

$$a_{13} = 4\ C_o^2\ T_x^{+4}\ T_z^{-4}\ S_x\ S_z$$

$$a_{21} = 4\ C_o^2\ T_x^{-4}\ T_y^{-4}\ S_x\ S_y$$

$$a_{22} = C_o^2\ (12 + 2\ C_x + 2\ C_z) - 1$$

$$a_{23} = 4\ C_o^2\ T_y^{-4}\ T_z^{-4}\ S_y\ S_z$$

$$a_{31} = 4\ C_o^2\ T_x^{-4}\ T_z^{+4}\ S_x\ S_z$$

$$a_{32} = 4\ C_o^2\ T_y^{+4}\ T_z^{+4}\ S_y\ S_z$$

$$a_{33} = C_o^2\ (12 + 2\ C_x + 2\ C_y) - 1 \qquad (2\text{-}54)$$

where

$$C_o = \frac{\sin(k_o d/2)}{2\ \sin(k_o d)}$$

$C_x = \cos(k_x d)$ $\quad C_y = \cos(k_y d)$ $\quad C_z = \cos(k_z d)$

$S_x = \sin(k_x d/2)$ $\quad S_y = \sin(k_y d/2)$ $\quad S_z = \sin(k_z d/2)$

$T_x = \exp(-jk_x d/2)$ $\quad T_y = \exp(-jk_y d/2)$ $\quad T_z = \exp(-jk_z d/2)$

Consider the case where only one electric field component, namely the E_x field (or V_x), is non-zero. Then the eigenvalue equation reduces to $a_{11}=0$ such that the dispersion relation becomes

$$2\frac{\sin^2(k_o d)}{\sin^2(k_o d/2)} = 6 + \cos(k_y d) + \cos(k_z d) \qquad (2\text{-}55)$$

For the special case where $k_y d=0$, Eq. 2-55 reduces to the dispersion relation given in [23] for propagation along the axis.

2.4.4 Dispersion Relation of the 3D Condensed Node

In deriving the dispersion relation for the condensed node a similar format is used as for the shunt and series nodes. An expression is written relating the port voltages of a particular node in an infinite 3D mesh, denoted as node "c", and the voltages of the six surrounding adjacent nodes at the ports directly connected to node "c". It is convenient to consider the six adjacent nodes as a single conglomerate node denoted by node "t". Node "t" has 12 ports which connect directly to the 12 ports of node "c". The numbering of the ports of node "t" is such that port "p" of node "c" is directly connected with port "p" of node "t". The table given below lists the ports of the conglomerate node and the node indices and ports to which they correspond. The indices given in the table are based on the assumption that the indices of node "c" are i,j,k.

Table 2-2 Adjacent node port correspondences of the condensed node

port of node "t"	corresponding adjacent node	
	indices	port
0	i,j-1,k	11
1	i,j,k-1	8
2	i-1,j,k	10
3	i,j,k-1	7
4	i,j-1,k	6
5	i-1,j,k	9
6	i,j+1,k	4
7	i,j,k+1	3
8	i,j,k+1	1
9	i+1,j,k	5
10	i+1,j,k	2
11	i,j+1,k	0

The following voltage vectors corresponding to nodes "c" and "t" are defined as:

V_c = vector of the total voltage at the ports of node "c"

V_t = vector of the total voltage at the ports of node "t"

V_{ci} = incident voltage vector corresponding to V_c

V_{cr} = reflected voltage vector corresponding to V_c

V_{ti} = incident voltage vector corresponding to V_t

V_{tr} = reflected voltage vector corresponding to V_t .

The relations between the total voltage and the incident and reflected components are

$$V_c = V_{ct} + V_{cr} \qquad (2\text{-}56a)$$

$$V_t = V_{tt} + V_{tr} \quad . \qquad (2\text{-}56b)$$

Furthermore, T is defined as the propagation matrix along the interconnecting lines such that

$$V_{tt} = T\, V_{cr}$$

$$V_{ct} = T\, V_{tr}$$

$$T = T_o\, I \qquad (2\text{-}57)$$

where T_o was defined in Eq. 2-34 and I is a 12x12 identity matrix. Combining the above equations we obtain

$$V_t = (I + T^2 S)\, V_{tr}$$

$$V_c = (I + S)\, V_{ct} = T\,(I + S)\, V_{tr} \quad . \qquad (2\text{-}58)$$

An additional relation is generated by applying Floquet's theorem to the mesh along the three coordinate axes. As before, a solution of the form given by Eq. 2-41 is assumed. Considering the node structure of Fig. 2-6, the following relations are obtained between the node voltages of node "c" and node "t":

$$
\begin{aligned}
V_{t0} &= V_{c11}\, e^{jk_y d} \\
V_{t1} &= V_{c8}\, e^{jk_x d} \\
V_{t2} &= V_{c10}\, e^{jk_x d} \\
V_{t3} &= V_{c7}\, e^{jk_x d} \\
V_{t4} &= V_{c6}\, e^{jk_y d} \\
V_{t5} &= V_{c9}\, e^{jk_x d} \\
V_{t6} &= V_{c4}\, e^{-jk_y d} \\
V_{t7} &= V_{c3}\, e^{-jk_x d} \\
V_{t8} &= V_{c1}\, e^{-jk_x d} \\
V_{t9} &= V_{c5}\, e^{-jk_x d} \\
V_{t10} &= V_{c2}\, e^{-jk_x d} \\
V_{t11} &= V_{c4}\, e^{-jk_y d}
\end{aligned}
\qquad (2\text{-}59)
$$

which can be summarized in matrix form as

$$\mathbf{V}_t = \mathbf{P}\,\mathbf{V}_c \qquad (2\text{-}60)$$

which defines matrix **P**. Finally, combining all the above equations yields

$$\mathbf{V}_c = \mathbf{T}\,(\mathbf{I} + \mathbf{S})(1 + \mathbf{T}^2\,\mathbf{S})^{-1}\,\mathbf{P}\,\mathbf{V}_c \qquad (2\text{-}61)$$

from which the required eigenvalue equation

$$\det\{\,\mathbf{T}\,(\mathbf{I} + \mathbf{S})(1 + \mathbf{T}^2\,\mathbf{S})^{-1}\,\mathbf{P} - \mathbf{I}\,\} = 0 \qquad (2\text{-}62)$$

is obtained. The eigenvalue equation is an implicit function of k_x, k_y, k_z and k_o. It results in the desired general dispersion equation.

Eq. 2-61 is the eigenvector equation corresponding to the node voltage vector V_c. Eq. 2-62 is used to determine the components of the mesh propagation vector. These results can then be used in Eq. 2-61 to determine the eigenvector

of V_c which is useful for determining the field distribution of the simulated plane wave. It is also possible to derive a corresponding eigenvector equation based on the incident voltage vector, V_{ci}. Using the equations above, the required equation is given as

$$(I - (P - T^{-1})^{-1} (P - T)) V_{ci} = 0 \qquad (2\text{-}63)$$

which can be simplified to

$$(I - T P S) V_{ci} = 0 \qquad (2\text{-}64)$$

using the property that S and P are unitary matrices. The characteristic equation of Eq. 2-64 is equivalent to Eq. 2-62. Hence either can be used as the general dispersion equation. Exploitation of the eigenvector relations above will be discussed in Section 2.6.

2.4.5 Calculated Dispersion Characteristics

In this section, results are given for the dispersive properties of the 3D expanded and condensed TLM node structures and Yee's FD-TD scheme. The dispersion of the various schemes was compared for the case of a plane wave propagating in the y-z plane such that k_x=0 as documented in reference [35].

The general dispersion relation for the Yee's FD-TD scheme is given as [37]:

$$\sin^2(k_o d\frac{s}{2}) = s^2 \left(\sin^2(\frac{k_x d}{2}) + \sin^2(\frac{k_y d}{2}) + \sin^2(\frac{k_z d}{2})\right) \quad (2\text{-}65)$$

where s is the stability factor defined as

$$s = \frac{\Delta t}{d\sqrt{e_o \mu_o}}$$

Fig. 2-10 shows a family of dispersion curves for the 3D FD-TD scheme based on Eq. 2-65 for various excitation frequencies. The stability factor used for this calculation was s=1/√3 which is the largest stability factor possible. The larger the stability factor, the lower the numerical dispersion [35]. Note that the FD-TD node mesh is isotropic only at low frequencies as seen by the circular curve for $k_o d = 0$. For $k_o d > 0$ the circular curve becomes distorted. The maximum dispersion occurs for propagation along the axis and the minimum dispersion occurs along the diagonal $k_y = k_z$.

Fig. 2-11 shows the resulting family of dispersion curves for the expanded TLM node. In order to compare the dispersion characteristics, the excitation frequencies in Fig. 2-11 correspond to the excitation frequencies in Fig. 2-10. The $k_o d$ values used for the TLM dispersion calculation are half the corresponding $k_o d$ value used in Fig. 2-10. The reason for this is that the mesh velocity in the TLM scheme is half the velocity of the link lines. Note that the dispersive characteristics are very similar to those of the FD-TD scheme. The dispersion of the FD-TD scheme in Fig. 2-10 is slightly better than the

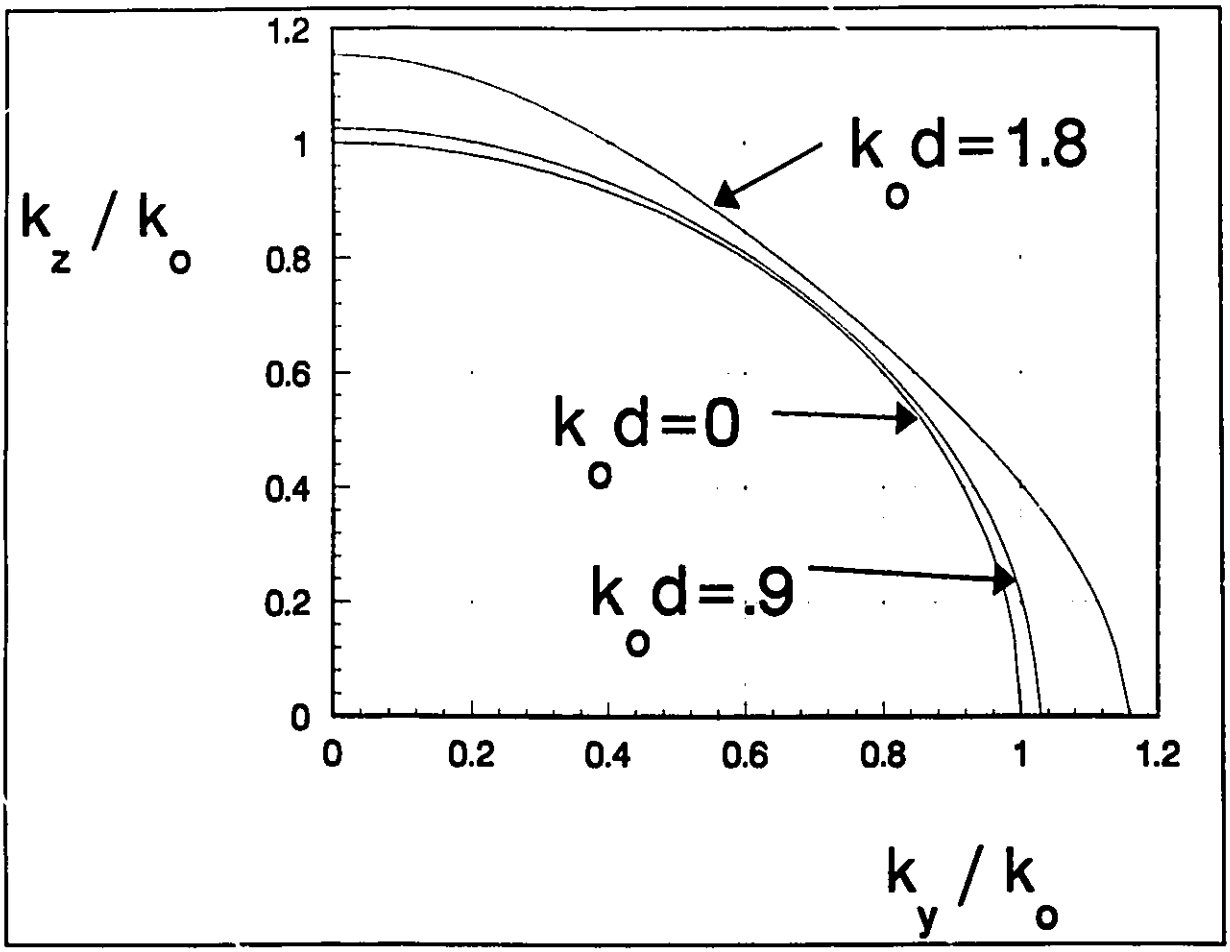

Fig. 2-10 Plot of the dispersion characteristics for a FD-TD mesh with a stability factor of $s=1/\sqrt{3}$

dispersion portrayed in Fig. 2-11. However, if the stability factor of the FD-TD scheme is increased to ½ then the dispersion becomes identical to that of the expanded TLM node. This is not surprising since the FD-TD and expanded node TLM are equivalent in the special case when s = 1/2 [38].

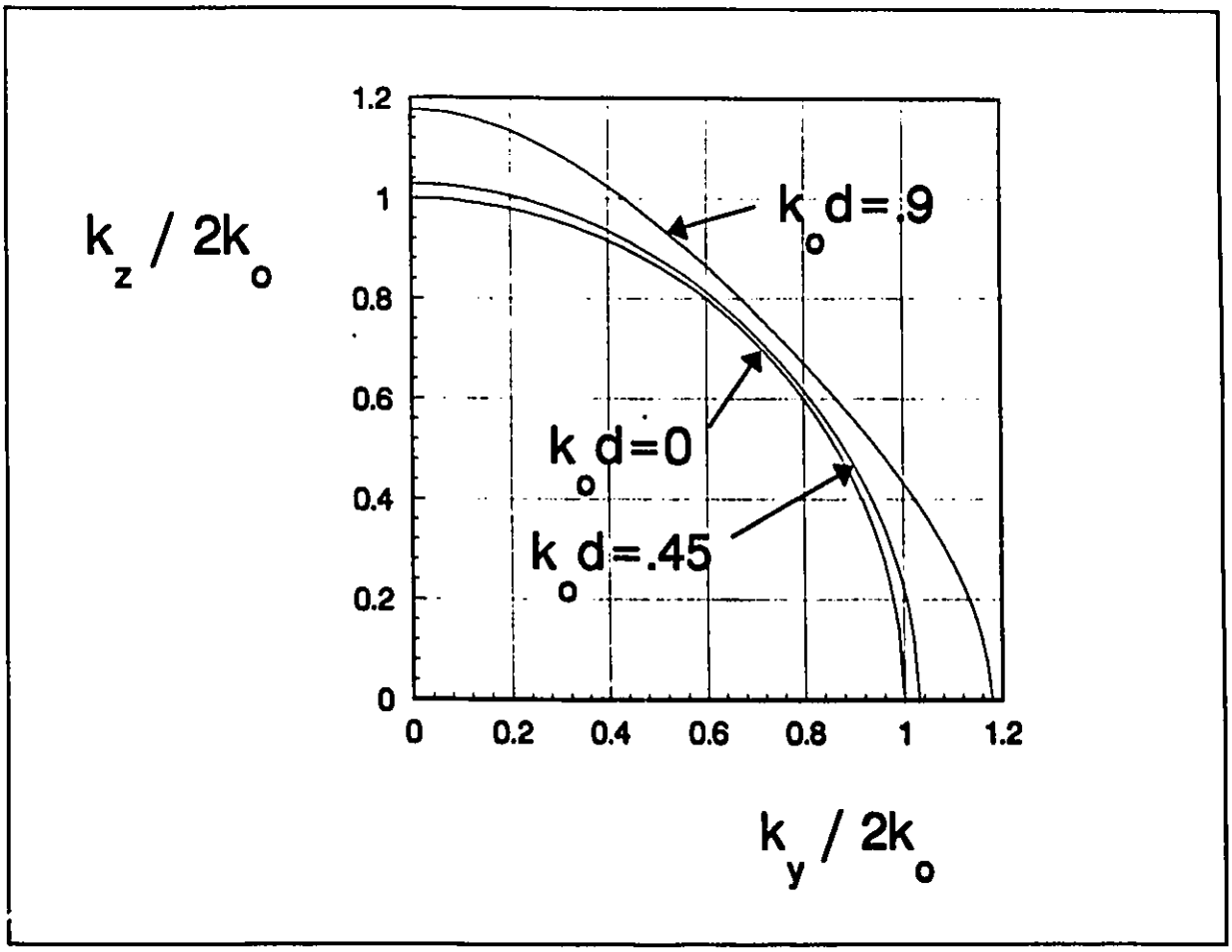

Fig. 2-11 Plot of the dispersion characteristics for a 3D expanded TLM node mesh

The corresponding dispersion curves for the condensed node are given in Fig. 2-12. The dispersion is zero along the y and z axes unlike in the expanded TLM node or the FD-TD mesh where the dispersion is maximum. The maximum dispersion occurs for propagation along the diagonal y=z. The dispersion along this bearing is the same as for the expanded TLM node. This observation was made earlier by Johns [21].

In comparing these plots, the superior dispersion characteristics of the condensed node mesh are demonstrated. The only region where the dispersion of the condensed node exceeds the FD-TD mesh is in the region of $k_y = k_z$ for

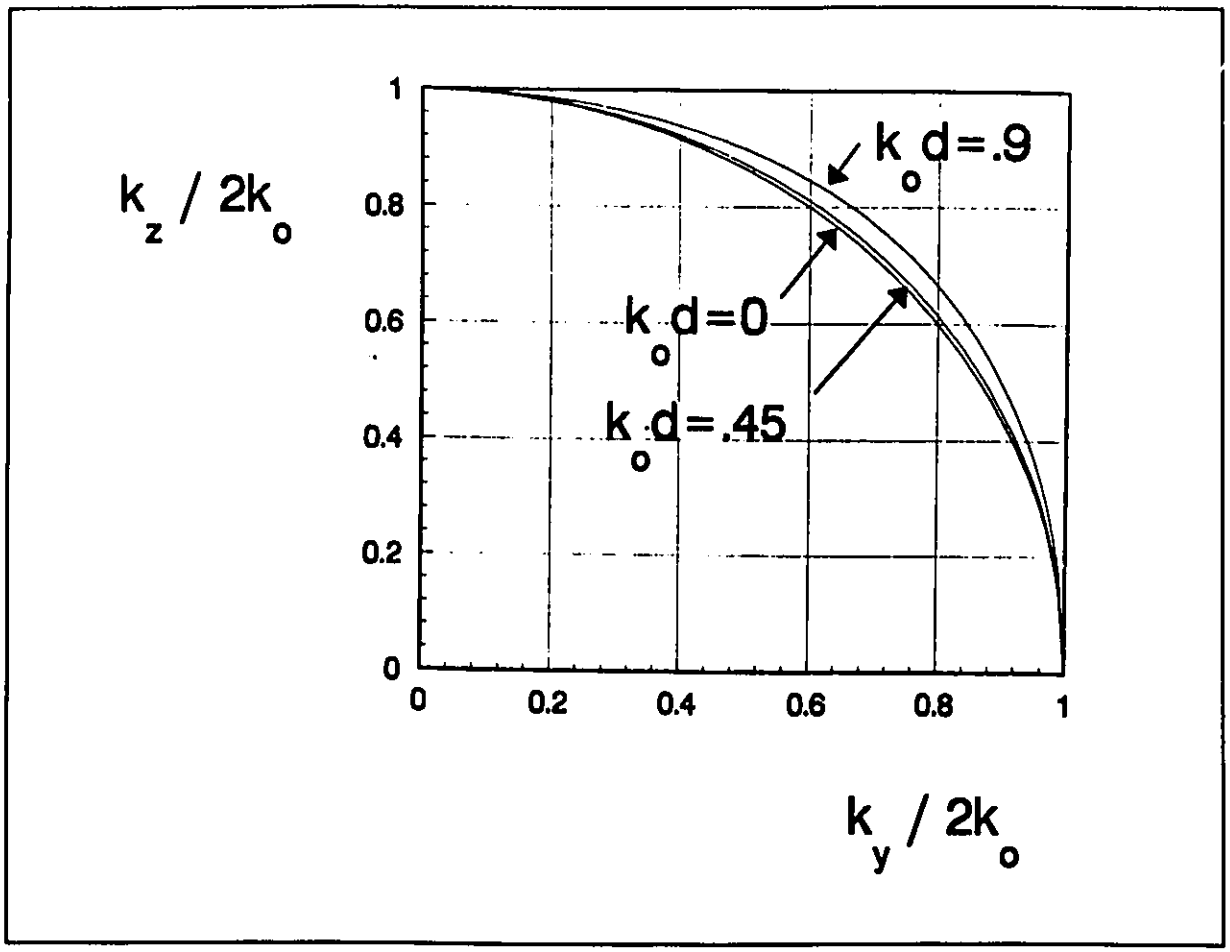

Fig. 2-12 Plot of the dispersion characteristics for a 3D TLM condensed node mesh

stability factors greater than 0.5 which are not generally used in practice.

As a further graphical demonstration of the dispersion characteristics, the dispersive solution surface is plotted for the condensed and expanded nodes for plane wave propagation in an arbitrary direction. If $k_o d=0$, then the solution surface is a perfect sphere for both cases as should be anticipated since the periodic mesh is dispersionless at very low frequencies. A plot of the dispersion surfaces for the expanded and condensed node for a high frequency of $k_o d=0.7$ is given in Fig. 2-13. As observed the surfaces for both the expanded and condensed nodes deviate from the ideal spherical form. However, the

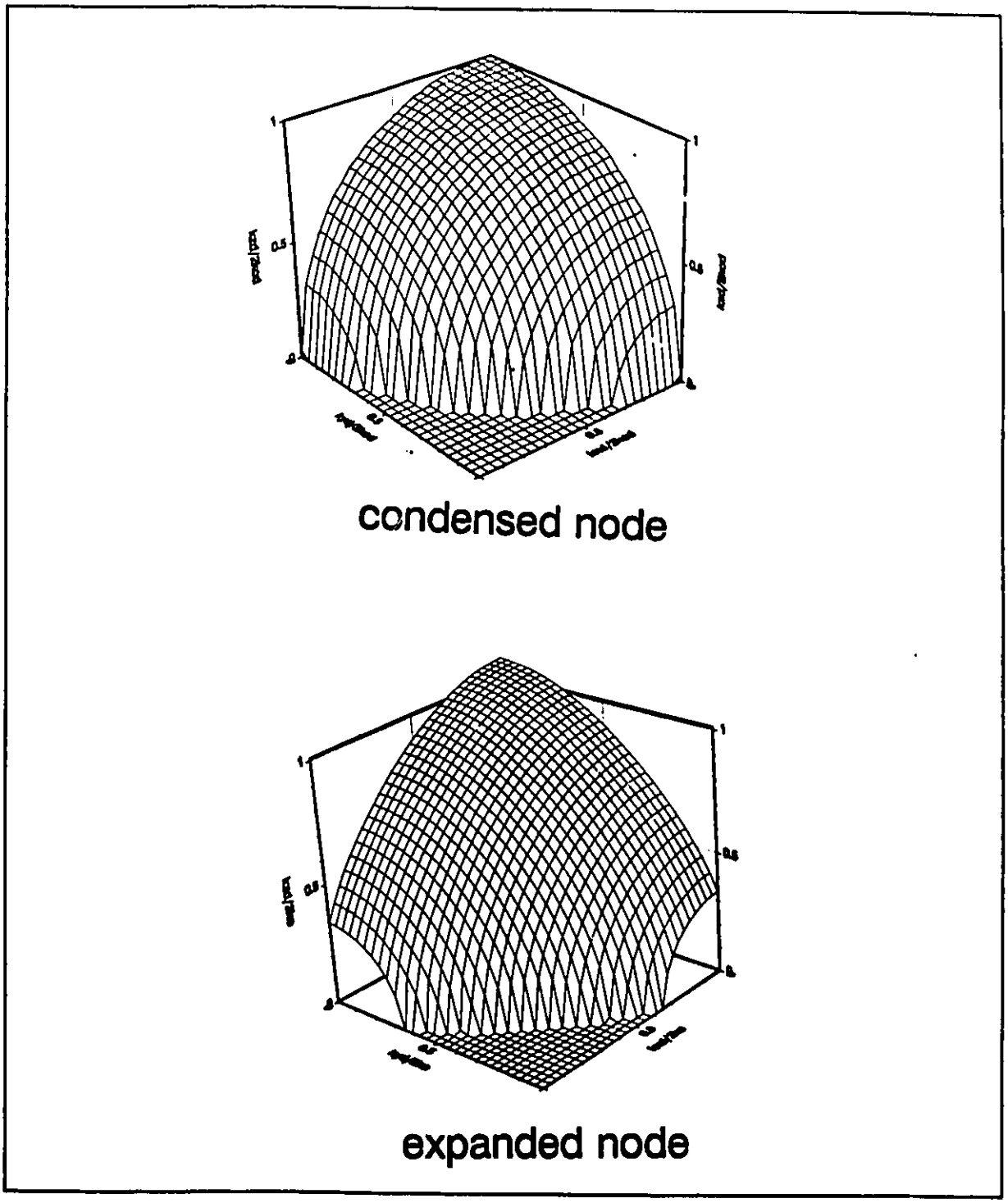

Fig.2-13 Plot of the dispersion surface for the condensed node and expanded node mesh for $k_0d=.7$

distortion of the expanded TLM node surface is much more severe especially in the neighbourhood of the x, y and z axes.

2.5 SPURIOUS MODES OF THE 3D CONDENSED NODE MESH

In addition to numerical dispersion, "non-physical" spurious modes are generally supported in spatially sampled schemes. Since spurious modes can be very detrimental in numerical simulations, they have been thoroughly investigated by numerous researchers. While the attributes of spurious modes are well known, a clear understanding of the origin of spurious modes is generally lacking. An excellent review of spurious modes in FE and FD schemes was recently given by Lynch and Paulsen [39]. Interesting numerical examples and explanations of spurious modes in the FD-TD method was discussed by Trefethen [37].

It is interesting to note that the shunt and series TLM nodes support no low frequency spurious modes. This can be observed from the general dispersion relation given by Eq. 2-43. The dispersion equation has eigensolutions of $k_x d$, $k_y d$ and $k_z d$ for a given $k_o d$ that are periodic with a period of 2π which is merely a consequence of the spatial sampling. No other solutions exist. As pointed out by Lynch and Paulsen [39], Yee's leap-frog FD-TD scheme does not support spurious modes. This is thought to be a consequence of the staggered mesh configuration. Since the 3D TLM expanded node is a special case of this FD-TD scheme with a stability factor of $\frac{1}{2}$, it also does not support spurious modes. This postulate was investigated by an analysis of the dispersion relation for the expanded node given by Eq. 2-53. The 3D condensed node does not have a staggered mesh structure and does support spurious modes as was recently revealed by Nielsen

[40]. Attributes of these spurious solutions will be discussed in Section 2.5.1, and examples of spurious mode excitation will be given in Section 2.5.2.

2.5.1 Attributes of the Spurious Modes

Consider first the solutions for $k_x d$, $k_y d$ and $k_z d$ for a small value of $k_o d$. The solutions form an approximate sphere with a radius of approximately $2 \cdot k_o d$. Along the diagonal, $k_x d = k_y d = k_z d$, the radius is slightly inflated, revealing some dispersion as discussed in Section 2.4.4. Due to the spatial sampling imposed by the mesh along x,y, and z, the solution to the dispersion relation, Eq. 2-62 or Eq. 2-64, is periodic along the $k_x d$, $k_y d$ and $k_z d$ axis. That is, if $k_x o$, $k_y d$, $k_z d$ are solutions to the dispersion relation for a particular $k_o d$ then

$$
\begin{aligned}
& k_x d + ii \cdot 2\pi \qquad ii = \pm 1, \pm 2, \ldots \\
& k_y d + jj \cdot 2\pi \qquad jj = \pm 1, \pm 2, \ldots \\
& k_z d + kk \cdot 2\pi \qquad kk = \pm 1, \pm 2, \ldots
\end{aligned}
$$

are also solutions. Consequently, the solution sphere centred around $k_x d = k_y d = k_z d = 0$ is replicated in a cubic node pattern with a spacing of 2π. All these solution spheres do not contribute to spurious modes but are merely a consequence of spatial sampling. In addition to the above solutions there is also a solution sphere centred at $k_x d = k_y d = k_z d = \pi$. This represents the spurious propagating mode solutions. As before, spurious solution spheres exist at intervals of 2π in $k_x d$, $k_y d$ and $k_z d$, due to spatial sampling. The total solution, assuming $k_o d$ is small, appears as a body-centred-cubic node structure as is shown in Fig. 2-

14.

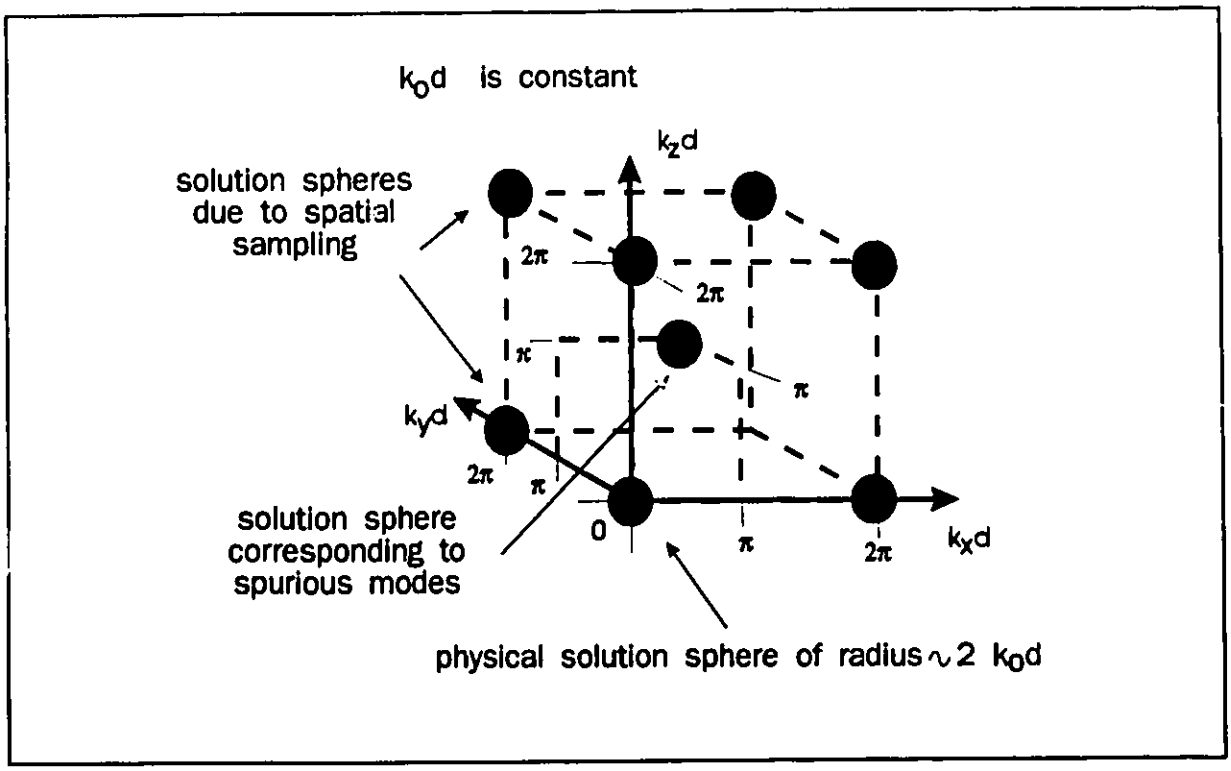

Fig. 2-14 Illustration of the solution spheres satisfying the dispersion equation showing a body-centred-cubic structure

The consequences of spurious solutions can be visualized by considering an infinite source plane in the xy plane radiating into an infinite 3D mesh. Assume that the source plane generates a plane wave at a single frequency corresponding to k_o and that it has a transverse dependence of $k_x x$ and $k_y y$. Using the dispersion relation, $k_z d$ can be evaluated for the radiated plane wave. The propagation characteristics of the radiated plane wave can be categorized into four regions as outlined in Fig. 2-15. The first region for small $k_x d$ and $k_y d$ is the "physical propagating modes" region. The propagating constant, $k_z d$, for these modes is real and close to the theoretical value of

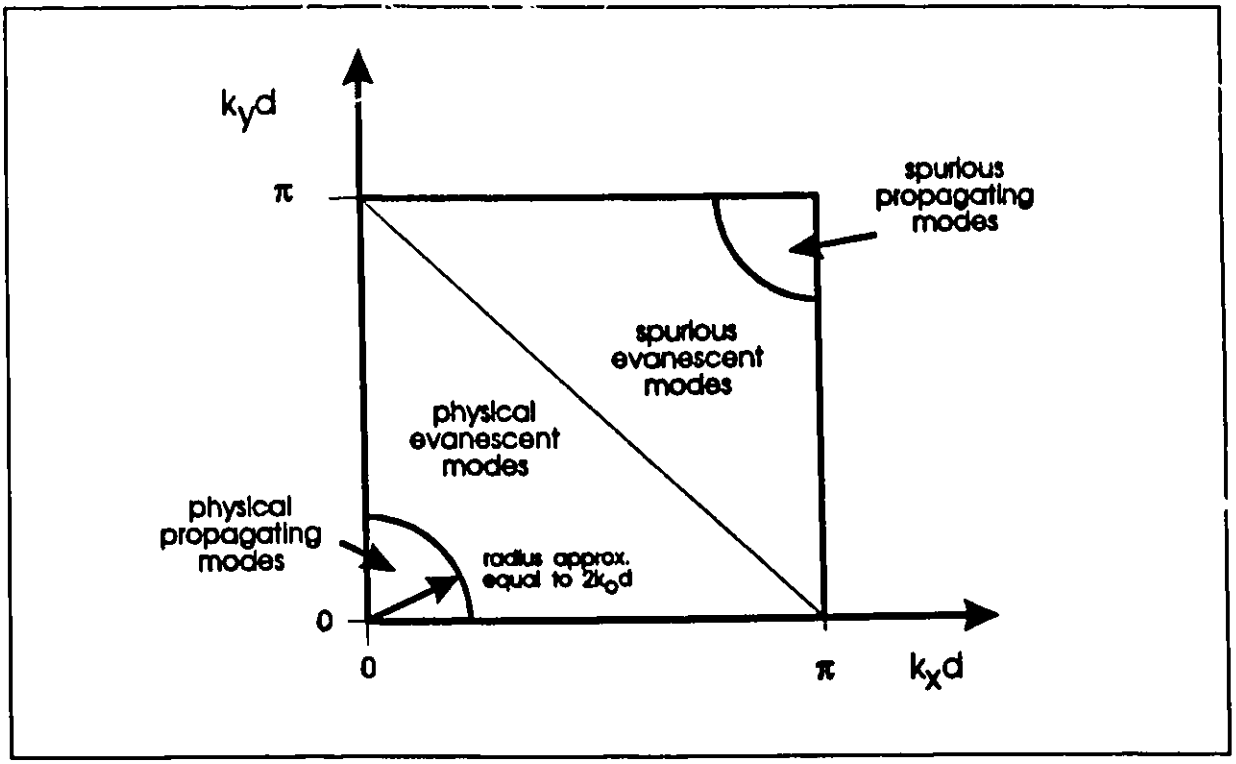

Fig. 2-15 Spectral regions corresponding to physical and spurious plane wave mode propagation for the 3D condensed node

$$k_z d = \sqrt{(2\,k_o d)^2 - (k_x d)^2 - (k_y d)^2} \qquad (2\text{-}66)$$

Assuming an excitation frequency such that $k_o d$ is small relative to π, the boundary of this region is approximately circular, with a radius of 2 $k_o d$. As $k_o d$ increases, the boundary will bulge slightly around the diagonal $k_x d = k_y d$.

The adjacent region is denoted as the "physical evanescent modes" region. It exhibits a purely imaginary $k_z d$ that increases in magnitude with the modal index, as expected in actual waveguide modes. Near the physical mode cutoff boundary, the imaginary part of $k_z d$ follows Eq. 2-67 accurately, provided $k_o d$ is reasonably small.

The propagation constant for a mode located along the diagonal line given

by

$$k_x d + k_y d = \pi,$$

has a negative infinite imaginary component which indicates no propagation at all. Crossing this line such that

$$k_x d + k_y d > \pi$$

the real part of $k_z d$ jumps to π. The modes in this region are denoted as the "spurious evanescent modes". In this region, the magnitude of the imaginary component of $k_z d$ decreases as the mode index increases.

The boundary between the spurious evanescent and propagating modes is a mirror image of the boundary separating the physical propagating and evanescent modes and is located approximately on the curve given by

$$2k_o d = \sqrt{(\pi - k_x d)^2 + (\pi - k_y d)^2}. \tag{2-67}$$

The spurious propagating modes have a propagation constant of approximately

$$k_z d \approx \pi \pm \sqrt{2k_o d - (\pi - k_x d)^2 - (\pi - k_y d)^2} \tag{2-68}$$

which is purely real, indicating lossless propagation. Note the constant offset factor of π. The upper sign in Eq. 2-68 denotes the forward propagating spurious mode and the lower sign the backward propagating mode.

Fig. 2-16 shows the real and imaginary parts of $k_z d$ as a function of $k_x d$ for

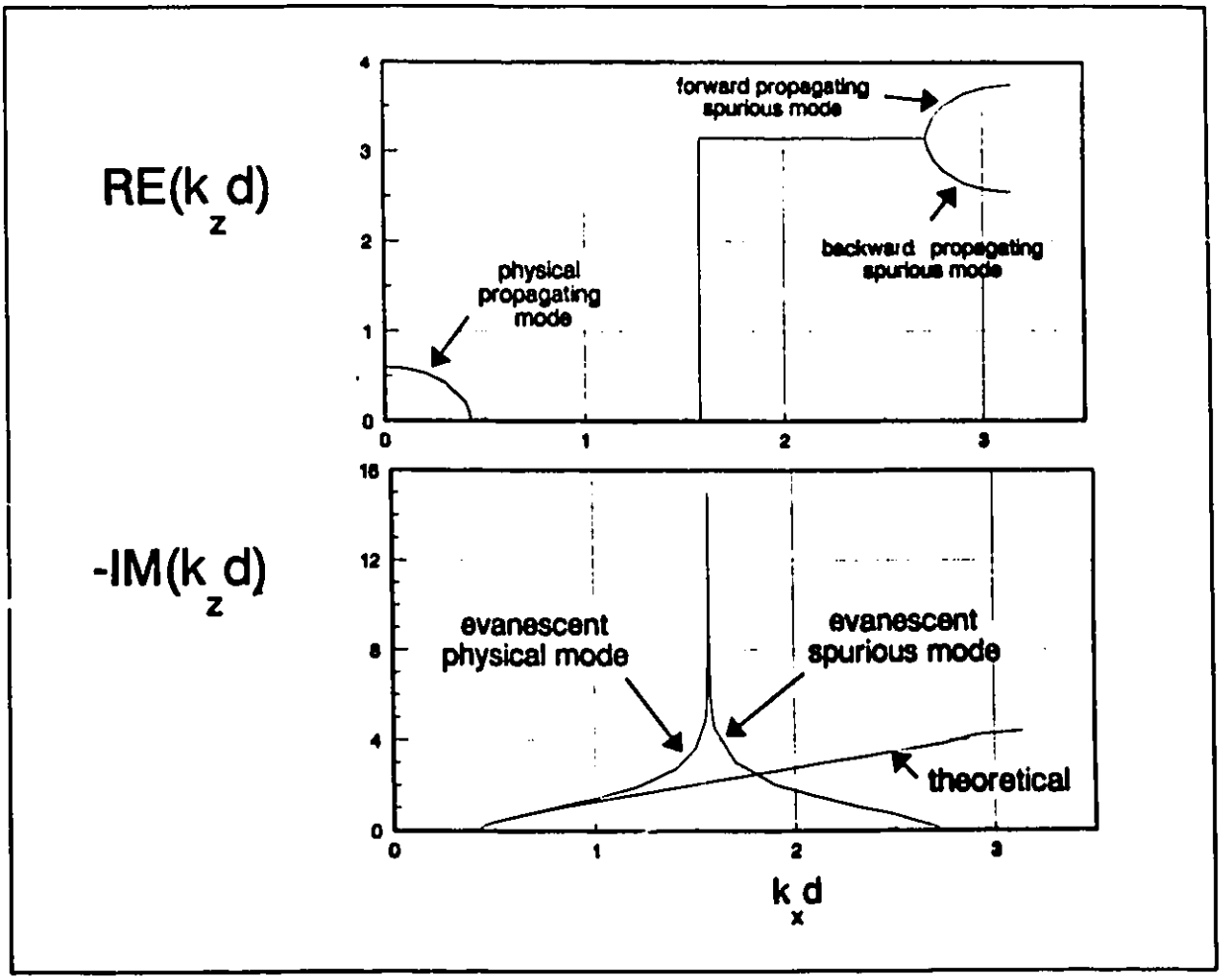

Fig. 2-16 Plot of the real and imaginary components of $k_z d$ as a function of $k_x d$ with $k_o d=0.3$ and $k_y d=k_x d$

$k_x d = 0$ to $k_x d = \pi$, with $k_y d = k_x d$. In this example $k_o d$ is chosen to be 0.3. For small values of $k_x d$, $k_z d$ is real until the cutoff point at $k_x d=0.42$. In the plot of the real part part of $k_z d$, the theoretical solution of Eq. 2-66 is superimposed and is indistinguishable from the curve given by the dispersion relation (Eq. 2-62). At $k_x d=\pi/2$, the real part of $k_z d$ jumps to a value of π. At the cutoff point of the spurious mode, given by

$$k_x d = \pi - 0.42$$

the spurious mode begins to propagate. At this point the curve splits into two parts which correspond to forward and backward mode propagation as indicated.

Consider next the curve of the imaginary part of $k_z d$ shown in Fig. 2-16. When $k_x d$ exceeds the cutoff point, the mode becomes evanescent. It follows the theoretical curve, given by Eq. 2-66, reasonably closely until $k_x d$ approaches the discontinuity at $k_x d = \pi/2$. Beyond the discontinuity, the mode becomes spurious. At the propagating spurious mode cutoff, the imaginary part of $k_z d$ becomes zero.

2.5.2 Examples of Spurious Mode Excitation

From the dispersion relation, Eq. 2-62 or Eq. 2-64, it can be verified that a solution exists with $k_x d = k_y d = k_z d = \pi$ and $k_o d = 0$. The existence of this DC spurious solution can be predicted directly from the scattering matrix of the condensed node given in Eq. 2-16. Using the eigenequation Eq. 2-64, it can be verified that an eigenvector for V^i is

$$
\begin{aligned}
V^i_0 &= 1 & V^i_6 &= -1 \\
V^i_1 &= 1 & V^i_7 &= 1 \\
V^i_2 &= -1 & V^i_8 &= -1 \\
V^i_3 &= -1 & V^i_9 &= 1 \\
V^i_4 &= 1 & V^i_{10} &= 1 \\
V^i_5 &= -1 & V^i_{11} &= -1
\end{aligned}
$$

The scattering matrix for the condensed node shows that for this case

$$V^r = S V^i = -V^i .$$

By calculating the incident and reflected voltages for the adjacent nodes assuming $k_x d=k_y d=k_z d=\pi$, it can be shown that the voltages V^i and V^r do not change when the mesh is updated. Consequently, this corresponds to a DC solution. This spurious solution was predicted in Fig. 2-14 for $k_o d=0$.

It is interesting to note that Johns originally approximated the six field components as an average of four port voltages [21]. As an example, the E_y field component is evaluated as the average of voltages at ports 2,3,7 and 10 as

$$E_y = \frac{1}{2d} \left(V^i_2 + V^i_3 + V^i_7 + V^i_{10} \right) \tag{2-70}$$

For the DC spurious mode, $k_x d=\pi$ and $k_y d=\pi$, resulting in $E_y=0$. For small values of $k_o d$, $k_x d$ and $k_y d$ will still be approximately equal to π, resulting in a small E_y value. This is perhaps why the presence of spurious modes has not been observed before.

Next, consider the case of a propagating spurious mode. Assume a y-polarized transverse field sheet of infinite extent in x and y with a variation of $k_x d = k_y d = \pi$. At t=0 we assume that the transverse field sheet is incident on the plane of nodes with k=0. For a particular node i,j,k=0 we assume that the incident voltages are zero except

$$v^i_3(i,j,0) = 1$$

The voltages incident on the adjacent nodes are also zero except

$$v^i_3(i+1,j,0) = v^i_3(i-1,j,0) = v^i_3(i,j+1,0) = v^i_3(i,j-1,0) = -1$$

Based on the scattering matrix, after two time increments, $t=2\Delta t$, we have $v^r_3(i,j,0) = 0$, and $v^r_7(i,j,0) = -1$. Consequently $v^i_3(i,j,1) = -1$. This corresponds to a propagating 2D impulse field moving in the +z direction at a velocity of $d/2\Delta t$. Note that the transverse impulse field does not spread, which indicates that axial propagation of a spurious mode is dispersionless. This is exactly the propagation characteristics of a "physical" transverse impulse field with $k_x d=k_y d=0$.

Consider a final example of a waveguide cavity that consists of an array of condensed nodes of dimension $N_x=14$, $N_y=6$ and $N_z=1$ that is surrounded by electric walls on all six sides. The cavity is initially excited with a mode with spatial variation

$$k_x d = \pi(N_x-1)/N_x \qquad k_y d = \pi \qquad k_z d = \pi$$

In order to obtain the actual spurious eigenmode, the simulation was started with some high pass spatial filtering. This spatial filtering promoted the spurious mode and attenuated the corresponding physical mode. The resulting voltage at node 3 of the node at i=7, j=5 and k=0 is plotted in Fig. 2-17. Note that the response quickly settles into a low frequency sinusoidal waveform. The spatial filter was switched off at $t=600\Delta t$. Hence the remaining oscillation is due to the pure spurious eigenmode. The period of oscillation is 56 Δt or $4N_x$ which is the cutoff frequency of the TE_{10} mode with $k_x d = \pi/Nx$, $k_y d=0$ and $k_z d = 0$. This is exactly as predicted by the dispersion relation.

Fig. 2-18 is a plot of the field distribution of the spurious mode at $t=1400\Delta t$. Here the total voltage of port 3 is used to represent the field distribution.

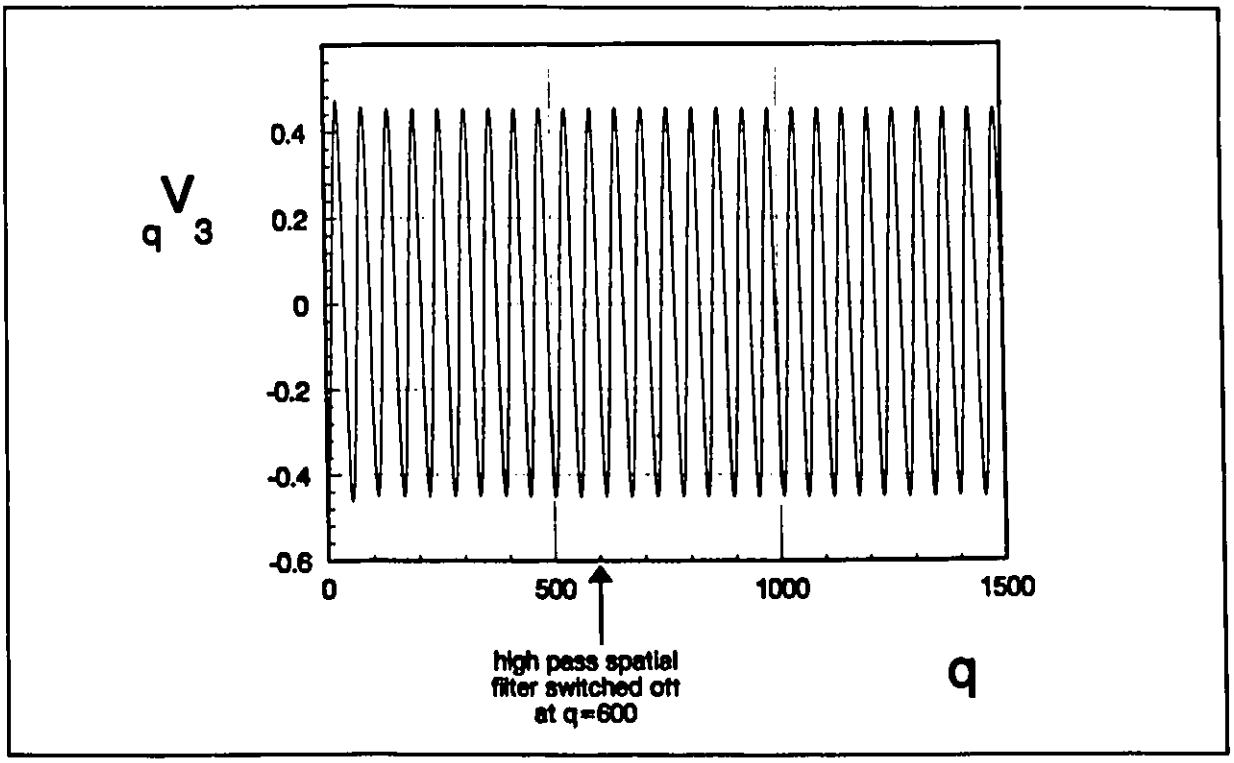

Fig. 2-17 Response of a waveguide cavity excited with a spurious mode. The voltage at port 3 of node i=7,j=5,k=0 is plotted.

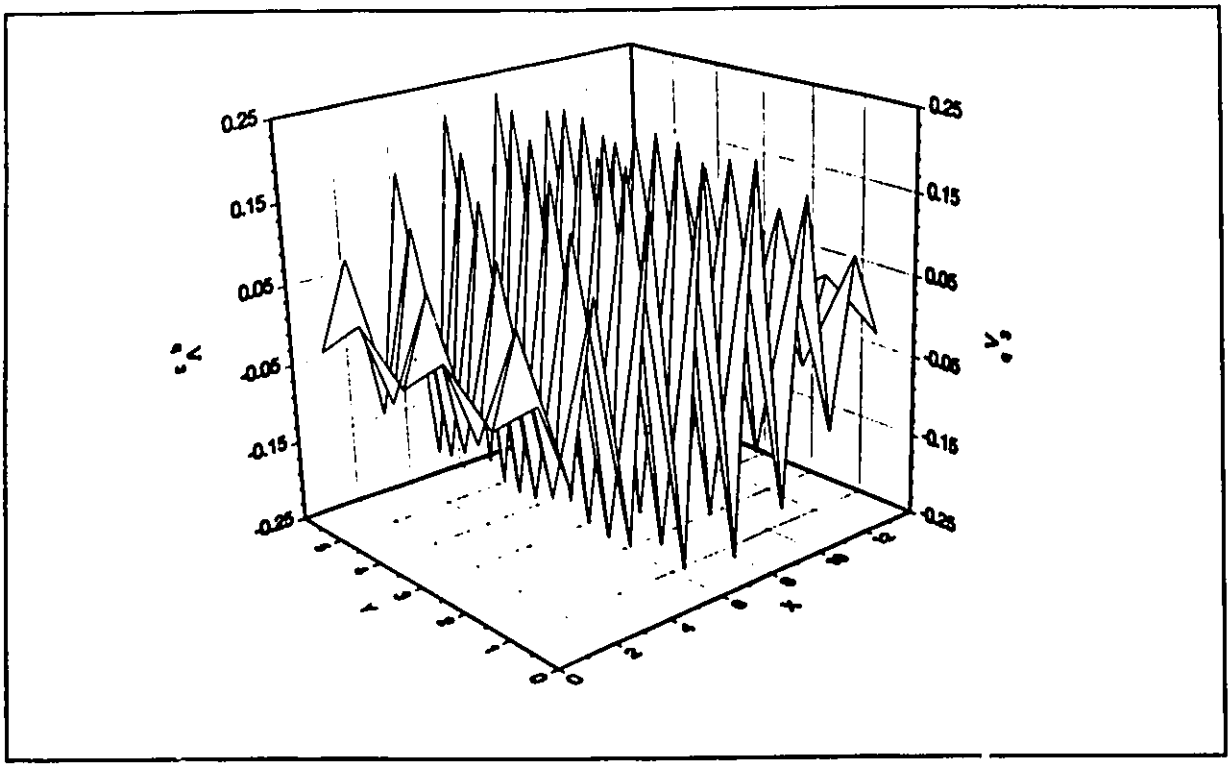

Fig. 2-18 Spatial plot of the spurious mode. Plotted is the total port voltage at port 3 of each node at q=1400.

2.6 FURTHER APPLICATIONS OF THE GENERAL DISPERSION RELATION

In the previous sections, the eigenmatrix equation of the condensed node was used to determine the general dispersion relation given by the characteristic equation. By imposing a spatial variation of $k_x d$ and $k_y d$, $k_z d$ can be determined as a function of $k_o d$. By substituting values of $k_o d$, $k_x d$, $k_y d$ and $k_z d$ back into the dispersion equation, Eq. 2-64, the eigenvector of the incident voltage can be determined. This has many applications. However, as this is a topic that is not directly in line with the main objective of this thesis, only a brief discussion will be given.

Consider an infinitely long waveguide along the z axis modelled by a TLM mesh that has transverse dimensions of N_x by N_y. Given k_xd and k_yd of a specific mode, k_zd is determined by the dispersion relation. For a specific solution set of k_od, k_xd, k_yd and k_zd, the rank of **(I-TPS)**, in Eq. 2-64, is 10 corresponding to two degenerate eigenmodes. The independent eigenvectors can be determined arbitrarily by applying two additional arbitrary conditions. For example if the TE mode is desired then the two additional conditions are $E_y = 1$ and $E_z = 0$. If the TM mode is required then the conditions $H_y=1$ and $H_z=0$ are used.

The conventional representation of the field quantities is that proposed by Johns [21]:

$$E_x = \frac{1}{2d} (V^i_0 + V^i_1 + V^i_8 + V^i_{11}) \qquad (2\text{-}71a)$$

$$E_y = \frac{1}{2d} (V^i_2 + V^i_3 + V^i_7 + V^i_{10}) \qquad (2\text{-}71b)$$

$$E_z = \frac{1}{2d} (V^i_4 + V^i_5 + V^i_6 + V^i_9) \qquad (2\text{-}71c)$$

$$H_x = \frac{1}{2d} (V^i_3 - V^i_4 + V^i_6 - V^i_7) \qquad (2\text{-}71d)$$

$$H_y = \frac{1}{2d} (-V^i_1 + V^i_5 + V^i_8 - V^i_9) \qquad (2\text{-}71e)$$

$$H_z = \frac{1}{2d} (-V^i_2 + V^i_0 + V^i_{10} - V^i_{11}) \qquad (2\text{-}71f)$$

The TE and TM simulated fields have been evaluated by the above procedure and

compared to analytical solutions. The error in the field components is of the order of the dispersion error, which is negligible for small values of $k_o d$, $k_x d$, $k_y d$ and $k_z d$.

Having the field components, it is possible to determine the simulated impedance of the mode and to compare it with the analytic value. A good approximation is to form the quotient of the transverse E and H field vectors. The impedance of the TE_{10} mode was evaluated and was very close to the analytic value for small values of $k_o d$. However, the impedance evaluated in this way is not exactly the equivalent impedance of the eigenmode in the mesh since the field components in Eq. 2-71 are based on an averaging of port voltages. While the difference is small, it is relevant in S-parameter extraction techniques, or if a perfect single frequency termination is required.

The method used to obtain the equivalent impedance is to determine the equivalent Green's function of the simulated waveguide. Consider a current sheet occupying the entire transverse plane of the waveguide as shown in Fig. 2-19. The current is distributed according to $k_x d$ and $k_y d$. The voltage incident into each TLM node adjacent to the current sheet is determined. The ratio of the total voltage at each node to the current flowing into each node from the current sheet is the desired impedance. Details of this development are lengthy and are therefore excluded from this thesis.

A new S-parameter extraction method was developed and successfully used, based on the availability of the exact simulated guide impedance as a function of $k_o d$. The waveguide with a discontinuity to be analyzed is terminated in a fixed impedance such that all the ports of the TLM nodes at the two ends of the waveguide are terminated with Z_o. A distributed voltage generator excites the TE_{10} mode distribution. The total voltage across the two terminations is

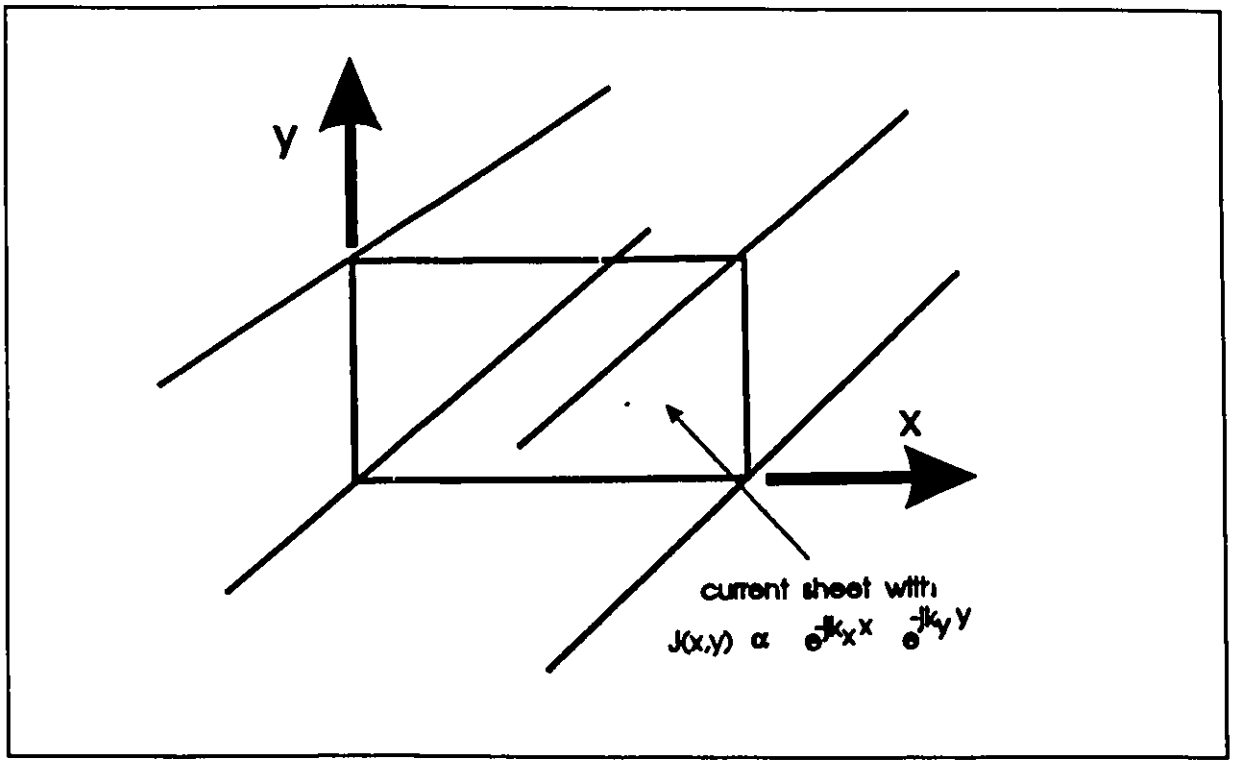

Fig. 2-19 Transverse current source sheet in a rectangular waveguide used in the calculation of the Green's function

evaluated and related to the desired S-parameters as discussed in Appendix C. The voltage generator waveform can be sinusoidal for single frequency S-parameter extraction, or an impulse function. In the latter case, the Fourier transform is used to extract the S-parameters. The advantage of this method is that absorbing boundaries are not required at the two ends of the waveguide.

Further applications of the dispersion equation relate to the study of modes supported by a finite TLM mesh. This results in a Hilbert space of basis functions. From this, field uniqueness can be demonstrated for a given excitation. Also the overall accuracy of the TLM simulation due to the limited number of modes and the dispersive properties of each mode can be analyzed. Knowing the attributes of the spurious modes from the dispersion equation can perhaps lead to an understanding of how they can be suppressed effectively.

Finally, knowing the simulated impedance of the propagating modes, absorbing boundary algorithms can be established that trade off bandwidth for increased numerical efficiency.

2.7 AN EQUIVALENT FD-TD FORMULATION OF THE CONDENSED NODE

Recently, Chen et al. [40] demonstrated that the condensed node could be regarded as a FD-TD procedure with coupled recursive equations in terms of voltages and currents. A different derivation will be given here, resulting in an alternative FD-TD interpretation of the condensed node that more directly shows the relation with respect to Maxwell's equations. As well, the terms responsible for the origin of the spurious modes in the condensed mesh can be identified by this derivation. Modifying these terms leads to a new FD-TD scheme based on the condensed node that is potentially free of troublesome spurious modes.

The FD-TD recursion relations will be developed in Section 2.7.1. A discussion of how these relate to Maxwell's equations will be given in Section 2.7.2 and 2.7.3. The origin of the spurious modes will be discussed in Section 2.7.4.

2.7.1 Development of the FD-TD Recursion Relation

For each condensed node there are twelve incident and twelve reflected voltage variables. Due to the twelve equations provided by the scattering matrix, the number of independent voltage variables associated with each node is reduced to twelve. In the FD-TD formulation, six voltage and six current samples will be associated with each node, sampled halfway along the link lines. Hence the total number of independent samples associated with the node remains at twelve. In the FD-TD formulation, the voltage and current samples are taken at a "port" of the node structure. The six ports of the FD-TD formulation correspond to the first six ports of the condensed node a distance of d/2 away from the node. The voltage and current at these six ports are defined as:

$_qV_{ijkp}$ - total voltage across the transmission line connected to port "p" of node i,j,k at time t=qΔt

$_qI_{ijkp}$ - total current flowing into port "p" of node i,j,k at time t=qΔt

The Table 2-3 gives attributes of V_{ijkp} and I_{ijkp}. The first column is the designated port number of the FD-TD formulation which corresponds to the port number of the condensed node. All the attributes of this table are observed directly from the condensed node structure given in Fig. 2-6. The second column gives the polarization of the voltage and current sample. For example, the voltage of port 0 is polarized in the x direction, and the current runs along the y axis. The third column gives the location of the port assuming that the node considered is centred at x=id, y=jd and z=kd. Finally the fourth column indicates which E and H field component is sampled at the port, and its relation to the port voltage and current.

Table 2-3 Location of sampled field quantities in the equivalent FD-TD formulation of the condensed node

p	polarization		port location			electromagnetic field component sampled	
	V	I	x	y	z	E field	H field
0	x	y	id	$(j-\frac{1}{2})d$	kd	$E_x=-V_0/d$	$H_z=I_0/d$
1	x	z	id	jd	$(k-\frac{1}{2})d$	$E_x=-V_1/d$	$H_y=-I_1/d$
2	y	x	$(i-\frac{1}{2})d$	jd	kd	$E_y=-V_2/d$	$H_z=-I_2/d$
3	y	z	id	jd	$(k-\frac{1}{2})d$	$E_y=-V_3/d$	$H_x=I_3/d$
4	z	y	id	$(j-\frac{1}{2})d$	kd	$E_z=-V_4/d$	$H_x=-I_4/d$
5	z	x	$(i-\frac{1}{2})d$	jd	kd	$E_z=-V_5/d$	$H_y=I_5/d$

The FD-TD recursion relations will be derived for the voltage and current at port p=0. The recursion relations for the other ports can be derived by inspection by taking the symmetry of the node into account. We begin by writing the updated voltages and currents at the new time of $t=(q+1)\Delta t$ in terms of incident and reflected voltages.

$$ {}_{q+1}V_{ijk0} = {}_{q+1}V^{i}_{ijk0} + {}_{q+1}V^{r}_{ijk0} \qquad (2\text{-}72a) $$

$$ {}_{q+1}I_{ijk0} = Y_o \left({}_{q+1}V^{i}_{ijk0} - {}_{q+1}V^{r}_{ijk0} \right) \qquad (2\text{-}72b) $$

where Y_o is the admittance of the link lines. From the scattering matrix of the condensed node

$$ {}_{q+1}V^{r}_{ijk0} = \tfrac{1}{2}\left[{}_{q}V^{i}_{ijk1} + {}_{q}V^{i}_{ijk2} + {}_{q}V^{i}_{ijk8} - {}_{q}V^{i}_{ijk10} \right]. \qquad (2\text{-}73) $$

Using

$$ {}_{q+1}V^{i}_{ijk0} = {}_{q+1}V^{r}_{i,j-1,k,11} \qquad (2\text{-}74) $$

and

$$ {}_{q+1}V^{r}_{i,j,k,11} = \tfrac{1}{2}[\ {}_{q}V^{i}_{ijk1} - {}_{q}V^{i}_{ijk2} + {}_{q}V^{i}_{ijk8} + {}_{q}V^{i}_{ijk10}] \qquad (2\text{-}75) $$

from the scattering matrix, we obtain

$$ {}_{q+1}V^{i}_{i,j,k,0} = \tfrac{1}{2}[\ {}_{q}V^{i}_{i,j-1,k,1} - {}_{q}V^{i}_{i,j-1,k,2} + {}_{q}V^{i}_{i,j-1,k,8} + {}_{q}V^{i}_{i,j-1,k,10}] \ . \qquad (2\text{-}76) $$

The relationship between the incident voltages of the condensed node and the total voltage and current is given as

$$ {}_{q+1}V^{i}_{ijkp} = \tfrac{1}{2}[\ {}_{q}V_{ijkp} + Z_o\ {}_{q}I_{ijkp}\ ] \qquad (2\text{-}77) $$

for p=0,1..5 where Z_o is the link line impedance. For the other ports (referred to the condensed node structure) we have the following relations

$$ {}_{q+1}V^{i}_{ijk6} = \tfrac{1}{2}[\ {}_{q}V_{i,j+1,k,4} - Z_o\ {}_{q}I_{i,j+1,k,4}\ ] $$

$$ {}_{q+1}V^{i}_{ijk7} = \tfrac{1}{2}[\ {}_{q}V_{i,j,k+1,3} - Z_o\ {}_{q}I_{i,j,k+1,3}\ ] $$

$$ {}_{q+1}V^{i}_{ijk8} = \tfrac{1}{2}[\ {}_{q}V_{i,j,k+1,1} - Z_o\ {}_{q}I_{i,j,k+1,1}\ ] $$

$$ {}_{q+1}V^{i}_{ijk9} = \tfrac{1}{2}[\ {}_{q}V_{i+1,j,k,5} - Z_o\ {}_{q}I_{i+1,j,k,5}\ ] $$

$$ {}_{q+1}V'_{i,j,k,1,0} = \tfrac{1}{2}\left[{}_{q}V_{i+1,j,k,2} - Z_o \, {}_{q}I_{i+1,j,k,2} \right] $$

$$ {}_{q+1}V'_{i,j,k,1,1} = \tfrac{1}{2}\left[{}_{q}V_{i,j+1,k,0} - Z_o \, {}_{q}I_{i,j+1,k,0} \right] . \qquad (2\text{-}78) $$

Combining all the above relations with some algebra results in the desired recursion relation given by

$$ \begin{aligned} {}_{q+1}V_{i,j,k,0} = {} & \tfrac{1}{4}\{ {}_{q}V_{i,j-1,k,1} + {}_{q}V_{i,j-1,k+1,1} + {}_{q}V_{i,j,k,1} + {}_{q}V_{i,j,k+1,1}\} \\ & + \tfrac{1}{4}\{-{}_{q}V_{i,j-1,k,2} + {}_{q}V_{i+1,j-1,k,2} + {}_{q}V_{i,j,k,2} - {}_{q}V_{i+1,j,k,2}\} \\ & + \tfrac{1}{4} Z_o\{ {}_{q}I_{i,j-1,k,1} - {}_{q}I_{i,j-1,k+1,1} + {}_{q}I_{i,j,k,1} - {}_{q}I_{i,j,k+1,1}\} \\ & + \tfrac{1}{4} Z_o\{-{}_{q}I_{i,j-1,k,2} - {}_{q}I_{i+1,j-1,k,2} + {}_{q}I_{i,j,k,2} + {}_{q}I_{i+1,j,k,2}\} \qquad (2\text{-}79) \end{aligned} $$

for the voltage at port 0. The corresponding current recursion relation is:

$$ \begin{aligned} {}_{q+1}I_{i,j,k,0} = {} & \{ {}_{q}V_{i,j-1,k,1} + {}_{q}V_{i,j-1,k+1,1} - {}_{q}V_{i,j,k,1} - {}_{q}V_{i,j,k+1,1}\} \,/\, (4\, Z_o) \\ & + \{-{}_{q}V_{i,j-1,k,2} + {}_{q}V_{i+1,j-1,k,2} - {}_{q}V_{i,j,k,2} + {}_{q}V_{i+1,j,k,2}\} \,/\, (4\, Z_o) \\ & + \tfrac{1}{4}\{ {}_{q}I_{i,j-1,k,1} - {}_{q}I_{i,j-1,k+1,1} - {}_{q}I_{i,j,k,1} + {}_{q}I_{i,j,k+1,1}\} \\ & + \tfrac{1}{4}\{-{}_{q}I_{i,j-1,k,2} - {}_{q}I_{i+1,j-1,k,2} - {}_{q}I_{i,j,k,2} - {}_{q}I_{i+1,j,k,2}\} . \qquad (2\text{-}80) \end{aligned} $$

In the following section these recursion relations will be considered in detail

demonstrating how they relate to Maxwell's equations in the limit of an infinitesimal mesh dimension.

2.7.2 Analysis of the Voltage Recursion Relation

Fig. 2-20 illustrates the contributing components to each of the four terms of Eq. 2-79. Each sub-figure shows a cluster of four nodes indicating which voltage or current contributes to the term. Also indicated is the position of the V_{ijko} voltage component. As observed, the first term is a sum of the ${}_qV_i$ voltage components of the surrounding nodes which can be regarded as a spatial average of ${}_qV_{ijko}$. The second term, illustrated is neither a curl nor a divergence and reduces to zero as the mesh size becomes finer. This is the term which is responsible for spurious modes as will be discussed later. The third term can be regarded as a numerical approximation to

$$-\frac{d\,Z_o}{2}\,\frac{\partial I_z}{\partial z}.$$

Using the table in Section 2.7.1,

$$H_y(id,(j-\tfrac{1}{2})d,kd) \;=\; -\frac{I_{i,j,k,1}}{d}. \qquad (2\text{-}81)$$

Consequently, the third term is an approximation of

$$term\ 3 \;\approx\; \frac{d^2\,Z_o}{2}\,\frac{\partial H_y}{\partial z}\ . \qquad (2\text{-}82)$$

The fourth term is a numerical approximation to

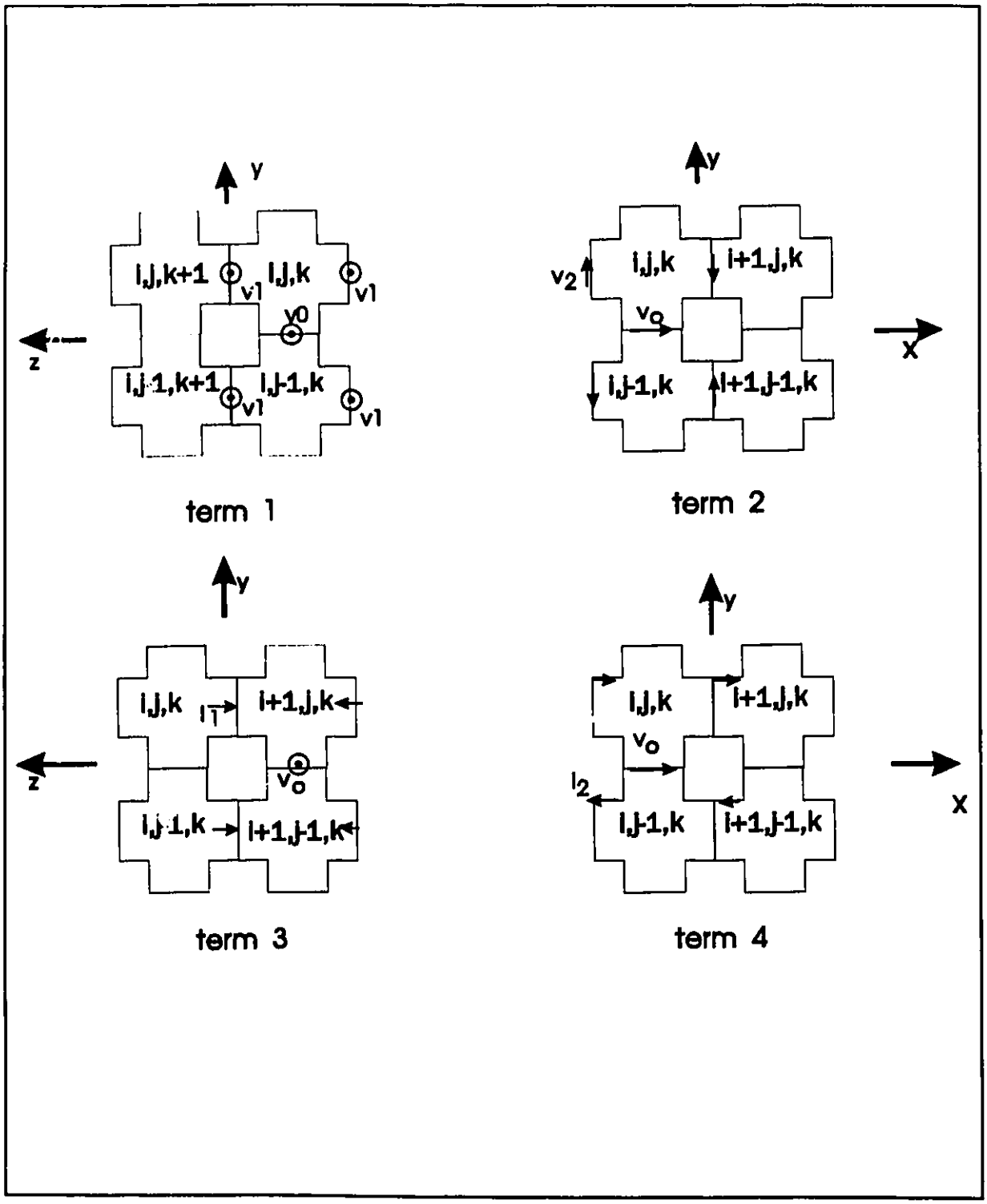

Fig. 2-20 Illustration of contributing voltages and currents to the terms of the right hand side of the voltage recursion relation

$$\frac{d\ Z_o}{2}\frac{\partial I_{i,j,k,2}}{\partial y}\ .$$

Again using the table in Section 2.7.1 we have,

$$H_z(id,(j-\frac{1}{2})d,kd) = -\frac{I_{i,j,k,2}}{d} \qquad (2\text{-}83)$$

and therefore the fourth term is an approximation of

$$term\ 4 \approx \frac{d\ Z_o}{2}\ \frac{\partial\ I_{i,j,k,2}}{\partial y} \qquad (2\text{-}84)$$

From Eq. 2-79, Eq. 2-82 and Eq. 2-84 the voltage recursion equation can be summarized as

$${}_{q+1}V_{i,j,k,0} \approx {}_qV_{i,j,k,0} + \frac{d^2\ Z_o}{2}\left(\frac{\partial H_y}{\partial z} - \frac{\partial H_z}{\partial y}\right) \qquad (2\text{-}85)$$

where the contribution from term 2 has been neglected.

Approximating the time derivative of E_x as

$$-\frac{\partial E_x(ix,jd,kd)}{\partial t} \approx \frac{1}{d\ \Delta t}\ ({}_{q+1}V_{i,j,k,0} - {}_qV_{i,j,k,0}) \qquad (2\text{-}86)$$

and using

$$\frac{2}{Z_o d^2}\cdot d\Delta t = \frac{2}{Z_o}\cdot\frac{1}{V_{link}} = e_o\ e_r \qquad (2\text{-}87)$$

we finally obtain

$$e_o e_r \frac{\partial E_x}{\partial t} = \boldsymbol{x}\cdot\nabla\times\boldsymbol{H} \qquad (2\text{-}88)$$

which is one component of Maxwell's equations given by Eq. 2-2.

2.7.3 Current Recursion Equation

The current recursion equation, Eq. 2-80, can be manipulated in a similar fashion resulting in the approximation to the component of Maxwell's equation

$$\mu_o \frac{\partial H_z}{\partial t} = -\boldsymbol{z} \cdot \nabla \times \boldsymbol{E} \qquad (2\text{-}89)$$

Similar approximations were made as above. As with the voltage recursion relation, the current recursion equation involves a term which is responsible for the spurious modes, which is the third term in Eq. 2-80.

2.7.4 Origin of Spurious Modes

The spurious modes of the condensed node, discussed in Section 2.5, showed that for every "physical" mode with propagation coefficients of k_x, k_y and k_z, there was a corresponding spurious mode with propagation coefficients of $k_x \rightarrow \pi/d - k_x$, $k_y \rightarrow \pi/d - k_y$, $k_z \rightarrow \pi/d - k_z$. In other words, the spurious modes originate from a confusion or degeneracy of a mode with low and high spatial frequency variation.

To show the origin of this degeneracy, a heuristic argument is given. Consider the terms of the voltage recursion relation illustrated in Fig. 2-20. The orientation of the component voltages and currents making up each term are indicated as they appear in the voltage recursion relation. Consider now the DC spurious mode with $k_x d = k_y d = k_z d = \pi$, the orientation of the voltages and currents in

Fig. 2-20 will be modulated with an alternating sign with a period of d in the x, y, and z directions. Careful consideration of term 1 and term 2 will indicate that term 2, given the DC spurious mode excitation i.e. $k_x d=k_y d=k_z d=\pi$, will be "similar" to term 1 with the DC physical mode excitation i.e. $k_x d=k_y d=k_z d=0$. Hence, considering the sum of term 1 and term 2, there is a confusion between the DC mode and the DC spurious mode. A similar argument can be made for terms 3 and 4. In other words, given that the FD-TD recursion relations are self-consistent for the DC physical mode with $k_x d=k_y d=k_z d=0$, they are also self-consistent for the DC spurious mode with $k_x d=k_y d=k_z d=\pi$. This degeneracy is believed to be a result of the symmetry of the condensed node. Removing the degeneracy by eliminating term 2 from Eq. 2-79 and term 3 for Eq. 2-80 will eliminate this form of spurious mode. This is equivalent to making the condensed node nonsymmetric. It remaines to be determined whether a new FD-TD node, created from the voltage and current recursion equations with these terms removed, will result in a spurious-free method. Spurious modes will likely be supported, but may be less troublesome than those presently encountered with the condensed node.

2.8 CONCLUSION

In this chapter a review of the various 2D and 3D TLM nodes was given. The general dispersion equation was developed for each node. It was demonstrated that the numerical dispersion and anisotropy of the condensed node is considerably better than for the expanded 3D TLM node and the FD-TD leap-frog formulation.

Spurious modes of the condensed node were discovered by careful analysis of the dispersion equation. The propagation attributes and field structure of the spurious modes have been quantified. It was determined that the condensed node supports an equal number of physical and spurious modes. Unfortunately, spurious modes are excited at low frequencies and are only removable by low-pass spatial filtering. While spatial filtering will suppress spurious mode propagation, it does not necessarily provide a more accurate overall field simulation. It is also a computationally expensive process.

On a positive note, the percentage of the total field energy in propagating spurious modes is typically low, being generally in the region of one or two percent. This will be shown by example in Chapter 5. Maintaining a low percentage in spurious modes hinges on three factors:

1. Discontinuity features have no high spatial frequency content.
2. The sources do not couple strongly into spurious modes.
3. The temporal frequencies of sources and of signal sources emanating from non-linearities are low relative to $1/\Delta t$.

The 2D shunt and series nodes do not support low frequency spurious modes. Careful examination of the expanded node dispersion equation reveals the rather surprising fact that the expanded TLM node does not support spurious modes either. This is consistent with the fact that Yee's leap-frog FD-TD scheme does not support any spurious modes for any stability factor less than the maximum value of $1/\sqrt{3}$. The key feature of the expanded node and Yee's scheme is the interlaced structure of the node [38]. Lack of spurious modes is an important advantage of these schemes.

The question then is 'why pursue development of the condensed node for nonlinear circuit analysis applications?'. To answer this, it must be borne in

mind that the errors resulting from spurious modes is generally limited to one or two percent. In nonlinear simulations, errors of this magnitude are not significant relative to the errors of characterizing the non-linear parameters of the devices. Also, generation of spurious modes can be suppressed, to some degree, by careful arrangement of the problem geometry. The condensed node remains an attractive node to use for circuit applications because of the possibilities of modelling conductor strips and interfacing to lumped devices. This will be discussed in detail in Chapter 3. Finally the condensed node does have superior numerical dispersion attributes as demonstrated.

CHAPTER 3

SIMULATION OF CONDUCTOR STRIPS

3.1. INTRODUCTION

The objective of this thesis is to develop a method of modelling 3D electromagnetic structures with embedded nonlinear devices connected by strip-like transmission lines. This chapter focuses on new condensed node structures developed explicitly to model conductor strips and to provide a realistic interface to the embedded devices.

Fig. 3-1 illustrates the conventional method of simulating conductor strips in a 3D condensed node mesh. Shown in Fig. 3-1a is a truncated conductor sheet, located halfway between two node layers. The conductor sheet is simulated by applying a Dirichlet boundary condition to the transmission link lines that intersect the conductor sheet as illustrated in Fig. 3-1b and Fig. 3-1c. As discussed in Section 2.2.5, a Dirichlet boundary is modelled by assuming a reflection coefficient of -1.

Two-terminal lumped devices can be embedded into the conductor strip by interrupting the Dirichlet boundary at the device location. Fig. 3-2 shows an example of a gap in the conductor strip oriented parallel to the x-axis that is straddled by a two-terminal device oriented in the z-direction. The 3D-node configuration is shown in Fig. 3-2a, and details of the indicated planes are given in Fig. 3-2b and Fig. 3-2c. Fig. 3-2b illustrates how the device is connected to the TLM mesh by shunting the z-polarized mesh transmission lines

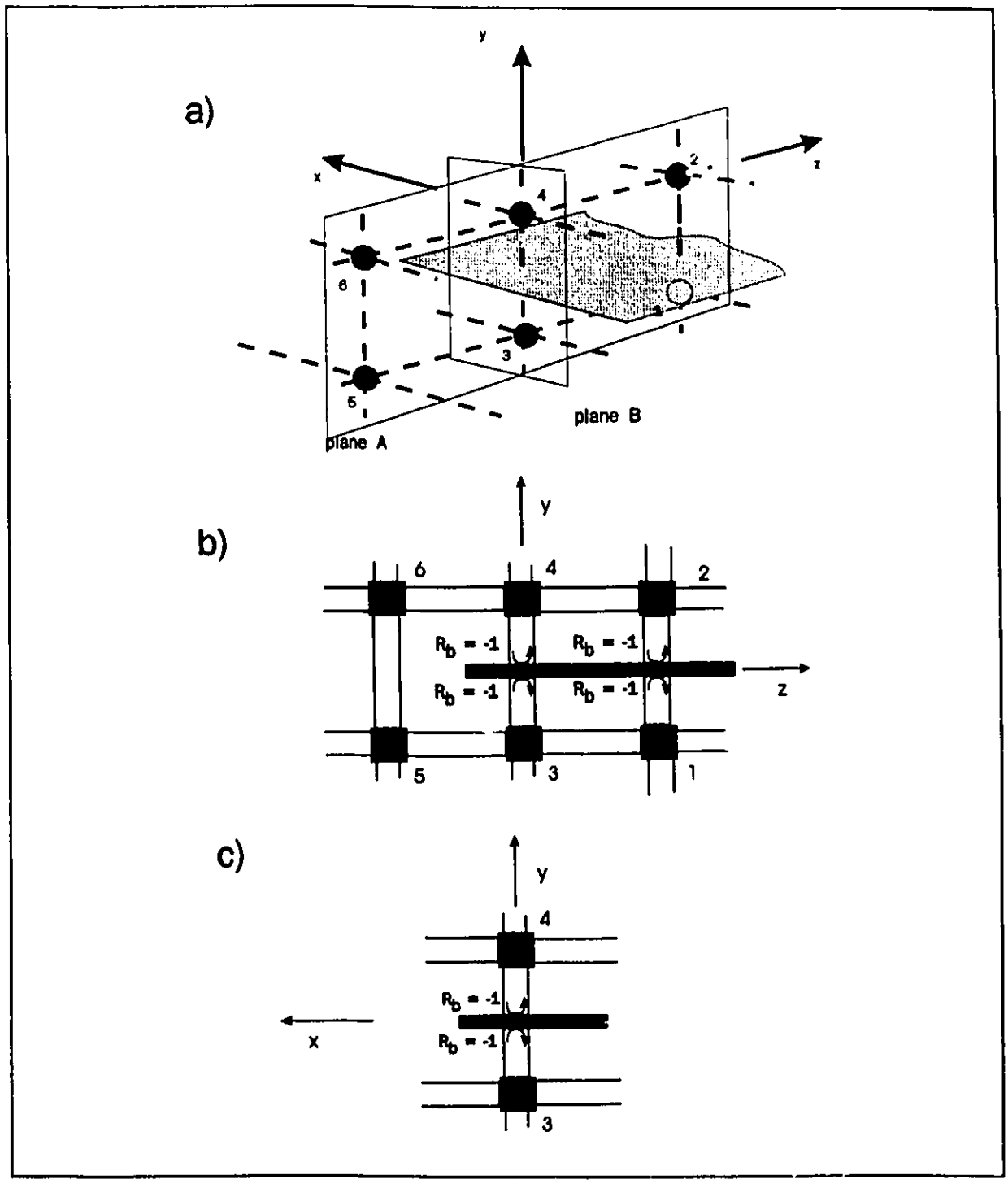

Fig. 3-1 Conventional modelling of a conductive strip using a truncated Dirichlet boundary. a) 3D orientation of the condensed nodes. b) Detail of plane A. c) Detail of plane B.

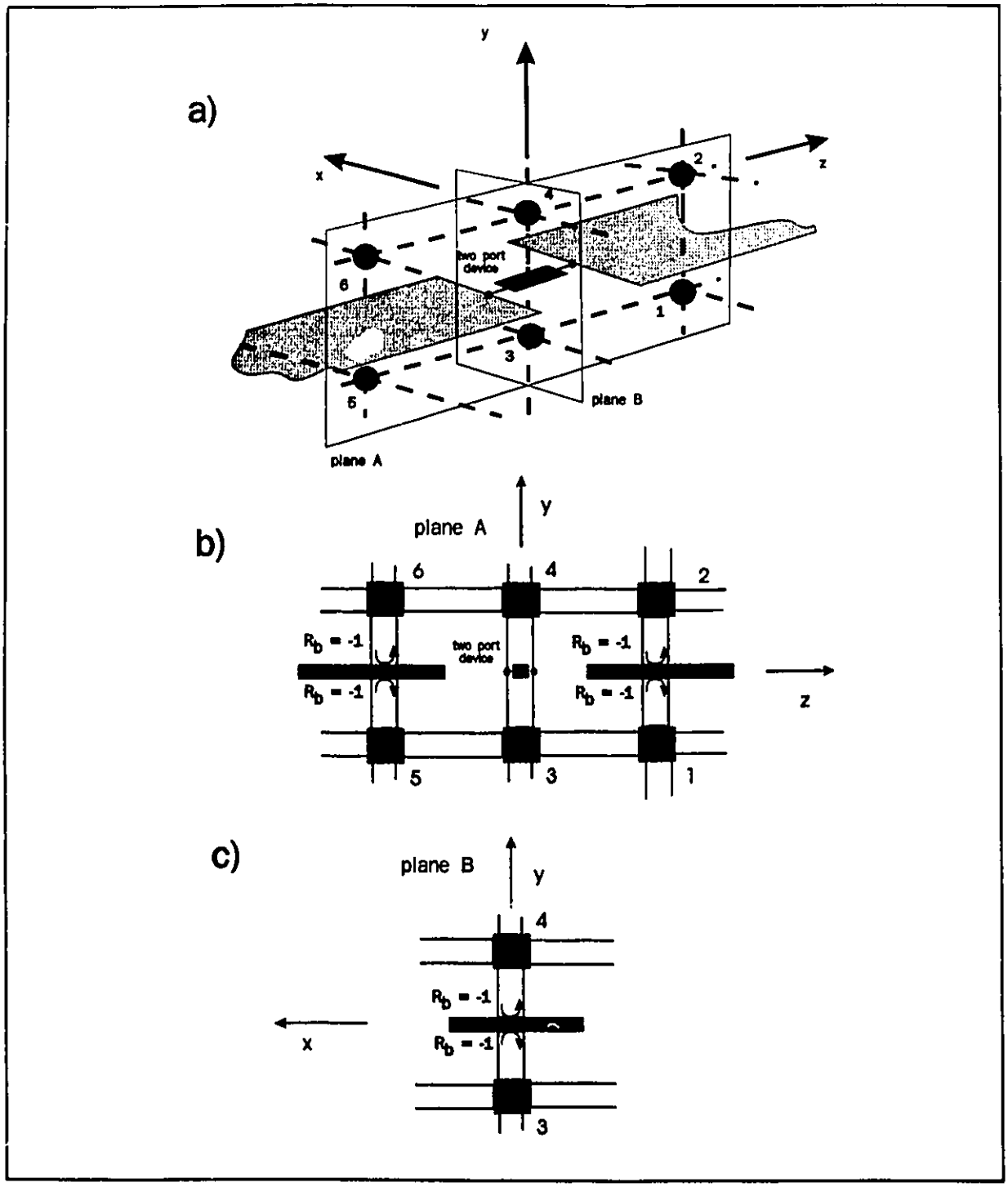

Fig. 3-2 Conventional modelling of a conductive strip with an embedded two-port device. a) 3D orientation of the condensed nodes. b) Detail of plane A. c) Detail of plane B.

between nodes 3 and 4. The x-polarized transmission line running between nodes 3 and 4 must be shorted as shown to model the Dirichlet (electric wall) boundary condition of the strip.

If the two-terminal device does not have any reactance, then it can be modelled by an equivalent two-port scattering matrix referenced to the line admittance of Y_o. As an example, if the device is a conductance G, then the S-parameters are:

$$S_{11} = S_{22} = \frac{-G}{2\,Y_o + G}$$

$$S_{12} = S_{21} = \frac{2\,Y_o}{2\,Y_o + G} \qquad (3\text{-}1)$$

At every time step the impulses on the link lines incident on the two port device are scattered according to Eq. 3-1. If the device has some reactance or energy storage associated with it then a time-dependent differential equation results that must be solved by the PWL routine that will be developed in Chapter 4.

Unfortunately, there are two problems with this direct elegant extension of the TLM mesh. First, as was discussed in references [41] and [42], conductor strip edges are not accurately modelled by using truncated Dirichlet boundaries. Hence, common planar transmission line structures generally used for interconnecting devices are poorly simulated. Secondly, the device sees an incorrect driving-point impedance when looking into the conductor strips. Hence the coupling of the device with the surrounding electromagnetic structure is not accurately simulated.

To explain the origin of these errors, consider the conductor edge modelled as a truncated Dirichlet boundary between node layers as illustrated in Fig. 3-1. Nodes 5 and 6, immediately adjacent to the conductor edge share a corner which

is coincident with the conductor edge and should therefore couple strongly with the resultant edge current. However, in the condensed node formulation, the coupling is indirect, having to pass through the nodes 3 and 4, which results in a weaker, delayed interaction. Hence the errors can be attributed to an insufficient coupling of the simulated strip edge current with the surrounding fields.

The origin of the second problem is similar. Consider the series conductance in Fig. 3-2. Current flowing in the conductance is not directly coupled to the current flowing in the adjacent conductor strips, but rather the interaction must pass through two nodes (paths 6-4, 2-4, 1-3 and 5-3 in Fig. 3-2). While this can be shown not to affect the DC bias simulation, it does significantly degrade the simulation fidelity at higher frequencies.

A solution to the first problem is to increase the interaction between the conductor edge and the surrounding nodes. This is possible by connecting nodes 5 and 6, in Fig. 3-1, directly to the conductor strip edge via shorting stubs. This has been demonstrated, in the 2D TLM shunt node mesh, to significantly improve simulation results [43].

However, this method does not solve the second problem of providing a direct connection of the conductor strip with the device element. Hence, another approach was developed which involved modifying the condensed node such that the conductor strip could be embedded directly into the node. This has resulted in a family of new node structures that are sketched in Fig. 3-3, denoted as "conductor strip nodes". The "half-node", Fig. 3-3a is a condensed node bisected by a conductor plane. The "edge-node", Fig. 3-3b is similar to the half-node except that the conductor sheet has an edge within the node. The edge current flowing in this node couples directly with the adjacent E and H fields. The

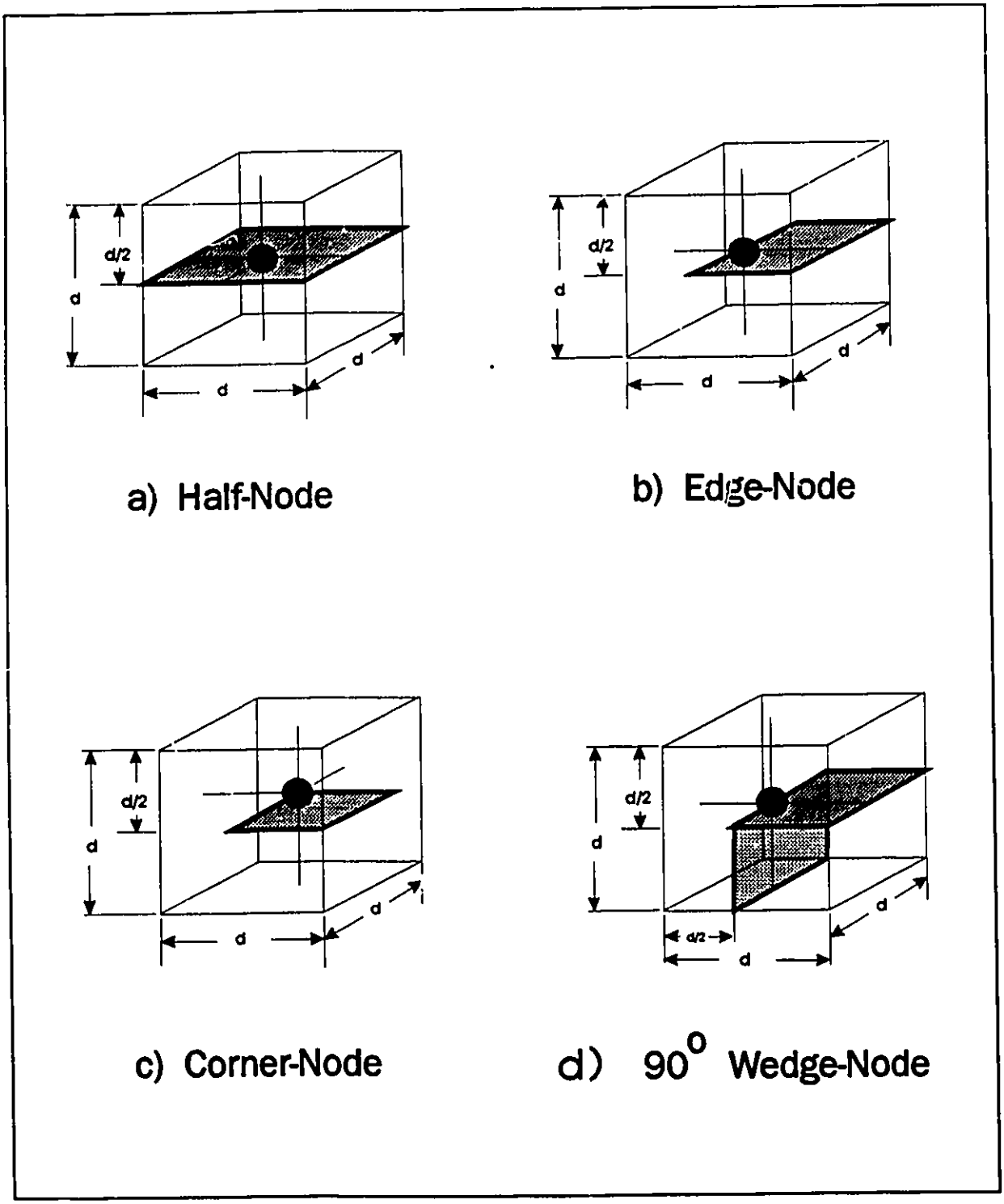

Fig. 3-3 Illustration of the set of Conductor Strip nodes. The scattering centre of the nodes is situated at the centre of the cells and is identified schematically.

corner node in Fig. 3-3c is necessary for simulating discontinuities in the planar transmission lines. Finally the 90° wedge node in Fig. 3-3d is useful for simulating ribbon bonds to devices and wrap-around conductor planes.

Fig. 3-4 shows the same problem as illustrated in Fig. 3-2, with the z-oriented two-terminal device embedded into a conductor strip. However, in Fig. 3-4, that the conductor is modelled with conductor strip nodes. Note in the detail of Fig. 3-4b, the conductor strip is embedded into the layer of half-nodes that is connected to the device. As discussed in Section 3.2, eight of the twelve state variables of the half-node correspond to the current flow on the two sides of the conductor which is directly accessible to the two terminal device. Hence the interaction between the device and the conductor strip is direct and does not need to pass through adjacent nodes. Details of the interface between the device and the conductor strips are developed in Section 3.6.

The scattering matrices for the conductor strip nodes are developed in Section 3.2. In Section 3.3 the problem of incorporating capacitive stubs into the half-nodes, for modelling dielectric material, will be addressed. A demonstration of the improved accuracy possible by using this new family of node structures is given in Section 3.4 based on the simulation of a half-wavelength stripline resonator and a microstrip resonator. In Section 3.5 a modification of the edge node is discussed. It leads to improved modelling of strip edges where the incident field is parallel to the conductor strip edges. The interface between devices and conductor strips which are modelled by half-nodes, will be addressed in Section 3.6. Only devices without energy storage or reactance will be considered in this chapter. Simulation of nonlinear devices with reactance will be developed in Chapter 4. In Section 3.7 modelling of distributed devices by conductor strip nodes will be introduced.

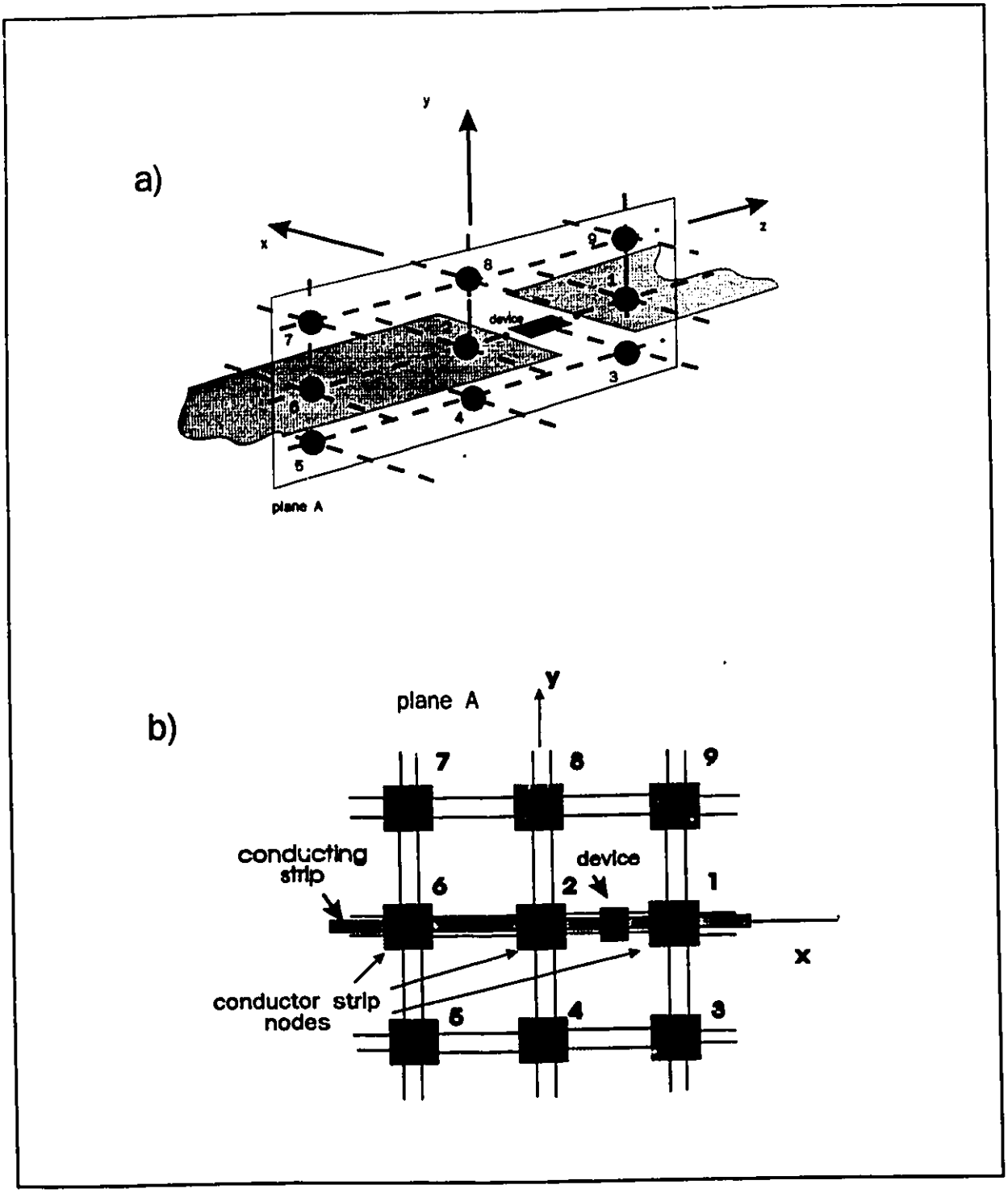

Fig. 3-4 Modelling of conductor strip with embedded device using conductor strip nodes. a) 3D configuration of conductor strip nodes and conventional condensed nodes. b) Detail of plane A.

3.2 SCATTERING MATRICES FOR THE CONDUCTOR STRIP NODE TYPES

3.2.1 Half-Node

The half-node is derived from the condensed node and therefore retains its energy and current conservation properties as well as its dispersion characteristics. A half-node configuration with the conductor sheet in the x-z plane is shown in Fig. 3-5. The conductor sheet splits ports 2,3,7 and 10 into eight ports 2a,3a,7a,10a above the conductor and 2b,3b,7b,10b below the conductor. The characteristic impedance of these split ports is half the characteristic impedance of the regular ports. Electric fields tangential to the conductor surface are forced to be zero and therefore ports 1,8,5 and 9 of the regular condensed node (Fig. 2-6) are omitted. Even though both half-nodes are electrically separated and thus uncoupled, it is nevertheless convenient to formulate the scattering matrix as a twelve port node containing both half-nodes.

The reflected and incident voltage vectors are defined as

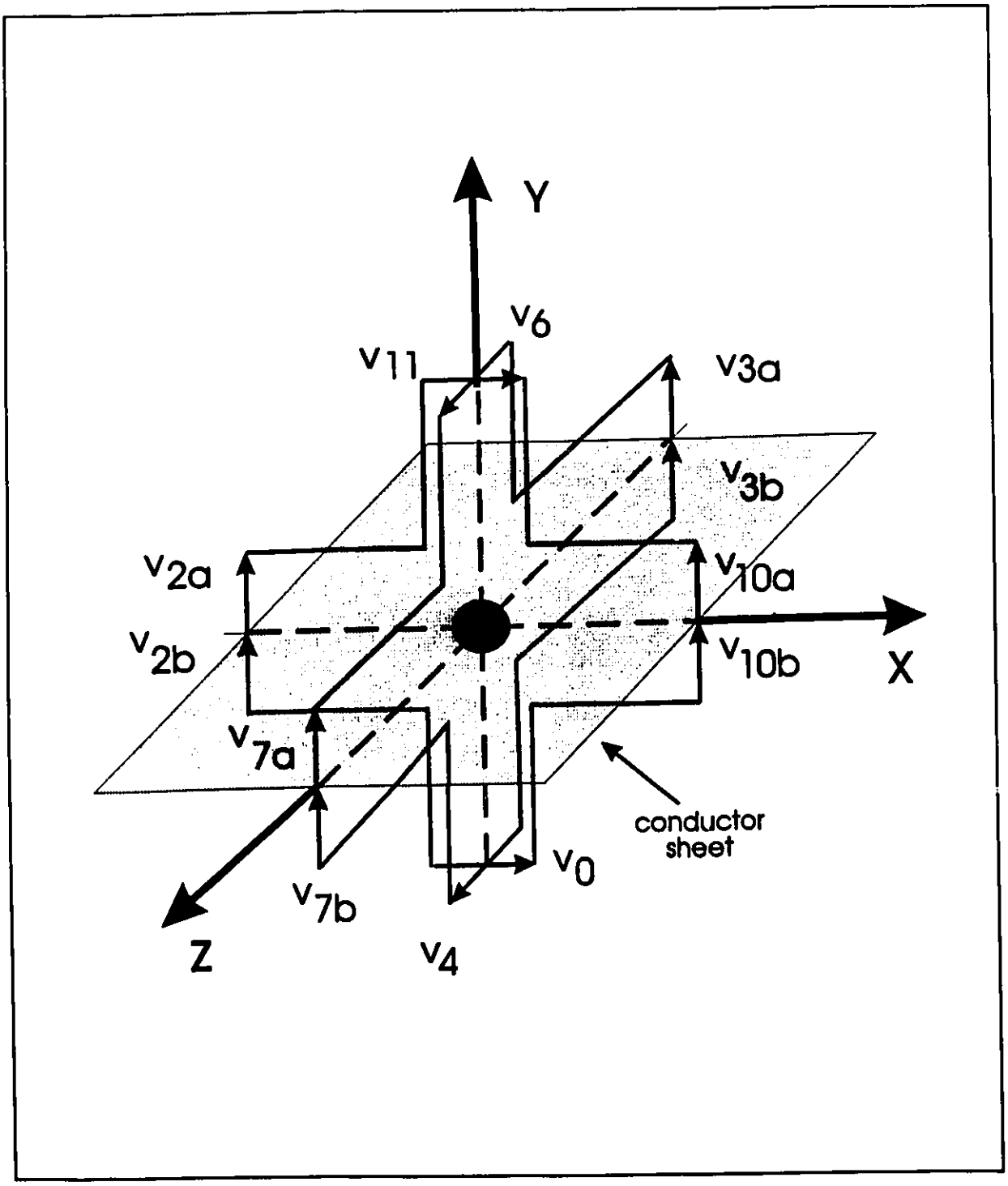

Fig. 3-5 Diagram of the half-node configuration. This is a condensed node split into two uncoupled half-nodes by a conducting sheet.

$$\mathbf{V}^r = \begin{pmatrix} V^r_0 \\ V^r_{2a} \\ V^r_{2b} \\ V^r_{3a} \\ V^r_{3b} \\ V^r_4 \\ V^r_6 \\ V^r_{7a} \\ V^r_{7b} \\ V^r_{10a} \\ V^r_{10b} \\ V^r_{11} \end{pmatrix} \qquad \mathbf{V}^i = \begin{pmatrix} V^i_0 \\ V^i_{2a} \\ V^i_{2b} \\ V^i_{3a} \\ V^i_{3b} \\ V^i_4 \\ V^i_6 \\ V^i_{7a} \\ V^i_{7b} \\ V^i_{10a} \\ V^i_{10b} \\ V^i_{11} \end{pmatrix} \tag{3-2}$$

which are related as $\mathbf{V}^r = \mathbf{S}_{hy}\,\mathbf{V}^i$ where the scattering matrix, $\mathbf{S}_{hy}$, is given by

$$\boldsymbol{S}_{hy} = \frac{1}{2}\begin{pmatrix} 0 & 0 & 2 & 0 & 0 & 0 & 0 & 0 & 0 & 0 & -2 & 0 \\ 0 & 0 & 0 & 1 & 0 & 0 & 0 & 1 & 0 & 0 & 0 & -1 \\ 1 & 0 & 0 & 0 & 1 & 0 & 0 & 0 & 1 & 0 & 0 & 0 \\ 0 & 1 & 0 & 0 & 0 & 0 & -1 & 0 & 0 & 1 & 0 & 0 \\ 0 & 0 & 1 & 0 & 0 & 1 & 0 & 0 & 0 & 0 & 1 & 0 \\ 0 & 0 & 0 & 0 & 2 & 0 & 0 & 0 & -2 & 0 & 0 & 0 \\ 0 & 0 & 0 & -2 & 0 & 0 & 0 & 2 & 0 & 0 & 0 & 0 \\ 0 & 1 & 0 & 0 & 0 & 0 & 1 & 0 & 0 & 1 & 0 & 0 \\ 0 & 0 & 1 & 0 & 0 & -1 & 0 & 0 & 0 & 0 & 1 & 0 \\ 0 & 0 & 0 & 1 & 0 & 0 & 0 & 1 & 0 & 0 & 0 & 1 \\ -1 & 0 & 0 & 0 & 1 & 0 & 0 & 0 & 1 & 0 & 0 & 0 \\ 0 & -2 & 0 & 0 & 0 & 0 & 0 & 0 & 0 & 2 & 0 & 0 \end{pmatrix} \tag{3-3}$$

where the subscript "h" denotes "half-node" and "y" denotes that the normal of the conductor plane is in the y-direction.

For the half-node with a conductor sheet normal to the x-axis, the reflected and incident voltage vectors are defined as

$$\boldsymbol{V}^r = \begin{pmatrix} V^r_{0a} \\ V^r_{0b} \\ V^r_{1a} \\ V^r_{1b} \\ V^r_{2} \\ V^r_{5} \\ V^r_{8a} \\ V^r_{8b} \\ V^r_{9} \\ V^r_{10} \\ V^r_{11a} \\ V^r_{11b} \end{pmatrix} \qquad \boldsymbol{V}^i = \begin{pmatrix} V^i_{0a} \\ V^i_{0b} \\ V^i_{1a} \\ V^i_{1b} \\ V^i_{2} \\ V^i_{5} \\ V^i_{8a} \\ V^i_{8b} \\ V^i_{9} \\ V^i_{10} \\ V^i_{11a} \\ V^i_{11b} \end{pmatrix} \tag{3-4}$$

which are related as $\mathbf{V}^r = \mathbf{S}_{hx}\,\mathbf{V}^i$ where the scattering matrix, $\mathbf{S}_{hx}$, is given by

$$\boldsymbol{S}_{hx} = \frac{1}{2}\begin{pmatrix} 0 & 0 & 1 & 0 & 0 & 0 & 1 & 0 & 0 & -1 & 0 & 0 \\ 0 & 0 & 0 & 1 & 1 & 0 & 0 & 1 & 0 & 0 & 0 & 0 \\ 1 & 0 & 0 & 0 & 0 & 0 & 0 & 0 & -1 & 0 & 1 & 0 \\ 0 & 1 & 0 & 0 & 0 & 1 & 0 & 0 & 0 & 0 & 0 & 1 \\ 0 & 2 & 0 & 0 & 0 & 0 & 0 & 0 & 0 & 0 & 0 & -2 \\ 0 & 0 & 0 & 2 & 0 & 0 & 0 & -2 & 0 & 0 & 0 & 0 \\ 1 & 0 & 0 & 0 & 0 & 0 & 0 & 0 & 1 & 0 & 1 & 0 \\ 0 & 1 & 0 & 0 & 0 & -1 & 0 & 0 & 0 & 0 & 0 & 1 \\ 0 & 0 & -2 & 0 & 0 & 0 & 2 & 0 & 0 & 0 & 0 & 0 \\ -2 & 0 & 0 & 0 & 0 & 0 & 0 & 0 & 0 & 0 & 2 & 0 \\ 0 & 0 & 1 & 0 & 0 & 0 & 1 & 0 & 0 & 1 & 0 & 0 \\ 0 & 0 & 0 & 1 & -1 & 0 & 0 & 1 & 0 & 0 & 0 & 0 \end{pmatrix} \tag{3-5}$$

For the half-node with a conductor sheet normal to the z-axis, the reflected and incident voltage vectors are defined as

$$\boldsymbol{V}^r = \begin{pmatrix} V^r_0 \\ V^r_3 \\ V^r_{4a} \\ V^r_{4b} \\ V^r_{5a} \\ V^r_{5b} \\ V^r_{6a} \\ V^r_{6b} \\ V^r_7 \\ V^r_8 \\ V^r_{9a} \\ V^r_{9b} \end{pmatrix} \qquad \boldsymbol{V}^i = \begin{pmatrix} V^i_0 \\ V^i_3 \\ V^i_{4a} \\ V^i_{4b} \\ V^i_{5a} \\ V^i_{5b} \\ V^i_{6a} \\ V^i_{6b} \\ V^i_7 \\ V^i_8 \\ V^i_{9a} \\ V^i_{9b} \end{pmatrix} \tag{3-6}$$

which are related as $\mathbf{V}^r = \mathbf{S}_{hz}\,\mathbf{V}^i$ where the scattering matrix, $\mathbf{S}_{hz}$, is given by

$$\boldsymbol{S}_{hz} = \frac{1}{2}\begin{pmatrix} 0 & 0 & 0 & 0 & 0 & 2 & 0 & 0 & 0 & 0 & 0 & -2 \\ 0 & 0 & 0 & 2 & 0 & 0 & 0 & -2 & 0 & 0 & 0 & 0 \\ 0 & 0 & 0 & 0 & 1 & 0 & 0 & 0 & -1 & 0 & 1 & 0 \\ 0 & 1 & 0 & 0 & 0 & 1 & 0 & 0 & 0 & 0 & 0 & 1 \\ 0 & 0 & 1 & 0 & 0 & 0 & 1 & 0 & 0 & -1 & 0 & 0 \\ 1 & 0 & 0 & 1 & 0 & 0 & 0 & 1 & 0 & 0 & 0 & 0 \\ 0 & 0 & 0 & 0 & 1 & 0 & 0 & 0 & 1 & 0 & 1 & 0 \\ 0 & -1 & 0 & 0 & 0 & 1 & 0 & 0 & 0 & 0 & 0 & 1 \\ 0 & 0 & -2 & 0 & 0 & 0 & 2 & 0 & 0 & 0 & 0 & 0 \\ 0 & 0 & 0 & 0 & -2 & 0 & 0 & 0 & 0 & 0 & 2 & 0 \\ 0 & 0 & 1 & 0 & 0 & 0 & 1 & 0 & 0 & 1 & 0 & 0 \\ -1 & 0 & 0 & 1 & 0 & 0 & 0 & 1 & 0 & 0 & 0 & 0 \end{pmatrix} \tag{3-7}$$

3.2.2 Edge-Node

The edge-node is derived directly from the half-node with only minor modifications required to simulate the conductor strip edge. Consequently, to describe the edge node, consider first the half-node of Fig. 3-5. Consider the case where the conductor strip has an edge at the pair of ports denoted by 2a and 2b. In the simulation of the strip edge, the half-node must interface to the conventional condensed node as shown in Fig. 3-6. An interface is required

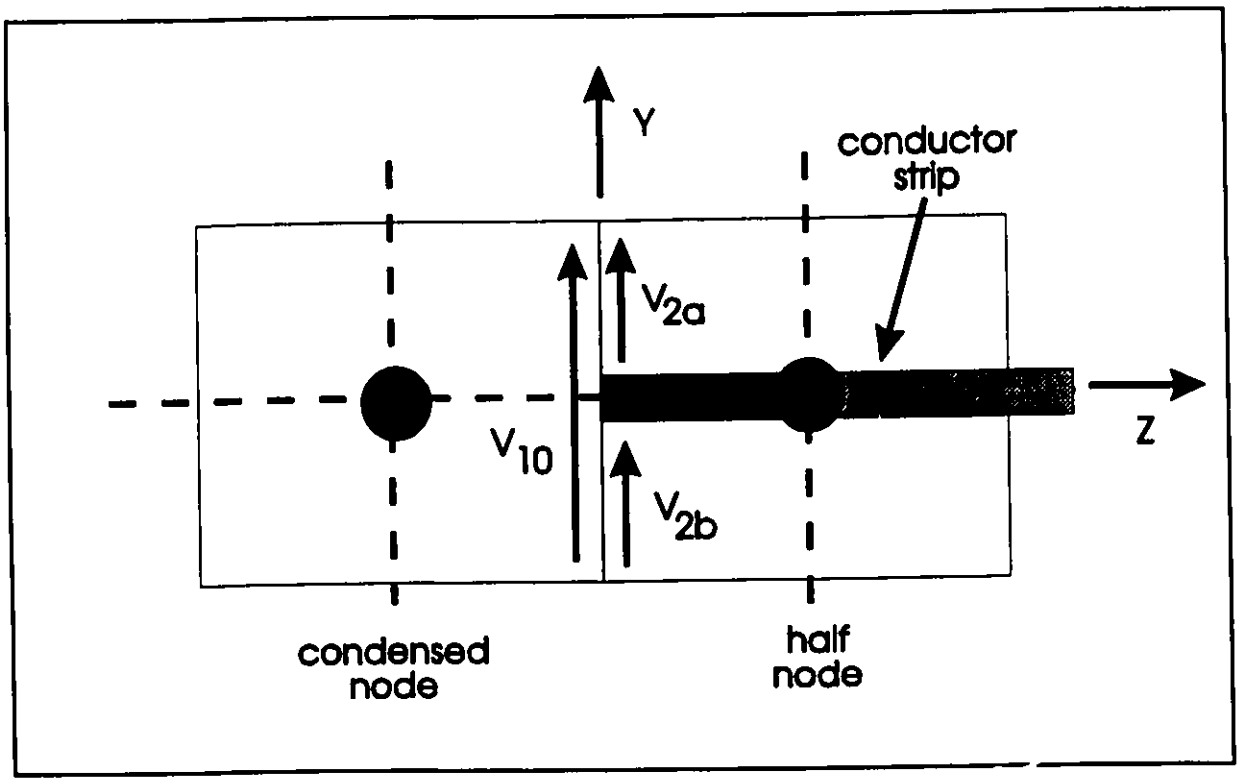

Fig. 3-6 Illustration of the simulation of a conductor strip edge modelled by a half-node and a conventional condensed node

between the pair of ports 2a and 2b of the half-node and port 10 of the conventional condensed node.

Consider first the voltages reflected from the half-node ports. At each time interval a pair of voltages V^r_{2a} and V^r_{2b} are generated by the scattering process of the half-node. The symmetrical component, $V^r_{2a} + V^r_{2b}$, couples directly into port 10 of the regular condensed node such that

$$V^i_{10} = V^r_{2a} + V^r_{2b} \tag{3-8}$$

The anti-symmetric voltage, $\frac{1}{2}(V^r_{2b} - V^r_{2a})$, represents the current flowing in the conductor sheet of the half-node which must be zero at the strip edge, (i.e. at port 2a and 2b). Consequently, the anti-symmetric voltage is reflected back into ports 2a and 2b with a reflection coefficient of unity. Hence,

$$V^i_{2a} = \tfrac{1}{2}(V^r_{2a} - V^r_{2b}) \tag{3-9a}$$

$$V^i_{2b} = \tfrac{1}{2}(V^r_{2b} - V^r_{2a}) \tag{3-9b}$$

The factor of $\frac{1}{2}$ ensures conservation of energy.

Considering the reflected voltage from port 10 of the regular condensed node, we must have

$$V^i_{2a} = \tfrac{1}{2}V^r_{10} \tag{3-10a}$$

$$V^i_{2b} = \tfrac{1}{2}V^r_{10} \tag{3-10b}$$

where the factor of $\frac{1}{2}$ ensures energy conservation. In addition, the regular condensed node reflects a voltage in port 9 which is polarized parallel to the

strip edge. As the tangential voltage on the strip edge must be zero, V^r_9 from the condensed node is reflected back into the condensed node with a reflection coefficient of -1. That is

$$V^i_9 = -V^r_9 \tag{3-11}$$

A problem with the simulation of the conductor strip edge as in Fig. 3-6 is that the link lines connecting ports 2a and 2b to the centre of the half-node represents a capacitive stub with regard to the antisymmetric voltage component. Hence, the simulated conductor strip edge is periodically loaded by capacitive stubs which slow down the wave propagation.

To avoid this problem the edge-node was created by modifying the half-node. The modification consists of reflecting the reflected antisymmetric voltage back into the node centre during the present update cycle rather than waiting till the next update cycle. This effectively moves the strip edge location to the centre of the node as illustrated in Fig. 3-3b. The scattering matrix for the edge-node is calculated by modifying the scattering matrix for the half-node to account for the antisymmetric voltage being reinserted into the scattering process.

The edge-node is illustrated in Fig. 3-7. Note that ports 2a and 2b are replaced by a single port denoted as port 2. Port 2 couples directly with port 10 of the adjacent regular condensed node. The voltage reflected from port 2 represents the y-polarized scattered symmetric voltage. Port 5 has been added to the edge node which mates with port 9 of the adjacent condensed node. The scattering coefficient for port 5 is -1 as discussed above.

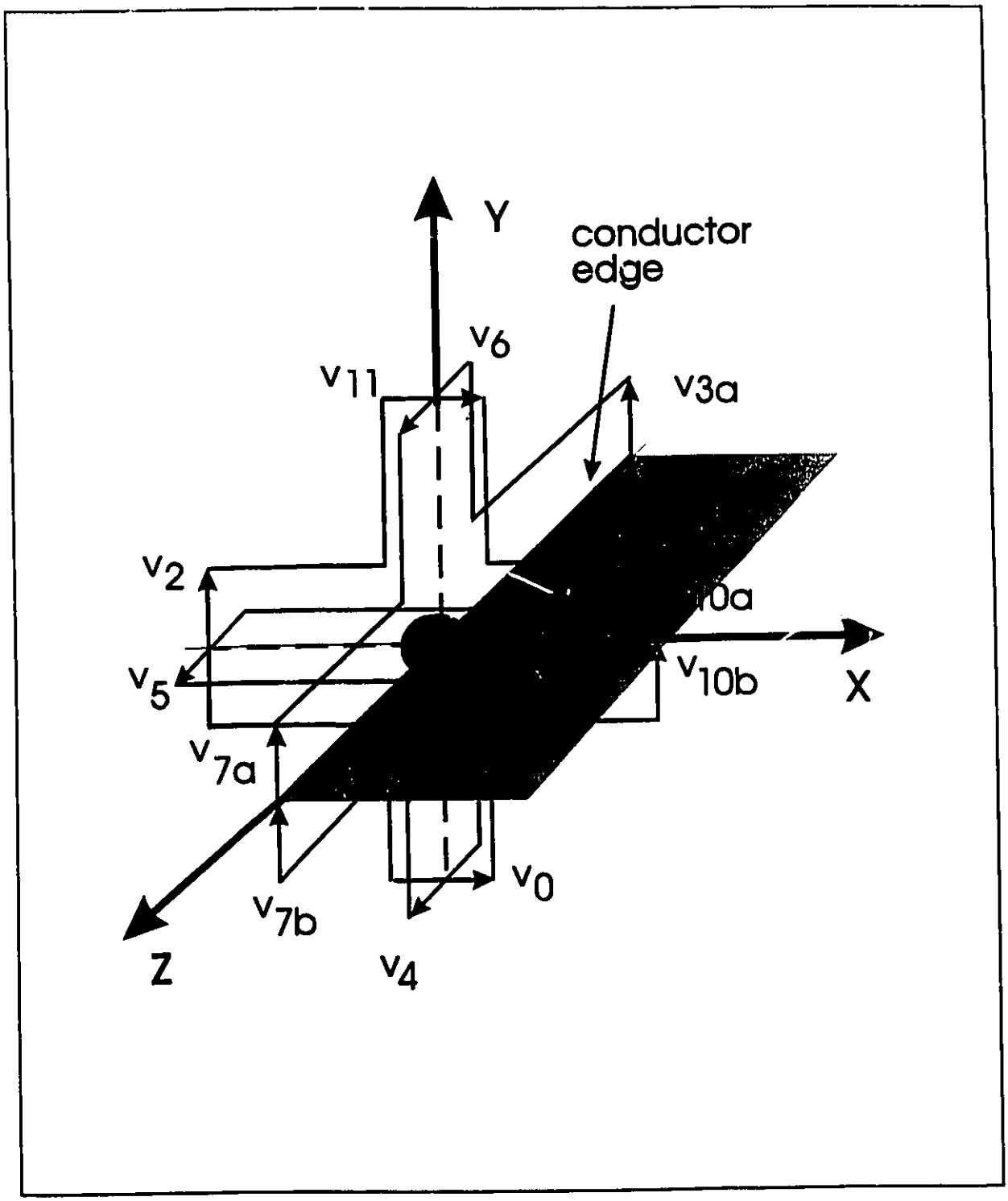

Fig. 3-7 Edge-node configuration for the conductor strip edge parallel to the z axis

The scattering matrix for this edge node is denoted by S_{ey2} where "e" denotes "edge", "y" indicates that the y axis is normal to the conductor plane, and "2" denotes that the edge is facing port 2 of the node. Likewise S_{ey3}, S_{ey7} and S_{ey10} are defined as the scattering matrices for the edge nodes corresponding to edges facing ports 3, 7 and 10 respectively.

3.2.3 Corner-Nodes

In order to model corners in the conductor strips, it is necessary to have a set of special corner nodes that can interface with the edge nodes as illustrated in Fig. 3-3c. One example is shown in Fig. 3-8 of an S_{cy23} node combined with an S_{ey2} and an S_{ey3} edge node. The subscript "c" denotes corner, "y" denotes orientation of the conductor plane normal to the y axis and "23" means it is inserted between edge nodes of type "2" and "3".

The scattering matrix for the corner node is derived in the same fashion as that for the edge node except that there are now two edges to contend with. The starting point is the scattering matrix S_{hy}, given in Eq. 3-3. Ports 2a and 2b of the corner node couple into a combined port 2, and ports 3a and 3b combine into port 3. In addition, ports 1 and 5, are accommodated in the same fashion as port 5 for the S_{ey2} node. At each time interval the symmetrical component of the voltages V^r_{2a} and V^r_{2b}, $(V^r_{2a} + V^r_{2b})$ is coupled directly to V^r_2. Likewise $(V^r_{3a} + V^r_{3b})$ couples directly to V^r_3. The antisymmetric components, $\frac{1}{2}(V^r_{2b} - V^r_{2a})$ and $\frac{1}{2}(V^r_{3b} - V^r_{3a})$ are reflected back into the node with a reflection coefficient of 1 during the same time interval as in the edge-node case. As with the edge-node, the reflection coefficient of unity forces the current flow normal to the

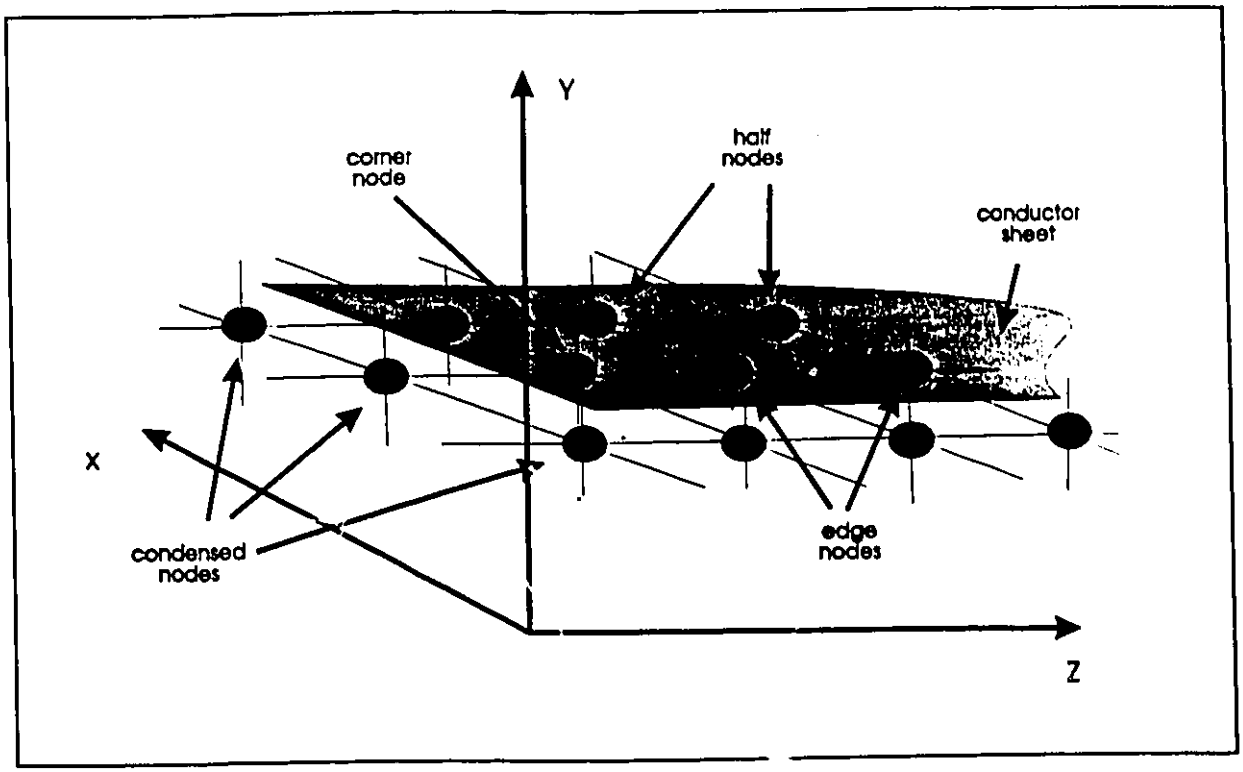

Fig. 3-8 Simulation of a corner in a planar conductor sheet using corner-nodes, edge-nodes and half-nodes.

edge to be zero at the edge. All the conditions listed above together with the scattering matrix of the half-node are compiled into a system of equations that is used to generate the appropriate scattering matrix for the corner-node.

3.2.4 90° Wedge-node

The last node type is the 90° wedge-node illustrated in Fig. 3-3d. The wedge-node is generally used as a coupling between two orthogonal half-nodes as illustrated in Fig. 3-9. Shown is a S_{wyz} node where "w" denotes wedge and "yz" denotes that it interfaces an S_{hy} and an S_{hz} node. The scattering matrix for this node is derived by assuming that the symmetric portion of the incident voltages

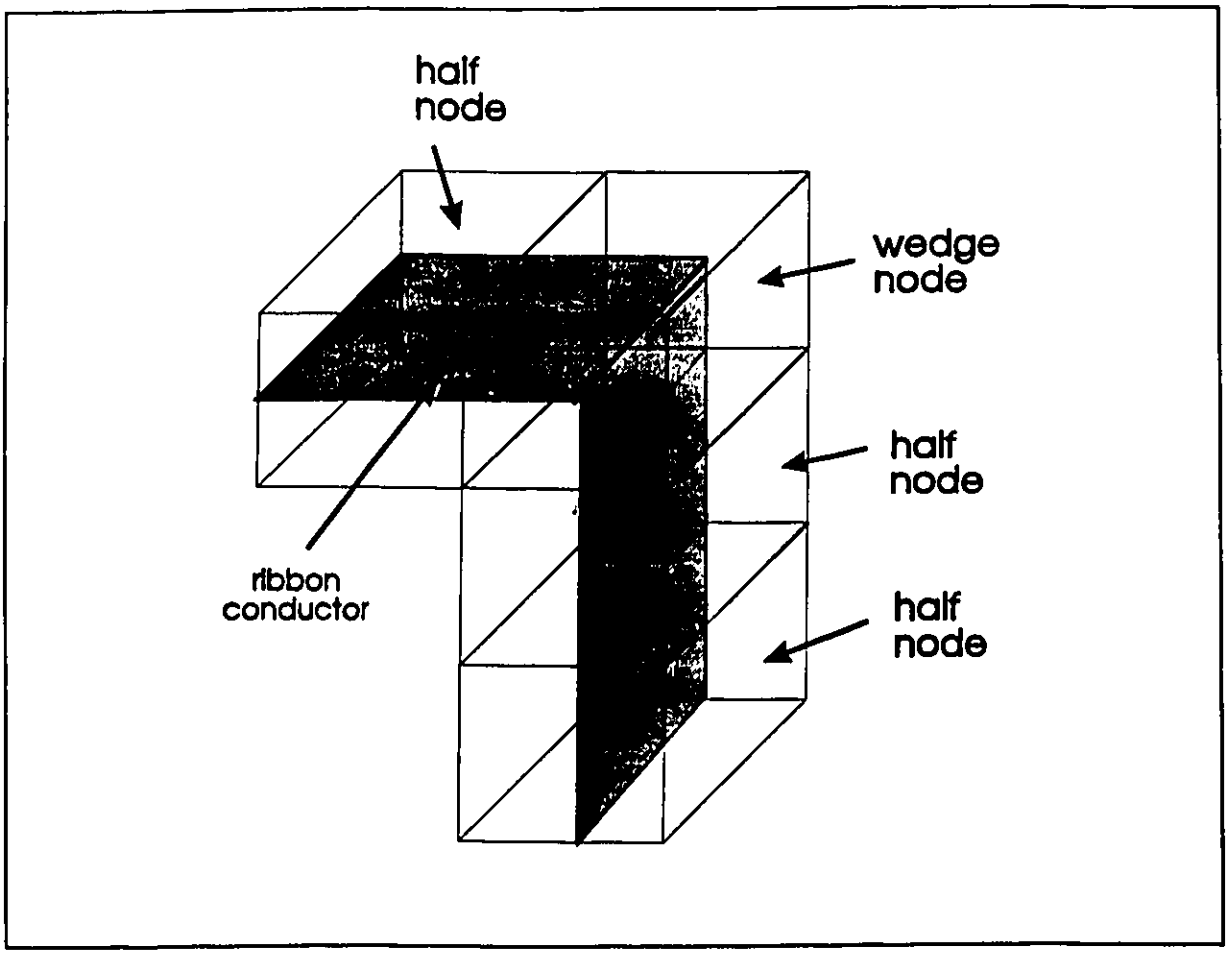

Fig. 3-9 Illustration of a possible application of a wedge-node to couple two orthogonal half-nodes

at the half-node ports propagates through the wedge-node as though it were a normal condensed node. The antisymmetric voltages, representing the surface currents, are assumed to be continuous. The wedge-node, as illustrated in Fig. 3-9, assumes no current in the x direction. The node satisfies the current continuity and energy conservation, however, it does not correctly model the edge current along the x axis, nor does it model further interaction between the current and the field. For our purpose, the node is used only in cases where short narrow wire and ribbon bonds to devices are required. The effect of neglecting the x-directed current flow is insignificant in this case.

3.3 MODELLING DIELECTRIC MATERIAL WITH HALF-NODES

In order to model microstrip line circuits, it is necessary that capacitive stubs be incorporated into the conductor strip nodes to simulate dielectric material. The conductor strip is generally coincident with the dielectric interface. Hence, the conductor strip nodes must accommodate two different dielectrics for which six capacitive stubs are required. However, to minimize the program complexity, it was decided to use a capacitive stub at each port. While this represents six additional variables per node, the conductor strip nodes are generally present in only one layer and hence, the overall increase in memory and computational effort is negligible.

In order to demonstrate the development of the overall scattering matrix for the conductor strip node types, the S_{hy} node is taken as an example. It is assumed that the conductor sheet located in the middle of the half-node is coincident with the dielectric interface. In general, the dielectric layers can be anisotropic with a diagonal permittivity tensor. Therefore, six dielectric constants are defined. $\epsilon_{r,1,x}$, $\epsilon_{r,1,y}$ and $\epsilon_{r,1,z}$, denote the permittivity in the x, y and z directions for region 1 above the conductor strip. Likewise $\epsilon_{r,2,x}$, $\epsilon_{r,2,y}$ and $\epsilon_{r,2,z}$, denote the permittivity in the x, y and z directions for region 2 below the conductor strip.

Across each of the twelve ports will be a shunt capacitive stub of normalized admittance $Y_{s,p}$ where "p" represents the port associated with the stub. Consider the upper half of the S_{hy} half-node. The total capacitance of the medium, relative to the y axis, is given by

$$C_{m,1,y} = 2\, e_{r,1,y}\, e_o\, d \qquad (3\text{-}12)$$

where the subscript "m" denotes "medium", "1" denotes the upper zone 1 of the node and "y" denotes "with respect to the y-axis" since anisotropic dielectrics may be modelled. $C_{m,1,y}$ must equal the node capacitance with respect to the y-axis which consists of the four link lines and the four capacitive stubs shunting the link lines.

The normalized admittance of the capacitive stub shunting port "p" is denoted as $Y_{s,p}$. For sake of simplicity, it is assumed that the four y-polarized capacitive stubs have the same normalized admittance of Y_s. Consequently

$$Y_{s,2a} = Y_{s,3a} = Y_{s,7a} = Y_{s,10a} = Y_s \, . \qquad (3\text{-}13)$$

The capacitance of each of these stubs was given by Eq.2-25 as

$$C_{stub} = \frac{Y_s \, Y_o \, d}{V_{link} \, 2} \, . \qquad (2\text{-}25)$$

As the total capacitance of the four y-polarized link lines in region 1 is $2\epsilon_o d$ we arrive at

$$Y_s = 2 \, (\epsilon_{r,1,y} - 1) \, . \qquad (3\text{-}14)$$

Consider now the capacitance relative to the x-axis. $C_{m,1,x}$ for the upper part of the node is

$$C_{m,1,x} = \frac{\epsilon_{r,1,x} \, \epsilon_o \, d}{2} \qquad (3\text{-}15)$$

which must equal the node capacitance with respect to the x-axis in region 1.

In this case only one port, p=11, is involved. Hence the node capacitance is the sum of the capacitance of the link line corresponding to p=11, given by $\frac{1}{2}\epsilon_0 d$, and the capacitive stub shunting port 11 with a normalized admittance $Y_{s,11}$. Hence

$$Y_{s,11} = 2\ (\epsilon_{r,1,z} - 1)\ . \qquad (3\text{-}16)$$

The remaining stub admittances for the S_{hy} node are given in the following table;

Table 3-1 Value of capacitance stub for each port of the half-node

stub no.	port no.	Y_s
0	0	$2(\epsilon_{r,2,z} -1)$
1	2a	$2(\epsilon_{r,1,y} -1)$
2	2b	$2(\epsilon_{r,2,y} -1)$
3	3a	$2(\epsilon_{r,1,y} -1)$
4	3b	$2(\epsilon_{r,2,y} -1)$
5	4	$2(\epsilon_{r,2,z} -1)$
6	6	$2(\epsilon_{r,1,z} -1)$
7	7a	$2(\epsilon_{r,1,y} -1)$
8	7b	$2(\epsilon_{r,2,y} -1)$
9	10a	$2(\epsilon_{r,1,y} -1)$
10	10b	$2(\epsilon_{r,2,y} -1)$
11	11	$2(\epsilon_{r,1,y} -1)$

Stub values for modelling dielectric material in edge nodes and corner nodes are determined by the same procedure as above, namely by equating the medium and node capacitance.

The stubs shunt each port just adjacent to the condensed node as illustrated in Fig. 3-10. Let V_p be the voltage at the external port connection of port p,

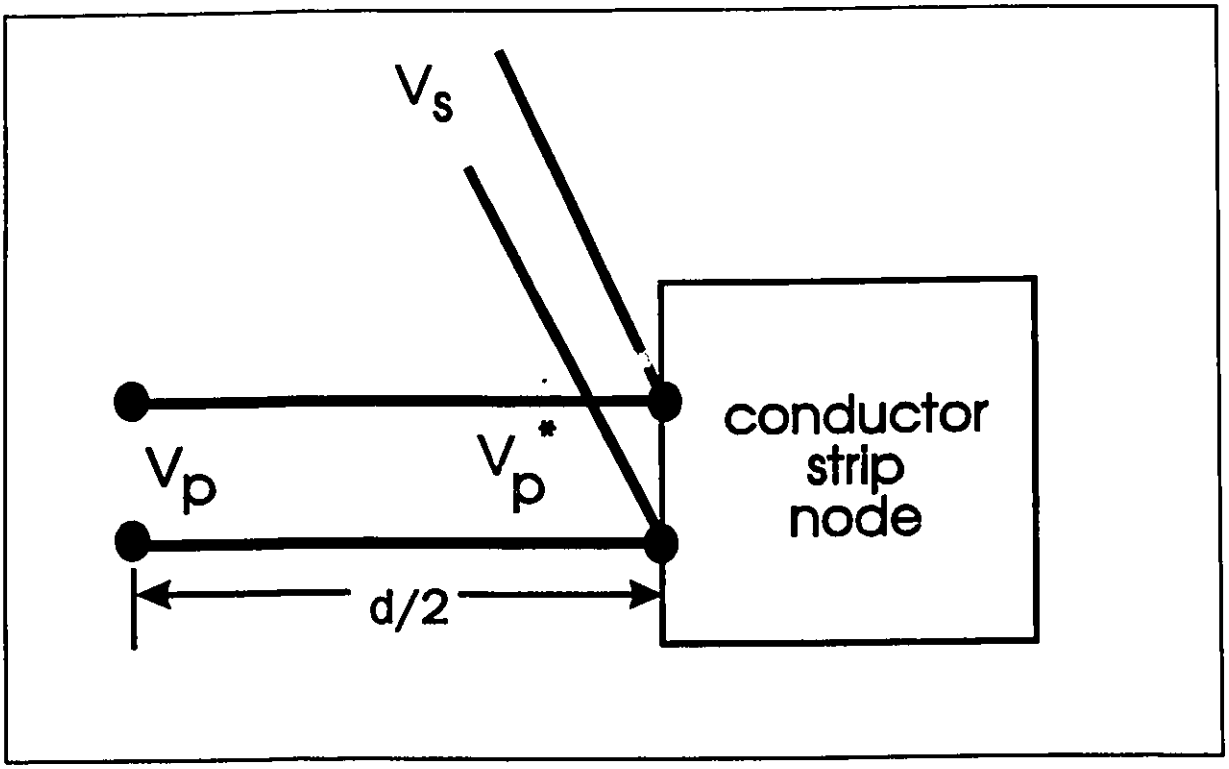

Fig.3-10 Shunt capacitive stub connected to port p at the node centre

V_p^* be the voltage associated with port p at the half, edge or corner-node, and V_s represent the stub voltage as illustrated. The scattering matrix relating the incident and reflected components of these voltages is given by

$$\begin{pmatrix} V_p \\ V_{p'} \\ V_s \end{pmatrix}^r = \begin{pmatrix} a & b & c \\ b & a & c \\ b & b & d \end{pmatrix} \begin{pmatrix} V_p \\ V_{p'} \\ V_s \end{pmatrix}^i \qquad (3\text{-}17)$$

where

$$a = -\frac{Y_{s,p}}{2\,Y_{l,p} + Y_{s,p}}$$

$$b = \frac{2\ Y_{l,p}}{2\ Y_{l,p} + Y_{s,p}}$$

$$c = \frac{Y_{s,p} - 2\ Y_{l,p}}{2\ Y_{l,p} + Y_{s,p}}$$

$$d = \frac{2\ Y_{s,p}}{2\ Y_{l,p} + Y_{s,p}} \quad .$$

$Y_{l,p}$ is the link line admittance and $Y_{s,p}$ is the stub admittance associated with port p.

The overall scattering matrix for the half-node with all the dielectric stubs is a 24-by-24 matrix. It is derived by considering the complete network of a half-node with twelve shunt stubs attached.

The derivation of the scattering matrix for the condensed node is based on the assumption that the dielectric is homogeneous throughout the node volume. Presently, there is no mechanism for accurately representing a dielectric interface within the condensed node volume. This mechanism is required for the condensed nodes in the conductor strip layer. Presently, the dielectric interface is modelled by merely setting the dielectric constant used in the condensed node to the average of the dielectric constants in regions 1 and 2. This is not a very accurate simulation of the actual boundary conditions at the dielectric interface. A detailed study of the condensed node is required to determine a more appropriate scattering matrix for this case.

3.4 DEMONSTRATION OF IMPROVED ACCURACY USING CONDUCTOR STRIP NODES

Two examples are provided to demonstrate the improved accuracy in modelling strip like transmission line structures using conductor strip nodes. The first is a half-wavelength stripline resonator assuming no dielectric. The second is a microstrip line bounded by conducting walls.

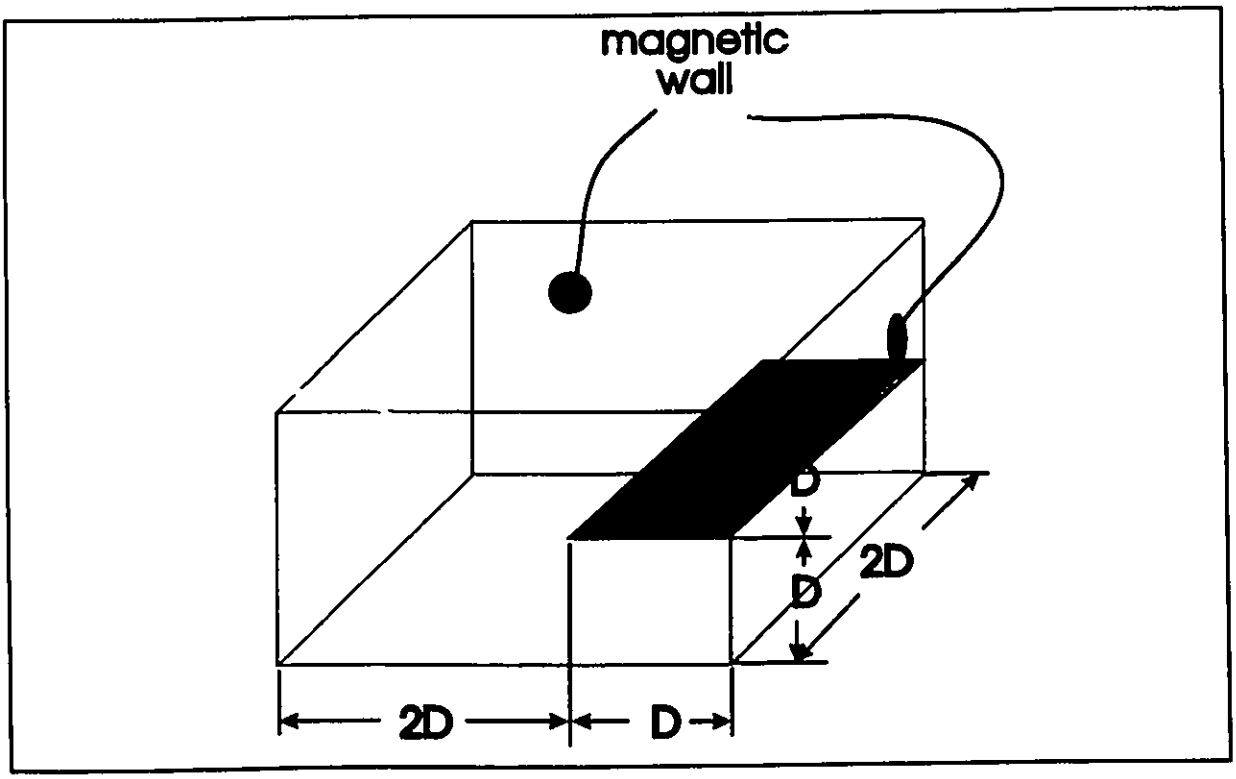

Fig. 3-11 Configuration of half-wavelength stripline resonator bounded by a rectangular box. Two walls are magnetic as indicated, the others are conductive.

A sketch of the strip line resonator is given in Fig. 3-11. The dimensions of the resonator are given in terms of the parameter "D" which represents an integral number of nodes. The TLM impulse response of the resonator structure is calculated, and its Fourier transform is computed. In the resulting spectrum, the lowest frequency peak is the fundamental resonance response of the desired

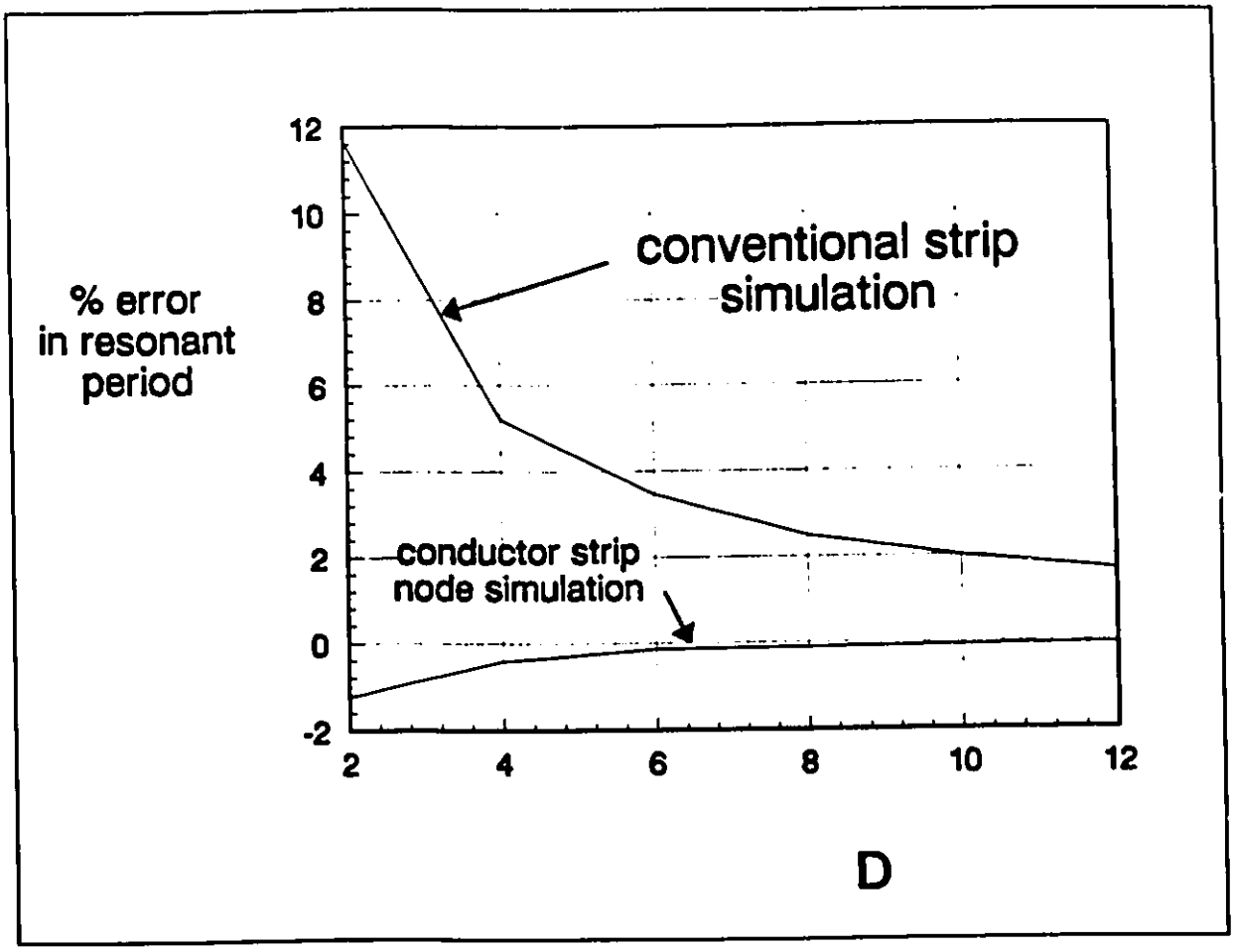

Fig. 3-12 Comparison of the convergence of the resonant period of the simulated stripline resonator as a function of the mesh dimension parameter D.

TEM mode. The centre of the peak corresponds to the calculated resonance frequency which is compared to the theoretical resonance frequency of

$$f_{res} = \frac{1}{16\ D\ \Delta t} \qquad (3\text{-}18)$$

The relative error in the resonant period as a function of the parameter D is given in Fig. 3-12. The results are compared with the conventional method of

simulating the strip as a truncated Dirichlet boundary between nodes as illustrated in Fig. 3-1. As observed, there is a substantial improvement in accuracy by incorporating conductor strip node types into the TLM mesh.

In order to test the simulation accuracy of the conductor nodes with capacitive stubs, the stripline resonator in Fig. 3-11 was modelled again with a dielectric of ϵ_r=2.5 and D=5. The resonant period was .25% high with respect to the theoretical resonant frequency, f_c, of the fundamental TEM mode, given by

$$f_c = \frac{1}{16\ D\ \sqrt{\epsilon_r}\ \Delta t} \qquad (3\text{-}19)$$

The error can be attributed to the slow wave structure formed by the periodically-placed stubs [23]. The sign of the error due to the dielectric stubs is opposite to that of the error due to the conductor strip modelling using half-nodes. Hence the errors will subtract rather than add.

As a further test of the accuracy of modelling conductor strips with conductor strip nodes, the microstrip line in Fig. 3-13 was simulated. Two TLM configurations are considered. The first, shown in Fig. 3-13a, consists of conventional condensed nodes with the strip modelled by a truncated Dirichlet boundary. In the second simulation, shown in Fig. 3-12b, the conductor strip nodes are employed. Two different microstrip geometries are necessary since the conductor strips in each simulation cannot be placed at exactly the same height. Fig. 3-14a and 3-14b show the effective dielectric constant of the simulated microstrip lines as compared to the empirical equation by Hammerstad and Jensen [44]. As observed in Fig. 3-14, the effective dielectric constant obtained with the conventional nodes is consistentiy high, indicating that the propagation is too slow. This is consistent with the discussion in Section 3.1. In the above

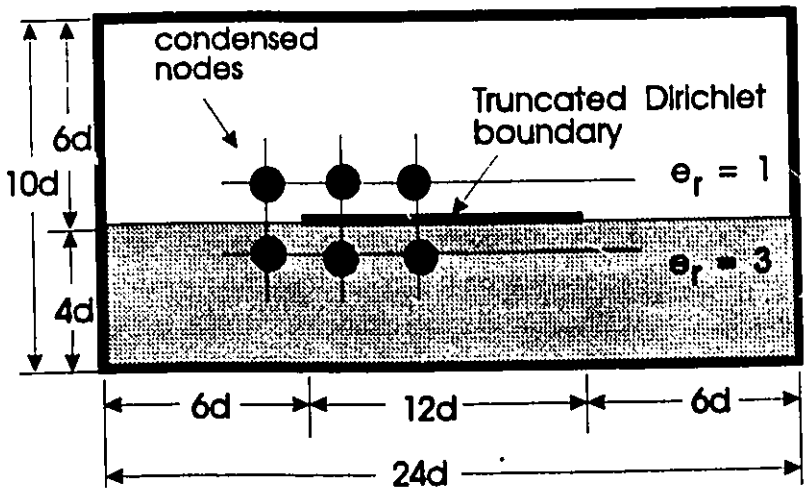

a) Conventional simulation with truncated Dirichlet boundary

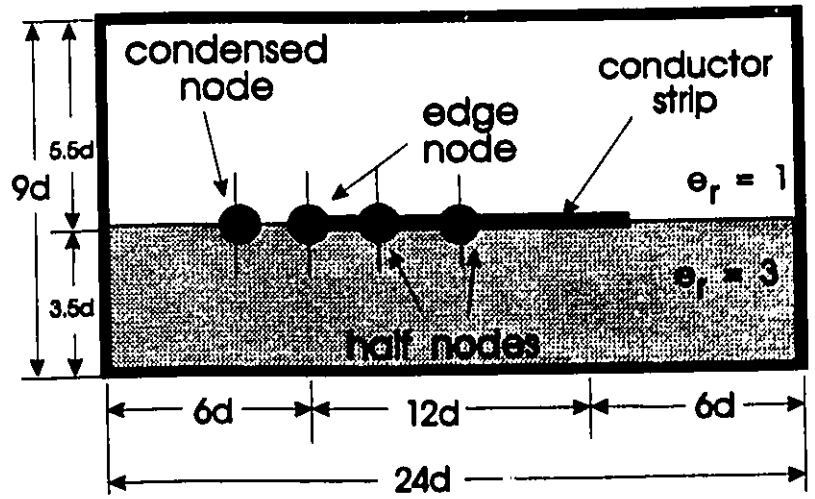

b) Simulation using conductor strip nodes

Fig. 3-13 TLM mesh configuration for modelling an enclosed microstrip line. a) Conventional simulation with a truncated Dirichlet boundary, b) simulation using conductor strip nodes

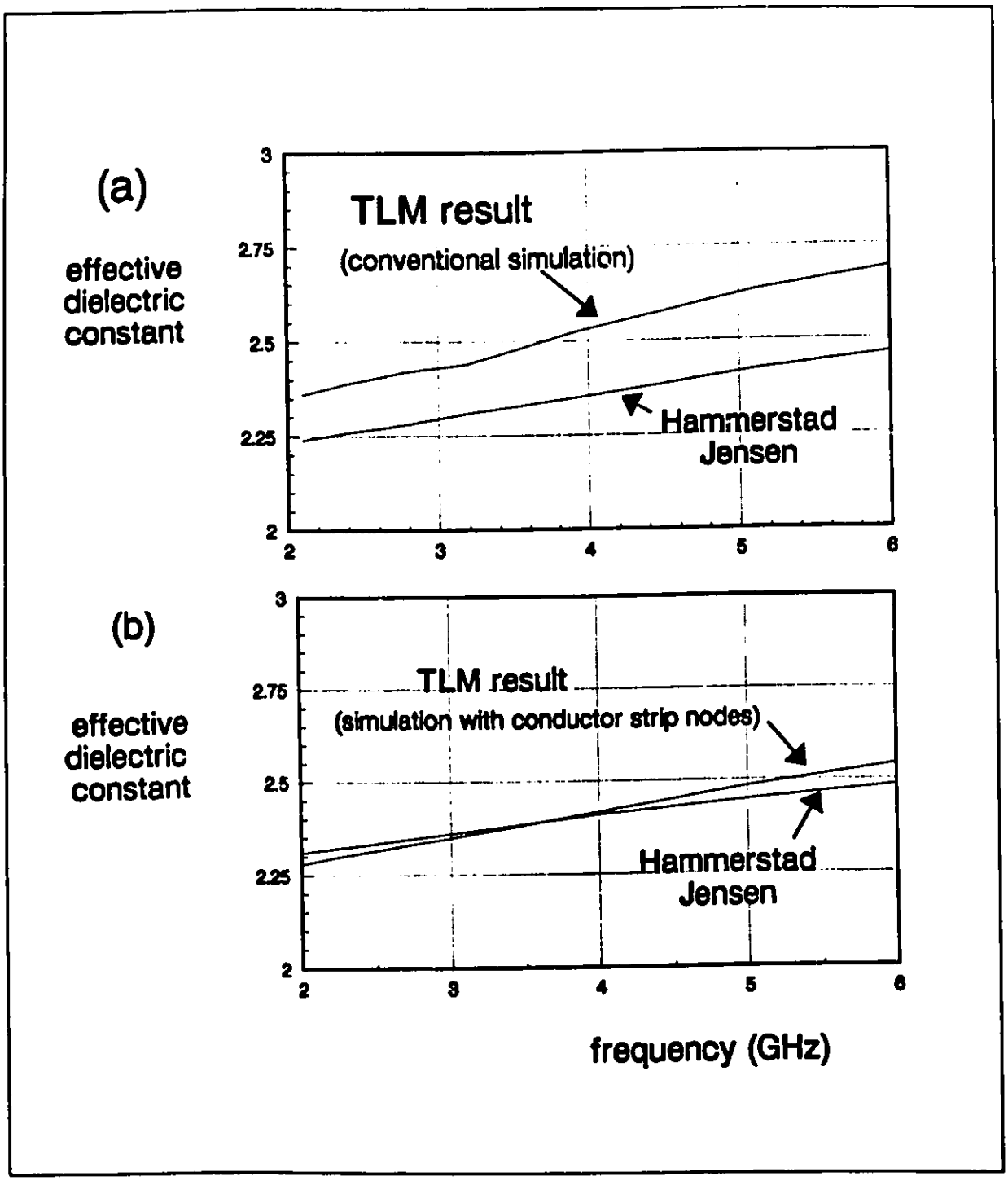

Fig. 3-14 Comparison of the TLM simulation of a microstrip line with the calculation by Hammerstad-Jensen [44]. a) Simulation using a truncated Dirichlet boundary b) Simulation using conductor strip nodes

simulations, d was taken as 1 mm. Hence the microstrip is 12 mm wide. For this reason, the simulation was only performed for frequencies up to 6 GHz.

3.5 CORRECTION FACTOR FOR EDGE-NODE

In the derivation of the scattering properties of the edge-node, $S_{\bullet y2}$, port 5 was heuristically assigned a reflection coefficient of -1. Hence the incident field parallel to the conductor edge is reflected as if it were incident on an infinite Dirichlet boundary. For planar transmission line structures where the electric field is primarily perpendicular to the conductor edge this treatment produces accurate results as evidenced in Section 3.4. Unfortunately, for conductor edges with a strong incident E-field component tangential to the conductor edge, the edge-node interacts too strongly with that component. An example of such a case is an inductive iris in a rectangular waveguide subject to an incident TE_{10} mode. Results for the inductive iris are presented here.

The inductive iris is shown in Fig. 3-15a with the conventional TLM model shown in Fig. 3-15b and the half-node model given in Fig. 3-15c. The mesh is only one node in height since there is no field variation in the y direction as a TE_{10} mode excitation was assumed. Appendix C describes the procedure developed to extract scattering parameters from the time domain simulation.

Fig. 3-16 is a plot of the normalized shunt susceptance of the inductive iris as a function of the quotient of the guide width and the free space wavelength. In the "conductor strip node simulation" plots, "a" is a parameter used in the node modification to be described. The "analytical solution" is based on the theoretical values given by Marcuvitz [45]. Note that the iris

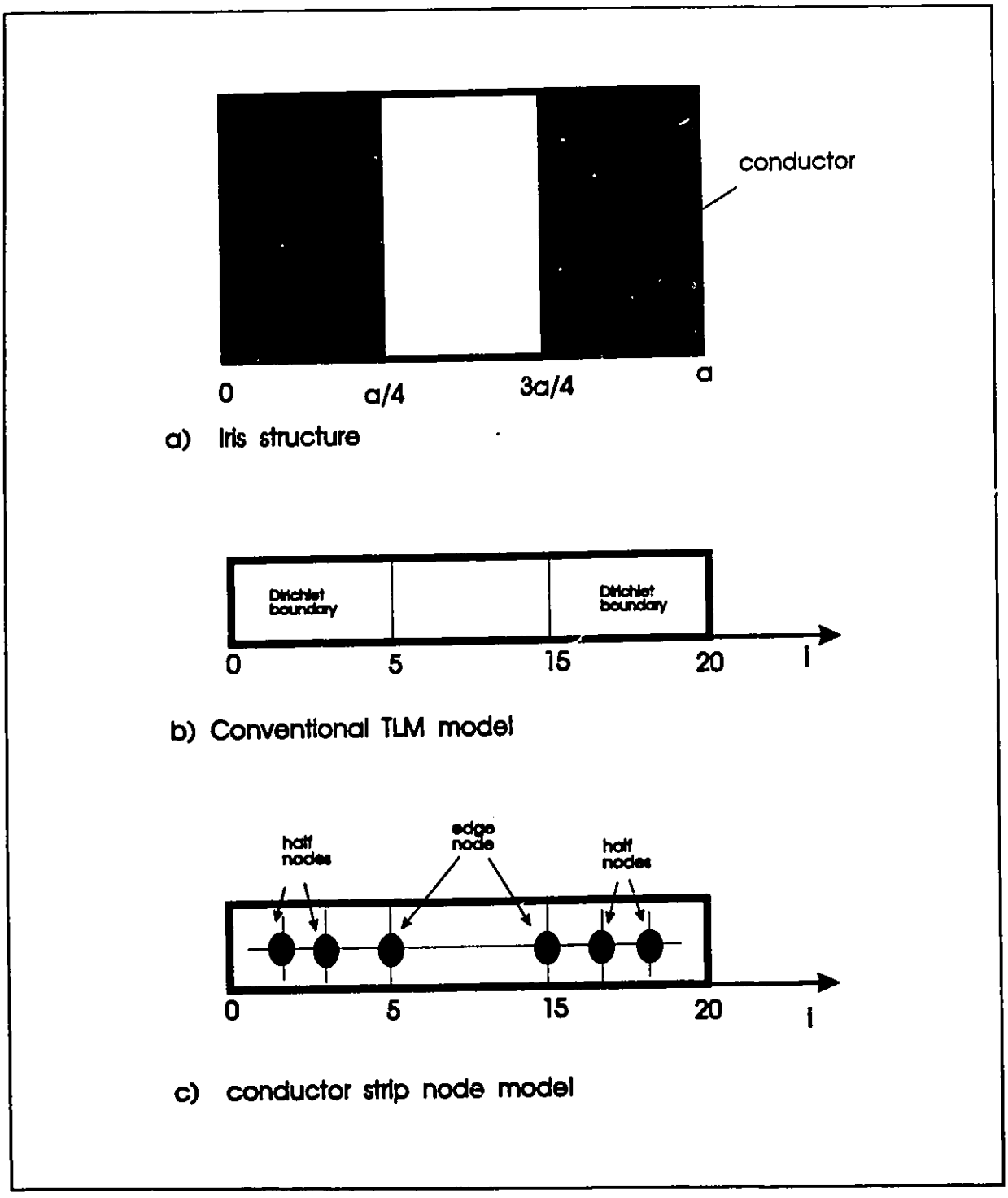

Fig. 3-15 Simulation of an inductive iris in a rectangular waveguide.

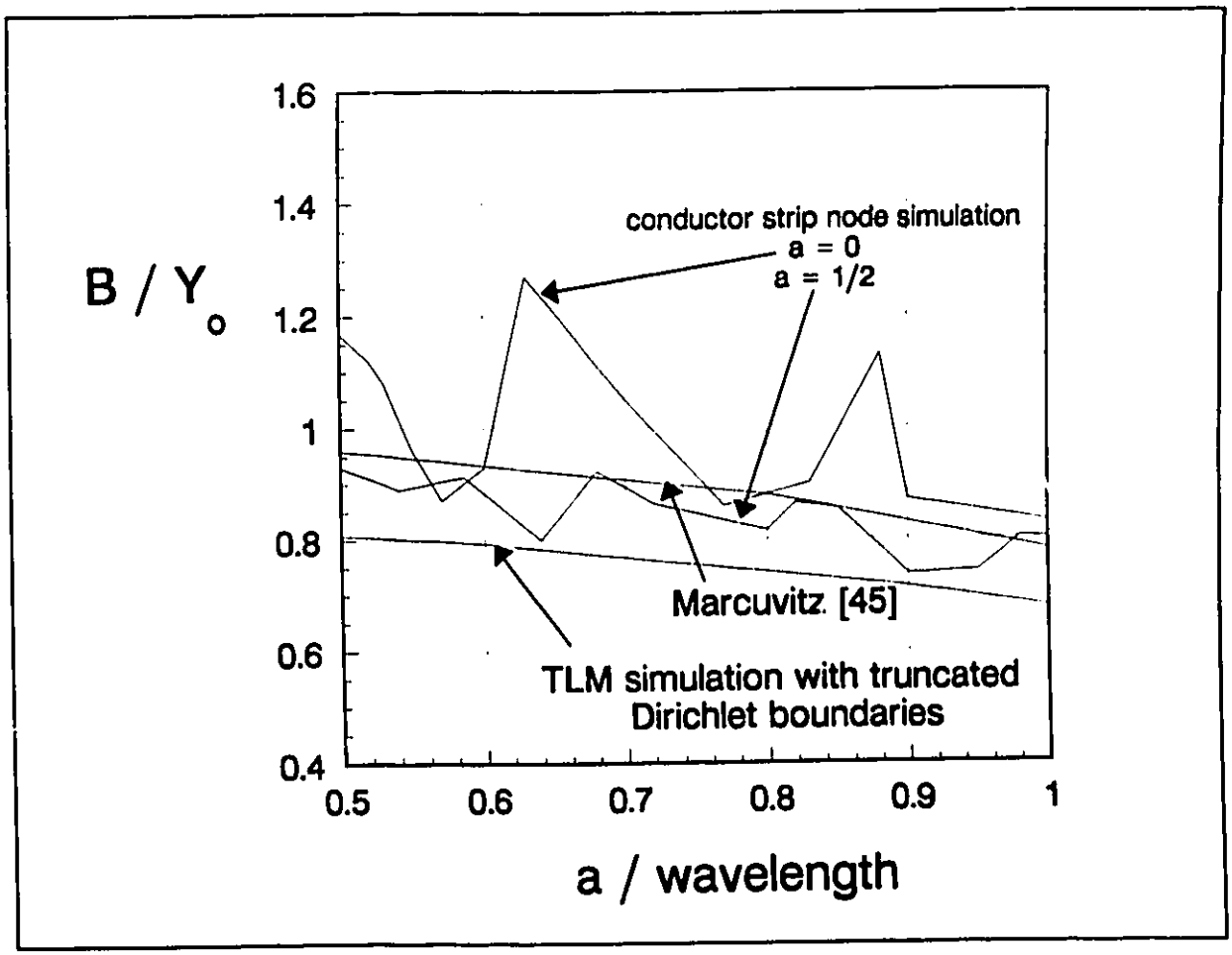

Fig. 3-16 Plot of the normalized iris susceptance as a function of the excitation frequency comparing the analytical solution with TLM simulations.

susceptance for the conventional modelling using truncated Dirichlet boundaries is consistently too small which complies with the initial postulate that conductor edges modelled in this fashion do not couple sufficiently with the surrounding mesh. On the contrary, the conductor strip modelling using the unmodified edge-node (trace with a=0) interacts too strongly displaying a strong resonant behaviour. While the modelling accuracy of the modified edge-node (trace with a=½) is not impressive, it is consistently better than the conventional Dirichlet boundary modelling. Also, as we are primarily interested

in planar structures, this inaccuracy is of minor concern in this research. Presently the choice of the parameter is empirical.

The modification to the edge-node will be discussed with reference to the $S_{\bullet yz}$ node. Instead of reflecting the incident voltage directly into port 5 with a reflection coefficient of -1, port 4, 5 and 6 are initially coupled using the following transformation matrix with is applied to both the incident and reflected voltages.

$$\begin{pmatrix} V_4 \\ V_5 \\ V_6 \end{pmatrix} = \boldsymbol{T} \begin{pmatrix} V_4' \\ V_5' \\ V_6' \end{pmatrix} \tag{3-20}$$

with

$$\boldsymbol{T} = \begin{pmatrix} x & a & b \\ a & y & a \\ b & a & x \end{pmatrix} \tag{3-21}$$

where "a" is the coupling factor with a value between 0 to 1, which can be empirically optimized for best accuracy. The other variables are determined from the requirement that T be a unitary matrix which is imposed in order to conserve energy. This results in

$$y = -\sqrt{1 - 2\,a^2} \tag{3-22a}$$

$$x = \frac{1 - y}{2} \tag{3-22b}$$

$$b = -\frac{1 + y}{2} \tag{3-22c}$$

The transformation matrix is used to modify the scattering matrix S_{eyz} as

$$S_{eyz} \leftarrow T \cdot S_{eyz} \cdot T \qquad (3\text{-}23)$$

For the results in Fig. 3-16, plots are given for a=0 and a=0.5.

3.6 INCLUSION OF LUMPED DEVICES IN CONDUCTOR STRIP

The conductor strip nodes were developed primarily to provide a means of modelling conductor strips that can couple directly with embedded lumped devices. The current flow on the conductor surface is directly available from the port voltages of the conductor strip nodes. This facilitates the interface with arbitrary devices. Details of the interface between the half-node and an embedded lumped device are developed in this section.

3.6.1 Embedded Two-Terminal Lumped Device

In order to simplify the explanation of the interface between an embedded device and the conductor strip nodes, the stripline structure shown in Fig. 3-17 is used. It consists of a 1D array of half-nodes bounded by conducting walls on the top and bottom surfaces, and by magnetic walls on both sides. A two-terminal device is embedded between two S_{hy} half-nodes denoted as "node 1" and "node 2". The gap between these nodes, denoted by δ, is assumed to be negligibly small. Hence the device is assumed to have infinitesimal dimensions. In Section 3.6.3 the simulation of distributed devices will be discussed. There are four ports

the simulation of distributed devices will be discussed. There are four ports involved in the interface as shown in the detail illustration of Fig. 3-17. These are ports 7a and 7b for node 1 and ports 3a and 3b for node 2. The voltages at the two pairs of ports 3a,3b and 7a,7b are initially partitioned into symmetric and antisymmetric components. The antisymmetric component relates directly to the current flowing in the half-node, and hence through the device. The symmetric component can be related to a displacement current propagating through the dielectric material surrounding the device.

The antisymmetric voltages for nodes 1 and 2 are defined as

$$V_{as,1} = \frac{V_{7b,1} - V_{7a,1}}{2} \qquad (3\text{-}24a)$$

$$V_{as,2} = \frac{V_{3b,2} - V_{3a,2}}{2} \qquad (3\text{-}24b)$$

Consider the incident current flowing into the conductor of node 2 as illustrated in Fig. 3-18. The current flow on the top and bottom surface of the conductor along the z axis is

$$I^i_{3a,2} = -2\ Y_o\ V^i_{3a,2} \qquad (3\text{-}25a)$$

and

$$I^i_{3b,2} = 2\ Y_o\ V^i_{3b,2} \qquad (3\text{-}25b)$$

respectively. The total incident current on the conductor is defined as $I'_{as,2}$ which from Eq. 3-25 is

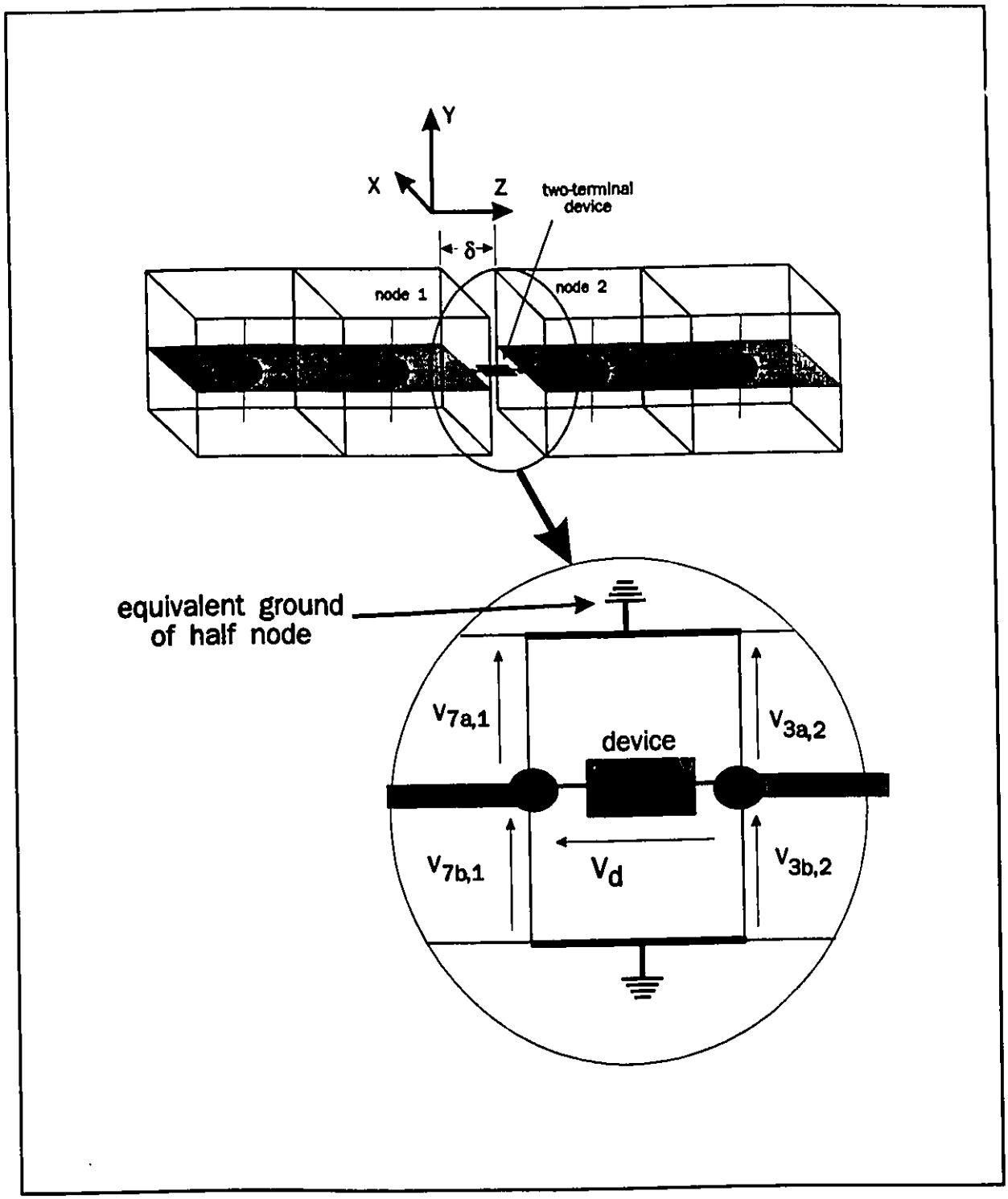

Fig. 3-17 Embedded two-terminal lumped device in a stripline configuration simulated by an array of half-nodes

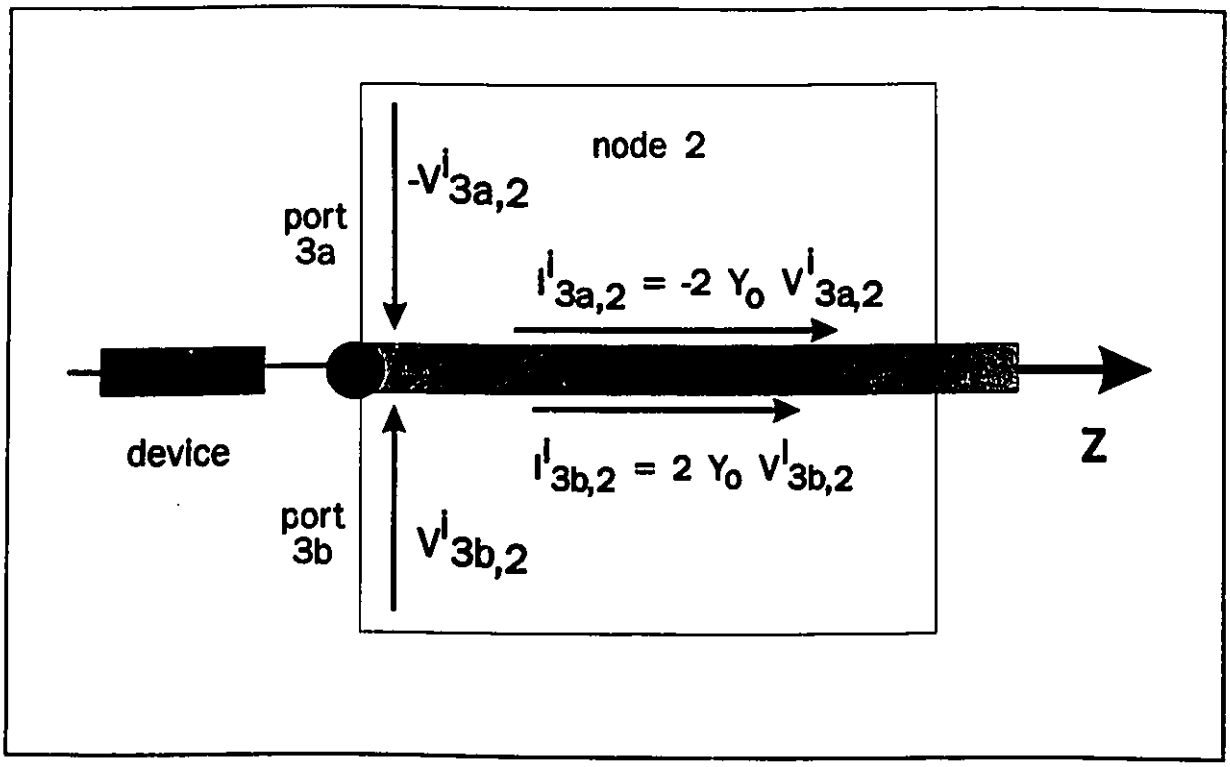

Fig. 3-18 Current flow on conductor strip in node 2

$$I^i_{as,2} = 4\ Y_o \frac{V^i_{3b} - V^i_{3a}}{2} = Y_{as}\ V^i_{as,2} \qquad (3\text{-}26)$$

where $Y_{as}=4Y_o$ is the admittance of the antisymmetric mode.

The symmetric voltages are defined as

$$V^i_{s1} = V^r_{7a,1} + V^r_{7b,1} \qquad V^i_{s2} = V^r_{3a,2} + V^r_{3b,2}$$
$$V^r_{s1} = V^i_{7a,1} + V^i_{7b,1} \qquad V^r_{s2} = V^i_{3a,2} + V^i_{3b,2} \qquad (3\text{-}27)$$

and the admittance associated with the symmetric mode is Y_o.

Fig. 3-19 shows a block diagram of the interface to the two-terminal device. The reflected voltages from the half-nodes 1 and 2 are first transformed into

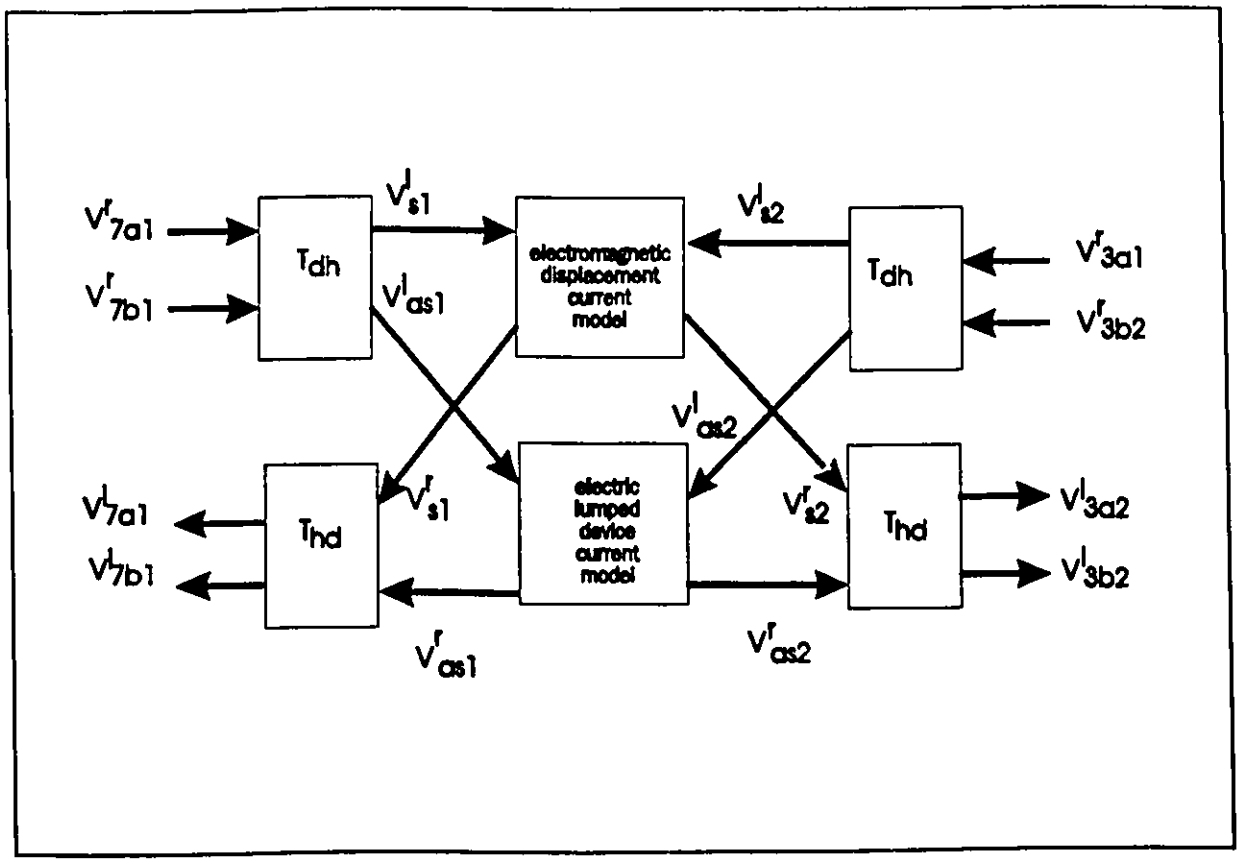

Fig. 3-19 Block diagram of the interface to the two port device

symmetric and antisymmetric components by a transformation matrix T_{dh} where "d" signifies "device" and "h" signifies "half-node". There are two separate models indicated in Fig. 3-19 for the lumped device for the symmetric and antisymmetric voltage components. The symmetric model includes particular electromagnetic modelling of the device packaging. The antisymmetric device model consists of the electric current model of the device. The reflected symmetric and antisymmetric voltages are transformed by T_{hd} resulting in the incident voltages to the half-nodes 1 and 2. T_{dh} and T_{hd} are given as

$$\begin{pmatrix} V^i_{s,p} \\ V^i_{as,p} \end{pmatrix} = \begin{pmatrix} 1 & 1 \\ -\frac{1}{2} & \frac{1}{2} \end{pmatrix} \begin{pmatrix} V^r_{a,p} \\ V^r_{b,p} \end{pmatrix} = T_{dh} \begin{pmatrix} V^r_{a,p} \\ V^r_{b,p} \end{pmatrix} \qquad (3\text{-}28)$$

and

$$\begin{pmatrix} V^i_{a,p} \\ V^i_{b,p} \end{pmatrix} = \begin{pmatrix} \frac{1}{2} & -1 \\ \frac{1}{2} & 1 \end{pmatrix} \begin{pmatrix} V^r_{s,p} \\ V^r_{as,p} \end{pmatrix} = T_{hd} \begin{pmatrix} V^r_{s,p} \\ V^r_{as,p} \end{pmatrix} \qquad (3\text{-}29)$$

where p denotes the port.

Consider first the case where the device in Fig. 3-17 is a short circuit. The antisymmetric device model reduces to the equations

$$V^r_{as,1} = V^i_{as,2}$$
$$V^r_{as,2} = V^i_{as,1}$$

since a short circuit does not disrupt the current flow. Likewise the symmetric model reduces to the equations

$$V^r_{s,1} = V^i_{s,2}$$
$$V^r_{s,2} = V^i_{s,1} .$$

Following the transformations it is clear that

$$V^i_{7a,1} = V^r_{3a,2}$$
$$V^i_{7b,2} = V^r_{3b,1}$$
$$V^i_{3a,1} = V^r_{7a,2}$$
$$V^i_{3b,2} = V^r_{7b,1}$$

as should be expected.

Consider next the case where the lumped element is replaced by an open circuit. The incident antisymmetric voltages are reflected with a reflection coefficient of 1 since there is no electric current flow across the gap as illustrated by the current flow in Fig. 3-20.

The incident symmetric voltages propagate unimpeded across the gap. To see this consider the case where $V^r_{7a1} = V^r_{7b1} = 1$ such that $V^t_{s1} = 2$ and $V^t_{s1} = 0$. Note that the current flows unimpeded around the conductor edges supporting a continuity of the symmetric field. Hence V^t_{s1} must couple directly to V^r_{s2}.

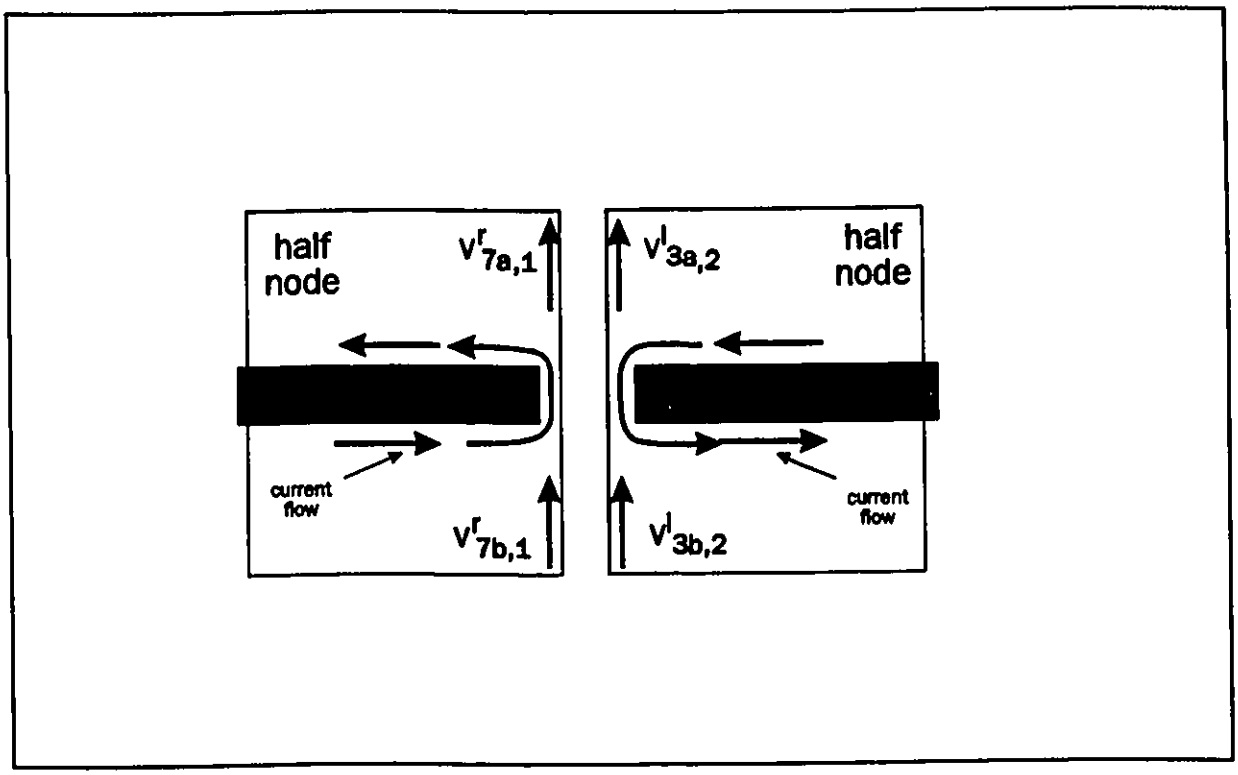

Fig. 3-20 Current flow in conductor strips when the lumped device is replaced by an open circuit

In the present simulation, the capacitance across the gap between the strips cannot be represented by the half-nodes. However, in an practical simulation, the layer of half-nodes will normally be sandwiched between multiple layers of condensed nodes. These nodes simulate the fringing fields of the gap and hence, model the equivalent capacitance.

With this groundwork in place, consider now the lumped device in Fig. 3-17 to be a resistor with resistance R. V_d is defined as the voltage across the device. Imposing the condition of continuity of the E field at the interface between node 1 and node 2 we have,

$$V_{7b,1} = V_d + V_{3b,2} \qquad (3\text{-}30a)$$

$$V_{7a,1} = -V_d + V_{3a,2} \; . \qquad (3\text{-}30b)$$

Subtracting Eq. 3-30b from Eq. 3-30b,

$$\frac{V_{7b,1} - V_{7a,1}}{2} = V_d + \frac{V_{3b,2} - V_{3a,2}}{2} \; .$$

or

$$V_{ss,1} = V_d + V_{ss,2} \; . \qquad (3\text{-}31)$$

I_d is defined as the current through the device such that

$$I_d = I_{ss,1} = -I_{ss,2} \qquad (3\text{-}32)$$

It follows that

$$I_d = Y_{as} (V^i_{as,1} - V^i_{as,2}) - \tfrac{1}{2} V_d \qquad (3\text{-}33)$$

Since $V_d = R\, I_d$ it follows that

$$I_d = Y_{as} \frac{V^i_{as,1} - V^i_{as,2}}{1 + 2R} \,. \qquad (3\text{-}34)$$

The reflected anti-symmetrical voltages are given by

$$V^r_{as,1} = V_{as,1} - V^i_{as,1} = V^i_{as,2} + \tfrac{1}{2} V_d$$

$$V^r_{as,2} = V_{as,2} - V^i_{as,2} = V^i_{as,1} - \tfrac{1}{2} V_d \qquad (3\text{-}35)$$

where Eq. 3-30 was used. The incident port voltages are then determined as

$$V^i_{7a,1} = \tfrac{1}{2} V^r_{s,1} - V^r_{as,1}$$

$$V^i_{7b,1} = \tfrac{1}{2} V^r_{s,1} + V^r_{as,1}$$

$$V^i_{3a,2} = \tfrac{1}{2} V^r_{s,2} - V^r_{as,2} \qquad (3\text{-}36)$$

$$V^i_{3b,2} = \tfrac{1}{2} V^r_{s,2} + V^r_{as,2} \,.$$

Energy is conserved in the above transformations as shown here by example. Suppose $V^r_{7b,1}=1$ such that $2Y_o$ Watts are incident on the device discontinuity. Hence $V^i_{as,1}=\frac{1}{2}$ and $V^i_{s,1}=1$. Using Eq. 3-34, $I=2/(1+2R)$ and $V_d=2R/(1+2R)$. Using Eq. 3-35 and Eq. 3-36,

$$V'_{7a,1} = -R / (1 + 2R)$$

$$V'_{7b,1} = R / (1 + 2R)$$

$$V'_{3a,2} = R / (1 + 2R)$$

$$V'_{3b,2} = (1 + R) / (1 + 2R)$$

adding up the impulse energies in these components in addition to the $V_d I$ power dissipated in the resistor we obtain $2Y_o$ Watts which is equal to the incident power.

For the development of the PWL algorithm interface in Chapter 4, it is more convenient to represent the interfaces to nodes 1 and 2 by a Thevenin equivalent circuit. Fig. 3-21a shows the incident and reflected voltages from a two-terminal device. Fig. 3-21b shows the equivalent circuit with voltage generators of $2V'_{as,1}$ and $2V'_{as,2}$. While this model is sufficient, the equivalent circuit shown in Fig. 3-21c is more tractable for two reasons. First the equivalent current sources can be used directly in Kirchhoff node circuit equation formulations describing the device without introducing additional variables. Secondly, the current flow from the generators in Fig. 3-21c is a physical quantity while the values of the voltage generators in Fig. 3-21b are not physical but are meaningful only in the context of the half-node.

Considering the example of the lumped resistor given above, the Kirchhoff nodal relations are

$$\begin{pmatrix} \frac{1}{R} + Y_1 & -\frac{1}{R} \\ -\frac{1}{R} & \frac{1}{R} + Y_1 \end{pmatrix} \begin{pmatrix} V_{as,1} \\ V_{as,2} \end{pmatrix} = Y_1 2 \begin{pmatrix} V^i_{as,1} \\ V^i_{as,2} \end{pmatrix} \qquad (3\text{-}37)$$

Note that the matrix is invertible for any G except G=∞ since V_1 and V_2 are then

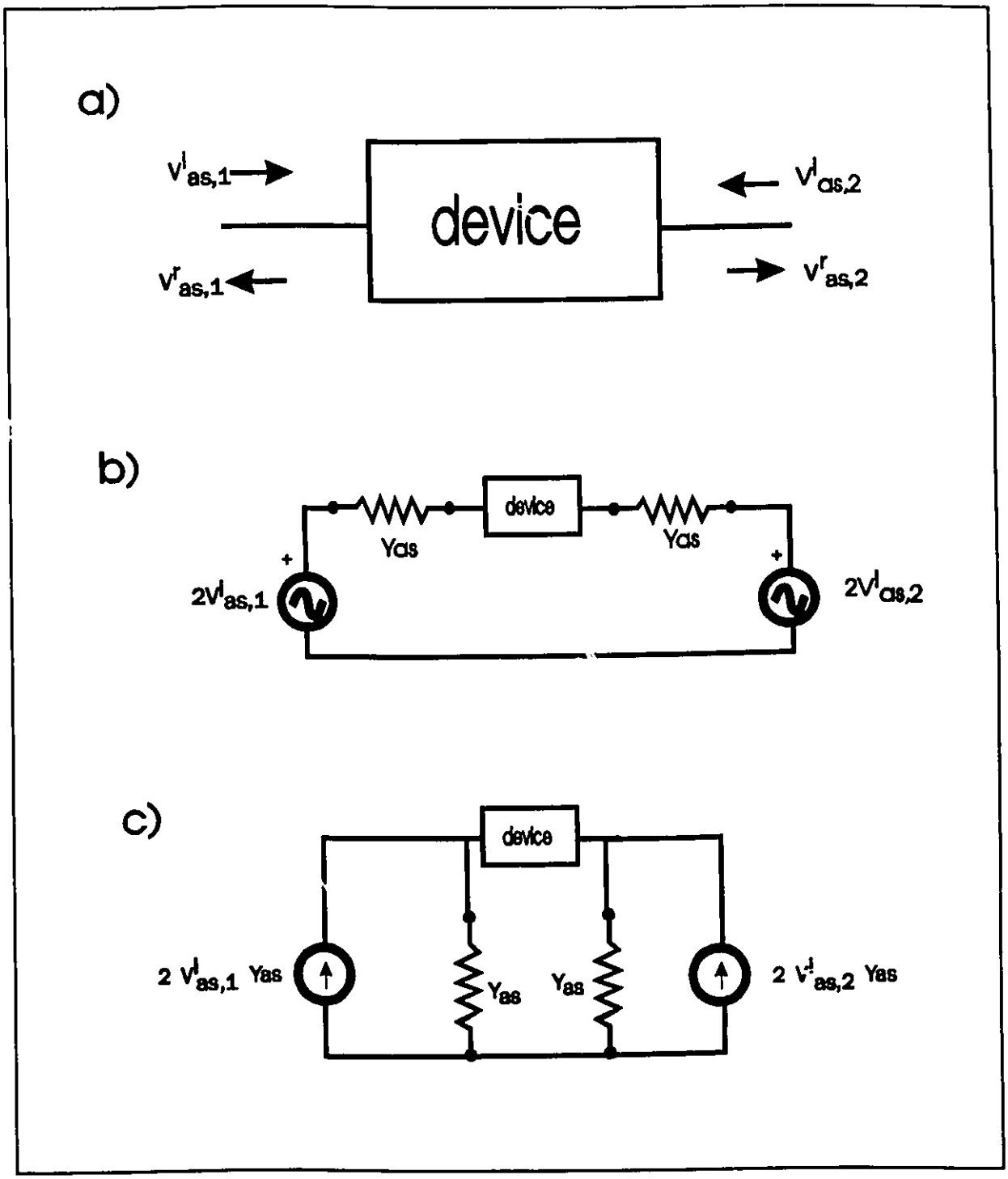

Fig. 3-21 Equivalent circuit formulations of the two-terminal device interface a) two-terminal device b) equivalent voltage source circuit c) equivalent current source circuit

no longer independent. Eq. 3-37 is used to determine V_{ss1} and V_{ss2} from which the voltages incident into the half-nodes can be determined as above.

3.6.2 Simulation Results for a 1D Array of Nodes

In this Section, a stripline with an embedded lumped element is simulated by the 1D node array configuration in Fig. 3-17. The TLM node configuration, shown in Fig. 3-22, is an array of ten half-nodes with a series lumped admittance, G_s, that is embedded between the 5th and 6th nodes. At the left end of the transmission line is a voltage generator with an admittance Y_g. The scattering parameters, referenced to the source admittance, were evaluated by generating an impulse voltage from the generator and taking the Fourier transform of the voltages across the generator and load admittance. The S_{11} parameter is plotted in Fig. 3-22b for the case when $Y_g=G_s=Y_{ss}$, and $\epsilon_r=1$. It was indistinguishable from the calculated results assuming standard transmission line theory. This ideal result is possible because of the direct interaction between the current on the strip and the current through the conductance and generator.

It is interesting to study the reduction of the usable bandwidth due to permittivity stubs introduced at the half-nodes when modelling dielectric material. Consider the 1D transmission line in Fig. 3-23a where the series admittance is now placed at the end of the transmission line. When $Y_g=G_s=Y_{ss}$, and $\epsilon_r=1$ we obtain the ideal result of $S_{11}=0$ and $S_{21}=\exp(-j4\pi f\Delta t)$. For $\epsilon_r>1$ the generator admittance and load admittance are changed to

$$Y_g = G_s = Y_{ss}\sqrt{\epsilon_r} \qquad (3\text{-}38)$$

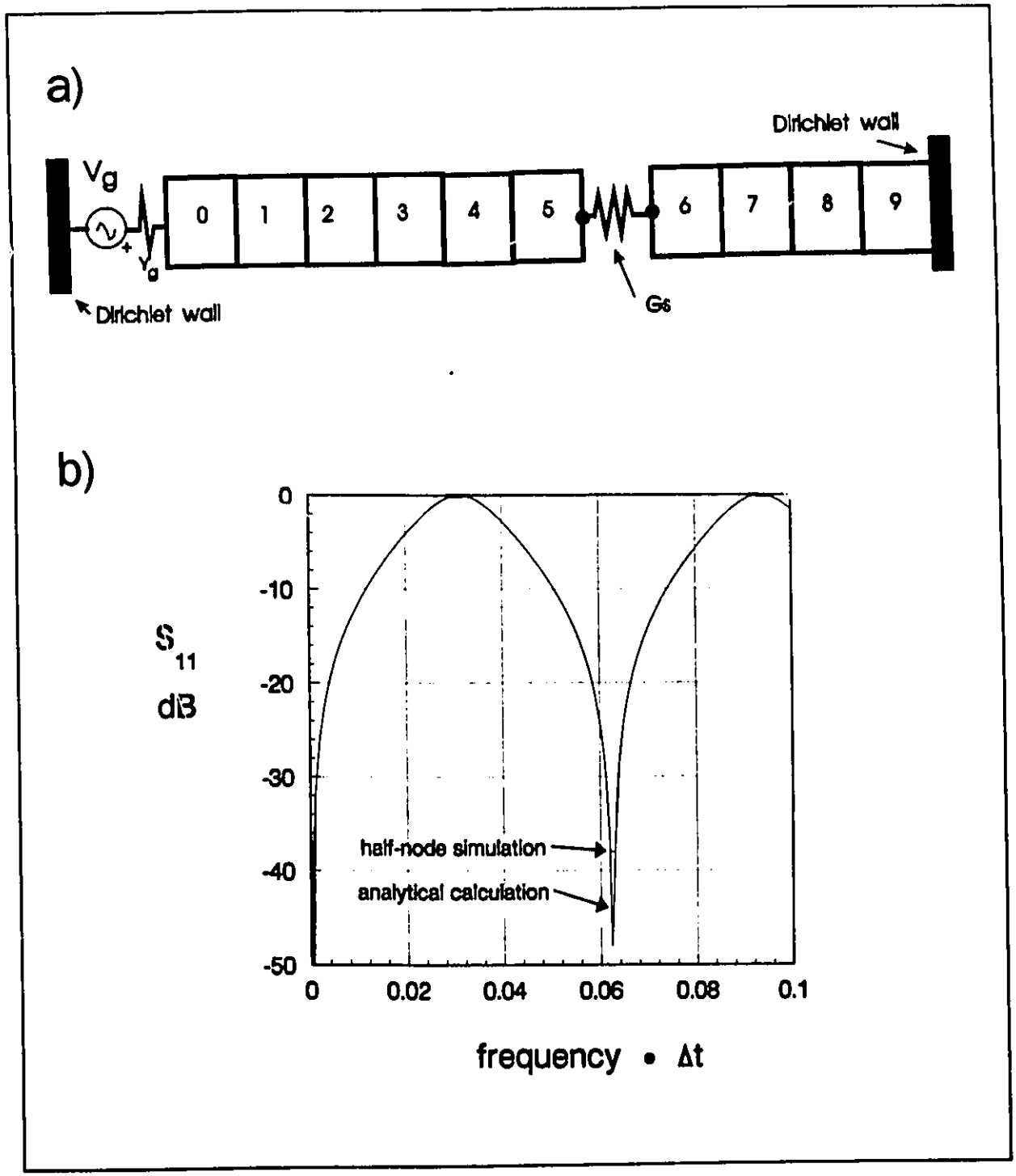

Fig. 3-22 Simulation of a stripline with a lumped series admittance using a 1D array of half-nodes. a) TLM node array configuration. b) comparison of theoretical and simulated estimation of the S_{11} parameter

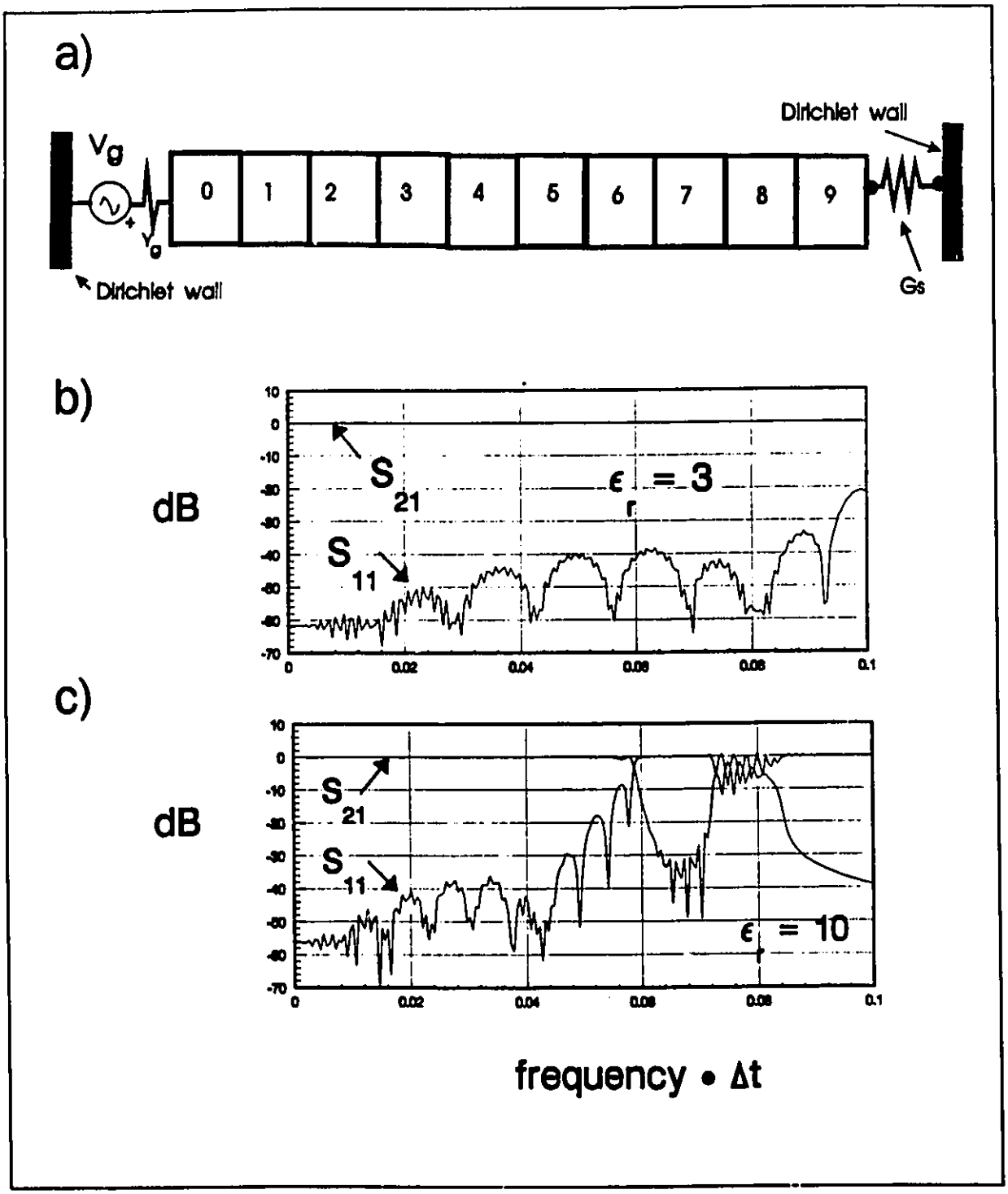

Fig. 3-23 Simulation of dielectrically loaded stripline by half-nodes. a) TLM node configuration b) Plot of S_{11} and S_{21} parameters for $\epsilon_r=3$ c) Similar plot for $\epsilon_r=10$

and the half-nodes were loaded with permittivity stubs of appropriate value.

The result is plotted in Fig. 3-23b for the case when ϵ_r=3, and in Fig. 3-23c for the case when ϵ_r=10. As observed, the usable bandwidth is reduced by the simulation of the dielectric with periodic stubs. As expected, the higher ϵ_r is, the lower the usable bandwidth.

3.6.3 Distributed Planar Devices

The methods presented in the previous section can be extended to distributed planar devices such as power FET's. As an example, consider extending the embedded two-terminal admittance above to a distributed resistor as illustrated in Fig. 3-24a. This diagram represents a top view of a stripline that is simulated by a mesh of half-nodes with a width of two nodes. The distributed resistor is modelled by a four-port admittance network as shown. Hence the resistor is distributed in the transverse direction and lumped in the longitudinal direction. The admittance network model is given in Fig. 3-24b and the overall equivalent circuit for solving the antisymmetric voltages is given in Fig. 3-24c. The Kirchhoff nodal equations are given by

$$\begin{pmatrix} G+G_s+Y_1 & -G & -G_s & 0 \\ G & G+G_s+Y_1 & 0 & -G_s \\ -G_s & 0 & G+G_s+Y_1 & -G \\ 0 & -G_s & -G & G+G_s+Y_1 \end{pmatrix} \begin{pmatrix} V_{as1} \\ V_{as2} \\ V_{as3} \\ V_{as4} \end{pmatrix} = Y_1 2 \begin{pmatrix} V^i_{as1} \\ V^i_{as2} \\ V^i_{as3} \\ V^i_{as4} \end{pmatrix} \qquad (3\text{-}39)$$

which again can be solved for the antisymmetric voltages to eventually determine the reflected antisymmetric voltages.

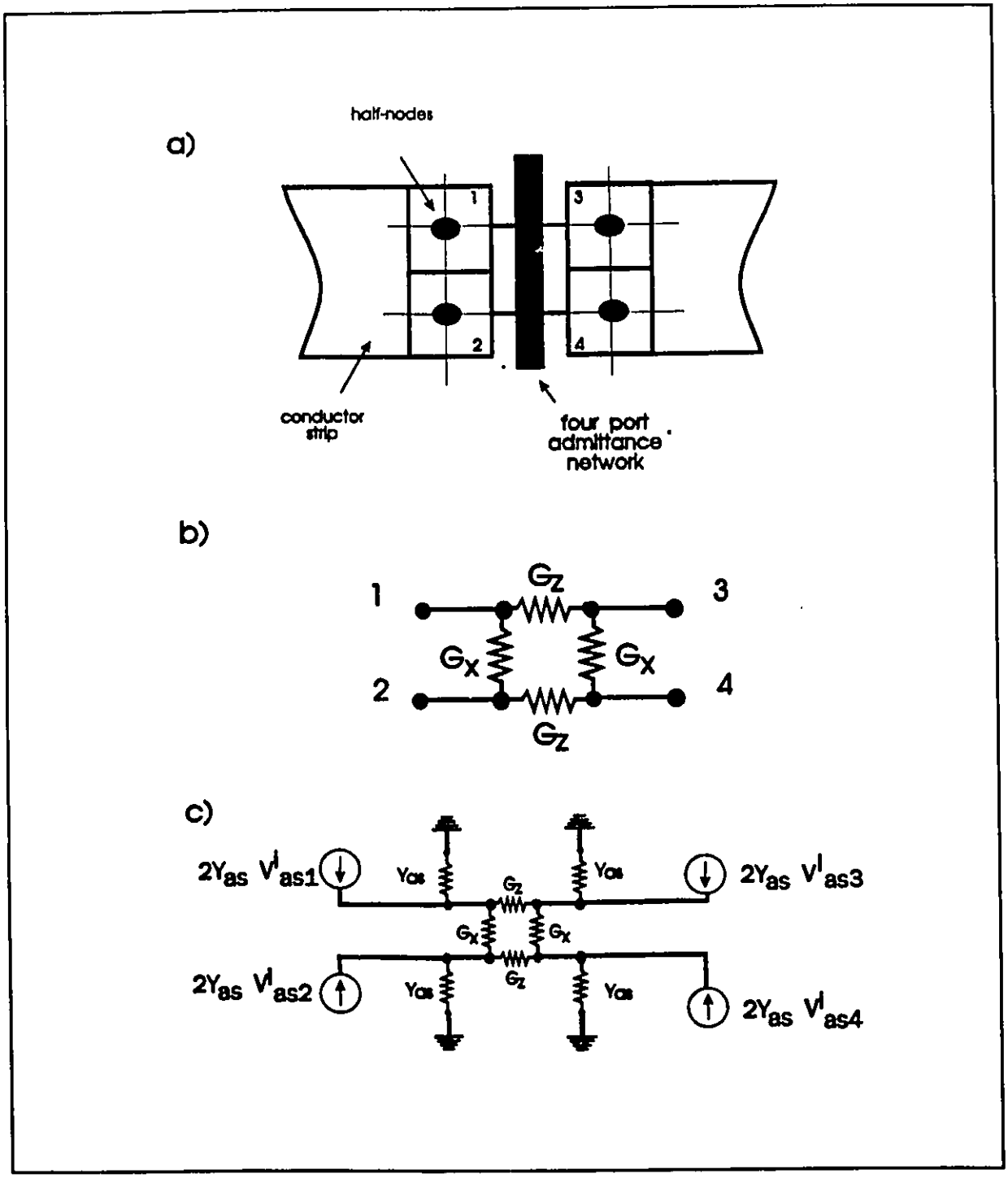

Fig. 3-34 Half-node model of a stripline with an embedded distributed resistor. a) TLM mesh configuration of device interface, b) admittance network model of resistor, c) overall equivalent network of device

Note that the current source admittances are all attached to a common ground. This is possible since the half-node has no electric field component tangential to the conductor plane at the half ports. Hence 1D distributed elements can be easily modelled.

The distributed resistor in Fig. 3-24 can be extended to an arbitrary width. The conductance elements can be replaced by nonlinear models representing FET channels. In this way it is possible to model distributed power FETs. This will be demonstrated in Section 5.4.3.

Distributed devices can be embedded into the TLM mesh if a common ground can be established such that the shunt conductances associated with the Thevenin current sources can be correctly terminated. For one-dimensional device models there is no problem since the half-nodes do not support E fields tangential to the conductor plane. Consequently a common ground is easily established.

For the 2D device, it is necessary to assume that the device is only one node in height. If such a model is not valid then it is necessary to go to a more elaborate model. The device would occupy a number of node cells. Every port into this group of nodes must mate with a port of the device displacement and electric current model. While this is possible the model becomes very complicated and not very practical.

A better way is to model the distributed device as an array of lumped elemental devices that are interconnected by half-nodes. As an example, consider the problem of modelling a 2D distributed resistor sheet that would, for example, be encountered in a large photo-conductive surface. Fig. 3-25a shows a sketch of the 2D resistor sheet configured as a stripline circuit. It is 30 nodes square in dimension. The resistor sheet was modelled by placing lumped resistors between all the interconnecting ports of the half nodes as illustrated by the top

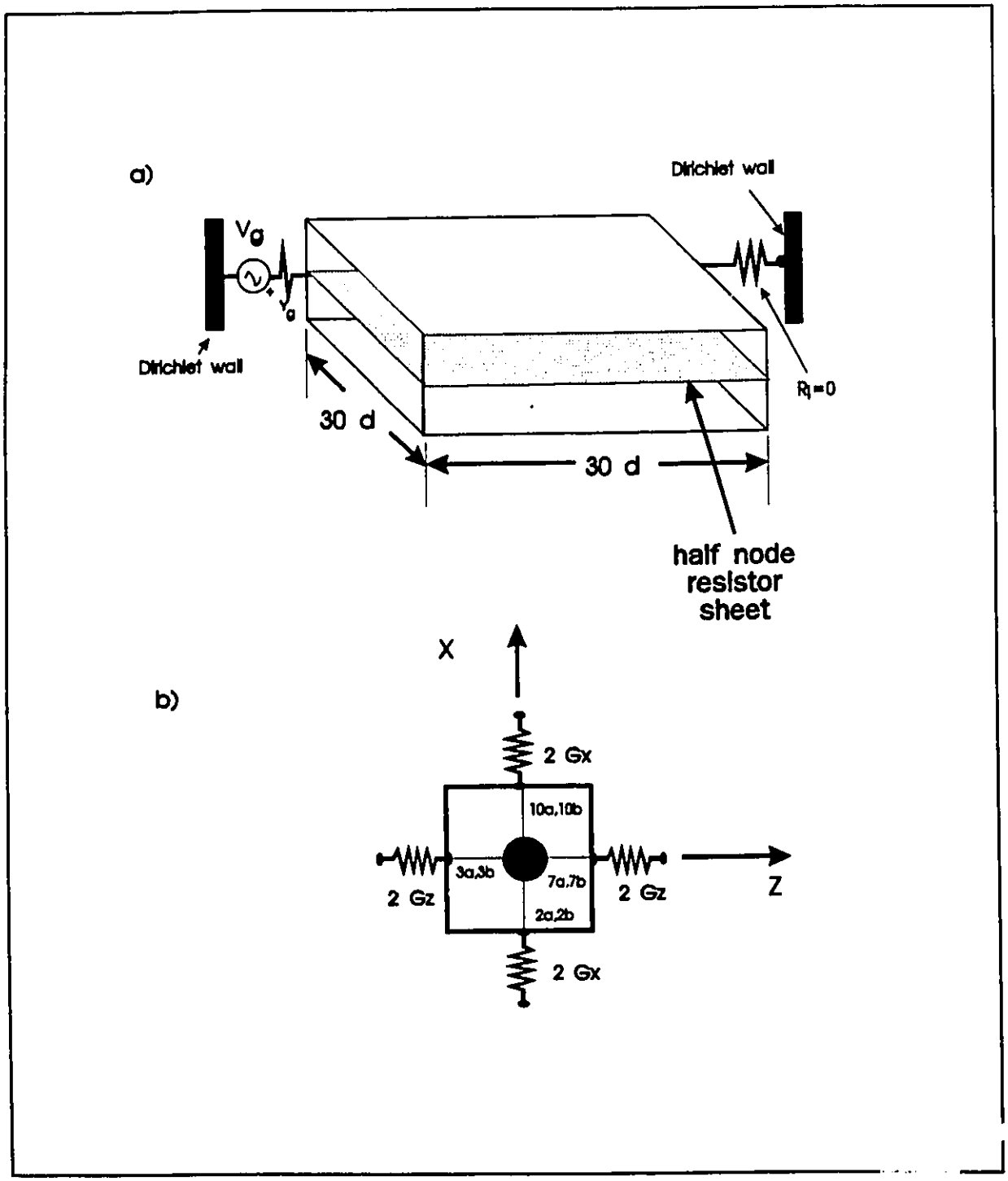

Fig. 3-25 Half-node model of a distributed 2D resistor sheet. a) Sketch of the resistor sheet configuration, b) Top view of an elemental half-node with lumped resistor attached to interconnecting ports

view of the elemental half-node configuration in Fig. 3-25b. One port of the overall current sheet was connected to a voltage source, V_0. The resulting current through the half nodes is shown in Fig. 3-26. The solution obeys Laplace's equation to a good approximation as expected for a current sheet [46].

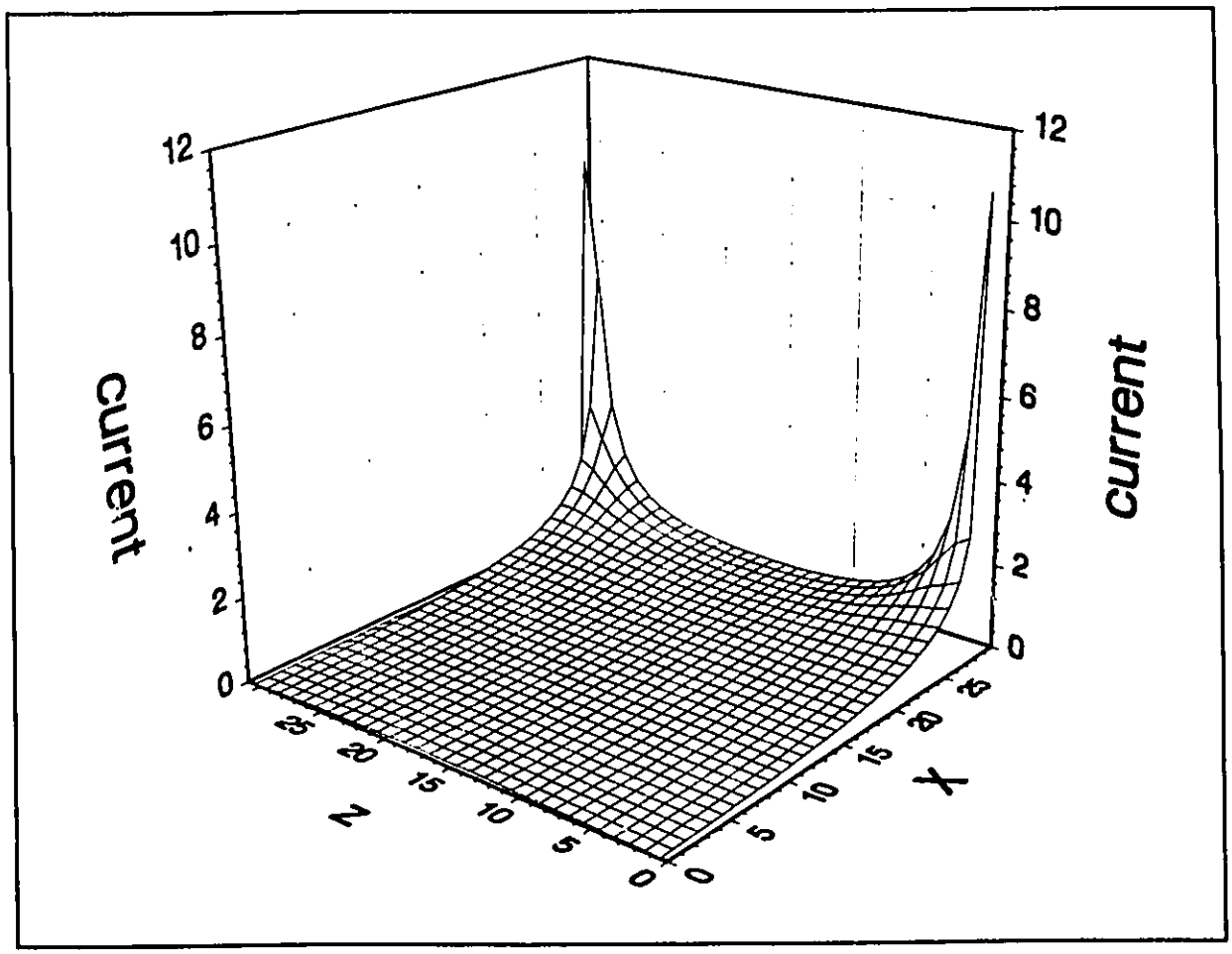

Fig. 3-26 Resulting current distribution in resistor sheet modelled by half-nodes.

3.7 CONCLUSION

In this chapter, a new family of node structures was introduced that accurately model conductor strips and allow embedded devices to be directly connected to the current flowing in the conductor strips. This was necessary since the conventional method of modelling strips by using truncated Dirichlet boundaries proved to be inaccurate.

The procedure for embedding devices into the TLM mesh and connecting them to the conductor strips was developed. Only devices without reactance were considered in this chapter. Chapter 4 will present a methodology for modelling nonlinear devices with reactance.

An auxiliary attribute of the half-node that has not been mentioned previously is that Dirichlet boundaries can now be positioned either between nodes or through the middle of the nodes which doubles the resolution of the geometric boundary description for a given mesh density.

CHAPTER 4

EMBEDDED NONLINEAR DEVICES IN THE TLM MESH

4.1 INTRODUCTION

In this chapter a methodology for simulating nonlinear devices with energy storage, that are embedded into conductor strips simulated by conductor strip nodes, will be developed. The method is based on a Piece-Wise Linear (PWL) integration algorithm that solves the differential equations associated with the device. The PWL algorithm will be interfaced with the half-nodes based on the methods developed in Section 3.6.

As was discussed in Chapter 1, previous researchers have modelled nonlinear devices using stubs attached to the TLM nodes. Nonlinear devices with time-varying behaviour can be modelled by making the admittances of the stubs dependent on time as well as on the voltages and currents in the node. Another option is to shunt the end of the stub with the device. The reflection coefficient of the device is calculated based on the time-dependent nonlinear differential equations describing the device.

The problem with these approaches is that the parameters of the device are updated at a regular clock rate that is fixed to the TLM mesh update time interval of Δt. Hence the device parameters must vary slowly with respect to Δt or else the simulation will become inaccurate. In more severe cases, the

simulation will likely become unstable.

A more accurate and computationally efficient algorithm is to integrate the differential equations describing the nonlinear device model using a variable time step that adjusts automatically to the local "stiffness" of the differential equations modelling the device. This is possible if the PWL algorithm, simulating the device, is uncoupled from the TLM mesh simulation. The combination of the TLM and PWL algorithms requires a special interface that will be developed in this chapter. This interface is developed specifically for compatibility with the conductor strip nodes described in Chapter 3. However, many of the concepts can be applied to conventional 2D and 3D TLM node meshes as well as to FD-TD schemes.

Fig.3-19 illustrates the interface between the half-node and the device as represented by two models, namely the electric current model and the displacement current model. These models can be arbitrarily complex and inter-related as required. However, complex models are only as good as the accuracy of the parameters inherent in the model. Obtaining accurate parameters from measurements or from a theoretical analysis of the device is still a nagging problem that limits the usefulness of detailed complex models.

In this thesis, the emphasis will be on simulating devices that are assumed to be adequately described by a nonlinear electric current model that does not interact with the displacement current model. Hence the physical dimensions of the device will be assumed to be much smaller than the TLM node. If the physical device is larger than the mesh parameter "d", then it can be subdivided into smaller sub-devices that are much smaller than "d" and interconnected by a mesh of half-nodes. The electric delay between these sub-devices is thus modelled by the half-nodes. The packaging material surrounding the device can be modelled

by dielectric stubs appropriately attached to surrounding nodes. There may be cases where a special displacement current model is required to simulate the packaging material, however, this is not considered here. Consequently, the emphasis will be primarily on interfacing the nonlinear electric current device model with the TLM mesh.

Consider the stripline model with an embedded series device that is shown in Fig. 3-17. The stripline is modelled by a one-dimensional array of half-nodes with an infinitesimal gap in the simulated conductor strip for the two-terminal device. Fig. 4-1 is a block diagram of the interface between the electric current device model and the two half-nodes attached to the device. The incident antisymmetric discretized signals are derived from the reflected voltages of nodes 1 and 2 using the T_{dh} transformation described in Section 3.6. The incident anti-symmetric voltages are interpolated resulting in continuous time signals $V^i_{ss1}(t)$ and $V^i_{ss2}(t)$. Then according to the procedure outlined in Section 3.6.1, equivalent Thevenin source currents, $J_1(t)$ and $J_2(t)$ are derived which are given by

$$J_1(t) = 2\, Y_{ss}\, V^i_{ss,1}(t) \qquad (4\text{-}1a)$$

$$J_2(t) = 2\, Y_{ss}\, V^i_{ss,2}(t) \qquad (4\text{-}1b)$$

These equivalent currents are the forcing functions for the PWL algorithm which simulates the device equivalent circuit. Included in the device model are the equivalent current source shunt admittances described in Section 3.6.1. The PWL operates at a variable time interval step, Δt_s, which is generally much smaller than the TLM mesh time step interval of Δt. The output of the PWL algorithm is $V_d(t)$, an estimate of the physical voltage across the two-terminal device.

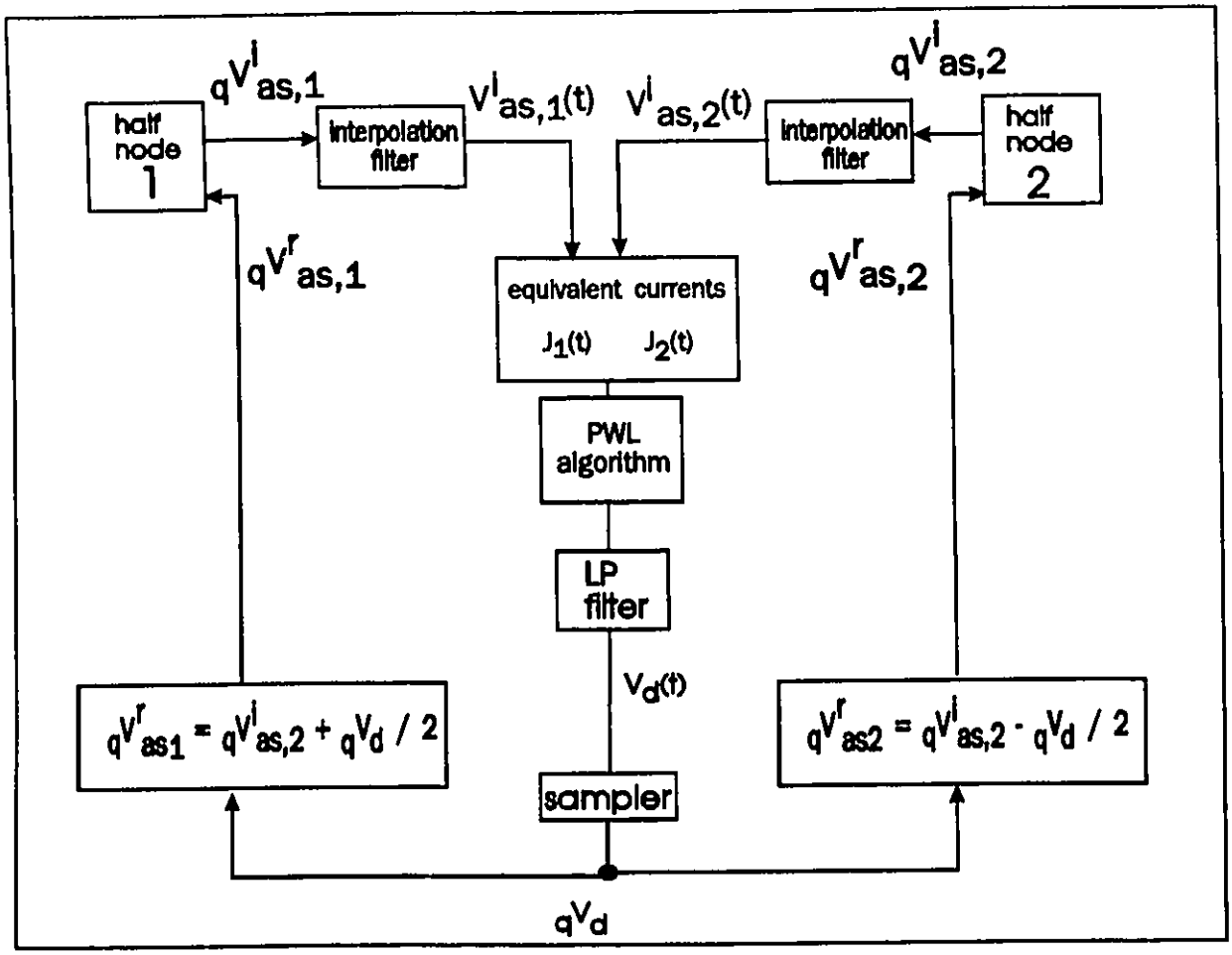

Fig. 4-1 Block diagram of the interface between the half-node ports and the Piece-Wise Linear (PWL) differential equation integration algorithm.

$V_d(t)$ is low-pass filtered to remove high frequency components that would otherwise cause aliasing errors in the TLM mesh. The filtered version of $V_d(t)$ is sampled at a time interval, Δt, the update time of the TLM mesh. This results in ${}_qV_d$, as denoted in Fig. 4-1. The reflected antisymmetric voltages, ${}_qV^r_{as,1}$ and ${}_qV^r_{as2}$ are then determined from ${}_qV_d$ using Eq.3-35. The voltages incident into the half-nodes are determined from the T_{hd} transformation given in Eq. 3-29.

For accurate simulation, the interpolation and filtering functions must not cause any extraneous time delay. Hence, a non-causal interpolation is necessary

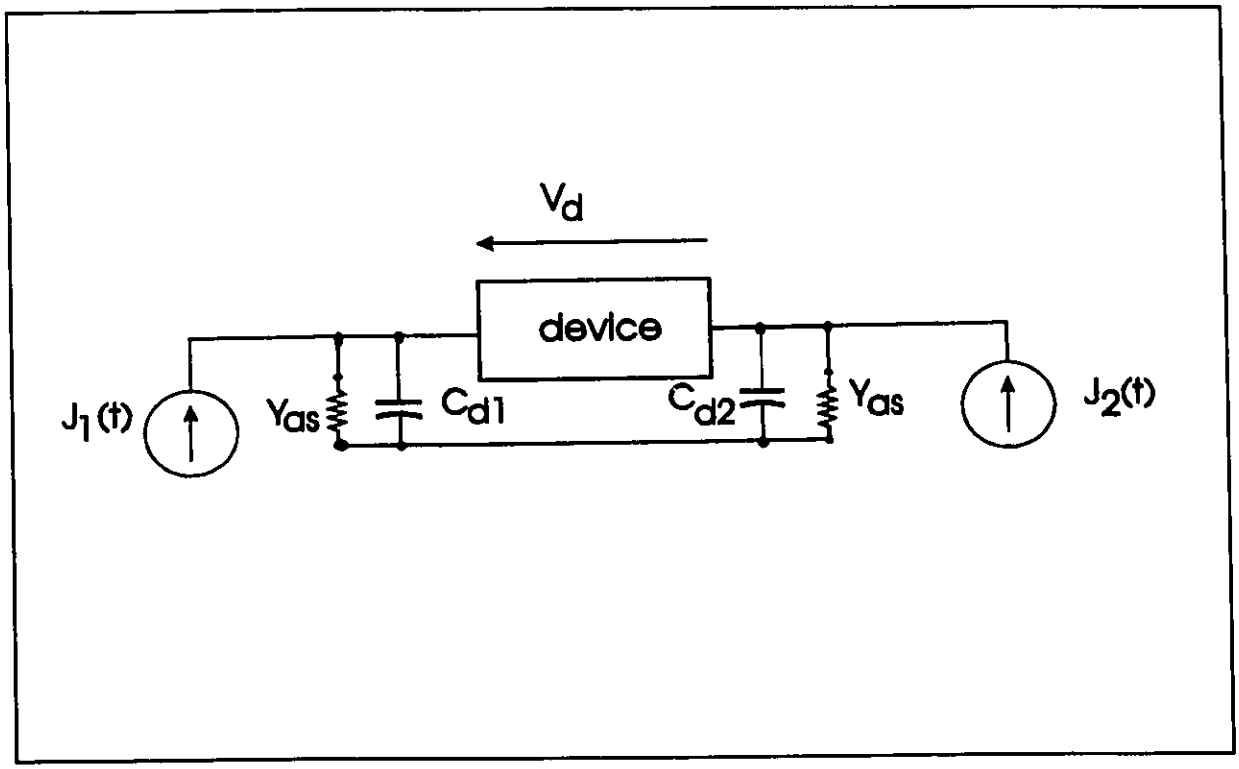

Fig. 4-2 Thevenin equivalent circuit of a two-port device interface showing the shunt capacitances C_{d1} and C_{d2} that correspond to the equivalent capacitance of the dielectric material in the half-nodes.

which requires the future incident voltages, ${}_{q+1}V^{i}_{ss,1}$ and ${}_{q+1}V^{r}_{ss,2}$. If the half-node does not have any stubs, then ${}_{q+1}V^{i}_{ss,1}$ will not depend on ${}_{q}V^{r}_{ss,1}$ which can be verified from the scattering matrix of the half-node. Hence, an explicit algorithm with zero time delay is possible. If the node contains stubs then ${}_{q+1}V^{i}_{ss,1}$ will depend on ${}_{q}V^{r}_{ss,1}$. Consequently, a zero time delay is only possible at the expense of resorting to an implicit algorithm where the PWL must solve each time interval in an iterative fashion until the solution converges. An implicit algorithm would be inefficient in terms of computational intensity. Also the PWL and TLM algorithm become strongly coupled which is contrary to the overall program philosophy. Hence, the capacitive stubs are removed from the half-nodes and replaced by capacitances shunting the Thevenin equivalent

admittances as illustrated in Fig. 4-2. From Section 3.3 it can be verified that

$$C_{d1} = C_{d2} = 2\,d\,\epsilon_o\,(\epsilon_{r1} + \epsilon_{r2} - 2). \qquad (4\text{-}2)$$

An additional advantage of these added capacitances is that they aid in suppressing the high frequency components generated by the PWL algorithm.

The outline of this chapter is as follows. Section 4.2 discusses the interpolation block of Fig. 4-1. Section 4.3 describes the low-pass filtering and sampling blocks. In Section 4.4, a discussion of the numerical solution of the device differential equations, by the PWL block, is given. This is followed by an example of a simple transmission line detector circuit. Practical examples will be presented in Chapter 5.

4.2 INTERPOLATION RECONSTRUCTION FILTER

As discussed in Section 4.1, in conjunction with Fig. 4-1, an interpolator is used to convert the time sampled sequence of ${}_qV'_{es1}$ and ${}_qV'_{es2}$ to a continuous time-varying function $v'_1(t)$ and $v'_2(t)$, respectively. Ideally, the interpolating function should be an infinite non-causal sin(x)/x or "sinc" function as discussed in appendix A. Since this is not practical, a truncated sinc function can be considered that is sufficiently delayed to be causal. However, the delay must be minimized as it affects the fidelity of the simulation and can, in some cases, result in numerical instability. If short truncated sinc interpolating functions are used, then some distortion is generated at zero frequency which can result in problems in simulating steady bias sources.

As a compromise, a triangular kernel, denoted by $h_{int}(t)$, is used for the

interpolating filter. This is given by

$$h_{int}(t) = 1 - |t| / \Delta t \qquad |t| < \Delta t \qquad (4\text{-}3)$$
$$= 0 \qquad \text{otherwise.}$$

The triangular form of this interpolation kernel causes $V^i_1(t)$ to be a linear extrapolation between the samples of ${}_qV^i_{as1}$ as

$$V^i_1(t) = {}_qV^i_{as,1} + \left(\frac{t}{\Delta t} - q\right)\left({}_{q+1}V^i_{as,1} - {}_qV^i_{as,1}\right) \qquad (4\text{-}4a)$$

for

$$q\,\Delta t < t < (q+1)\,\Delta t\ .$$

Likewise

$$V^i_2(t) = {}_qV^i_{as,2} + \left(\frac{t}{\Delta t} - q\right)\left({}_{q+1}V^i_{as,2} - {}_qV^i_{as,2}\right)\ . \qquad (4\text{-}4b)$$

The triangular interpolation kernel of Eq. 4-4 relies on the future samples ${}_{q+1}V^i_{as,1}$ and ${}_{q+1}V^i_{as,2}$. The reason for this is to achieve an interpolating filter with no time delay. Because of the scattering properties of the conduction strip nodes, ${}_{q+1}V^i_{as,1}$ and ${}_{q+1}V^i_{as,2}$ are known at $t=q\Delta t$, provided the conduction strip node does not contain any stubs. Consider, for the moment, the half-node called "node 1" in Fig. 4-1, as having node indices i,j,k. Then the incident antisymmetric voltage at $t=(q+1)\Delta t$ is given by

$${}_{q+1}V^i_{as,1} = \tfrac{1}{2}\left({}_{q+1}V^r_{7a,1} + {}_{q+1}V^r_{7b,1}\right)\ . \qquad (4\text{-}5)$$

Now

$$ {}_{q+1}V^{r}_{7a} = \tfrac{1}{2}\left({}_{q}V^{i}_{2a} + {}_{q}V^{i}_{6} + {}_{q}V^{i}_{10a}\right) $$

$$ {}_{q+1}V^{r}_{7b} = \tfrac{1}{2}\left({}_{q}V^{i}_{2b} + {}_{q}V^{i}_{4} + {}_{q}V^{i}_{10b}\right) . \qquad (4\text{-}6) $$

Assuming node 1 to have indices i,j,k, Eq. 4-6 can be written in terms of reflected signals from surrounding nodes as

$$ {}_{q+1}V^{r}_{7a} = \tfrac{1}{2}\left({}_{q}V^{r}_{i-1,10a} + {}_{q}V^{r}_{j+1,4} + {}_{q}V^{r}_{i+1,2a}\right) \qquad (4\text{-}7a) $$

$$ {}_{q+1}V^{r}_{7b} = \tfrac{1}{2}\left({}_{q}V^{r}_{i-1,10b} + {}_{q}V^{r}_{j-1,6} + {}_{q}V^{r}_{i+1,2b}\right) . \qquad (4\text{-}7b) $$

In Eq. 4-7, the notation is used that shows only the indices that are different from i,j,k.

The interpolating filter should be bandwidth-limited to $1/(2\Delta t)$ to avoid aliasing errors, as explained in Appendix A. However, as the interpolating filter has a kernel of finite duration it cannot be bandwidth-limited and therefore some distortion due to aliasing will result. In order to quantify this distortion, assume a sinusoidal signal of frequency f_b. This is sampled at a rate $1/\Delta t$ through the TLM process. Hence, the signal into the interpolating filter will consist of equal amplitude harmonics at frequencies $f_b \pm n/\Delta t$, $n=0,1,2....$ The Fourier transform of $h_{int}(t)$, denoted by $H_{int}(f)$, is given by

$$ H_{int}(f) = \frac{\sin^2(\pi f \Delta t)}{(\pi f \Delta t)^2} . \qquad (4\text{-}8) $$

Consider a sampled harmonic signal of frequency, f_b, that is interpolated by the

filter. At the output of the interpolation filter, the ratio of the signal power contained in harmonics of f_b to the fundamental harmonic signal power at f_b is defined as the distortion which is called $D(f_b)$. $D(f_b)$ is given by

$$D(f_b) = 10 \log\left(\frac{\sum_{n=1}^{\infty} H_{int}\left(f_b + \frac{n}{\Delta t}\right)^2}{H_{int}(f_b)^2} \right) \qquad (4\text{-}9)$$

A plot of $D(f_b)$ as a function of f_b is given in Fig. 4-3 for the triangular interpolation filter. Note that the distortion is negligible for frequencies much less than $1/\Delta t$. At higher frequencies the distortion is not negligible, however, distortions due to mesh dispersion will generally dominate as discussed in Chapter 2.

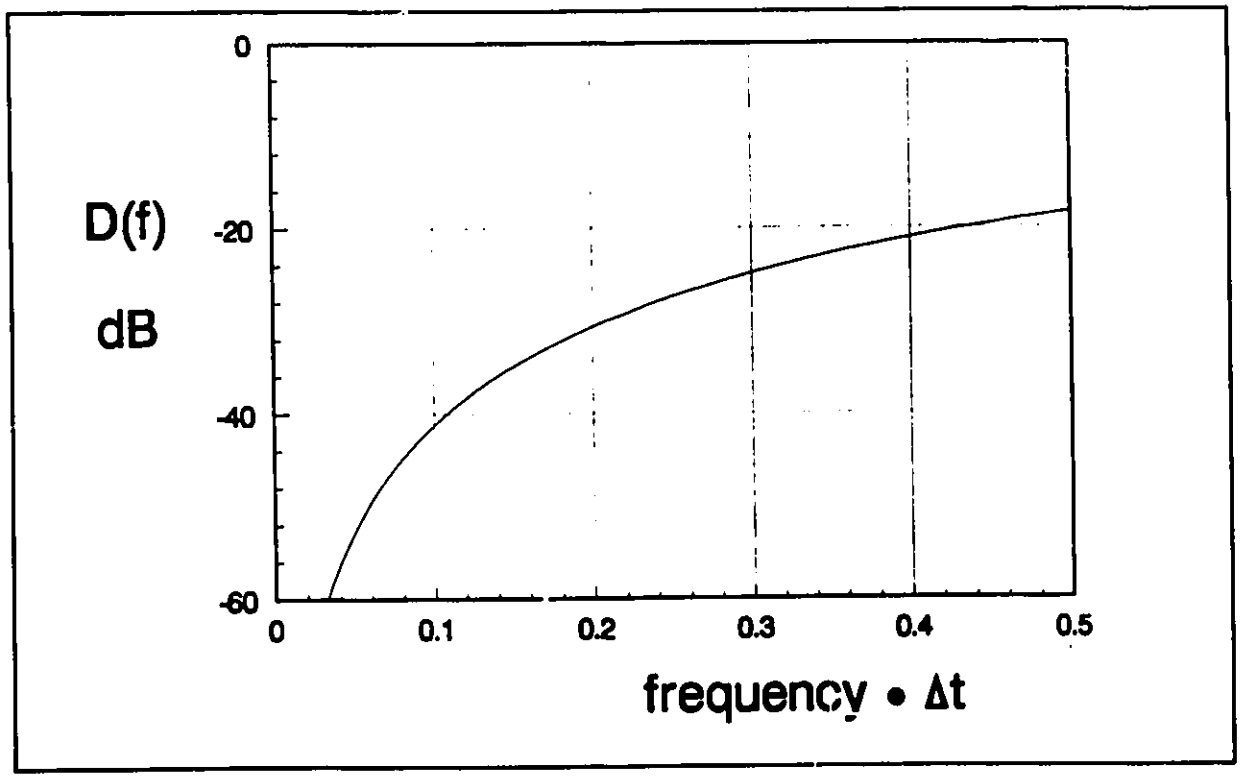

Fig. 4-3 Plot of the distortion of a triangular interpolation filter as a function of frequency

Note that the distortion vanishes for as f_b approaches zero. This is to be expected since the triangular interpolation is exact at DC. This is not necessarily the case for other interpolations such as the truncated sinc function.

4.3 LOW-PASS FILTER AND SAMPLING BLOCK

In this section, the low-pass filter and sampling blocks of the device interface, illustrated in Fig. 4-1, will be discussed. $V_d(t)$, the estimated voltage across the device, emanates from the PWL block in a form of a vector of samples taken at irregular time intervals. As mentioned earlier, irregular time intervals are necessary for computational efficiency of the PWL as it adapts to the local stiffness of the differential equation. Hence, the digital low-pass filter must adapt automatically to the dynamically varying time step. A transversal Finite Impulse Response (FIR) filter is used because of the low computational overhead required to make the filter adapt to the varying time interval. Using an Infinite Impulse Response (IIR) filter would require more overall computation effort.

Assume that the instant t lies in the q^{th} time interval such that

$$q\Delta t < t < (q+1)\Delta t \ .$$

Consequently $V_d(t)$ is estimated by the PWL algorithm up to $t=(q+1)\Delta t$. Hence a non-causal filter can be used which reduces the overall delay of the filter as discussed earlier. The FIR filter kernel will span over the time interval of

$$(q + 1 - N_{mesh})\,\Delta t < t < (q + 1)\,\Delta t$$

where N_{mesh} is an integer and denotes the number of TLM mesh time intervals the kernel spans. A functional block diagram of the FIR low pass filter is given in Fig. 4-4. During the time interval between $t=q\Delta t$ and $t=(q+1)\Delta t$, the vector of samples of V_d is stored in an array $V_{d,Nmesh}$. The data from the previous interval $t=(q-1)\Delta t$ and $t=q\Delta t$ is stored in an array $V_{d,Nmesh-1}$ and so forth to the oldest segment used in the filter which spans the time of $(q+1-N_{mesh})\Delta t$ to $(q+2-N_{mesh})\Delta t$.

At $t=(q+1)\Delta t$, the sampling is complete for evaluating ${}_qv^r_{ss1}$ and ${}_qv^r_{ss2}$. The samples in all the vector arrays are multiplied by the FIR filter kernel coefficients and summed, resulting in ${}_qV_d$, the filtered sample of $V_d(t)$ that is reflected back into the TLM mesh. In the next interval, the $V_{d,n}$ vectors are shifted to the left by one position, and the new data from the PWL algorithm is stored in $V_{d,Nmesh}$.

The object of the filter is primarily to suppress frequency components above $0.5/\Delta t$ to avoid aliasing errors. However, due to mesh dispersion it is generally necessary to have the filter cut off at a lower frequency. Dispersion results in errors in the input impedance seen by the device as discussed in Chapter 2. This can lead to errors in the device behaviour or, in the worst case, to numerical instabilities.

Various low-pass filter kernels have been considered. These are sketched in Fig. 4-5 as the rectangular, triangular and convolved triangular. Note that they are all non-causal as they start at $t=-\Delta t$. Salient attributes of these

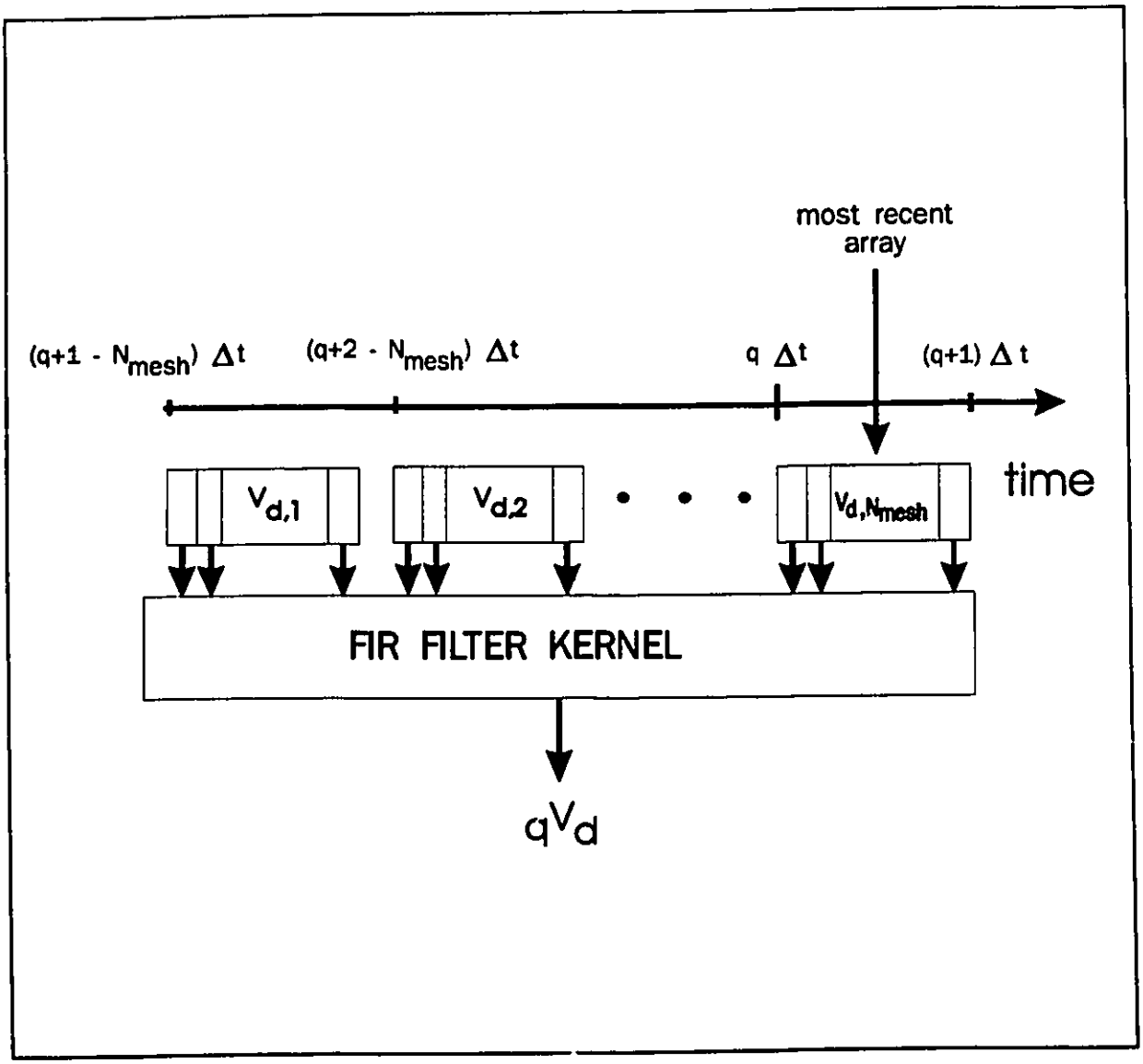

Fig. 4-4 A block diagram of the low-pass FIR filter showing the various data array segments and their relation to the time scale

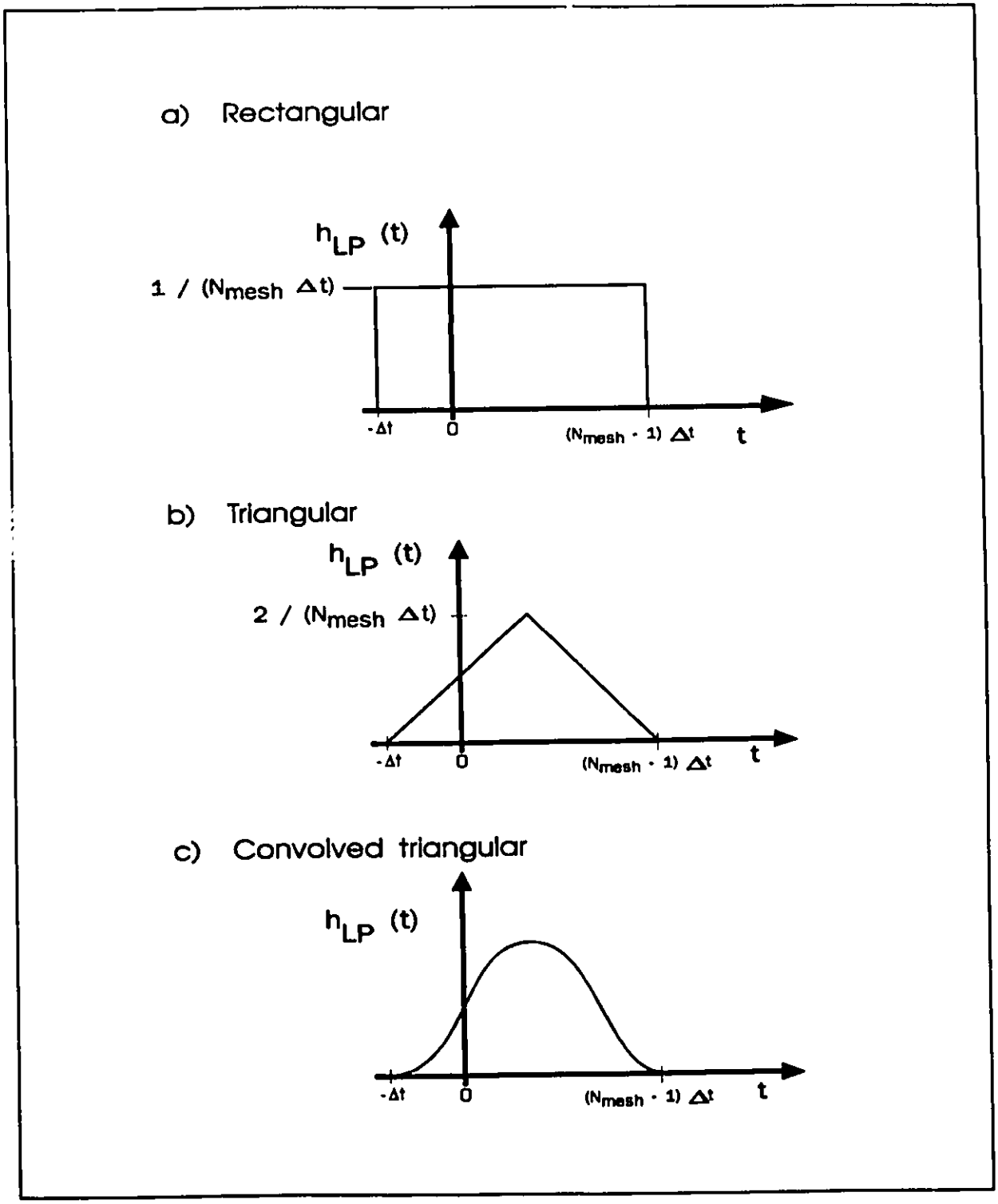

Fig. 4-5 Plot of the various low-pass filter kernels considered, a) rectangular, b) triangular and c) convolved triangular.

filter kernels are discussed in the following sections.

4.3.1 Rectangular Moving Average Low-Pass Filter

The simplest form of filter is merely a moving average or a rectangular filter with an impulse response

$$h_{LP}(t) = \frac{1}{N_{mesh}} \quad . \tag{4-10}$$

It is sketched in Fig. 4-5a. The filter frequency response is the standard sinc function given by

$$H_{LP}(f) = \frac{\sin(\pi\ f\ N_{mesh}\ \Delta t)}{\pi\ f\ N_{mesh}\ \Delta t} \exp\left(-j\ 2\ \pi\ f\ (\frac{N_{mesh}}{2} - 1)\ \Delta t\right) . \tag{4-11}$$

A drawback of this filter is the high sidelobe centered at the frequency $1.5/(N_{mesh}\ \Delta t)$ of -13.6 dB.

A quantitative measure of the amount of distortion caused by the filter sidelobes is possible by considering that the device simulated by the PWL routine is a perfect reflector such as an open circuit, and by assuming that Δt approaches zero. The interpolation filter generates some distortion as discussed with reference to Eq. 4-9. This distortion consists of higher-order frequency components that pass through the sidelobes of the low-pass filter. A quantitative measure of the overall distortion is given by

$$D(f_b) = 10 \log \left(\frac{\sum_{n=1}^{\infty} H_{int}^2(f_b + \frac{n}{\Delta t})\ H_{LP}^2(f_b + \frac{n}{\Delta t})}{H_{int}^2(f_b)\ H_{LP}^2(f_b)} \right) \qquad (4\text{-}12)$$

which is a modification of Eq. 4-9. A plot of $D(f_b)$ is shown in Fig. 4-6. Note that the distortion becomes significant at higher frequencies. However, as stated earlier, the distortion due to the interface will generally be minor in comparison with the distortion due to dispersion and spurious mode contributions.

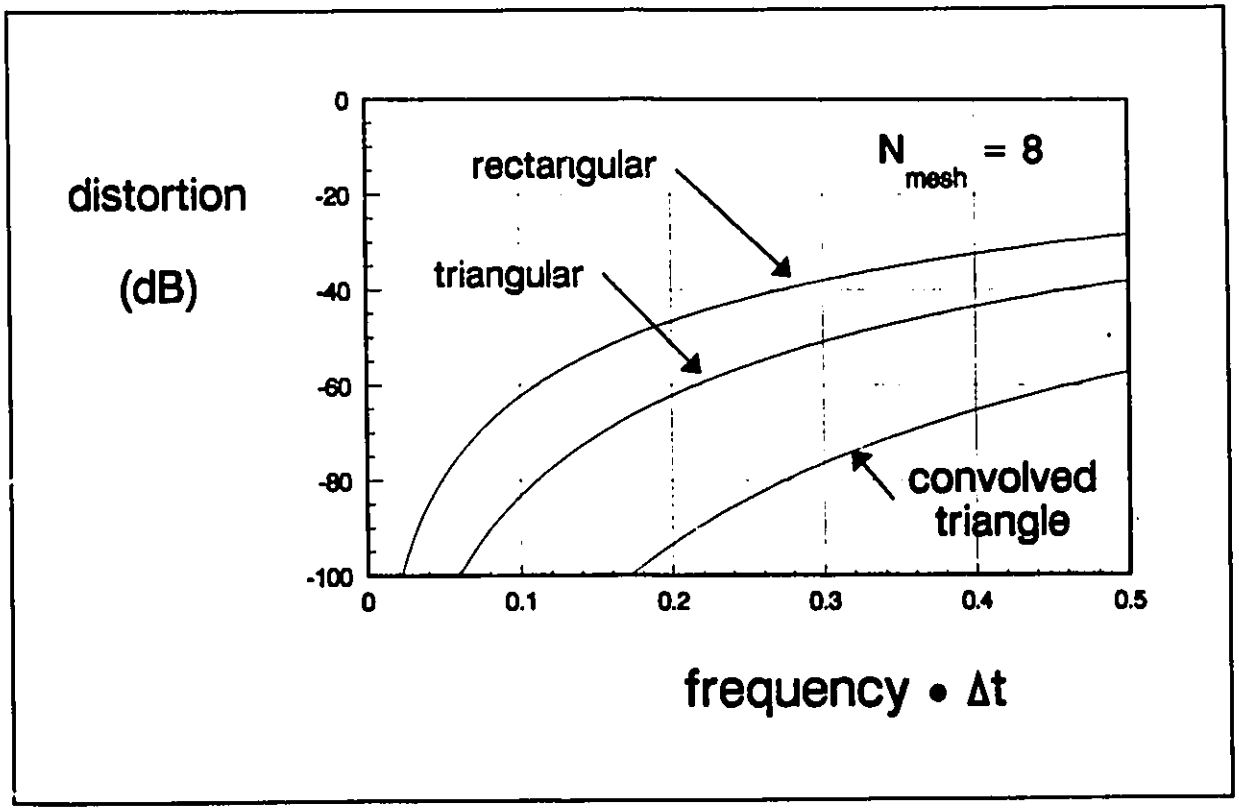

Fig. 4-6 Overall sampling distortion resulting from the linear interpolation filter and the low-pass filter for various low-pass filter kernels

4.3.2 Triangular Low Pass Filter

The triangular filter impulse response is sketched in Fig. 4-5b and is given by

$$h_{LP}(t) = \frac{2}{N_{mesh}} \left(1 - \frac{\left| \left(\frac{N_{mesh}}{2} - 1 \right) - \frac{t}{\Delta t} \right|}{\frac{N_{mesh}}{2}} \right) \qquad (4\text{-}13)$$

It has a frequency response of

$$H_{LP}(f) = \frac{\sin^2 \left(\frac{\pi f N_{mesh} \Delta t}{2} \right)}{\left(\frac{\pi f N_{mesh} \Delta t}{2} \right)^2} \exp\left(-j2\pi f \left(\frac{N_{mesh}}{2} - 1 \right) \Delta t \right) \qquad (4\text{-}14)$$

The triangular filter has a first sidelobe amplitude of -27 dB which is an improvement over the rectangular filter. The penalty paid for the lower side lobes is that to achieve the same low frequency cutoff point as the rectangular filter, N_{mesh} must be increased by a factor of 2. The distortion figure of merit D(f) of the triangular filter is better than that of the rectangular filter as demonstrated in Fig. 4-6. This is to be expected since the sidelobes of the triangular filter are lower.

4.3.3 Convolved Triangular Low-Pass Filter

A filter that offers a first sidelobe of -54 dB is achievable if $h_{LP}(t)$ is formed by convolving two triangular functions. This filter kernel is called the

"convolved triangular" and is sketched in Fig. 4-5c. The filter has a frequency response

$$H_{LP}(f) = \frac{\sin^4\left(\frac{\pi f N_{mesh} \Delta t}{4}\right)}{\left(\frac{\pi f N_{mesh} \Delta t}{4}\right)^4} \exp\left(-j2\pi f \left(\frac{N_{mesh}}{2} - 1\right) \Delta t\right) \qquad (4\text{-}15)$$

It has nulls at the frequencies

$$f = 4\ m\ /\ N_{mesh} \qquad m = 1,2,\ldots N_{mesh}/2$$

and a first sidelobe of -54 dB. The distortion is shown in Fig. 4-6 indicating an improvement over the triangular filter, as whould be expected. A drawback of this filter is that the kernel extends over $4\Delta t$. Consequently, considering the symmetry of $h_{lp}(t)$, a time delay of $1\Delta t$ is imposed by this filter.

4.4 THE PWL ALGORITHM

In this section, the methodology used to solve the nonlinear differential equations of the electric current model of the device will be presented. Time domain simulation of nonlinear circuit problems is a mature field. The PWL algorithm is based on existing techniques that are used in current SPICE programs for numerical integration of differential equations.

In order to simplify the development of the PWL algorithm, we will consider the case where node 2 in Fig. 3-17 is replaced by a short circuit. The resulting node configuration with a two-port device is shown in Fig. 4-7a.

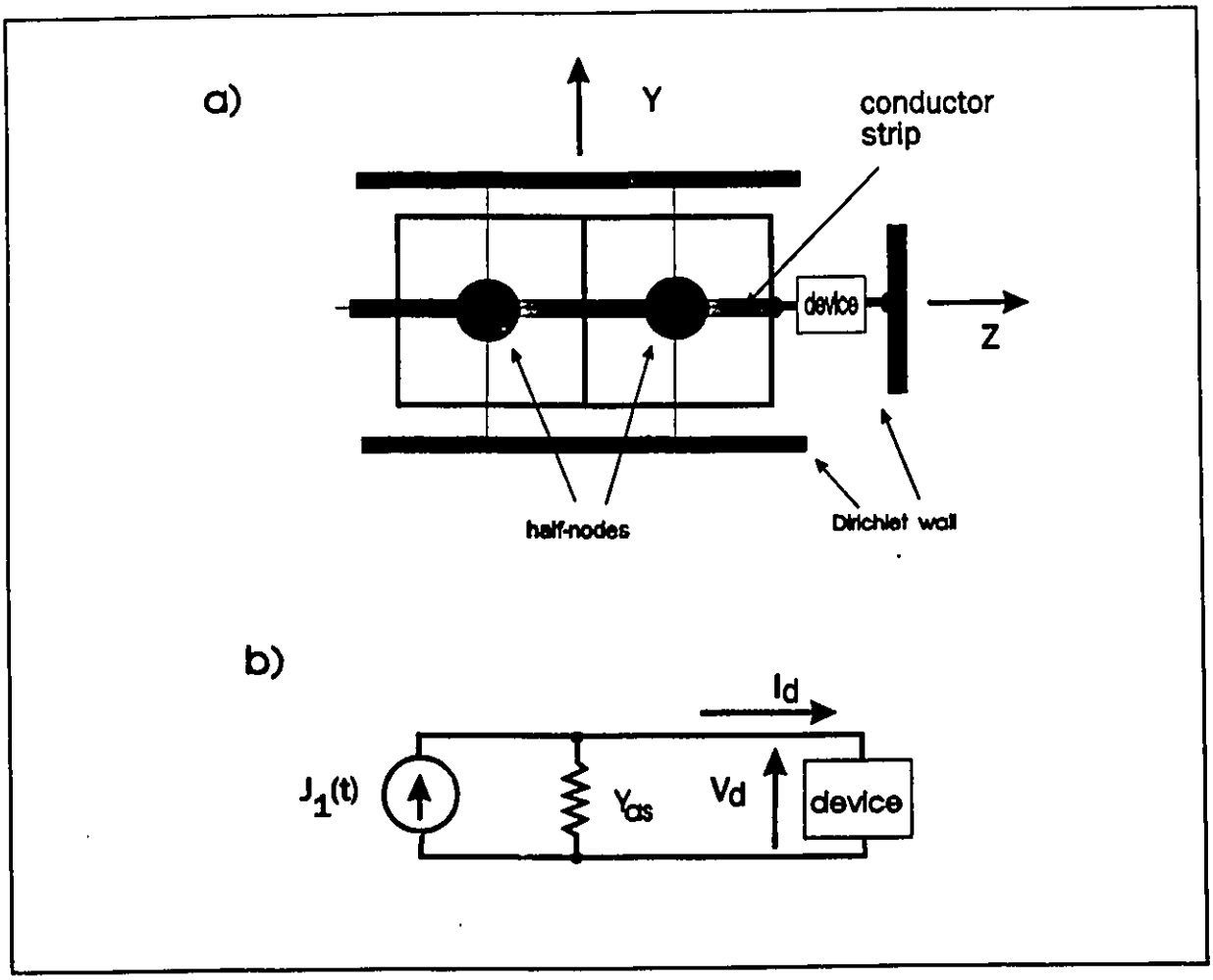

Fig. 4-7 Simulation of a stripline circuit with a two-terminal device where one terminal is shorted to ground. a) half-node configuration b) equivalent Thevenin circuit

The equivalent interface circuit, based on the methodology presented in Section 4.1, is shown in Fig. 4-7b. As before, V_d is the voltage across the device, and I_d is the current through it.

In Section 4.4.1 the treatment of devices without energy storage will be considered. In Section 4.4.2, a linear capacitor device will be considered. Then a multi-element nonlinear equivalent circuit will be evaluated, and the Predictor-Corrector algorithm will be introduced, which is the numerical integration routine used to solve the differential equations.

4.4.1 Nonlinear Devices Without Energy Storage

Consider the two-terminal device in Fig. 4-7 to be a diode with a current-voltage relationship

$$I_d = I_o \left(e^{\alpha V_d} - 1\right) \tag{4-16}$$

where I_o and α are constants. V_d is obtained as a function of time by solving the implicit equation

$$J_1(t) = V_d(t)\ Y_{as} + I_o\, e^{\alpha\, V_d(t)} \ . \tag{4-17}$$

From a solution for $V_d(t)$, the desired reflected antisymmetric voltage into node 1 can be determined as discussed in Section 3.6.

Eq. 4-17 is solved by the Newton-Raphson (NR) method [48]. An error function E_r is defined in this case by

$$E_r = V_d(t)\ Y_{as} + I_o\, e^{\alpha\, V_d(t)} - J_1(t) \ . \tag{4-18}$$

The Jacobian of the error function is denoted by J_b and is given by

$$J_b = \frac{\partial E_r}{\partial V_d} = Y_{as} + I_o\, \alpha\, e^{\alpha\, V_d(t)} \ . \tag{4-19}$$

The new estimate of V_d, denoted by V^*_d, is obtained from

$$V^{\bullet}_{d} = V_{d} - \frac{E_{r}}{J_{b}} \quad . \tag{4-20}$$

$V_d^{\bullet}$ is substituted for V_d, and Eq. 4-18 and Eq. 4-19 result in a new estimate for the device voltage. This cycle is repeated until the error is sufficiently small. In this example the convergence is fast, requiring only a few iterations to reduce E_r to almost zero.

4.4.2 Linear Devices With Reactance

Using the equivalent Thevenin interface circuit given in Fig. 4-7b, consider the two-terminal device to be a linear capacitor, C. The node equation now becomes

$$C\frac{d\,V_d(t)}{dt} + V_d(t)\,Y_{as} = J_1(t) \quad . \tag{4-21}$$

Let V_d be the estimate of $V_d(t)$ at the present time, and $V^{\bullet}_d$ an estimate of $V_d(t + \Delta t_e)$. Using the implicit backward Euler method we have [48]

$$V^{\bullet}_{d} = V_{d} + \Delta t_{e}\,\frac{d\,V^{\bullet}_{d}}{dt} \quad . \tag{4-22}$$

The error function to be nulled now becomes

$$E_{I} = C\frac{V^{\bullet}_{d} - V_{d}}{\Delta t_{e}} + V^{\bullet}_{d}\,Y_{as} - J_{1} \tag{4-23}$$

Since the device is linear, $V^{\bullet}_d$ can be solved directly as

$$V^{*}_{d} = \frac{J_1 \Delta t_e + C V_d}{C + Y_{aa} \Delta t_e} \qquad (4\text{-}24)$$

without having to resort to the Newton-Raphson iteration.

4.4.3 Gear's Second Order Predictor-Corrector Method

A multitude of numerical integration methods have been developed for estimating the solution to nonlinear differential equations. Of these, Gear's second order predictor-corrector method was chosen as it is generally not susceptible to numerical instabilities [48]. Furthermore, being a predictor-corrector method it naturally provides an estimation of the truncation error involved in the numerical integration process at each time step. This error estimation is used to dynamically adjust the step size to accommodate the fluctuating stiffness of the differential equation. Another advantage is that it is significantly more accurate than a first order method [48].

Gear's method will be introduced in this section by considering a general first-order differential equation

$$\frac{d\,x(t)}{dt} = f(x(t), t) + g(t) \qquad (4\text{-}25)$$

Assume that the solution has been approximated by the predictor-corrector method at the previous times t_n, t_{n+1} and t_{n+2} corresponding to the estimated solutions of x_n, x_{n+1} and x_{n+2} which are indicated in Fig. 4-8. It is desired to estimate the solution at t_{n+3}, the present time, where the estimated solution is x_{n+3} also indicated in Fig. 4-8. An explicit second-order predictor is initially used to

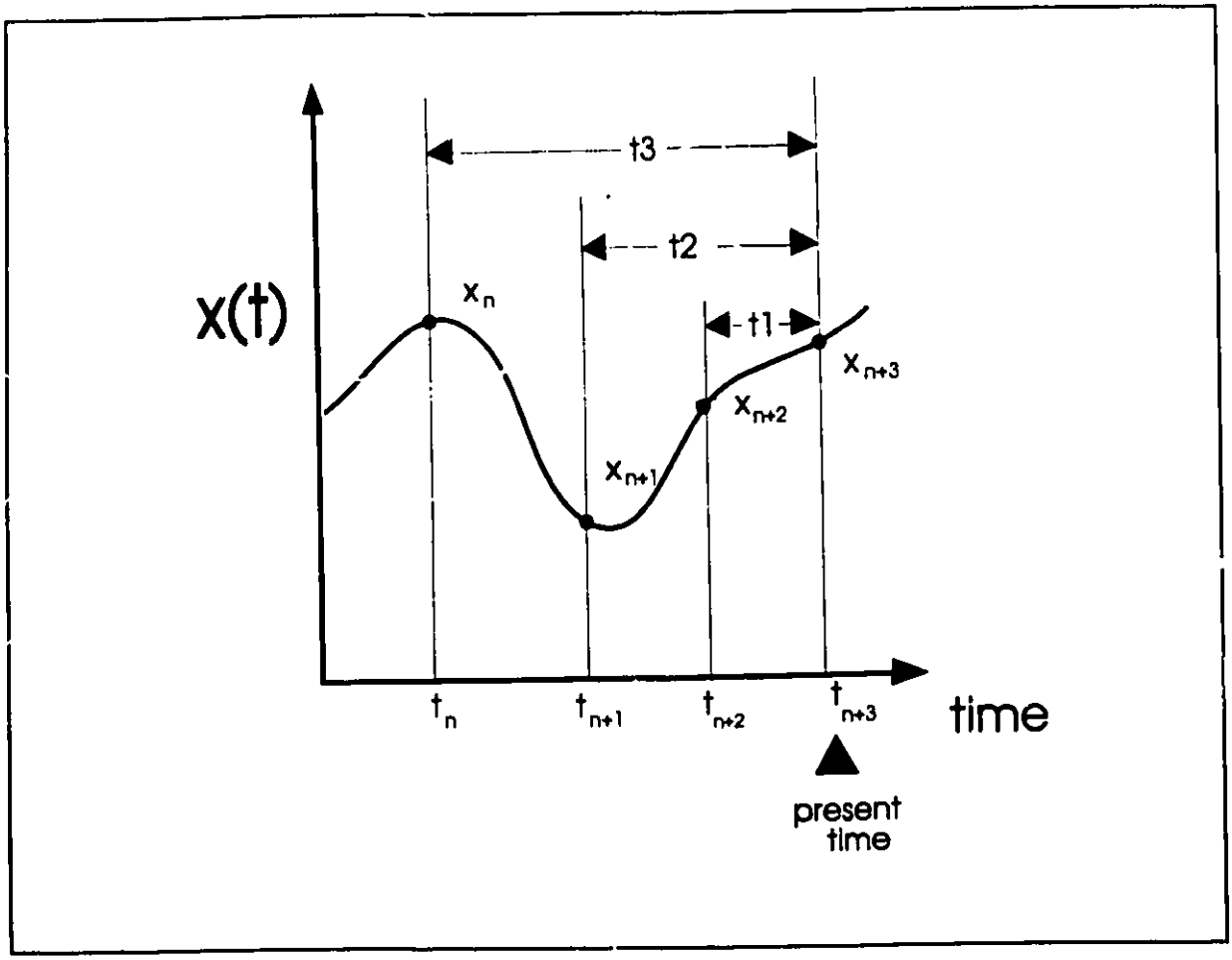

Fig. 4-8 Definition of the variables used in Gear's second-order predictor-corrector method

estimate a value of x_{n+3} which is given as [47]

$$x_{n+3} = a_1 x_{n+2} + a_2 x_{n+1} + a_3 x_n \qquad (4\text{-}26)$$

where

$$a_1 = \frac{t_2 t_3 (t_3 - t_2)}{D}$$

$$a_2 = \frac{t_3\ (1 - t_3)}{D}$$

$$a_3 = \frac{t_2\ (t_2 - 1)}{D}$$

with D given by

$$D = (t_3 - t_2)\ (1 + t_2\ t_3 - t_2 - t_3)\ .$$

The time intervals t_1, t_2 and t_3 are defined in Fig. 4-8. The predictor routine is followed by a corrector routine which is given as [47]

$$\frac{d\ x_{n+3}}{dt} = -\frac{1}{t_1}\ (ac_o\ x_{n+3} + ac_1\ x_{n+2} + ac_2\ x_{n+1}) \qquad (4\text{-}27)$$

where

$$ac_o = \frac{1 - t_2^2}{D}$$

$$ac_1 = \frac{t_2^2}{D}$$

$$ac_2 = -\frac{1}{D}$$

with

$$D = t_2\,(t_2 - 1)\ .$$

Note that the corrector equation is implicit in that it requires the present value of x_{n+3}. This is solved by first defining an error function by combining Eq. 4-25 and Eq. 4-27 and eliminating the time derivative of x_{n+3} in the process. The error function, denoted again by E_r is given by

$$E_r = f(x_{n+3}, t_{n+3}) + g(t_{n+3}) + \frac{1}{t_1}(ac_o\, x_{n+3} + ac_1\, x_{n+2} + ac_2\, x_{n+1}) \quad (4\text{-}28)$$

The initial estimate of x_{n+3} comes from the predictor routine. E_r is nulled by using the NR routine resulting in a more accurate estimate of x_{n+3}.

In order to control the step size, the truncation error is estimated at each time step. Various formulas may be used but the most accurate estimate is provided by Brayton [49]:

$$Error_{truncation} = \frac{t_1\ (x_{predicted} - x_{corrected})}{ac_o\ t_3} \quad (4\text{-}29)$$

where $X_{predicted}$ is the estimate of x_{n+3} that was initially obtained by using the predictor routine, and $X_{corrected}$ is the final corrected estimate of x_{n+3} at the output of the NR procedure.

The predictor-corrector algorithm discussed above applies equally well to a system of differential equations. Let u(t) denote the vector of state variables at time t that is a solution of the system of differential equations

$$\frac{\partial \boldsymbol{u}}{\partial t} = \boldsymbol{f}(\boldsymbol{u}(t), t) + \boldsymbol{g}(t) \ . \quad (4\text{-}30)$$

The following vectors are defined according to the time variables of Fig. 4-8:

$$\mathbf{u}_3 = \mathbf{u}(t)\Big|_{t = t_{n+3}}$$

$$\mathbf{u}_2 = \mathbf{u}(t)\Big|_{t = t_{n+2}}$$

$$\mathbf{u}_1 = \mathbf{u}(t)\Big|_{t = t_{n+1}}$$

$$\mathbf{u}_0 = \mathbf{u}(t)\Big|_{t = t_n} \ .$$

The corrector in vector format is given by

$$\frac{\partial \boldsymbol{u}_3}{\partial t} = -\frac{1}{t_1}(ac_o\,\boldsymbol{u}_3 + ac_1\,\boldsymbol{u}_2 + ac_2\,\boldsymbol{u}_1) \ . \qquad (4\text{-}31)$$

An error vector, denoted by $\mathbf{E}_r$, is formed from Eq. 4-30 and Eq. 4-31, eliminating $\partial u_3/\partial t$. $\mathbf{E}_r$ is given by

$$\boldsymbol{E}_r = \boldsymbol{f}(\boldsymbol{u}_3, t_{n+3}) + \boldsymbol{g}(t_{n+3}) + \frac{1}{t_1}(ac_o\,\boldsymbol{u}_3 + ac_1\,\boldsymbol{u}_2 + ac_2\,\boldsymbol{u}_1) \ . \qquad (4\text{-}32)$$

$\mathbf{E}_r$ is nulled as before using the NR procedure with an initial guess of u_3 from the predictor estimate

$$\boldsymbol{u}_3 = a_1\,\boldsymbol{u}_2 + a_2\,\boldsymbol{u}_1 + a_3\,\boldsymbol{u}_0 \ . \qquad (4\text{-}33)$$

In each NR iteration, the Jacobian matrix of $\mathbf{E}_r$, denoted by $\mathbf{J}_b$, is evaluated as

$$J_b(i,j) = \frac{\partial E_r(i)}{\partial u_3(j)} \ . \qquad (4\text{-}34)$$

Let $u_{3,old}$ denote the previous estimate of the u_3 vector, and let $u_{3,new}$ denote the new value of u_3 at the outcome of the NR iteration. Then $u_{3,new}$ is obtained from the equation

$$\boldsymbol{J}_b\,(\boldsymbol{u}_{3,old} - \boldsymbol{u}_{3,new}) = \boldsymbol{E}_r \ . \qquad (4\text{-}35)$$

4.4.4 Example of a Diode Detector Circuit

A simple example of solving a nonlinear circuit using the predictor-corrector method is given in this section. The example consists of an idealized two-

a) detector device circuit

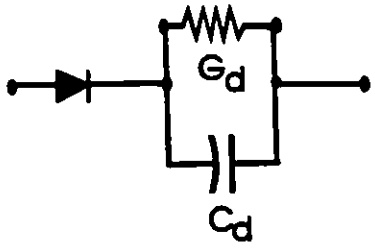

b) equivalent circuit

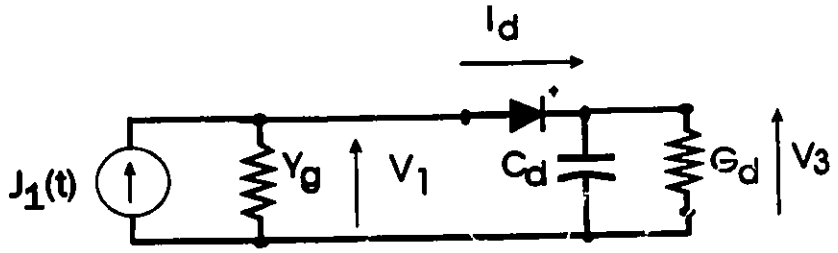

Fig. 4-9 Example of an idealized diode detector circuit. a) two-port detector device b) Overall equivalent circuit used in the PWL routine

terminal diode detector circuit shown in Fig. 4-9a. The detector device is attached to the stripline simulated by the half-node as shown in Fig. 4-7. A voltage generator with an internal admittance of Y_g was attached to the other end of the stripline as illustrated in Fig. 3-23. The equivalent circuit is shown in Fig. 4-9b with a current source $J_1(t)$ given by

$$J_1(t) = \tfrac{1}{2}\, Y_{aa}\, V_g(t)\,. \qquad (4\text{-}36)$$

The three node equations describing the equivalent circuit are:

$$V_1\, Y_{as} + I_d - J_1 = 0 \qquad (4\text{-}37a)$$

$$C_d \frac{d}{dt} V_3 = I_d - V_3\, G_d \qquad (4\text{-}37b)$$

$$I_d = I_o\, e^{\alpha (V_1 - V_3)} \qquad (4\text{-}37c)$$

where V_1, V_3 and I_d are indicated in Fig. 4-9 and I_o and α are diode constants introduced in Section 4.4.1.

The equations above are put into a matrix form as follows:

$$\boldsymbol{C} \frac{d\boldsymbol{U}}{dt} = \boldsymbol{G}\,\boldsymbol{U} + \boldsymbol{\Phi} + \boldsymbol{S} \qquad (4\text{-}38)$$

where

$$\boldsymbol{C}=\begin{pmatrix} 0 & 0 & 0 \\ 0 & C_d & 0 \\ 0 & 0 & 0 \end{pmatrix}$$

$$\boldsymbol{G}=\begin{pmatrix} Y_{ss} & 0 & 1 \\ 0 & -G_d & 1 \\ 0 & 0 & -1 \end{pmatrix}$$

$$\boldsymbol{\Phi}=\begin{pmatrix} 0 \\ 0 \\ I_o\, e^{\alpha(V_1 - V_3)} \end{pmatrix}$$

$$\boldsymbol{B}=\begin{pmatrix} -J_1 \\ 0 \\ 0 \end{pmatrix}$$

$$\boldsymbol{U}=\begin{pmatrix} V_1 \\ V_3 \\ I_d \end{pmatrix}$$

In most cases **C** is not invertible, as in this case, and hence the form in Eq. 4-37 is not simplified further.

The error vector is derived as explained above by combining Eq. 4-31 and Eq. 4-38. However, since **C** is not invertible, the error vector is defined with respect to

$$\boldsymbol{C}\,\frac{\partial \boldsymbol{u}_3}{\partial t}$$

such that

$$\boldsymbol{E}_r = \boldsymbol{G}\,\boldsymbol{U}_3 + \boldsymbol{\Phi}\,\boldsymbol{U}_3 + \boldsymbol{S}\,\boldsymbol{U}_3 + \frac{1}{t1}\left(ac_o\boldsymbol{C}\boldsymbol{U}_3 + ac_1\boldsymbol{C}\boldsymbol{U}_2 + ac_2\boldsymbol{C}\boldsymbol{U}_1\right) \qquad (4\text{-}39)$$

or

$$\boldsymbol{E}_r = \left(\frac{ac_o}{t1}\boldsymbol{C} + \boldsymbol{G}\right)\boldsymbol{U}_3 + \frac{ac_1}{t1}\boldsymbol{C}\boldsymbol{U}_2 + \frac{ac_2}{t1}\boldsymbol{C}\boldsymbol{U}_1 + \boldsymbol{\Phi}(\boldsymbol{U}_3) + \boldsymbol{S}(u_3) \ .$$

The Jacobian matrix of E_r is given by

$$\boldsymbol{J} = \frac{\partial \boldsymbol{E}_r}{\partial \boldsymbol{U}_3} \qquad (4\text{-}40)$$

where

$$\boldsymbol{J} = \frac{a_{0c}}{t1}\boldsymbol{C} + \boldsymbol{G} + \frac{\partial \boldsymbol{\Phi}}{\partial \boldsymbol{U}_3} + \frac{\partial \boldsymbol{S}}{\partial u_3} \ .$$

For this example

$$\frac{\partial \boldsymbol{\Phi}}{\partial \boldsymbol{U}_3} = \begin{pmatrix} 0 & 0 & 0 \\ 0 & 0 & 0 \\ G_{diode} & -G_{diode} & 0 \end{pmatrix} \qquad (4\text{-}41)$$

where G_{diode} is the conductance of the diode at the present voltage across the diode given by $v_1 - v_3$. Finally, since the source vector for the implementation of the predictor-corrector method will be independent of u_3, we have

$$\frac{\partial \boldsymbol{S}}{\partial u_3} = 0 \ . \qquad (4\text{-}42)$$

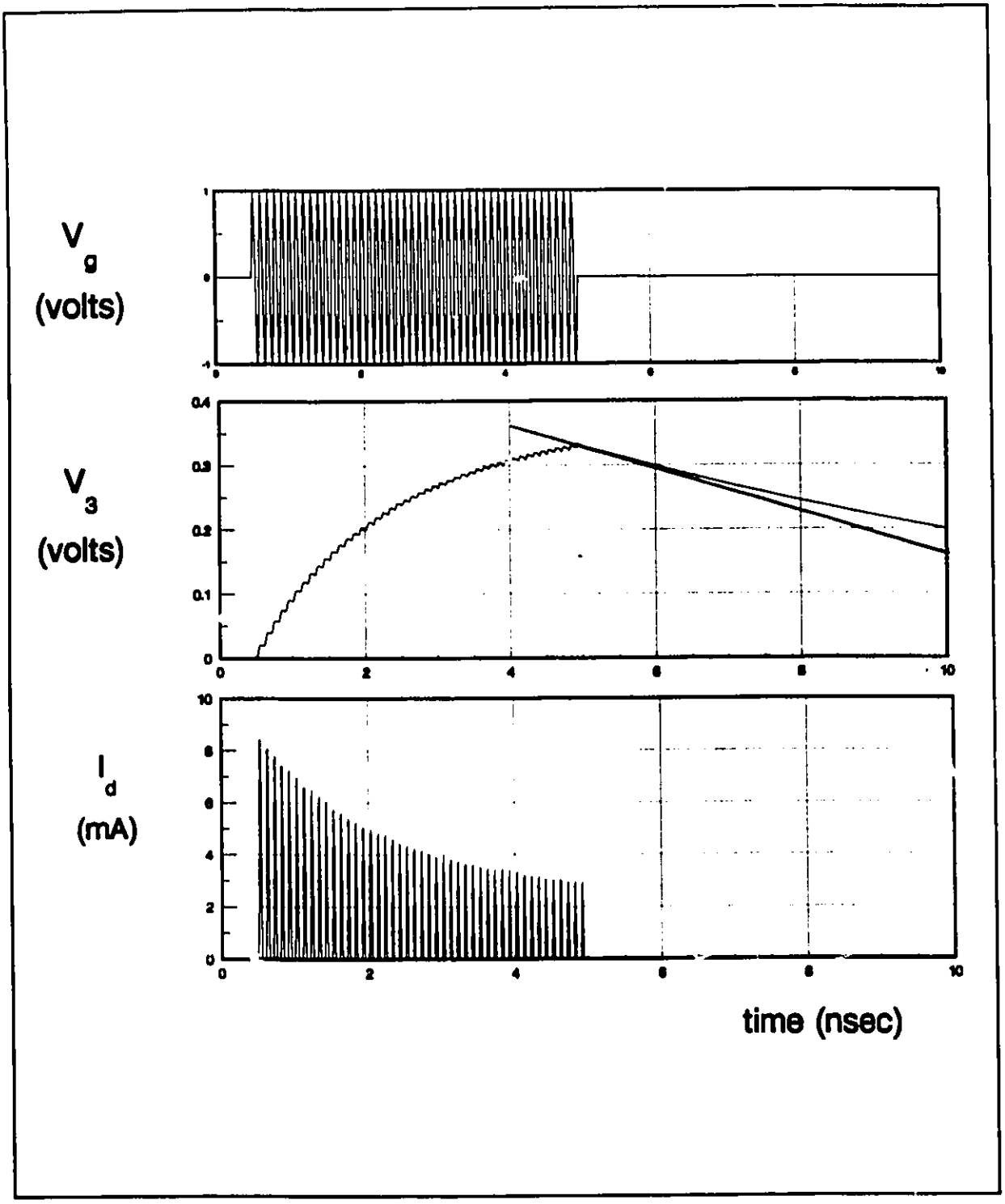

Fig. 4-10 Transient response of ideal diode detector circuit subject to an RF pulse of 10 GHz. The TLM time step is 5 psec.

As in the previous examples it is convenient to normalize the network circuit parameters such that $\Delta t=1$. Hence the capacitance C_d is multiplied by $1/\Delta t$. To take a specific example, assume that the frequency of the generator is 10 GHz, and that we want 20 samples per cycle, hence we require a Δt of 5 picoseconds. Let C_d be 10 pF, then in the simulation $C_d\Delta t$ is 2 S. In this simulation G_d was .001 S.

The transient response for a 10-GHz pulse signal is shown in Fig. 4-10 with the initial condition that the voltage across the capacitor is zero. The detector is excited by a short RF pulse that starts at t=0.5 nsec and stops at t=5 nsec. The plot of V_3, the voltage across the capacitor, reveals a typical RC response as expected. I_d, the current through the diode is also plotted. It is always greater than zero since the diode is assumed ideal with no parallel capacitance. As expected, the diode current only flows during the positive half cycle of the generator output. As the detector voltage increases, the diode current decreases accordingly.

The response can be verified to some extent by considering the slope of $v_3(t)$ at $t > 5$ nsec. Since the diode is ideal, the capacitor discharges through the load admittance G_d. As $v_3=.34$ volts at t=5 nsec we have

$$\frac{\partial v_3}{\partial t} = -\frac{v_3 G_d}{C_d} = -3.4 \times 10^7$$

This slope is drawn in Fig. 4-10. As observed, the slope line is tangent to $v_3(t)$ at t=5 nsec which gives us some degree of confidence in the accuracy of the simulation.

4.5 CONCLUSIONS

In this chapter, a methodology for interfacing nonlinear devices with TLM half-nodes has been developed. The method involves a PWL algorithm with a variable time step. The time step adjusts itself dynamically based on an indication of the local stiffness of the differential equations governing the device.

A simple detector example was analyzed to demonstrate the methodology. In Chapter 5 more practical examples will be given which will demonstrate the applicability of the method to solving more general microwave circuit problems.

CHAPTER 5

APPLICATIONS

The algorithms and methodologies developed in Chapters 3 and 4, were combined into a general 3D TLM simulation program, suitable for modelling planar microwave and millimetre wave circuits containing multi-port nonlinear devices. The acronym associated with the program is "TMDS" for TLM Microstrip Device Simulation. This chapter provides a description and applications of the TMDS algorithm.

An overview of the algorithm is given in Section 5.1. In Section 5.2, the idealized detector circuit that was introduced in Section 4.4.4, will be analyzed using the TMDS algorithm. This will highlight various attributes of the program. An example of an idealized diode switch will be given in Section 5.3. In Section 5.4, a three-terminal FET model is described and simulated by the TMDS algorithm. In Section 5.5, S-parameter measurements are provided of an experimental stripline diode switch circuit that was constructed. These measurements were compared with the calculated S-parameters provided by the TMDS simulation program. An estimation of the spurious mode content generated in a typical simulated microstrip circuit will be given in Section 5.6.

5.1 OVERVIEW OF THE TMDS ALGORITHM

In this section a brief description of the TMDS algorithm will be given. As the overall object was to develop the methodologies rather than a general user-friendly program, a specific geometry was chosen which is sketched in Fig. 5-1. The simulation volume consists of a rectangular box with two layers of dielectrics. The conductor strips of the microstrip lines, bias lines and ground connections lie in a plane coincident with the dielectric interface. The conductor strips are modelled by conductor strip nodes and the surrounding volume is modelled by condensed nodes as described in Chapter 3. The position and shape of these ground planes and conductor strips can be arbitrarily configured for different simulations. RF stimulation is provided by a lumped generator, V_g, with an internal admittance Y_g as shown. V_{b1} and V_{b2} are programmable bias supplies with internal admittances of Y_{b1} and Y_{b2} respectively. Finally a load admittance of G_l connects the microstrip line to the ground plane as shown. The algorithm can accommodate a distributed network with multiple ports to model distributed devices of arbitrary complexity. The boundaries of the simulation volume are assumed dispersionless with programmable reflection coefficients.

A block diagram of the environment of the TMDS program is given in Fig. 5-2. A simple user interface program, "MSPAR", prompts the user for required parameters such as mesh geometry, voltage and bias supply parameters and the device model characteristics. These parameters are used in the functional blocks of the TMDS as illustrated in Fig. 5-2.

The TMDS consists of four functional blocks as shown. The "TLMS" block is the TLM mesh simulator and provides the overall loop control. The "DRIVER" block models the time varying generator and bias voltage sources. The "DEVICE" block

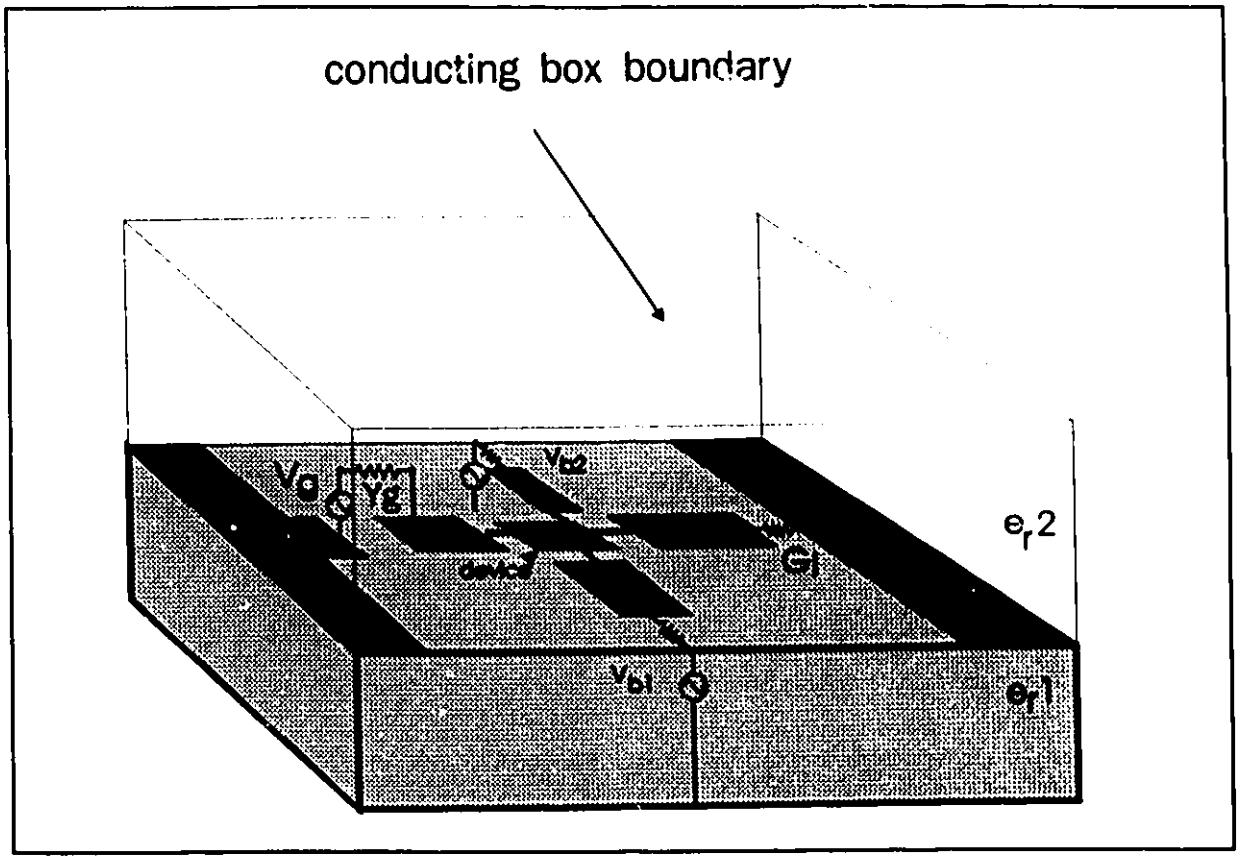

Fig. 5-1 Geometry of the planar microstrip circuit that is simulated by the TMDS algorithm

contains the PWL differential equation integration algorithm for simulating the multi-port embedded device. Finally the "OUTPUT" block determines the appropriate data to be recorded for later reference.

During each TLM mesh interval, the time variable is passed to the DEVICE and DRIVER blocks from the TLMS, and the required parameters are returned to the TLMS block. As discussed in Chapter 4, the incident antisymmetric voltages from the conductor strip nodes attached to the device are fed to the device solver at each TLM mesh iteration. The reflected antisymmetric voltages are then fed back from the device solver to the conductor strip nodes. This is indicated in Fig. 5-2 as the "incident" and "reflected" parameters passing between the TLMS, DEVICE and

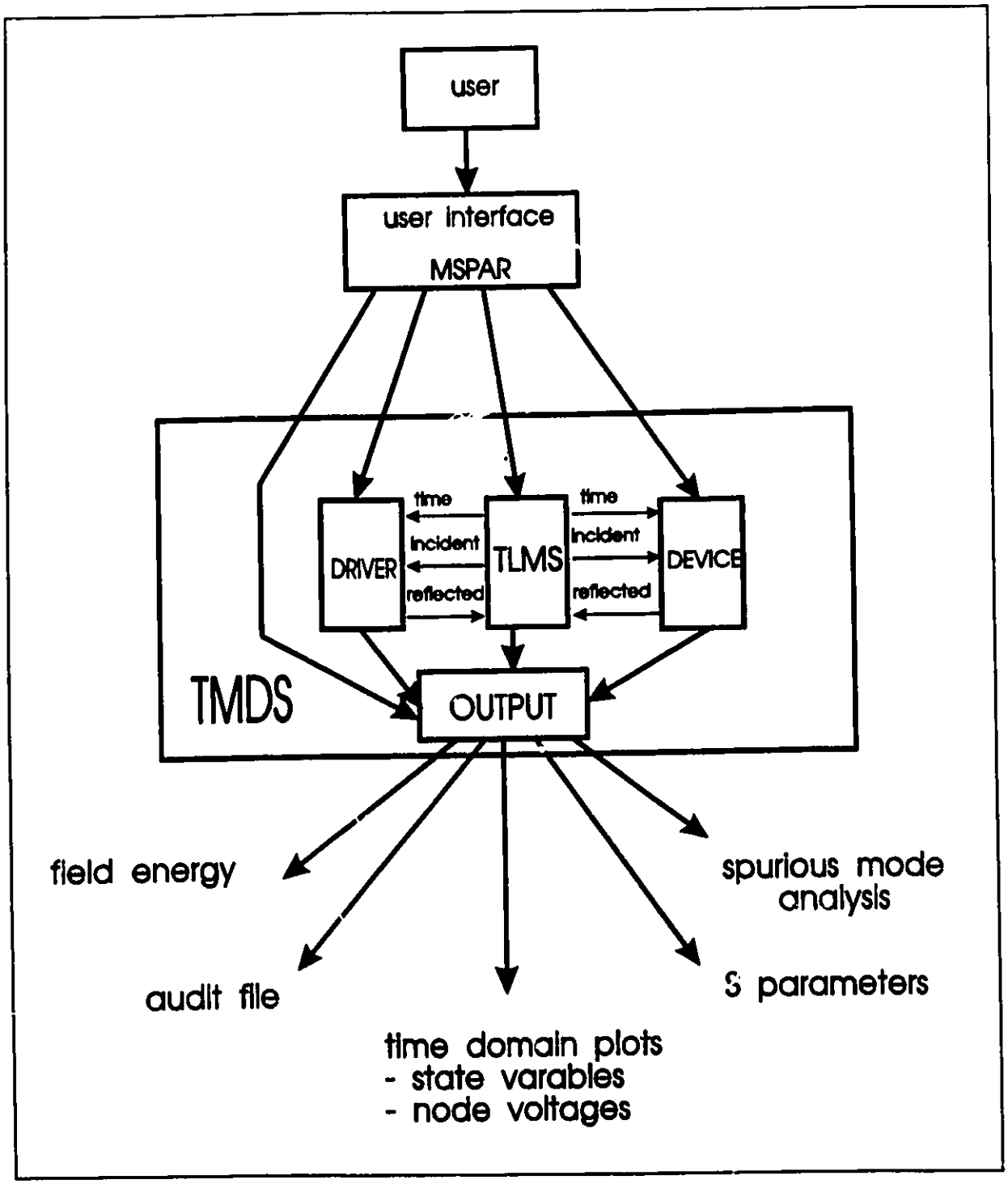

Fig. 5-2 Block diagram of the TMDS program environment. The MSPAR program interfaces with the user for the required simulation parameters.

DRIVER blocks.

The OUTPUT block has access to all the node voltages in the TLMS block and state variables of the DEVICE and DRIVER blocks. Based on user requirements, the data is reduced and formatted into appropriate files for later reference. The OUTPUT block contains a frequency-domain Discrete Fourier Transform (DFT) for extracting response frequencies in the output response of the circuit, as well as for S-parameter extraction. A spatial-domain DFT algorithm is also included for observing the spatial frequency distribution of the field distribution in the covered microstrip cavity. This is necessary to study the influence of spurious modes. Finally, a routine is included such that the total field energy and the dissipated energy can be calculated to verify the conservation of energy. This proved to be a very useful diagnostic tool that identifies devices, boundaries, or node interfaces that violate energy conservation.

5.2 DIODE DETECTOR CIRCUIT

As an initial application, the diode detector circuit of Section 4.4.4 is revisited, as it exemplifies various points. The detector is embedded into an array of half-nodes simulating a 1D strip transmission line. The array is eight nodes long with the device located between the 5^{th} and 6^{th} node as sketched in Fig. 5-3a. The equivalent circuit of the detector is the same as in Fig. 4-9b except for with the addition of the equivalent current from port 2. Furthermore, a switch is added that can short out port 2. If this switch is closed then the response of the detector is the same as in Section 4.4.4. If it is open then the detector is connected to ground via the equivalent conductor strip modelled by

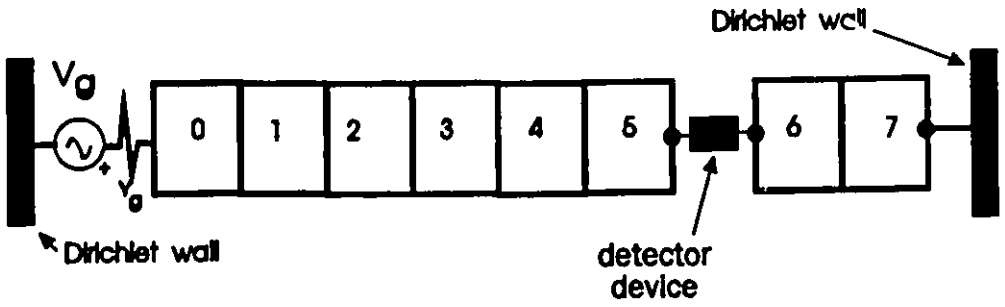

a) Half-node mesh connected to detector

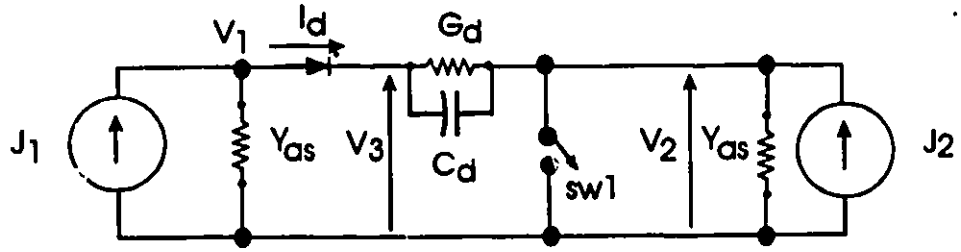

b) Equivalent circuit of detector device

Fig. 5-3 Idealized diode detector device embedded in a 1D array of half-nodes simulating a stripline. a) Configuration of half-nodes. b) Equivalent circuit of device for PWS routine.

nodes 6 and 7. The response for a 10-GHz generator signal of 2 volts peak amplitude that is switched on at t=0 is shown in Fig. 5-4. In this case the switch is closed and Δt is assumed to be 1 psec such that C_d of 10 pF is modelled as a 10 F capacitor similar to the scaling discussed in Section 4.4.4. Next the switch is opened such that port 2 attached to the detector represents a short section of shorted transmission line which at low frequencies can be represented by an inductance. The response is shown in Fig. 5-5. Note that the "average" value of the detector voltage, V_3, is the same as in Fig. 5-4, however there is a significant amount of high frequency ringing generated by the nonlinear switching characteristics of the diode. This ringing is merely a consequence of the short transmission line resonance section composed of nodes 6 and 7. It is "physical" as far as the oversimplified model of the diode is valid, and is not induced by any numerical instability of the method.

The high frequency ringing, visible in Fig. 5-5, can be observed experimentally. However, it is generally highly damped. This damping is a consequence of the packaging capacitance C_p, the series resistance R_{sd}, the depletion capacitance C_{dep}, the diffusion capacitance C_{dif} and the series inductance L_{ser}, present in any physical diode. In order to avoid unnecessary details, modelling of the diffusion and depletion capacitance will be postponed until Section 5.5. The damping effect can be observed adequately by adding R_{sd} and C_p to the equivalent circuit of the detector which is updated in Fig. 5.6.

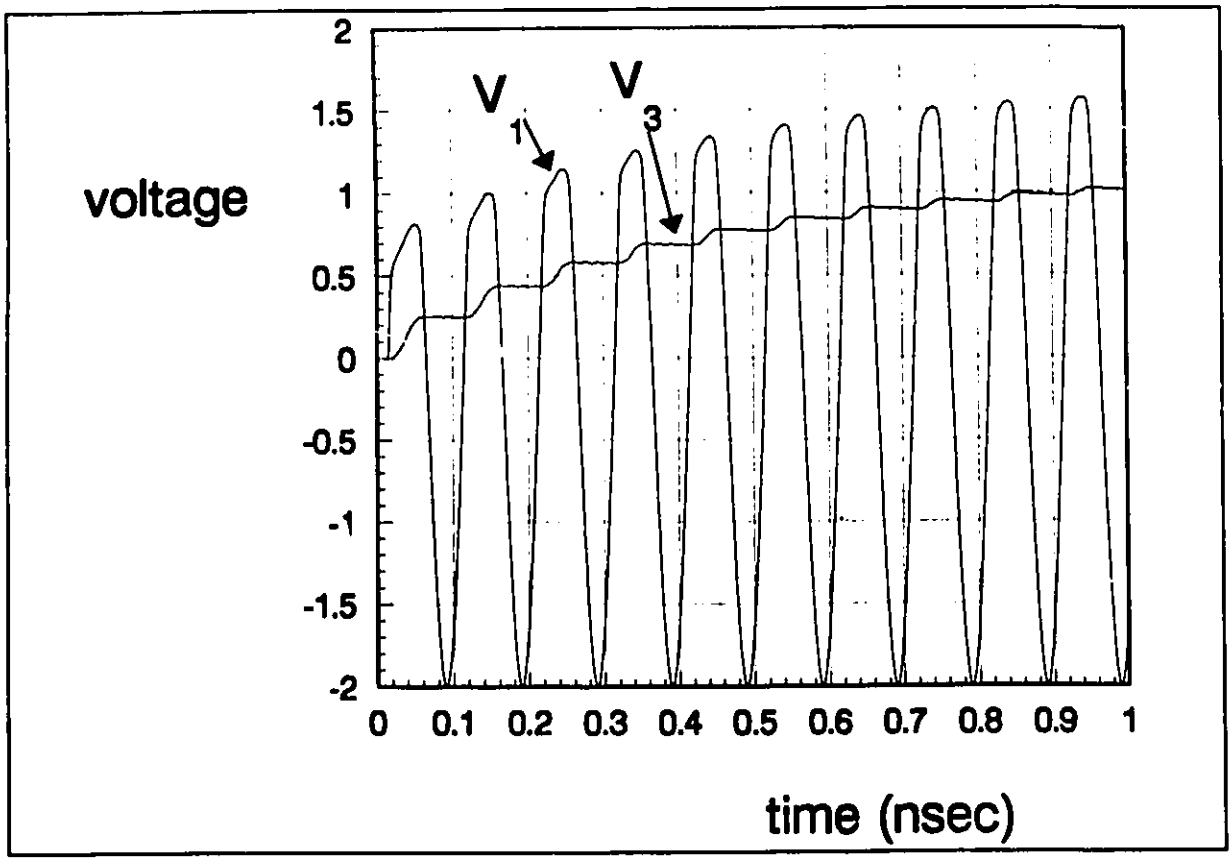

Fig. 5-4 Transient response of diode detector circuit with the switch closed (sw1 in Fig.5-3b). V_1 and V_3 are defined in Fig.5-3b.

There are now five node equations describing the equivalent circuit are

$$V_1 Y_{as} + I_d - J_1 + C_p \frac{d}{dt} (V_1 - V_3) = 0 \qquad (5\text{-}1a)$$

$$C_d \frac{d}{dt} (V_2 - V_3) = -V_2 (G_d + Y_{as}) + V_3 G_d \qquad (5\text{-}1b)$$

$$\frac{d}{dt} (-C_p V_1 - C_d V_2 + (C_d + C_p) V_3) = I_d + (V_2 - V_3) G_d \qquad (5\text{-}1c)$$

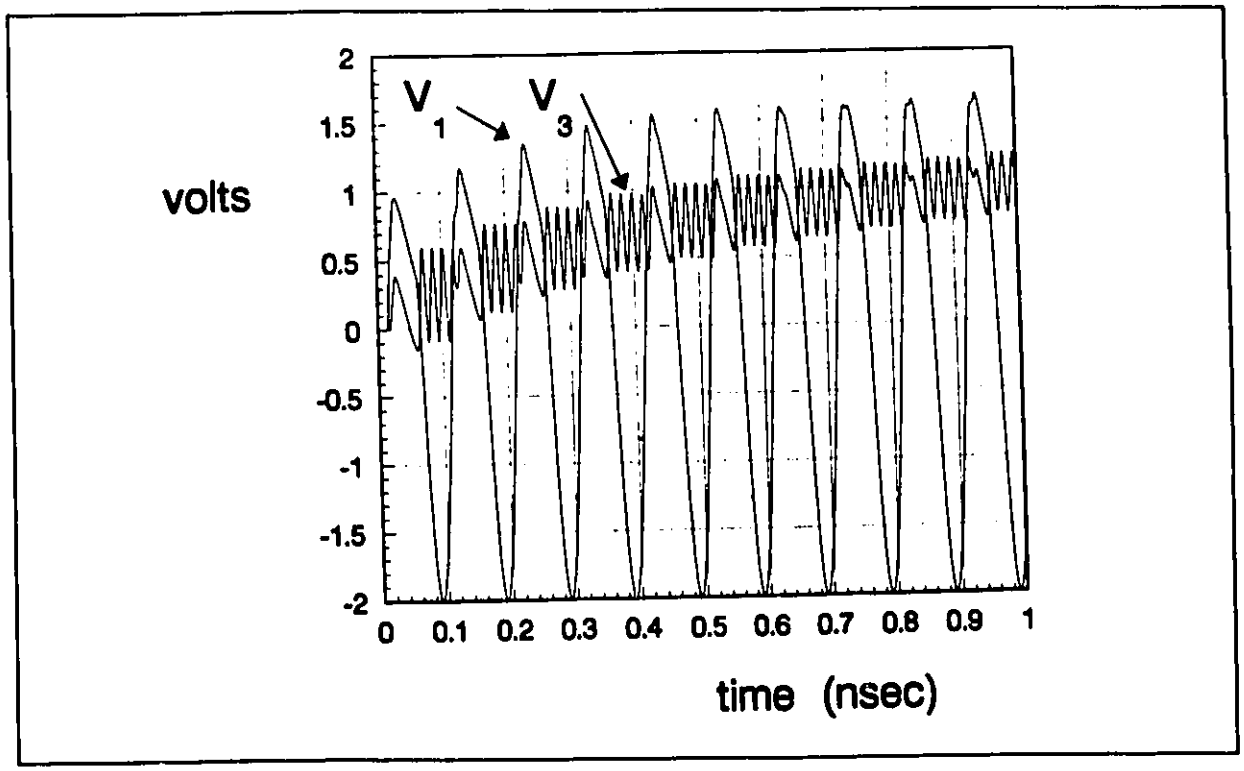

Fig. 5-5 Transient response of diode detector circuit with switch open (sw1 in Fig.5-3b). V_1 and V_3 are defined in Fig.5-3b.

$$I_d = I_o\, e^{\alpha (V_1 - V_4)} \qquad (5\text{-}1d)$$

$$I_d = \frac{1}{R_{sd}} (V_4 - V_3) \qquad (5\text{-}1e)$$

where V_1, V_2, V_3, V_4 and I_d are indicated in Fig. 5-6 and I_o and α are diode constants introduced in Section 4.4.1.

The equations above are put into the matrix form given in Section 4.4.4 as

$$C\frac{d\bar{U}}{dt} = G\bar{U} + \bar{\Phi} + \bar{S} \qquad (4\text{-}38)$$

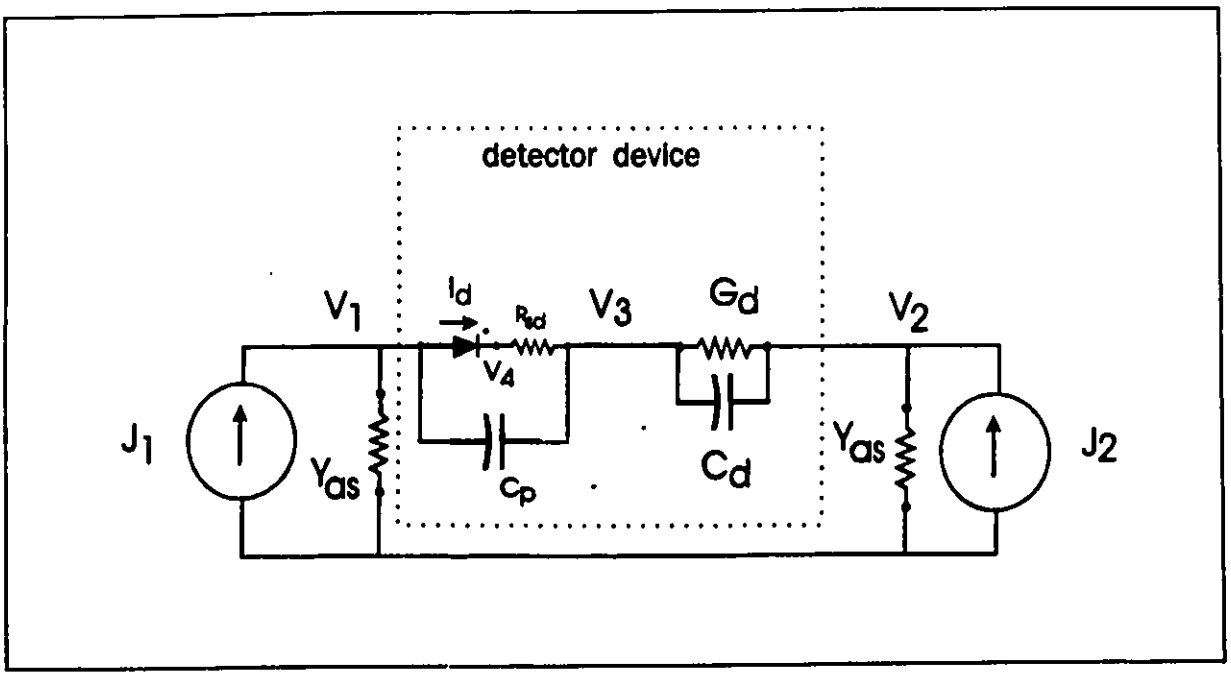

Fig. 5-6 Equivalent circuit of the detector with parasitics included in diode model

and solved by the PWL algorithm as described in Chapter 4. In order to determine the reflected antisymmetric voltages into the half-nodes, the total device current, I_{dev}, is estimated to be

$$I_{dev} = I_d + C_p \frac{\partial}{\partial t}(V_1 - V_3) \qquad (5\text{-}2)$$

The simulation results of the detector with the non-ideal diode model are shown in Fig. 5-7 for the same 10 GHz generator signal used previously. For this simulation, C_p was chosen to be 0.1 pF and R_{sd} was 0.5 ohm. As expected, these added components damp the high frequency signals in the detector output as observed in Fig. 5-7.

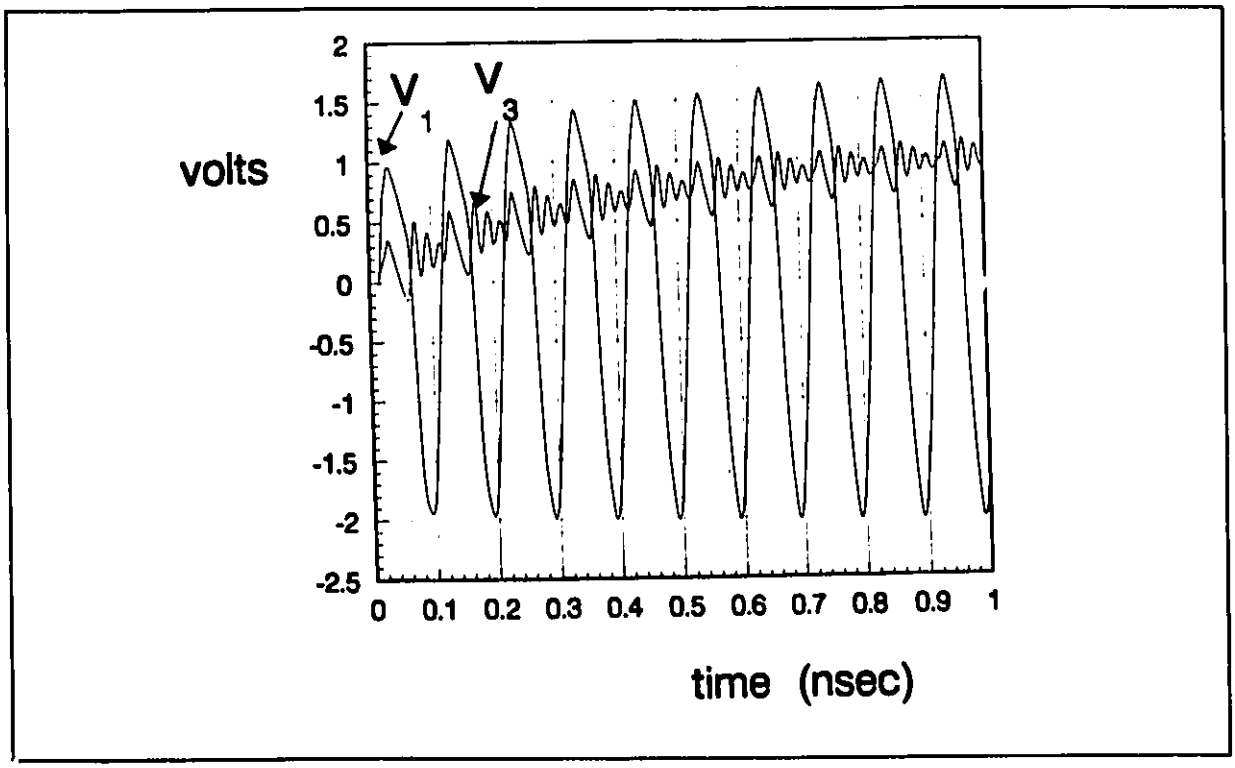

Fig. 5-7 Transient response of detector with a parasitic capacitance and series resistance included in diode model.

5.3 EXAMPLE OF A DIODE SWITCH

In this section an example is given of a diode switch in a 1D transmission line as shown in Fig. 5-8a. The equivalent circuit is shown in Fig. 5-8b. There are seven state variables used and seven node equations derived in a similar fashion as in the detector example. The state variables are V_1, V_2, V_3, V_4, V_b, I_d and I_b as indicated in Fig. 5-8b. Note that the bias voltage is supplied within the device model. This approximation is generally reasonable when the bias parameters are insensitive to the surrounding electromagnetic fields. However, in cases where the bias circuitry does couple to some extent with the surrounding fields, it is necessary to model the bias circuitry as a distributed

network involving conductor strip nodes.

The switch circuit has a connection to ground. In this configuration of a single layer of half-nodes the ground is naturally present. When the microstrip line is modelled with more than a single layer, the microstrip ground is not the same ground as the conductor strip node ground as mentioned in Section 3.6.3. Hence a ground contact must be provided and connected to the device. This will be elaborated further in Section 5.4.2. It is interesting that this grounding problem is analogous to a practical problem experienced in MIC design.

Another consequence of the grounding connection in the diode switch is that current flows through the grounding connection and therefore the switch is a three-terminal rather than a floating two-terminal device, such as the detector in Section 5.2. In the detector example the current flow through the device, I_{dev}, was calculated by the PWL algorithm. The voltages reflected into the half nodes were calculated with a filtered and sampled version of I_{dev} using the procedure described in Section 4.3. For the diode switch it is necessary to filter V_1 and V_2 resulting in ${}_qV_1$ and ${}_qV_2$. The reflected antisymmetric voltages in Fig. 4-1 are then

$$ {}_qV^r_{as1} = {}_qV_1 - {}_qV^i_{as1} \qquad (5\text{-}3a) $$

$$ {}_qV^r_{as2} = {}_qV_2 - {}_qV^i_{as2} \qquad (5\text{-}3b) $$

Fig. 5-9 shows the turn-off transient response of the diode switch when the generator is set at 10 GHz with an amplitude of 50 mV. The bias voltage, V_{b1}, in Fig. 5-9 was initially set to -2 volts such that the diode would be an open circuit. At 2 nsec, V_{b1} is increased linearly at 3 volts/nsec to 4 volts turning on the diode. This is reflected in the plot of the resultant bias current, I_{bias},

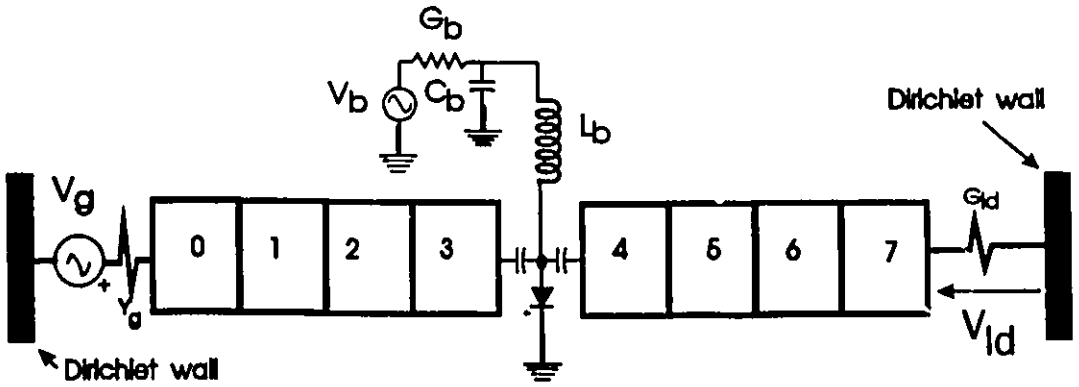

a) Half-node mesh connected to diode switch

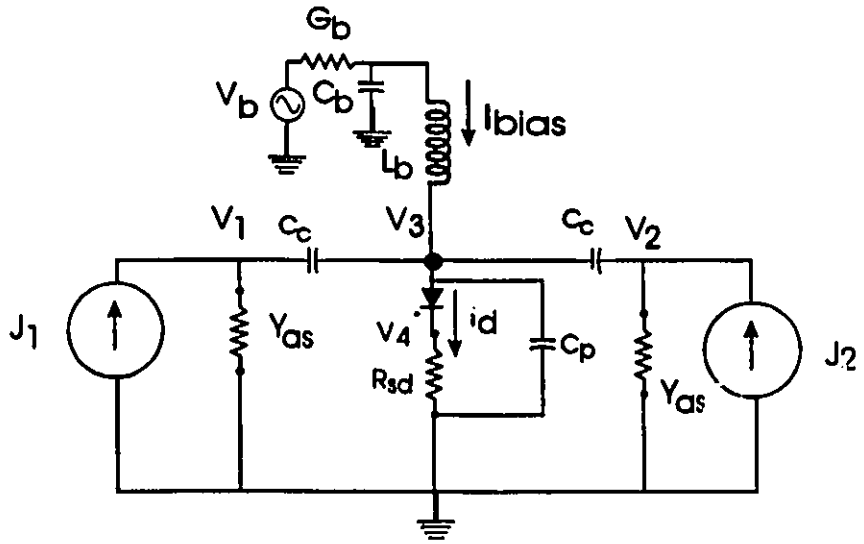

b) Equivalent circuit of switch device

Fig. 5-8 Simulation of a diode switch shunting a transmission line. a) Half-node configuration showing connection with switch device. b) Equivalent circuit of switch device.

in Fig. 5-9. The plot of V_3 shows the changing voltage across the diode. Note that the 10 GHz signal becomes much smaller as the diode is forward biased, as one would expect. Finally Fig. 5-10 is a plot of the generator voltage, V_g, and the voltage across the load resistor, V_{1d}. The effect of the switch diode turning on is evident. Note that there is a pulse due to the switching transient of the bias circuitry, which is a characteristic of this type of switch.

5.4 TLM MODELLING OF MESFET CIRCUITS

In this section, a method of coupling a MESFET device model to the conductor strip nodes will be developed. In Section 5.4.1, a simple MESFET model is presented. A 1D and a 2D single stage MESFET gain stage circuit is discussed in Section 5.4.2. A 2D distributed MESFET model is developed in Section 5.4.3.

5.4.1 Lumped MESFET Model

The model of the MESFET is shown in Fig. 5-11. In order to simplify the model, the capacitances are approximated as being linear, the diode conductances are modelled as ideal diodes and the propagation delay through the channel is neglected. The reason for this simplification is not due to limitations of the simulation method but rather an attempt to avoid unnecessary details. The channel current is given by a practical model presented by Hwang and Itoh [50].

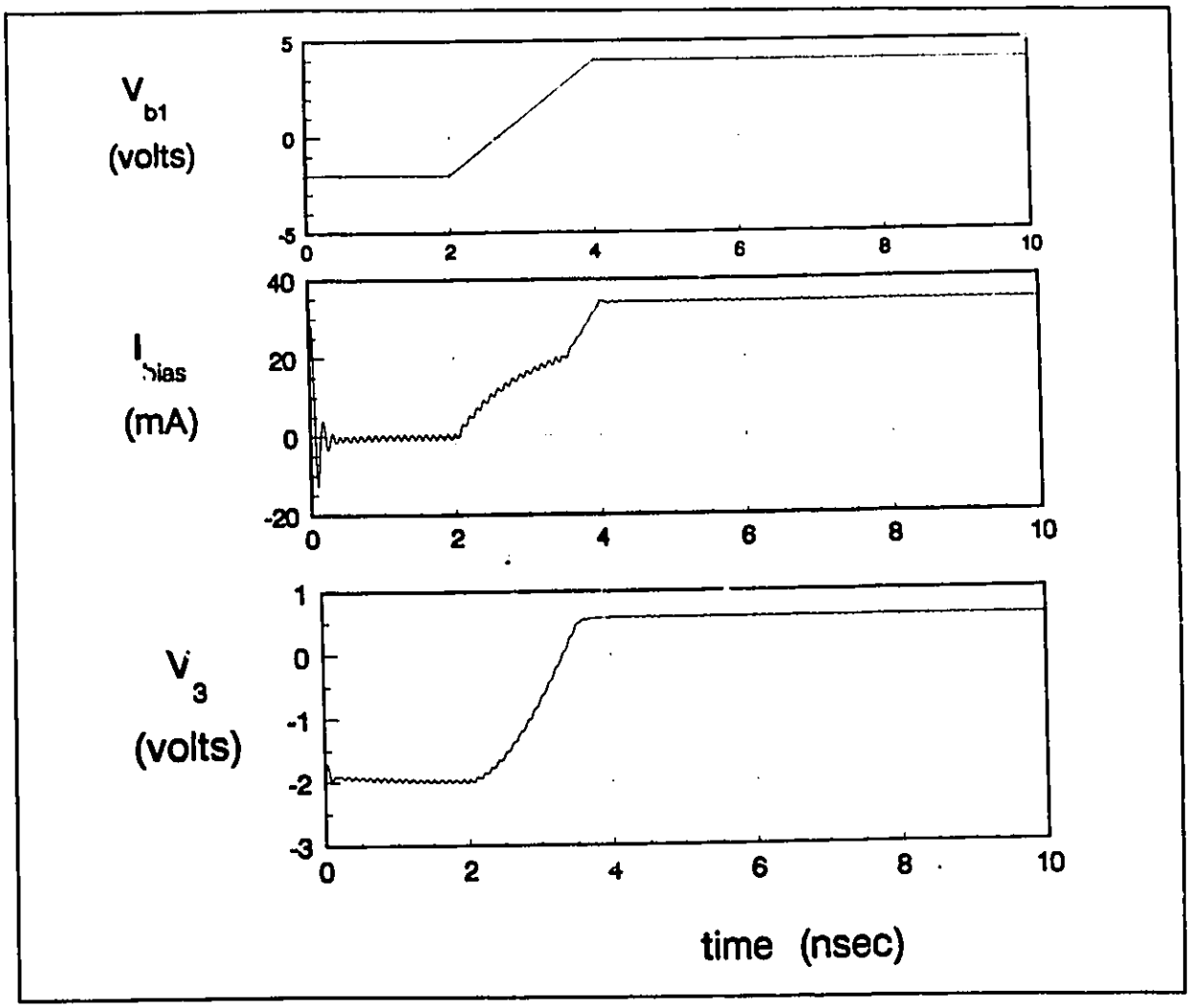

Fig. 5-9 Transient response of diode switch. V_{b1}, I_{bias} and V_3 are defined in Fig.5-8.

The channel current of the FET, I_{chan} is a function of V_{gs} and V_{ds} and can be emperically modelled as described in [50]

$$I_{chan}(V_{gs}, V_{ds}) = I_{dss}\left(1 - \frac{V_{gs}}{V_{po}}\right)^2 \tanh\left(\frac{c\ V_{ds}}{V_{gs} - V_{po}}\right) \qquad (5\text{-}4)$$

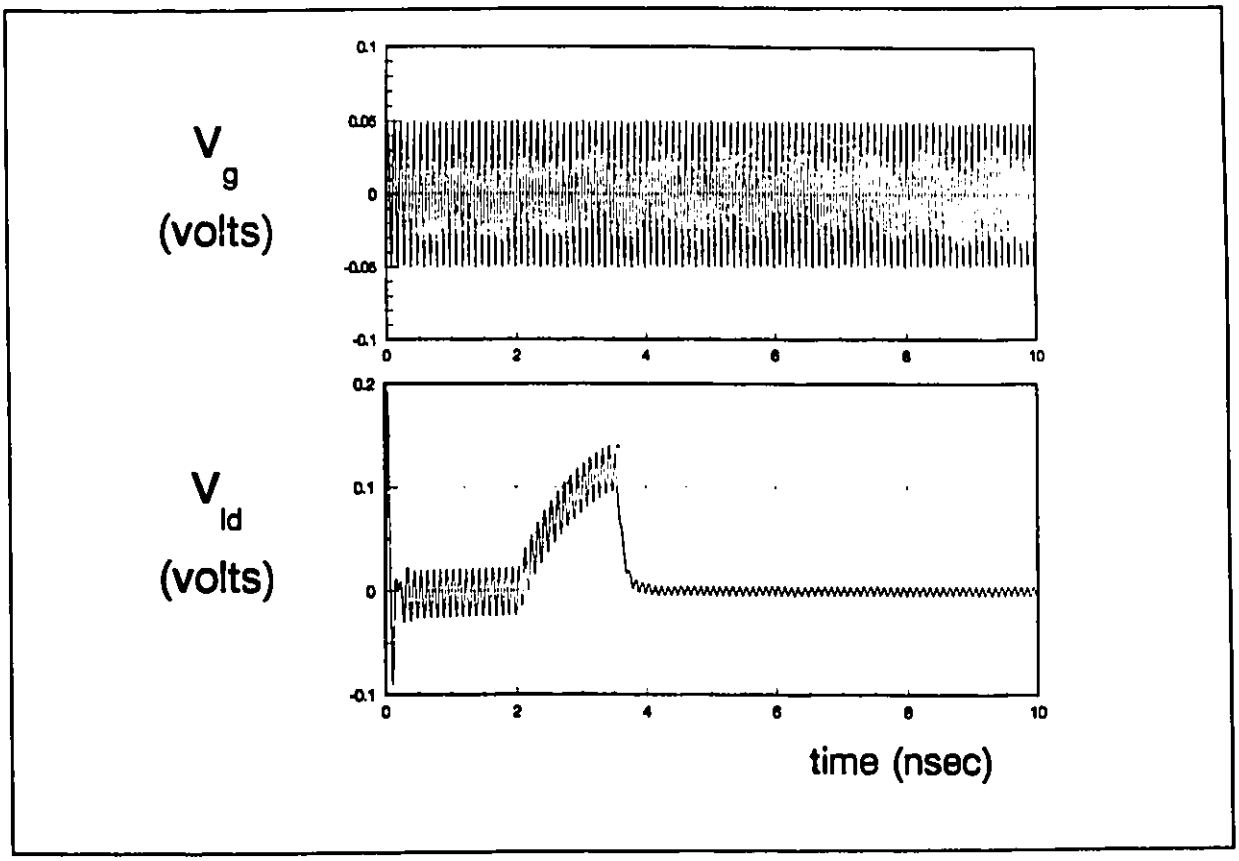

Fig.5-10 Transient response of diode switch. V_g is the generator voltage and V_{ld} is the voltage across the load admittance, G_{ld}, as defined in Fig.5-8a.

in the linear region for $V_{ds} < V_{sat}$, where the constants (for a 0.6 μm Hughes MESFET [50]) are given by

$$I_{dss} = 496 \text{ mA}$$

$$V_{po} = -5.28 \text{ volts}$$

$$c = 4.52$$

$$V_{sat} = 1.85 \text{ volts}$$

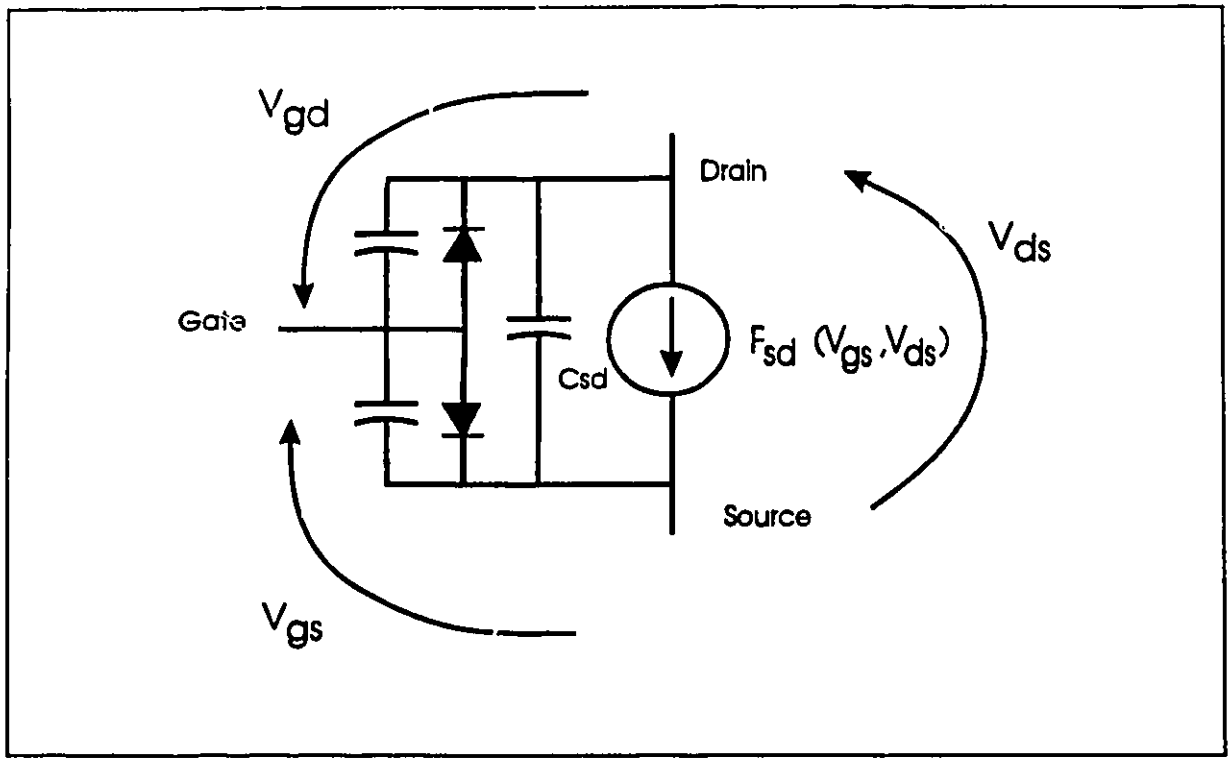

Fig. 5-11 Simplified equivalent circuit of a MESFET

In the saturated region where $V_{ds} > V_{sat}$, a correction factor of

$$\left(V_d \frac{g_o}{V_s - V_g}\right)^q$$

is subtracted from the quantity in Eq. 5-4 where

$V_s = 2.23$ volts

$q = 2.56$

$g_o = 0.279$

This factor models the negative resistance observed in typical MESFETs. The I-V curves of this MESFET model are given in Fig. 5-12.

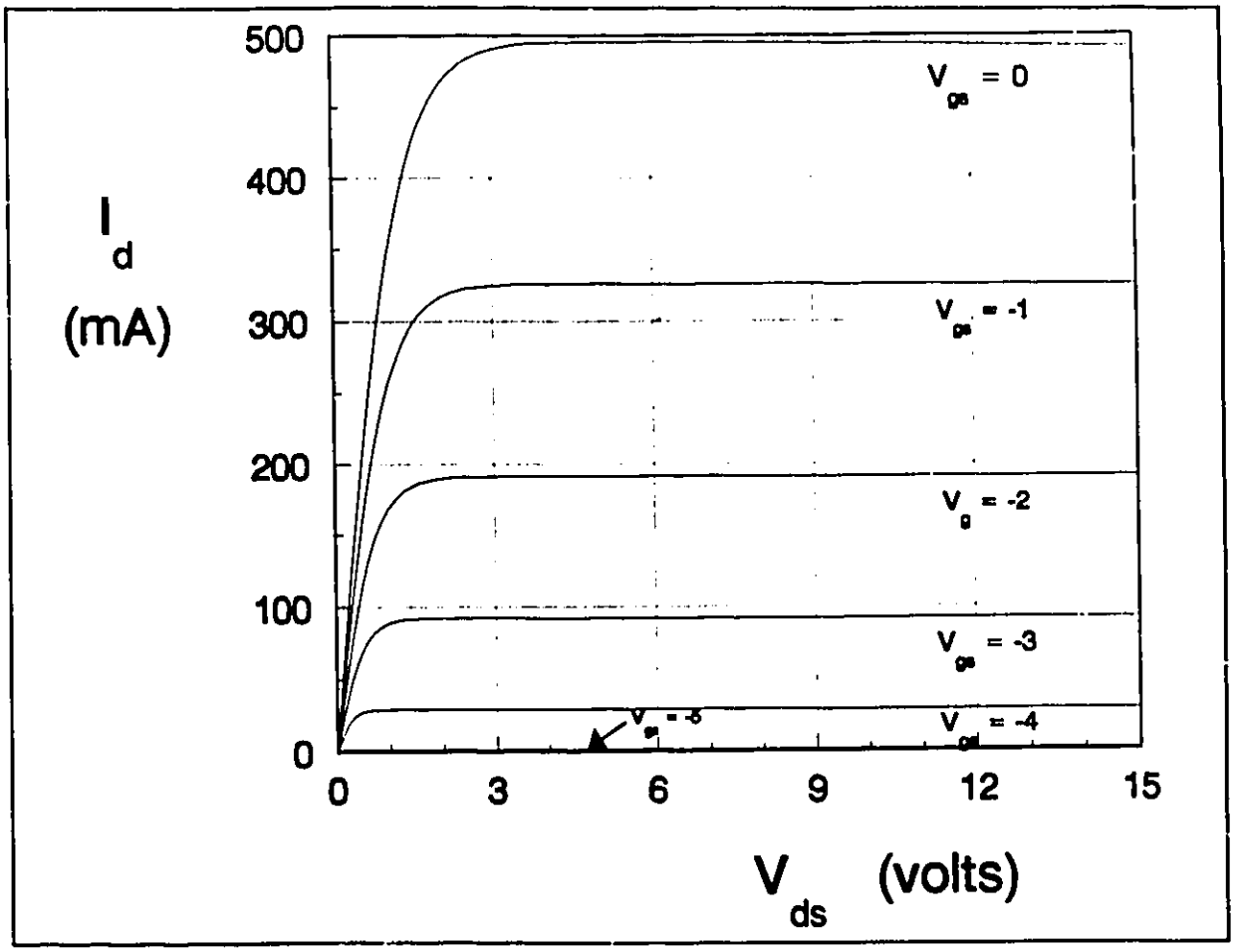

Fig. 5-12 I-V curves for the MESFET model described by Eq.5-4 and Eq.5-5 for various values of V_{gs}.

5.4.2 Example of a MESFET Gain Stage

In this section an example of a simple single-FET gain stage device connected with striplines is shown in Fig. 5-13a with the half node simulation given in Fig. 5-13b. For the present a 1-D line is assumed. The device equivalent circuit is shown in Fig. 5-14. Note that there are two distinct "grounds" indicated in Fig. 5-14, the device and the half-node ground. In general these are not connected, however, for the half-node configuration in Fig. 5-13b, where N_y is 1, these grounds are the same.

The response of this circuit to a 400-mV, 10-GHz pulse is shown in Fig. 5-15. The pulse starts at 0.5 nsec and ends at 2.5 nsec. For this example Δt is again 1 ps such that the period of the carrier frequency of the excitation pulse is 100 Δt. Note the gain of about 3 dB which is typical for a MESFET connected to unmatched 50 ohm loads.

Next consider a 2D simulation of the stripline FET amplifier with the node layout as shown in Fig. 5-16. The stripline consists of a conductor strip that is modelled by a string of edge nodes. The source of the FET is attached to a short ground strip simulated by half, edge and corner nodes. The purpose of this example is to demonstrate how a multi-port device, integrated with a network of conductor strips can be simulated. As shown in Fig. 5-16, two new ports, "3" and "4", are added. These are combined and attached to the source of the FET. The ports "5" and "6" of nodes 1 and 2 respectively are terminated as if there was an open circuit between ports 3 and 5, and ports 4 and 6. Hence the symmetric voltage passes unimpeded between port pairs 3,5 and 4,6 but the anti-symmetric voltages from ports 5 and 6 are reflected with a reflection coefficient of 1.

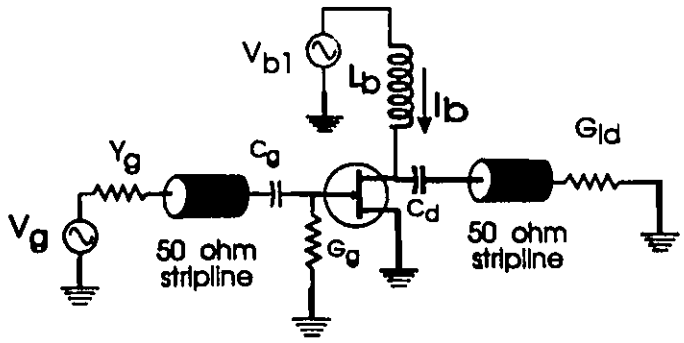

a) FET gain stage circuit model

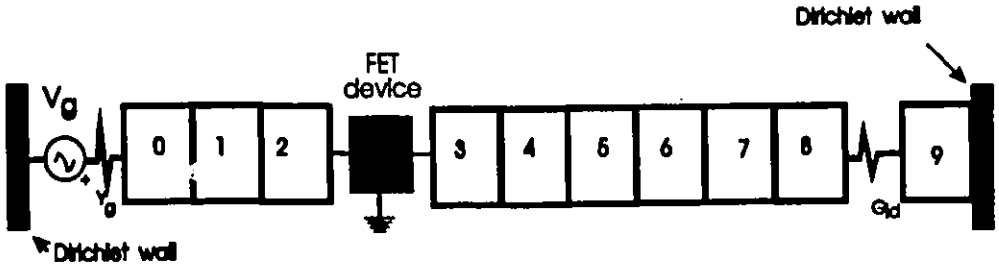

b) Half node simulation

Fig. 5-13 TLM simulation of a FET gain stage, with the FET embedded into a 1D stripline simulated by half-nodes. a) FET gain stage circuit. b) configuration of half-nodes interfaced to FET

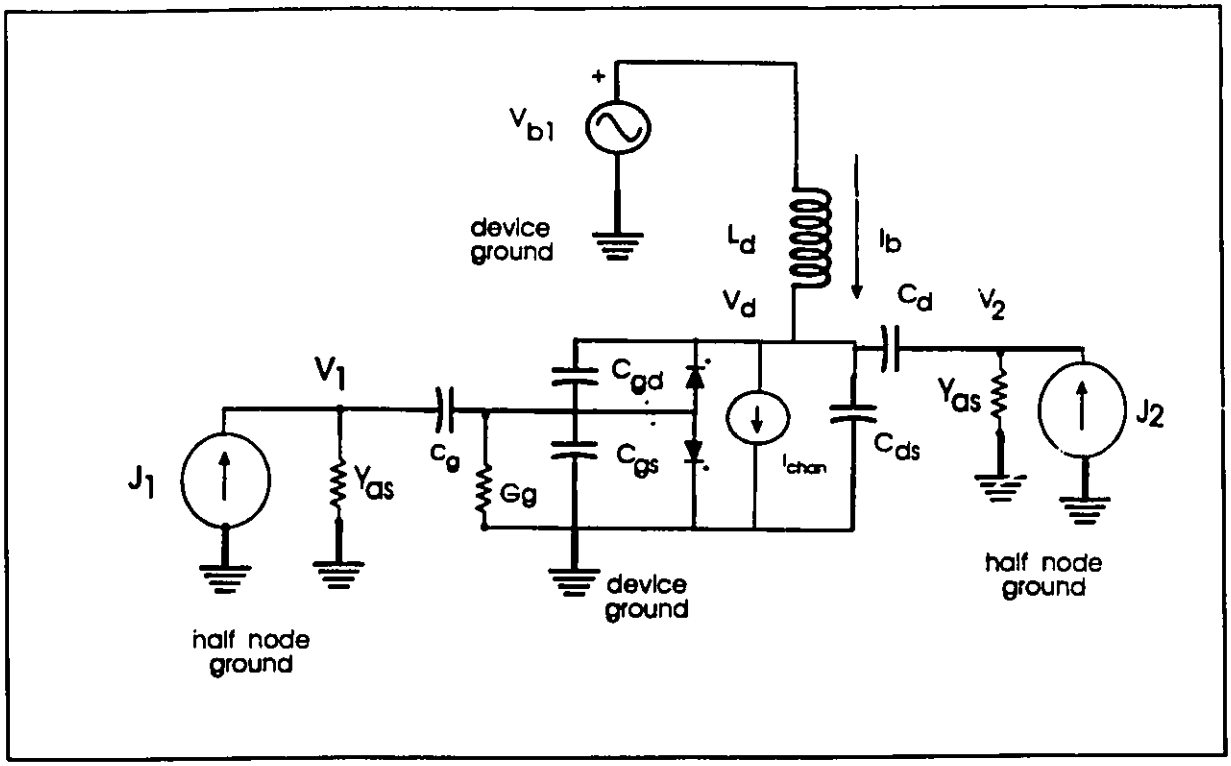

Fig. 5-14 Equivalent circuit of MESFET gain stage as used in the PWL algorithm.

The equivalent device circuit to be solved by PWL algorithm is now altered as shown in Fig. 5-17. The equivalent current sources J_3 and J_4 are given by

$$J_3 = 2\, Y_{as}\, V'_{as3} \qquad (5\text{-}6a)$$

$$J_4 = 2\, Y_{as}\, V'_{as4} \qquad (5\text{-}6b)$$

Fig. 5-18 shows the resulting drain voltage (V_d) response of the 2D FET circuit. Comparing with Fig. 5-15, there are small differences which are a result of the inductance and delay caused by the finite length of the source ground connection.

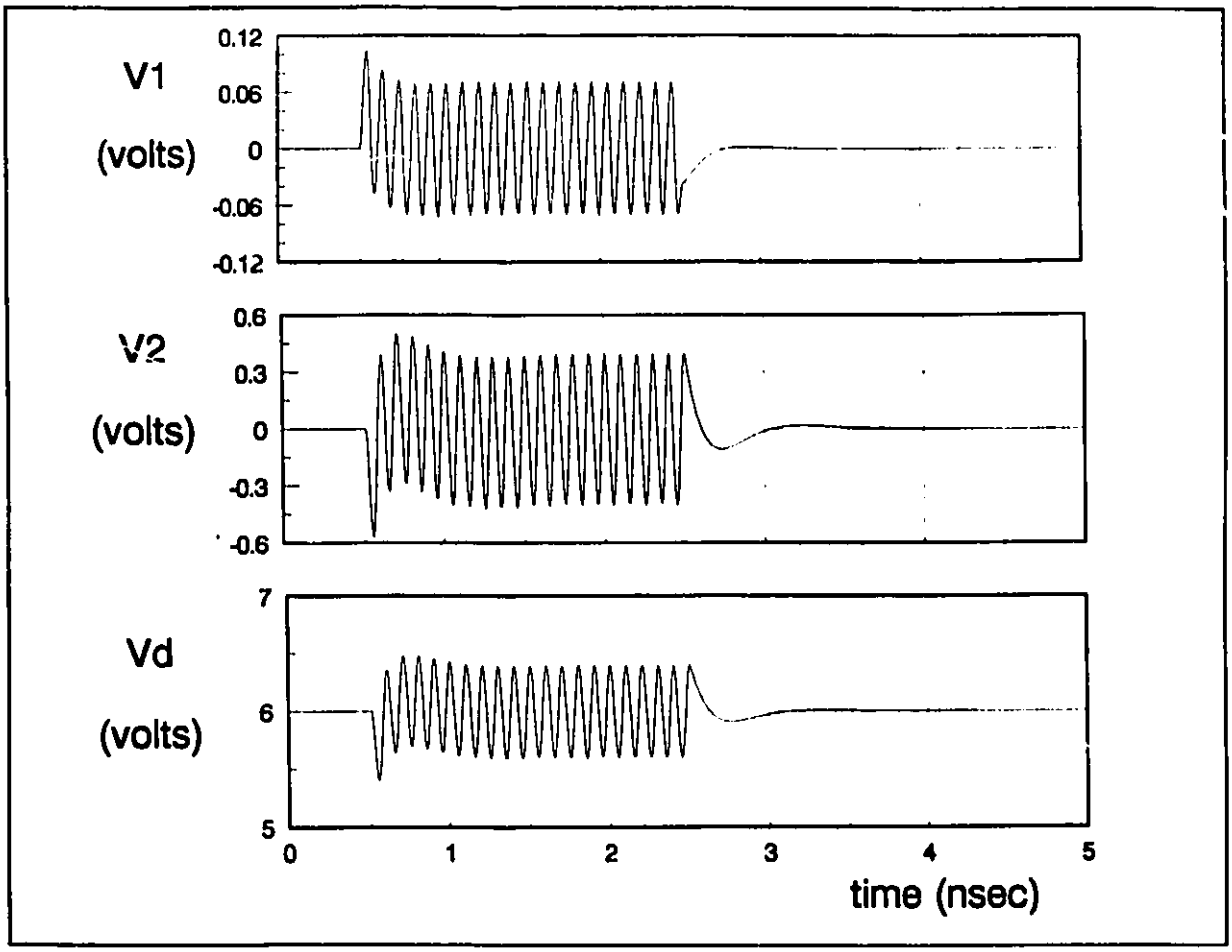

Fig. 5-15 Transient response of simulated FET gain stage to an RF pulse excitation. V_1, V_2 and V_d are defined in Fig.5-14.

Results for a very short source ground length are given here to demonstrate that the conductor strip nodes can model ground connections without introducing extraneous behaviour.

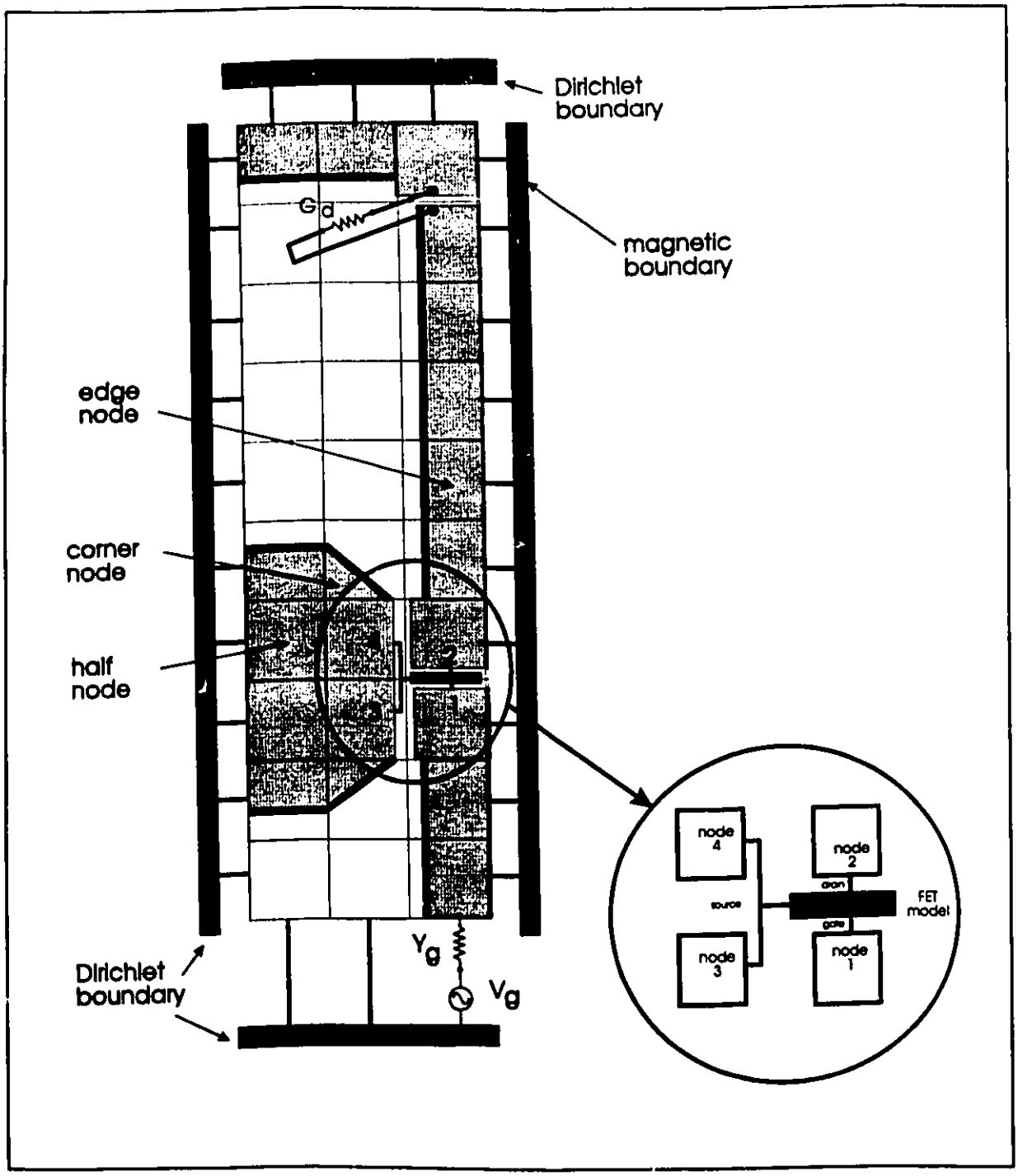

Fig. 5-16 Configuration of conductor strip nodes for 2D FET gain stage simulation. The source of the FET is grounded through the ground strap shown via ports 3 and 4.

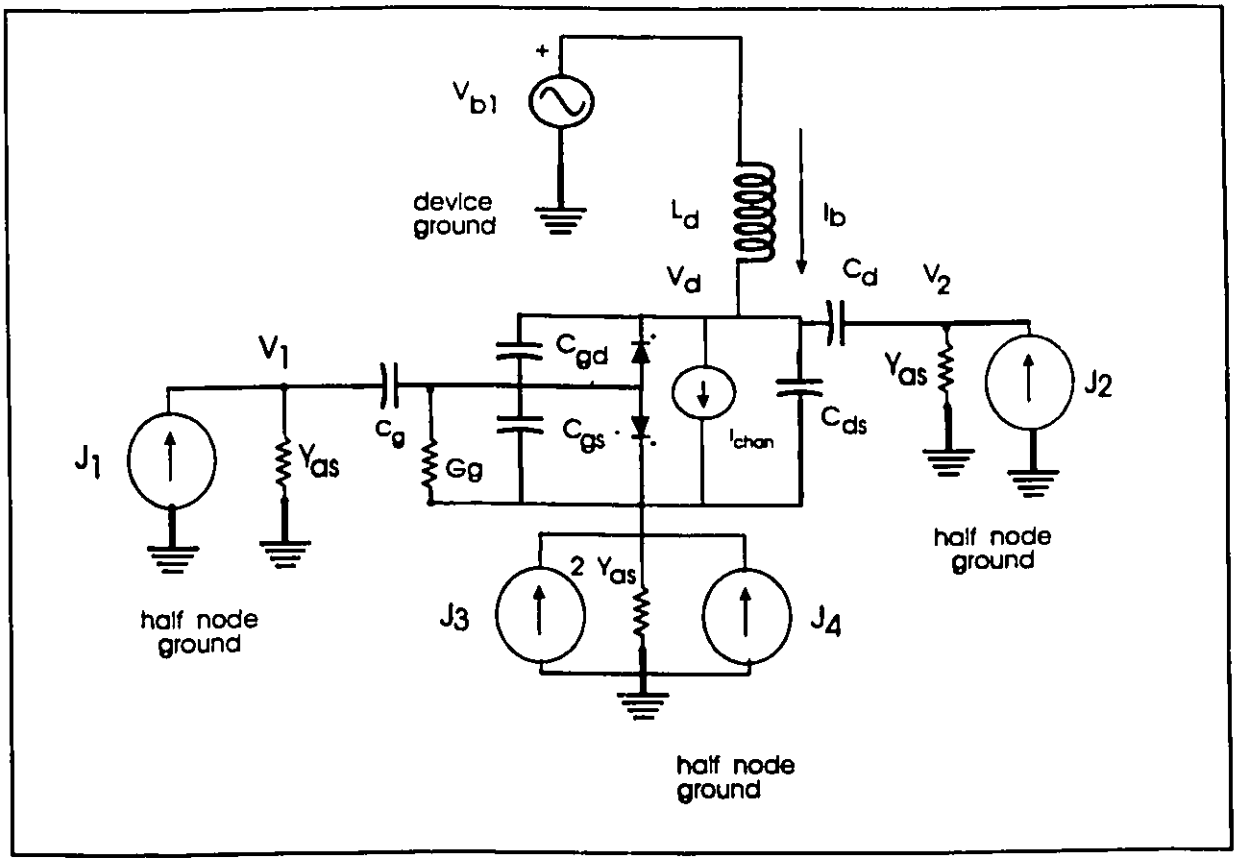

Fig. 5-17 Equivalent circuit of the MESFET gain stage device with ports 3 and 4 connected to the source ground strap.

5.4.3 Model of a distributed MESFET

Presently, MMIC amplifiers capable of generating more than 20 Watts of output RF power are being developed. A design problem, which to some extent limits obtained MMIC performance, is that power MESFETs are not well modelled. One reason for this is that they are physically large and cannot be considered as lumped devices at microwave frequencies. A possible application of the TLM method is to simulate large distributed MESFETs such that more accurate circuit

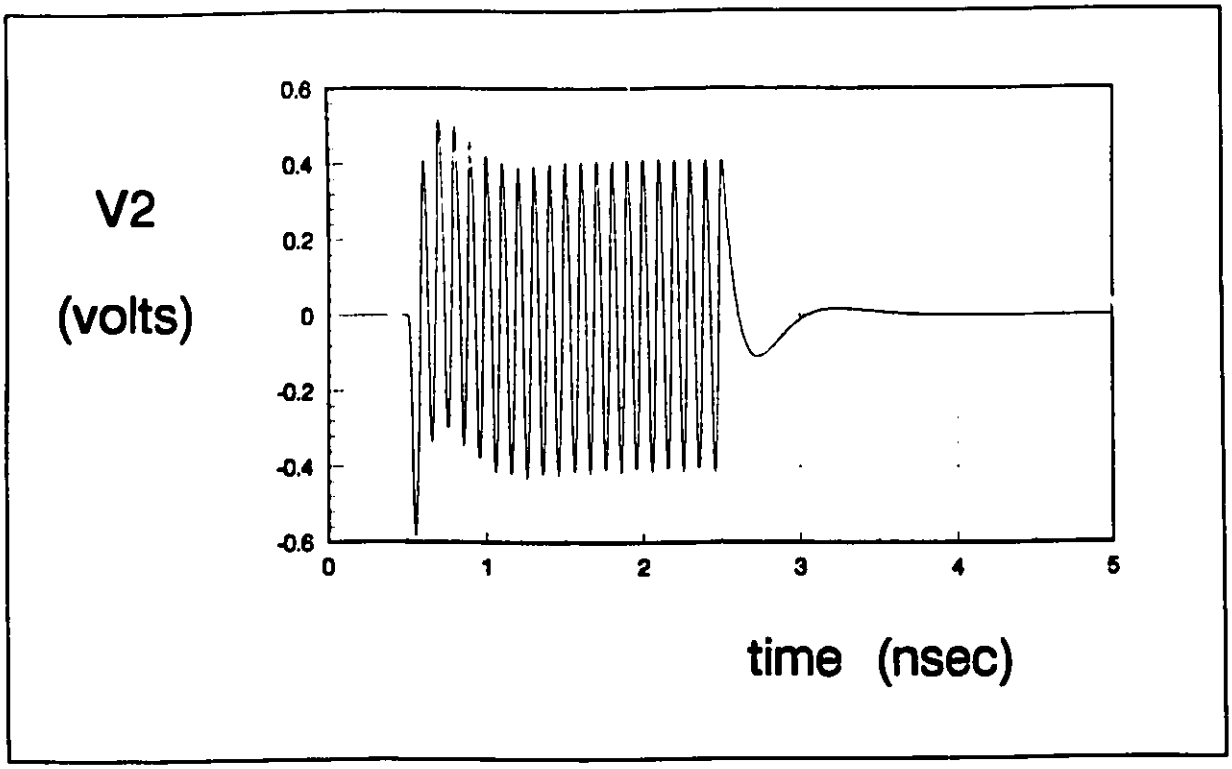

Fig. 5-18 Transient response of 2D MESFET gain stage where V_2 is defined in Fig.5-17.

modelling is possible.

In this section an example will be given of a simple distributed MESFET model consisting of three lumped MESFETs in parallel. The arrangement of these MESFETs and the connected half-nodes is shown in Fig. 5-19a. The distributed gate finger is modelled as a network of lumped inductors, resistors and capacitors as shown. The complete conductor strip node layout is given in Fig. 5-19b. The individual MESFETs are identical to the MESFET model in Section 5.4.1.

One interesting feature of this model is that the gate conductor strip is modelled by lumped components since it is so narrow that using TLM simulation would require a very fine localized mesh that would be complicated to implement.

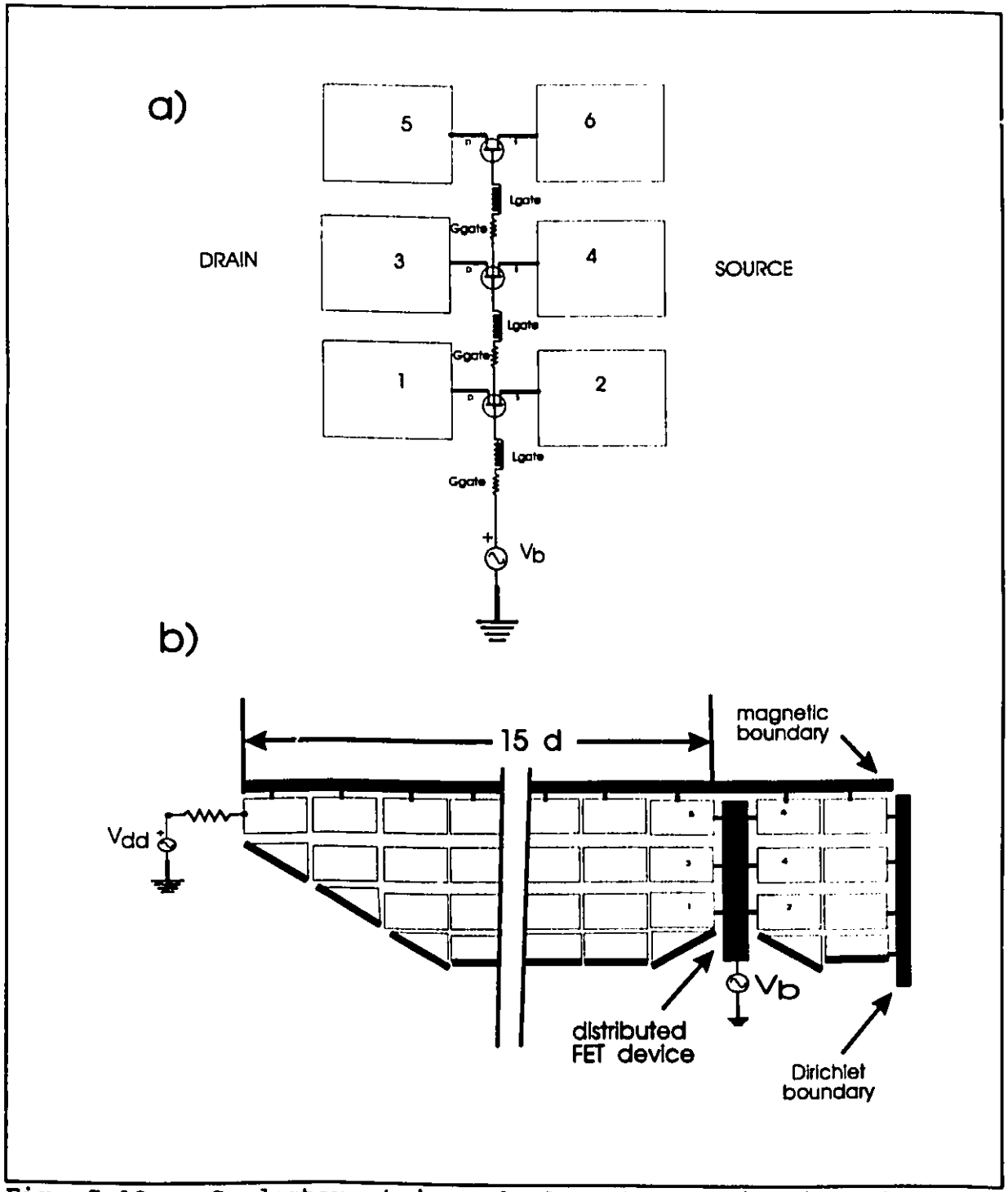

Fig. 5-19 Conductor strip node layout for distributed MESFET model. a) Schematic of distributed MESFET modelled by three MESFET's in parallel. b) Configuration of conductor strip nodes modelling stripline connection to the simulated MESFET drain.

Given a relatively coarse mesh, the gate conductor strip is more accurately modelled using a network of lumped components. This requires considerably less computational effort. In general, computationally efficient distributed models will be a mixture of TLM nodes and a network of lumped elements.

Fig. 5-20 shows the resulting turn-on transient of the distributed FET device. The gate bias voltage, V_{b1}, is governed by the relation

$$V_{b1} = -4.9 + 4.9\left(.5 + .5 \tanh\left(\frac{time-1500}{100}\right)\right) \quad volts \qquad (5\text{-}7)$$

such that the gate is initially at -4.9 volts pinching the FET channel off, and is switched to 0 volts at about 1.5 nsec. The drain voltage, V_{dd}, is shown in Fig. 5-20a as being originally at 0 volts and then switched to 5 volts at 0.5 nsec. A plot of the overall drain current injected by the generator is shown in Fig. 5-20b. The oscillations observed are due to the inductance and capacitance of the drain conductor strip. Fig. 5-20c shows the drain current in the middle FET. The value is about a third of the total drain current as expected. Note the oscillations in the drain current sunk by the individual FETs is very small since the FETs are operating in the saturated region.

For the example in Fig. 5-20, the gate resistances shown in Fig. 5-19a were taken to be 0.5 ohm. If this resistance is reduced to zero, then the circuit became unstable as shown by the corresponding plot of the drain current of the middle MESFET plotted in Fig. 5-21. This instability is physical, resulting from the feedback between the gate and the drain circuits. It is not a result of the instability of the TLM node mesh. This example demonstrates an application of the TLM method to model power FETs for determining internal stability problems.

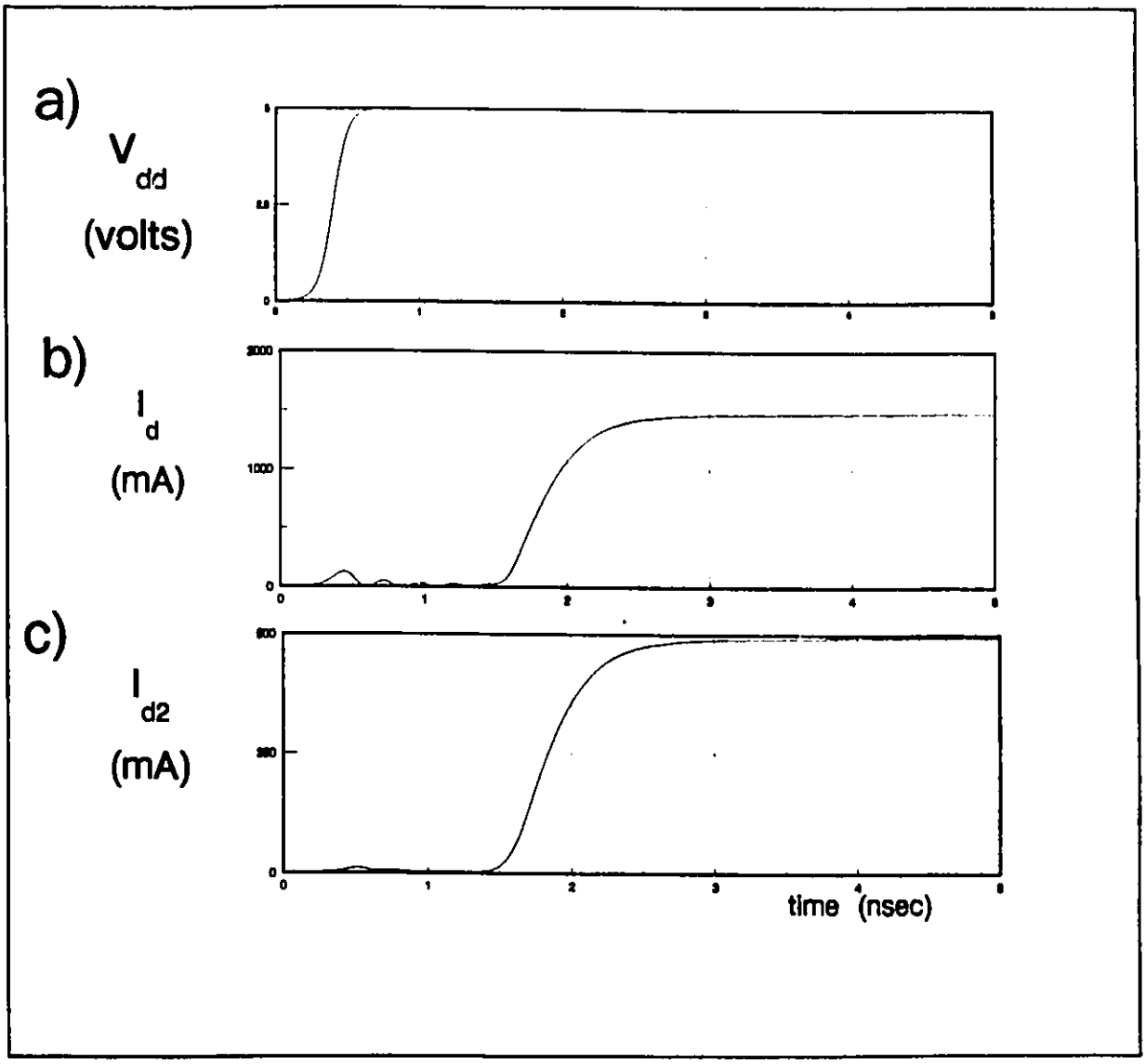

Fig. 5-20 Transient response of distributed MESFET model. V_{dd} is the drain bias voltage, I_d is the total drain current and I_{d2} is the drain current of the middle MESFET.

5.5 3D DIODE SWITCH MODEL

In this final example, a simple stripline diode switch is modelled by a 3D TLM simulation. The purpose of this example is to demonstrate the capability of modelling circuits in 3D and to compare the simulated circuit behaviour with

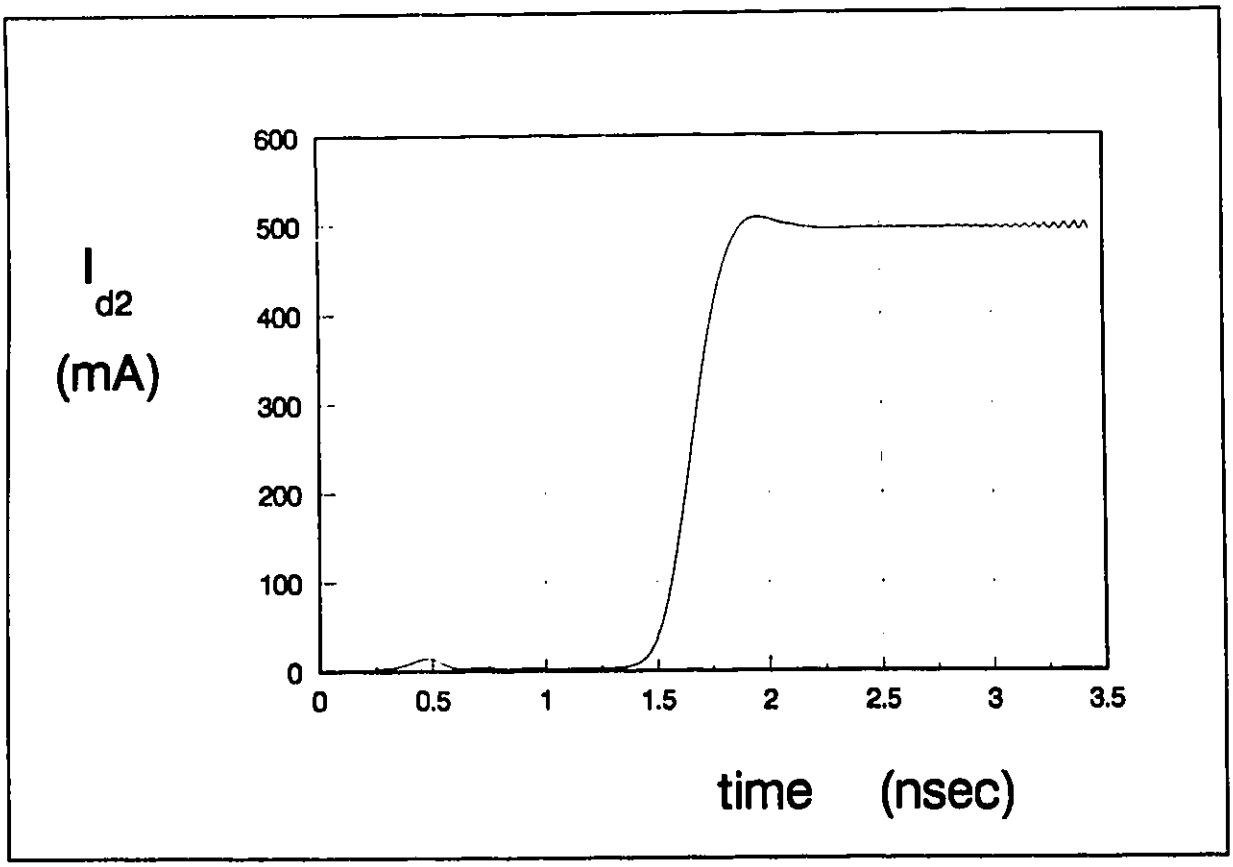

Fig. 5-21 Unstable behaviour of distributed MESFET model when the gate resistance is reduced to zero. Plotted is the drain current of the middle MESFET.

experimental measurements.

A sketch of the switch circuit is shown in Fig. 5-22. The overall 3D TLM mesh volume of 30 x 5 x 30 is sketched in Fig. 5-22a showing the plane of the stripline circuit at y=2.5d. Fig. 5-22b shows the layout of the stripline circuit. Note that due to circuit symmetry, only half the circuit is modelled, bounded by magnetic wall indicated at x=15d. Fig. 5-22c shows the details of the connection of the switch diode to the conductor strip nodes. The RF signal generator, V_g, and a bias voltage generator, V_b, are placed in series as shown. V_b is used to bias the diodes off and on. It is not uncoupled from the signal

generator and load resistor with coupling capacitors as in the example presented in Section 5.3. The reason for this simplification is that the primary objective is to compare simulated and experimental measurements and not to design a practical switch.

In the experimental switch, Alpha beam lead Schottky diodes (DMJ6784) were used. The equivalent circuit of this diode is given in Fig. 5-23a. Here C_p is a packaging capacitance of about 0.1 pF. G_{ser} is a series conductance of about .14 mho which is due to the finite conductivity of the ohmic contacts in the device. L_{ser} is the accumulated inductance of the external conductor leads which is approximately 0.1 nH. Finally C_{dep} is the depletion capacitance of the device which is related to the charge on the capacitor, Q_{dep}, and the voltage across it, denoted by V_{dep}, by the following expressions [51]

$$Q_{dep} = -2\, C_{jo}\, V_{bj} \left(1 - \frac{V_{dep}}{V_{bj}}\right)^{\frac{1}{2}} \qquad (5\text{-}8a)$$

$$C_{dep} = \frac{C_{jo}}{\left(1 - \frac{V_{dep}}{V_{bj}}\right)^{\frac{1}{2}}} \qquad (5\text{-}8b)$$

where C_{jo} is about 0.4 pF and V_{bj} is the built in junction voltage of about 0.7 volts. In the equivalent circuit of Fig. 5-23,

$$V_{dep} = V_3 - V_1$$

Since the depletion capacitance is variable, it cannot be taken into account as a regular capacitor. Updating the value at each time step can lead to inaccuracies and numerical instabilities. A better method is to define an

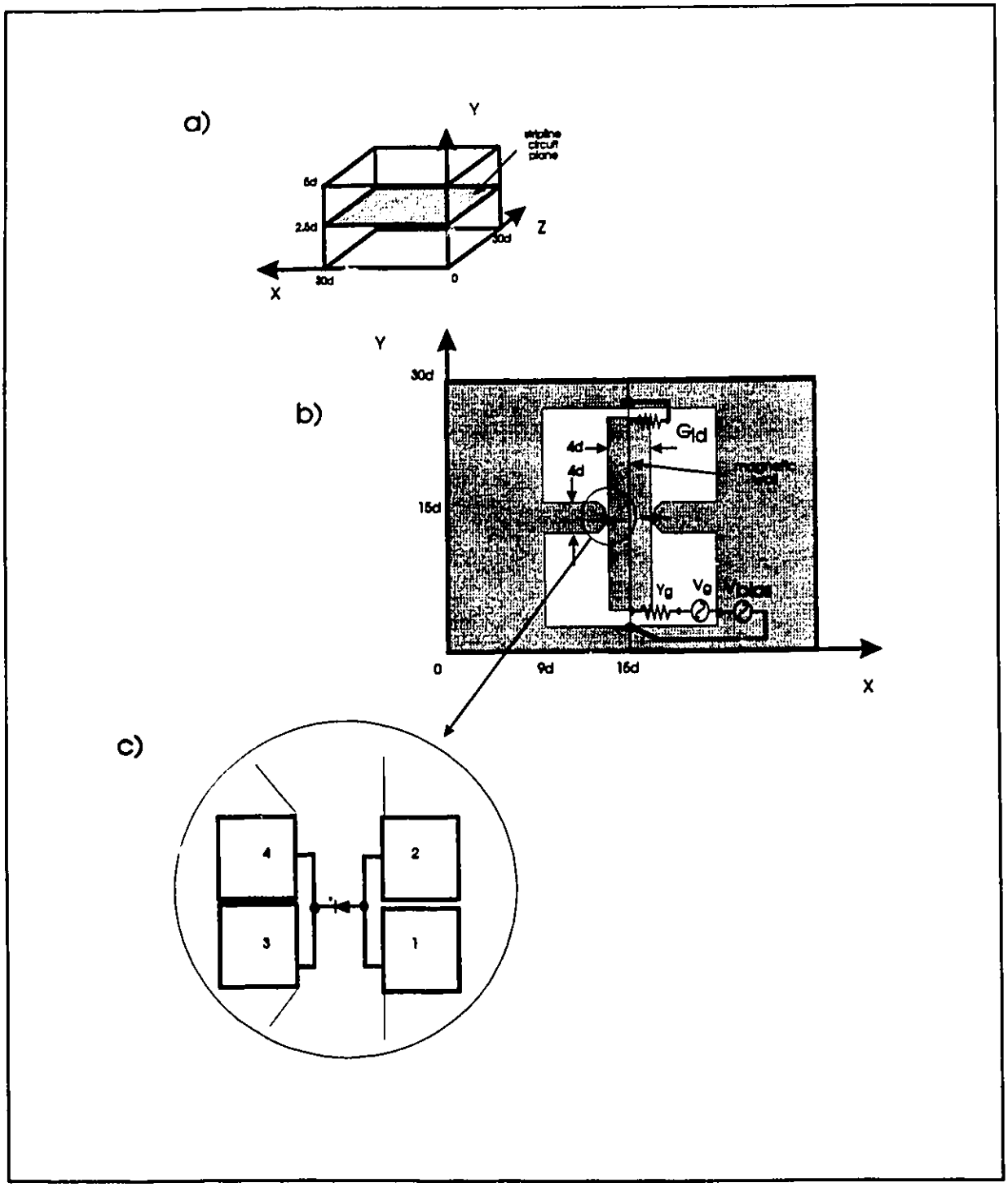

Fig. 5-22 3D simulation of diode stripline switch circuit. a) Overall TLM mesh dimensions, b) layout of switch circuit, c) detail of the connection of the diode device to the half-nodes.

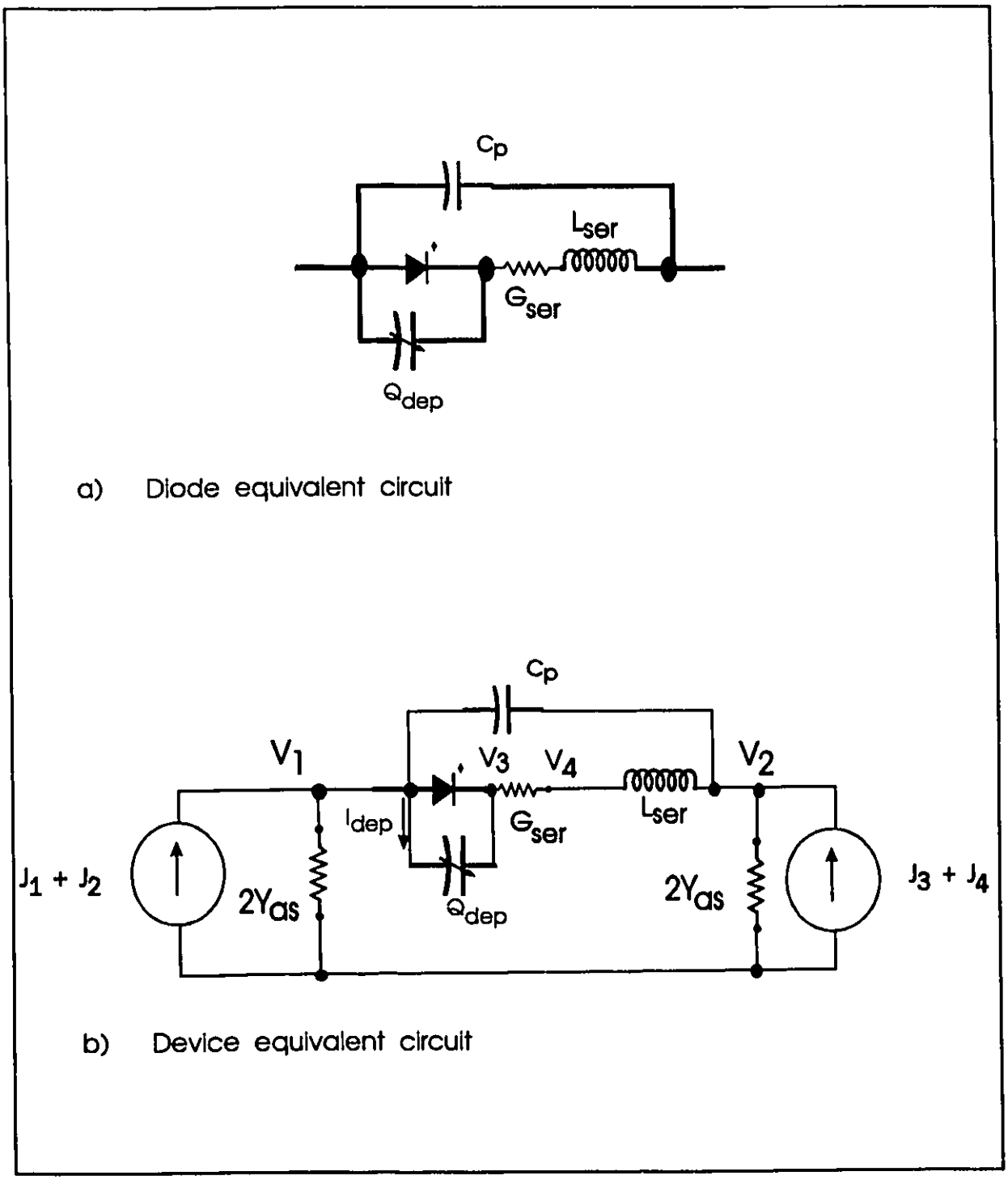

Fig. 5-23 Equivalent circuit of diode switch device, a) equivalent circuit of diode, b) overall device equivalent circuit used in PWL algorithm

additional variable, I_{dep}, as the current through the depletion capacitance. I_{dep} is related to Q_{dep} as

$$I_{dep} = \frac{\partial Q_{dep}}{\partial t} \qquad (5\text{-}9)$$

The experimental switch was constructed using two copper-backed teflon substrates that were 1.5 mm thick with a dielectric constant of ϵ_r=2.3. The stripline circuit and ground connections were fabricated according to the outline given in Fig. 5-22b and sandwiched between the two teflon substrates. Given that the substrate height was modelled by 2.5 node heights (i.e. 1.5mm = 2.5d), Δt can be evaluated as

$$\Delta t = \frac{d\sqrt{\epsilon_r}}{2c} = \frac{1.5mm\sqrt{2.3}}{2 \cdot 2.5 \cdot 2.998 \times 10^{11}\ mm/\text{sec}} .$$

As indicated in Fig. 5-22b, four ports to the conductor strip nodes are combined in pairs and connected to the diode device. This is reflected in the equivalent current generators of Fig. 5-23b.

Fig. 5-24 shows the switching transient of the diode switch. Fig. 5-24a shows the bias voltage, V_b, as it is changed from -5 volts to 5 volts in 2 volt steps. The generator, V_g, produces a sinusoidal signal of 0.5 volts peak at 2.5 GHz. The output voltage across the load resistor, G_{1d}, is shown in Fig. 5-24b. The bias voltage component is "clamped" by the diode as expected. Also, note the attenuation of the 2.5 GHz signal as the diode is switched on.

Fig. 5-25 shows the S_{21} parameter of the diode switch as a function of the bias voltage, V_b. Experimental results are also shown for comparison as measured on an HP8510 network analyzer. As observed the simulation is reasonably accurate

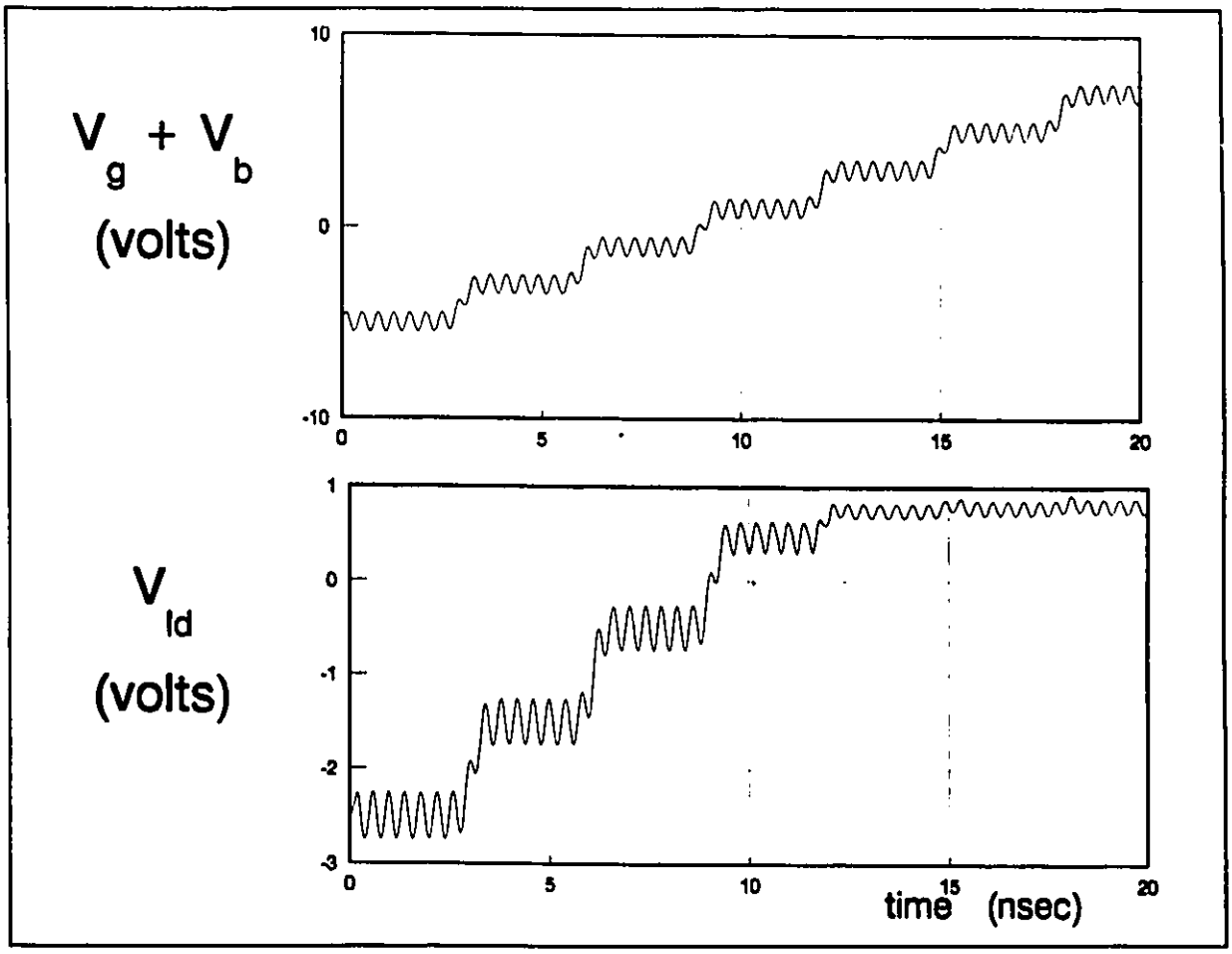

Fig. 5-24 Response of the diode switch to a multi-step change in the bias voltage, V_b. V_g is the RF generator voltage (.5 volts peak at 2.5 GHz), V_{ld} is the voltage across the load resistor.

and can be considered within experimental error.

5.6 PRESENCE OF SPURIOUS MODES IN TLM SIMULATION

The TLMS program contains a two-dimensional spatial DFT located in a x-z plane above the conductor strip plane. The purpose of this DFT is to estimate the percentage of the field energy that is contained in spurious modes. This

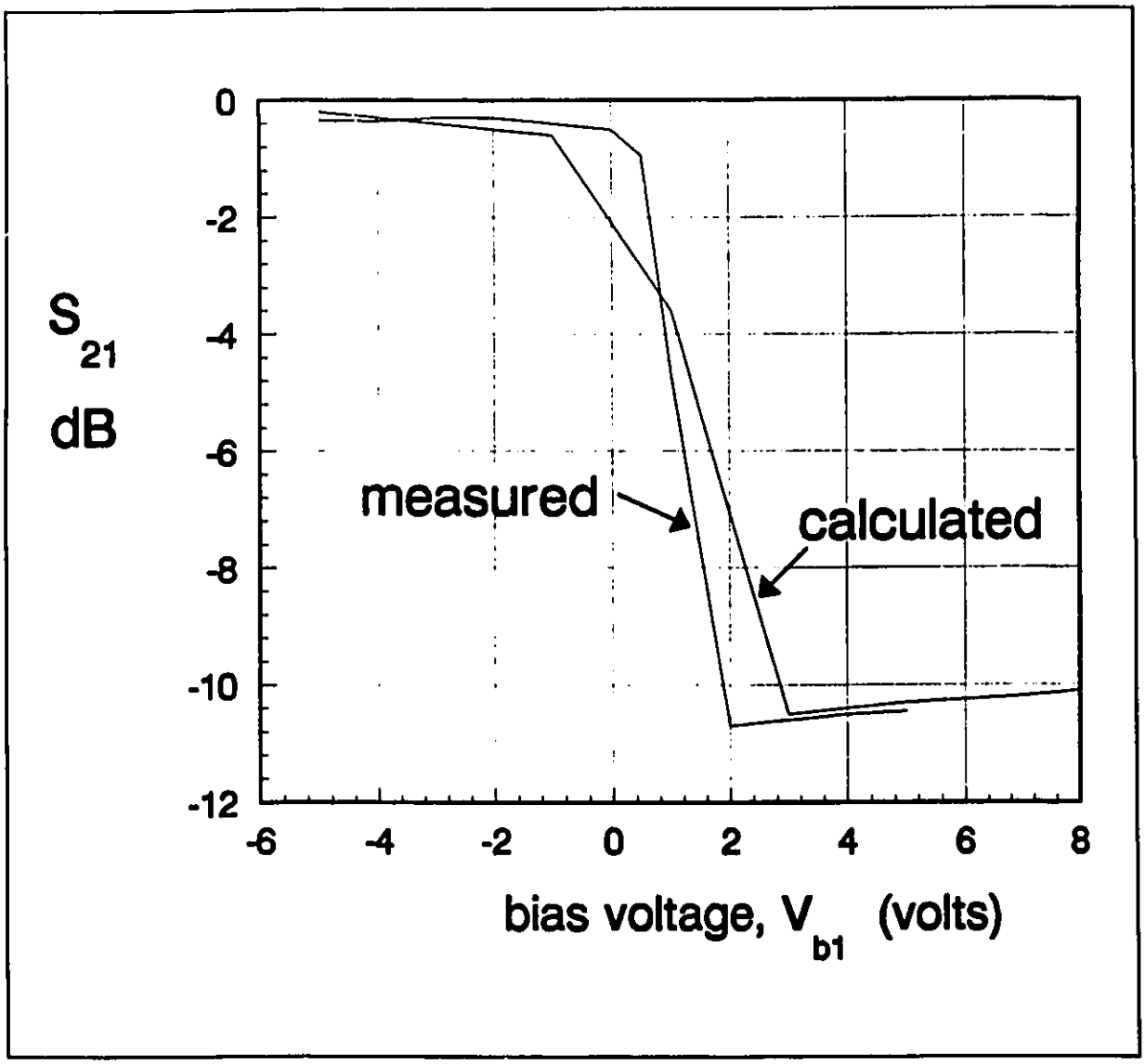

Fig. 5-25 Small signal S_{21} parameter of stripline diode switch as a function of bias voltage, V_b. A comparison of simulated and measured results is shown.

analysis has revealed that while the percentage of the field energy contained in spurious modes is high, most of this energy is in highly attenuating evanescent modes. Typically less than 2% is contained in propagating spurious modes.

As a typical example, the microstrip line in Fig. 5-26 was analyzed. The TLM box dimensions are shown in Fig. 5-26a and the layout of the conductor strip

nodes is given in Fig. 5-26b. Also indicated in Fig. 5-26a is the plane in which the percentage of the field energy contained in spurious modes was estimated. The percentage was calculated by first evaluating the modal field composition of the x and z directed voltages incident into the fourth node layer. Each mode is associated with a $k_x d$ and $k_z d$ constant. If the sum of $k_x d$ and $k_z d$ is greater than π, then the mode is spurious as discussed in Section 2.6. If

$$(k_o d)^2 > (\pi - k_x d)^2 + (\pi - k_z d)^2 \qquad (5\text{-}10)$$

where k_o corresponds to the maximum excitation frequency, the mode is a propagating spurious mode as discussed in Section 2.6. In this example, a 10 GHz sinusoidal excitation signal was used and Δt was 1 psec as before. In this case k_o was chosen to correspond to 12 GHz to ensure that all the components associated with 10 GHz were included.

Fig. 5-27a shows the resulting estimate of the percentage of the incident field in spurious modes and Fig. 5-27b shows the percentage of the incident field contained in propagating spurious modes. As observed, about 35% of the incident field energy is contained in spurious modes while only .4% is contained in propagating spurious modes. Hence the errors resulting from the influence of propagating spurious modes should be very small.

The propagation attributes of the spurious modes have been determined for the regular TLM condensed nodes. However, as spurious modes of conductor strip nodes have not yet been analyzed, it is not obvious how spurious modes interact with devices embedded in the half-nodes. A detailed study is required to determine how the spurious modes affect the coupling and driving point impedances of devices interconnected with half-nodes. At this stage only a few observations can be made.

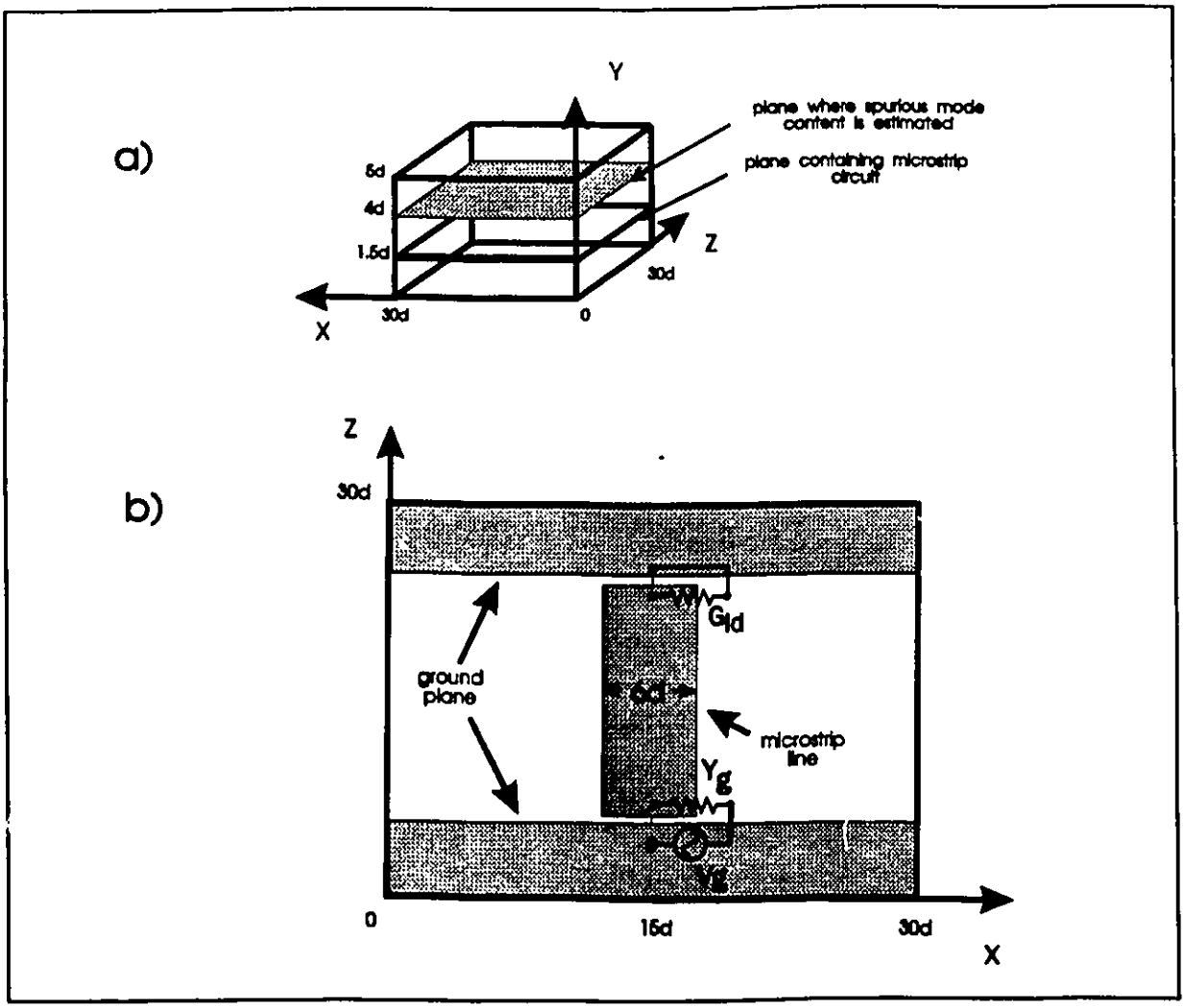

Fig. 5-26 Configuration used for the estimation of spurious mode content. a) 3D TLM mesh indicating microstrip circuit plane and plane where spurious mode content is estimated, b) microstrip layout

The driving point impedance, as seen by an embedded device, is related to the propagation and evanescent modes that it excites. The reactance of the driving point impedance is dependent on the reactance of the excited evanescent modes. It can be shown that the reactance of the spurious evanescent modes have the "wrong sign" with respect to the impedance of the corresponding analytical

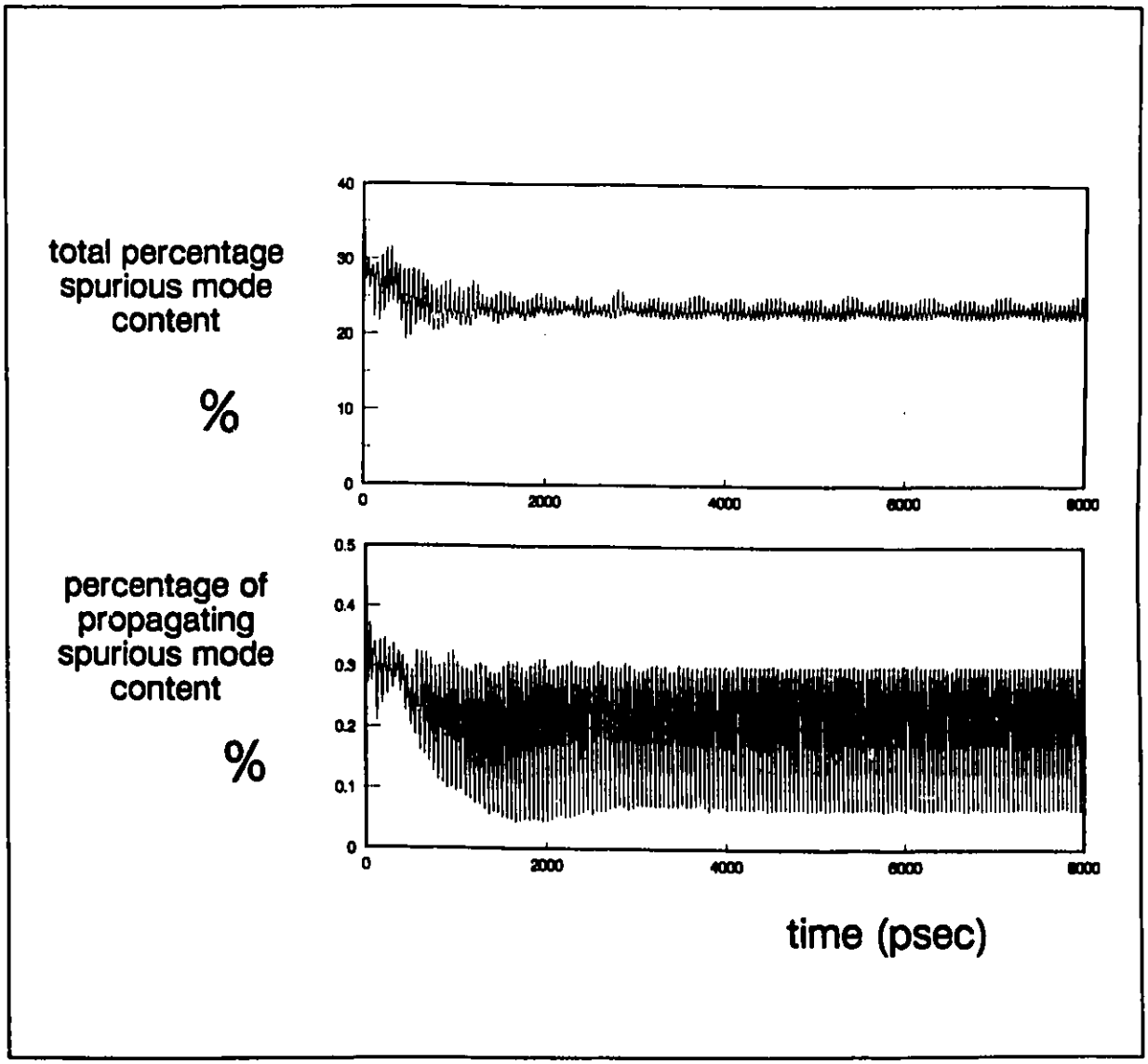

Fig. 5-27 Estimate of the percentage of energy in spurious modes showing the total spurious mode content as well as the percentage in propagating modes

solution. This will certainly have an effect on the resonance behaviour of high Q devices.

For every propagating mode in the TLM mesh, there is a corresponding spurious mode. Hence, even at very low frequencies, there is still a propagating spurious mode. As the spatial frequency of this spurious mode is approximately

1/(2d), the coupling into this mode can be significantly suppressed by distributing the devices over several nodes which, in effect, results in some spatial filtering.

In the case of devices embedded into a microstrip line, the devices are coupled by electric conduction currents and by displacement currents. At low frequencies, the coupling is essentially all electrical with no influence due to spurious modes. It is only at higher frequencies that displacement current coupling becomes relevant. This is one of the reasons that there was no noticeable influence due to spurious modes in the results in this chapter. In the above example, there was a large portion of the field energy contained in spurious modes. However, this did not noticeably affect the coupling of the generator to the load as most of the coupling was by the electrical conduction through the microstrip conductor rather than by displacement currents.

5.7 CONCLUSION

In this chapter, various examples of applications of the TLM method to solving non-linear circuit problems have been given. Although the methodology developed is geared toward a full 3D simulation it can be very powerful as a general 2D circuit simulation tool as well. By choosing the appropriate admittance values for Y_o and Y_{oo}, planar 2D circuits can be modelled accurately provided that there is no field variation in the y direction. An example of 2D modelling of a varactor-tuned Gunn oscillator circuit in a waveguide cavity is given in reference [52].

The accuracy of the method has to some degree been demonstrated using, as

an example, a 3D stripline diode switch circuit. Experimental and simulated results compared favourably.

The percentage of the field energy contained in spurious modes was estimated using a 2D DFT. The results showed that for a typical microstrip problem, about 40% of the field energy is in spurious modes. However, only a small portion of the field is contained in propagating spurious modes. Consequently, while spurious modes are a source of error, the error should be negligible for microstrip type circuits.

CHAPTER 6

CONCLUSIONS

6.1 DISCUSSION

The objective of this thesis was to develop a methodology to extend the 3D TLM method such that electromagnetic structures with embedded nonlinear devices of arbitrary complexity could be analyzed. This has been accomplished through two main developments. First a new family of node structures, denoted as the "conductor strip nodes", were developed. The main objectives for developing this new node set were;

1) To improve the simulation accuracy of conductor strips over that achievable by the 3D TLM condensed node

2) To provide a direct connection between the conductor sheet simulated by the node and the embedded device.

3) To ensure compatibility between the new node set and the regular 3D TLM condensed node.

The set of conductor strip nodes met all of these objectives.

The second development goal was to combine the TLM method with the PWL algorithm. The primary advantage of the approach taken was that the integration step size could be varied dynamically resulting in an accurate algorithm that was very time efficient. Another feature was the low-pass filtering provided by the interface which made stable simulation of active embedded devices possible.

In order to demonstrate the performance of the conductor strip nodes, several simulations were performed. It was determined that in simulating planar

transmission line structures, the use of conductor strip nodes significantly improved the simulation accuracy with respect to conventional modelling using truncated Dirichlet boundaries. This was demonstrated by using a microstrip line and a half-wave stripline resonator. Another simulation was developed for an inductive strip in a waveguide with an incident TE_{10} field. The use of the conductor strip nodes improved the simulation accuracy but the improvement was not as significant as for the planar transmission lines. The reason was that the incident electric field is parallel with the strip edge of the inductive iris. The edge node, as presently configured, interacts too strongly with the tangential electric field. However, as the primary interest was to simulate planar circuits, this problem was not of major concern.

A general 3D TLM program was developed such that an arbitrarily configured microstrip circuit could be simulated with the condensed nodes and the complete family of conductor strip nodes. Several nonlinear circuits were investigated including a detector, switch, amplifier and a distributed FET. A diode switch circuit was experimentally constructed that was compatible with the parameters used in the TLM simulation of the circuit. The experimental unit was characterized using an HP8510 network analyzer. It was determined that there was good agreement between the measured and simulated scattering parameters.

To support the main developments outlined above, a detailed analysis of the propagation properties of the 2D and 3D TLM mesh was made. The objective was to determine any instabilities that may occur, due to numerical dispersion of the TLM mesh, when nonlinear active devices are embedded into the mesh. The general dispersion relations were determined for the shunt and series 2D nodes, the expanded 3D node and the condensed node. Various interesting insights were gained through this activity.

A comparison of the derived dispersion relations showed that the condensed node had better dispersion characteristics than the expanded TLM node or Yee's leap-frog 3D FD-TD algorithm.

Detailed analysis of the dispersion relation for the condensed node led to the discovery of spurious mode excitation and propagation. It was found that the condensed node supports spurious modes that propagate without loss which results in some errors. Most of the spurious modes are evanescent and do not influence the field solution significantly. The reason spurious modes were not identified before is that the field components of the condensed node are generally based on an average summation of four port voltages which almost eliminates the spurious mode contribution.

The FD-TD equivalent of the condensed node was determined to show the relation between the scattering matrix of the condensed node and Maxwell's equations. This also showed the origin of the spurious modes as being a confusion in the mesh between modes of low and high spatial frequencies. This is believed to be due to the symmetry of the node.

A routine was added to the general 3D TLM program to calculate the percentage of energy contained in spurious modes for a variety of problems. In typical problems, there was generally less than 2% of the field energy contained in propagating spurious modes. The conclusion that can be drawn from this is that while spurious modes are an unfortunate by-product of the condensed node, the errors introduced by spurious mode propagation are generally small, provided that the discontinuities and excitation sources do not couple strongly into the spurious modes.

The eigen-matrix equation which was used to provide the dispersion equation also provided eigenvectors of the incident voltage vector of the TLM condensed

node. These could be used to determine the simulated field quantities for a given waveguide mode excitation. Also the impedance of the simulated mode could be determined. This has applications in providing exact absorbing boundaries at a given frequency. Also a scattering parameter extraction method was developed based on the knowledge of the exact simulated mode impedance.

7.2 Future Research

The main obstacles facing the condensed node TLM method as a means for analyzing practical circuits with nonlinearites are computational efficiency and the proliferation of errors as a result of spurious modes. In developing the algorithms required for this research, emphasis was placed on obtaining accurate simulation fidelity rather than generating computationally efficient code.

A graded mesh has been implemented into the 3D TLM electromagnetic field simulator program by So and Hoefer [53]. Graded mesh conductor strip nodes should be developed such that a higher density of nodes can be placed at strip edges where the field quantities and currents are the highest and exhibit large non-uniformities. This can be implemented by including series stubs into the conductor strip nodes along with the shunt stubs. Another requirement for more computationally efficient code is to streamline the scattering update procedure of the conductor strip nodes as was done for the regular condensed node [54].

There are a number of means of suppressing the spurious modes which need to be looked at. The most obvious is using 3D low pass spatial filtering which was suggested in Chapter 2. While this does provide some attenuation of spurious modes it does not eliminate them. Also, merely absorbing the spurious modes in

a spatial filter does not produce the correct field distribution, nor does it correct the driving point impedance of the source or discontinuity that originally excites the spurious modes.

A possibility for eliminating the spurious modes is to use the FD-TD version of the condensed node developed in Section 2.7. Terms in the FD-TD recursion equations were identified that result in the type of spurious modes observed. If these terms are removed, then the node will lose its symmetry and will not support the present type of spurious modes. However, it is necessary to determine the overall dispersion equation of this new FD-TD node to establish whether other types of spurious modes are generated.

7. REFERENCES

[1] R.F. Harrington "Matrix Methods for Field Problems", Proceedings of the IEEE, Feb.1967, Vol. 55, No.2, pp. 136-149

[2] M. Ney "Method of Moments as Applied to Electromagnetic Problems", IEEE MTT, Vol. MTT-33, No.10, pp.972-980, Oct.1985

[3] P.L.Arlett, A.K. Bahrani, O.C.Zienkiewicz "Application of Finite Elements to the Solution of Helmholz's Equation", Proc. IEE, Vol.115, No.12, pp.1762-1766, Dec.1968

[4] A. Wexler "Solution of Waveguide Discontinuities by Modal Analysis", IEEE MTT, Vol.MTT-15, No.9, pp.508-517, Sept.1967

[5] S.B. Cohn "Properties of Ridge Wave Guide" Proc.IRE, Vol.35, pp.783-788, Aug.1947

[6] K. Kundert, G. Sorkin, A.Sangiovanni-Vincentelli "Applying Harmonic Balance to Almost Periodic Circuits", IEEE MTT, Vol.36, No.2, Feb.1988

[7] J.W. Bandler "Unified Framework for Harmonic Balance Simulation and Sensitivity Analysis", Trans. MTT, Dec 1988, pp.1661-1669

[8] M.J. Chien, E.S.Kuh "Solving Nonlinear Resistive Networks Using Piecewise-Linear Analysis and Simplical Subdivision", IEEE Trans. on Cir. and Sys., Vol.CAS-24, pp.305-317, June 1977

[9] J. Vlach, K. Singhal "Computer Methods for Circuit Analysis and Design", Van Nostrand Reinhold, New York, 1983

[10] J.I.Alonso, J.Borja, F.Perez "An Universal Model for Lossy and Dispersive Transmission Lines for Time Domain CAD of Circuits", IEEE MTT-S Digest 1991, pp.991-994

[11] T. Tang, M. Nakhla, R. Griffith "Analysis of Lossy Multiconductor Transmission Lines Using the Asymptotic Waveform Evaluation Technique", IEEE MTT-S Digest 1991, pp. 983-986

[12] M.S.Basel, M.Steer, P. Franzon, D. Winkelstein "High Speed Digital System Simulation using Frequency Dependent Transmission Line Network Modeling", IEEE MTT-S Digest 1991, pp. 987-990

[13] D. Winkelstein "Transient Simulation of Complex Lossy Multi-port Transmission Line Methods with Nonlinear Digital Device Termination Using a Circuit Simulator", IEEE Proceedings 1989 Southeastcon

[14] K.S. Yee "Numerical Solution of Initial Boundary Value Problems Involving Maxwell's Equations in Isotropic Media", IEEE Trans. Ant. Prop., Vol.AP-14, pp.302-307, May 1966

[15] P.B. Johns, R.L. Beule "Numerical Solution of 2-Dimensional Scattering Problems Using a Transmission Line Matrix", Proc. IEE, Vol.118, no. 9 pp. 1203-1208, Sept.1971

[16] S. Akhtarzad "Analysis of Lossy Microwave Structures and Microstrip Resonators by the TLM Method", Ph.D. Dissertation, University of Nottingham, England, July 1975

[17] P. Saguet "Analyse des Milieux Guides: la Method MTLM", Doctoral Thesis, Inst. Natl. Polytech., Grenoble, France, 1985

[18] G.E. Mariki "Analysis of Microstrip Lines on Inhomogeneous Anisotropic Substrates by the TLM Numerical Technique", Ph.D. Thesis, University of California, Los Angeles, June 1978

[19] W.J.R. Hoefer, A.Ros "Fin Line Parameters Calculated with the TLM Method," IEEE-MTT Int. Microwave Symp. Dig., pp. 341-343, Apr.1979

[20] S. Akhtarzad, P.B. Johns "Solution of 6-Component Electromagnetic Fields in Three Space Dimensions and Time by the T.L.M. method,"Electron. Lett., vol.10, pp.535-537, Dec.12,1974

[21] P.B. Johns "A Symmetrical Condensed Node for the TLM Method",IEEE MTT, Vol. MTT-35, No.4, April 1987, pp.370-377

[22] W.J.R Hoefer "The Transmission Line Method - Theory and Application", IEEE MTT, vol.MTT-33, pp.882-893, Oct.1985

[23] W.J.R. Hoefer "Thee Transmission Line Matrix (TLM) Method",Chapter 8 of T. Itoh, "Numerical Techniques for Microwave and Millimetre-Wave Passive Structures", John Wiley & Sons 1989

[24] P.B.Johns "On the Relationship Between TLM and Finite Difference methods for Maxwell's Equations", IEEE MTT, Vol.MTT-35, No.1, Jan 1987

[25] A.C. Cangellaris, C. Lin, K.K. Mei "Point-Matched Time Domain Finite Element Methods for Electromagnetic Radiation and Scattering", IEEE Trans. Ant. Prop., Vol.AP-35, No.10, Oct.1987

[26] Z. Chen, W.J.R.Hoefer, M.M.Ney "A New Finite Difference Time Domain Formulation Equivalent to the TLM Symmetrical Condensed Node", MTT-S Digest 1991

[27] P.B.Johns, O'Brien, "Use of the Transmission-Line Modelling (T.L.M.) Method to Solve Nonlinear Lumped Networks", Radio Electron. Eng., vol.50, pp. 59-70, Jan/Feb 1980

[28] S.A.Kosmopoulos, W.J.R. Hoefer, A. Gagnon "Nonlinear TLM Modelling of High-Frequency Varactor Multipliers and Halvers", International Journal of Infrared and Millimetre Waves, 1989, pp.342-352

[29] R. Voelker, R. Lomax "A Finite-Difference Transmission Line Matrix Method Incorporating a Nonlinear Device Model", IEEE MTT, Vol. MTT-38, No. 3, March 1990, pp.302-312

[30] P. Russer, P. So, W. Hoefer "Modeling of Nonlinear Active Regions in TLM", Microwave and Guided Letters, Jan. 1991, Vol.1, No.1, pp.8-10

[31] I.S.Kim "Contributions to the Time Domain-Finite Difference Method for the Modelling of Microwave Structures", Ph.D. Dissertation, University of Ottawa, 1990

[32] Eswarappa "New Developments in the Transmission Line Matrix and Finite Element Methods for Numerical Modelling of Microwave and Millimeter-wave structures", Ph.D. dissertation, University of Ottawa, 1990

[33] Z. Chen, M. Ney, W. Hoefer "Study of Absorbing Boundary Conditions in the 3D-TLM Symmetrical Condensed Node Model", MTT Symp. Digest 1992, pp.369-372

[34] P. Naylor, R. Desao "New Three Dimensional Symmetrical Condensed Lossy Node for Solution of Electromagnetic Wave Problems by TLM", Electronics Letters, March 1990, Vol.26, pp.492-4

[35] J. Nielsen, W.J.R. Hoefer "A Complete Dispersion Analysis of the Condensed Node TLM Mesh", IEEE Trans. on Mag., Vol.27, No.5, Sept. 1991, pp. 3982-3985

[36] J. Nielsen, W.J.R. Hoefer "Effects of Dispersion in the 3D Condensed Node TLM Mesh", IEEE 1992 MTT Symposium Digest, pp. 853-855

[37] L. N. Trefethen "Group Velocity in Finite Difference Schemes", SIAM Review Vol.24, No. 2, pp 113-35, April 1982

[38] R. Voelker, R. Lomax "A Finite-Difference Transmission Line Matrix Method Incorporating a Nonlinear Device Model", IEEE Microwave Theory and Techniques, Vol.38, No.3, March 1990, pp. 302-12

[39] D.R.Lynch, K.D.Paulsen "Origin of Vector Parasites in Numerical Maxwell Solutions", IEEE MTT, Vol.39, No.3, March 1991, pp. 383-394

[40] J.S. Nielsen "Spurious Modes of the TLM-Condensed Node Formulation", IEEE Microwave and Guided Letters, Vol.1, No.8, Aug. 1991, pp. 201-203

[41] J.S. Nielsen, W.J.R. Hoefer "Modification of the 3D TLM Node to Improve Modelling of Conductor Edges", IEEE Microwave and Guided Wave Letters, March 1992 pp. 105-107

[42] J.S. Nielsen, W.J.R. Hoefer "New 3D TLM Condensed Node Structures for Improved Simulation of Conductor Strips", IEEE 1992 MTT Symp. Digest, pp.1221-1224

[43] U. Mueller, P. So, W.J.R.Hoefer "The Compensation of Coarseness Error in 2D TLM Modeling of Microwave Structures", IEEE 1992 MTT Symp. Digest, pp.373-376

[44] E. Hammerstad, O. Jensen "Accurate Models for Microstrip Computer Aided Design", IEEE MTT Symposium Digest 1980

[45] N. Marcuvitz "Waveguide Handbook",IEE Electromagnetic Series 21, 1986

[46] J.B. Davies "The Finite Element Method", chap.2 of T. Itoh, "Numerical Techniques for Microwave and Millimeter-Wave Passive Structures", John Wiley and Sons, 1989

[47] W. Press, B. Flannery, S. Teckolsky, W. Vetterling "Numerical Recipes in C" 1990

[48] J. Vlach, K. Singhal "Computer Methods for Circuit Analysis and Design" Van Norstrand Reinhold, New York 1983

[49] R. K. Brayton et al. "A New Efficient Algorithm for Solving Differential-Algebraic Systems Using Implicit Backward Differentiation Formulas", Proceedings of the IEEE, Vol.60, No.1, pp. 98-108, Jan.1972

[50] V.D.Hwang, T. Itoh "An efficient Approach for Large-Signal Modeling and Analysis of the GaAs MESFET", IEEE MTT, Vol.MTT-35, No.4, April 1987, pp. 396-402

[51] A. Grove "Physics and Technology of Semiconductor Devices", John Wiley 1967

[52] J. Nielsen, W. Hoefer "Modelling of Nonlinear Elements in a 3D condensed Node TLM mesh", International Journal of Microwave and Millimeter Wave Computer Aided Engineering", Vol. 2, No. 4, Oct. 1992

[53] P. So, W. Hoefer, private communication

[54] C.E.Tong,Y.Fujino "An Efficient Algorithm for Transmssion Line Matrix Analysis of Electromagnetic Problems Using the Symmetrical Condensed Node", IEEE Trans. Microwave Theory and Tech., Vol.39, No.8, Aug.1991, pp.1420-1424

APPENDIX A

TEMPORAL SAMPLING PROPERTIES OF THE TLM MESH

From a signal processing viewpoint the TLM method can be considered as a linear sampling system as illustrated in Fig.A-1. Here we define e(t) as the

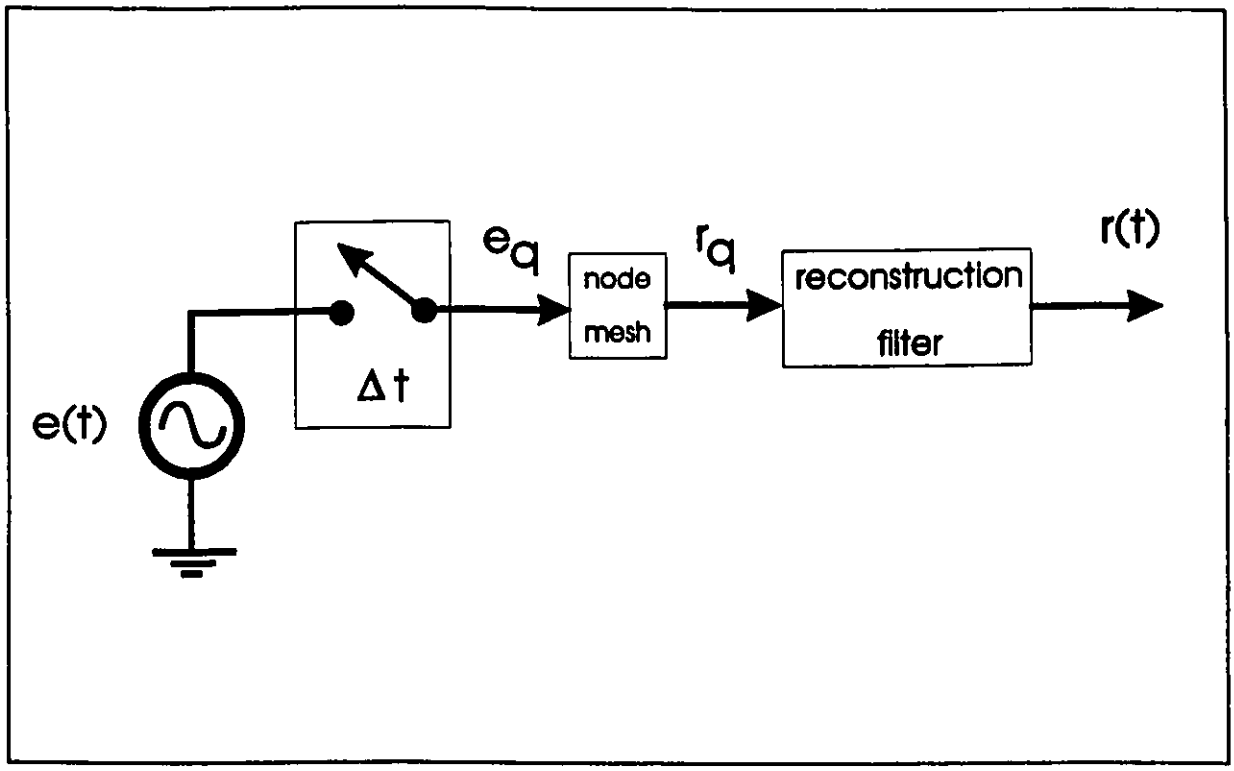

Fig. A-1 Temporal sampled system equivalence of the TLM mesh

input excitation signal and r(t) as the observed signal. The excitation signal is first sampled in time generating a sequence of discrete sampled values e_q such that

$$e_q = e(t) \Big|_{t = q\Delta t} \qquad \text{(A-1)}$$

where Δt is the sampling interval. The time samples e_q are applied to a source node in the TLM mesh. In general, e_q may be applied to a sequence of nodes in a structure to excite, for example, a particular waveguide mode. However, for the moment there is no loss in generality by considering only one source node.

Somewhere within the TLM mesh there will be a set of observation nodes where an output sequence of samples will be extracted. For the moment only one output node is considered, and the sample extracted at $q=n\Delta t$ is denoted as r_q. To reconstruct a continuous signal from the output sample stream, a reconstruction filter, based on the conventional sinc function is used such that the continuous output waveform, $r(t)$ is given by

$$r(t) = \sum_{q=-\infty}^{\infty} r_q \, sinc\left(\frac{t}{\Delta t} - q\right) \qquad \text{(A-2)}$$

As usual, the ideal reconstruction filter is non-causal and a practical filter would depend on a delayed truncated sinc kernel. Details of the reconstruction filter are not important to the development given here.

The discretized response of the TLM network considered must be linear. Consequently we can discuss the relation between e_q and r_q in terms of the discretized impulse response denoted by h_q. The relationship between the input and output samples is then

$$r_q = h_q * e_q$$

$$= \sum_{q'=0}^{q} h_{q'} \, a_{q-q'} \qquad \text{(A-3)}$$

where * denotes a discrete convolution.

In addition to the discrete impulse response, the TLM mesh is a real physical network with a linear continuous time signal impulse response. This impulse response, relating the source and observation nodes will be denoted by $h_c(t)$, where the subscript "c" denotes "continuous". A simple relationship exists between $h_c(t)$ and h_q as will be shown below.

Consider a continuous sinusoidal excitation signal, e(t), at frequency f_o such that

$$e(t) = Re[E(f_o)\exp(j\ 2\ \pi\ f_o\ \Delta t)] \qquad \text{(A-4)}$$

where $E(f_o)$ denotes the complex amplitude at frequency f_o. At the observation point the continuous signal that is extracted is

$$r(t) = Re[H_c(f_o)\ E(f_o)\ \exp(j\ 2\ \pi\ f_o\ \Delta t)] \qquad \text{(A-5)}$$

where $H_c(f_o)$ is the Fourier transform of $h_c(t)$. Next consider a time sampled version of e(t) denoted by $e_s(t)$ such that

$$e_s(t) = Re[e(t) \sum_{q=0}^{\infty} \delta(t - p\Delta t)]$$

$$= Re[E(f_o) \sum_{i=-\infty}^{\infty} \exp\left(j\ 2\ \pi \left(f_o + \frac{i}{\Delta t}\right) t\right) \qquad \text{(A-6)}$$

The response to $e_s(t)$ is denoted by $r_s(t)$ which is given by

$$r_s(t) = Re\left[E(f_0) \sum_{i=-\infty}^{\infty} H_c(f_o+\frac{i}{\Delta t}) \exp\left(j2\pi (f_o+\frac{i}{\Delta t}) t\right)\right] \qquad \text{(A-7)}$$

In the TLM mesh, the scattering nodes are frequency independent and the link lines are dispersionless. The impulse response of a link line is thus $\delta(t-\Delta t)$. Consequently the frequency response of the link line has a periodicity in frequency of $1/\Delta t$. As the link lines are the only members of the homogeneous TLM mesh that are frequency dependent, it must follow that $H_c(f)$ also has a periodicity in frequency of $1/\Delta t$. Consequently

$$r_s(t) = Re\left[E(f_o)\ H_c(f_o) \sum_{i=-\infty}^{\infty} \exp\left(j2\pi (f_o+\frac{i}{\Delta t}) t\right)\right] \qquad \text{(A-8)}$$

and hence

$$r_s(t) = Re[H_c(f_o)\ e_s(t)] \qquad \text{(A-9)}$$

Comparison of Eq.A-5 and Eq.A-8 shows that the TLM network has the same frequency response whether the input signal is continuous or sampled. It follows that

$$h_c(q\ \Delta t) = h_q \qquad \text{(A-10)}$$

The implication of Eq.A-10 is that the transfer function for the TLM mesh is the

same for a continuous or sampled signal provided the excitation sources are band-limited to frequencies below $1/2\Delta t$. In other words, if the excitation sources are sufficiently band-limited, there is no distortion caused by temporal sampling in the TLM mesh. This essentially means that the effects of temporal and spatial sampling can be analyzed separately, a property that is exploited in the dispersion analysis of the TLM mesh in Chapter 2.

APPENDIX B

DERIVATION OF EIGENMATRIX FOR 3D EXPANDED TLM NODE

In this appendix the derivation of the 3D dispersion relation is given. Consider the expanded node as illustrated in Fig. 2-5. It consists of three shunt nodes and three series nodes. The voltages V_x, V_y and V_z are represented at the three shunt nodes of the unit cell. The three series nodes of the expanded node are shown in Fig. B-1. The voltages associated with the series nodes, x_1, x_2, x_3, x_4, y_1, y_2, y_3, y_4, z_1, z_2, z_3 and z_4 are defined in Fig. B-1. The initial step of deriving the dispersion relation is to write the voltages V_x, V_y and V_z, at the shunt nodes, in terms of the voltages of the surrounding series nodes to which they are connected. Using the dispersion relation of the shunt node (Eq. 2-40) and Fig.B-1, the following relations are obtained

$$V_x = C_o\,(-z_3\,T_y - y_3\,T_z^{-1} - z_1 - y_1) \tag{B-1a}$$

$$V_y = C_o\,(x_3\,T_z^{-1} - z_2\,T_x^{-1} + x_1 - z_4) \tag{B-1b}$$

$$V_z = C_o\,(y_2\,T_x^{-1} + x_4 + y_4 + x_2\,T_y) \tag{B-1c}$$

where

$$C_o = \frac{\sin(\frac{k_o d}{2})}{2\sin(k_o d)} \tag{B-2}$$

$$T_x = e^{-jk_x d}$$

$$T_y = e^{-jk_y d}$$

$$T_z = e^{-jk_z d}$$

Next corsider a single series node connected to four surrounding shunt nodes with $\mathbf{V}^s$ as the vector of the port voltages at the series node centre and $\mathbf{V}$ is the vector of node voltages at the ends of the interconnecting lines (at the centre of the shunt nodes). Define $\mathbf{V}^{i s}$ as the vector of voltages incident at the series node centre. Consequently

$$\mathbf{V}^s = (\mathbf{I} + \mathbf{S})\, \mathbf{V}^{i s} \qquad \text{(B-3)}$$

$$\mathbf{V} = (\mathbf{T}^{-1} + \mathbf{T}\,\mathbf{S})\, \mathbf{V}^{i s} \qquad \text{(B-4)}$$

where $\mathbf{S}$ is the scattering matrix of the series node and $\mathbf{T}$ is defined as

$$\mathbf{T} = T_o\, \mathbf{I} \qquad \text{(B-5)}$$

where $\mathbf{I}$ is a 12x12 identity matrix and

$$T_o = e^{-\frac{jk_o d}{2}}$$

Using Eq. B-4 in Eq. B-3 we obtain

$$\mathbf{V}^s = (\mathbf{I} + \mathbf{S})\, (\mathbf{T}^{-1} + \mathbf{T}\,\mathbf{S})^{-1}\, \mathbf{V} = \mathbf{Q}\, \mathbf{V} \qquad \text{(B-6)}$$

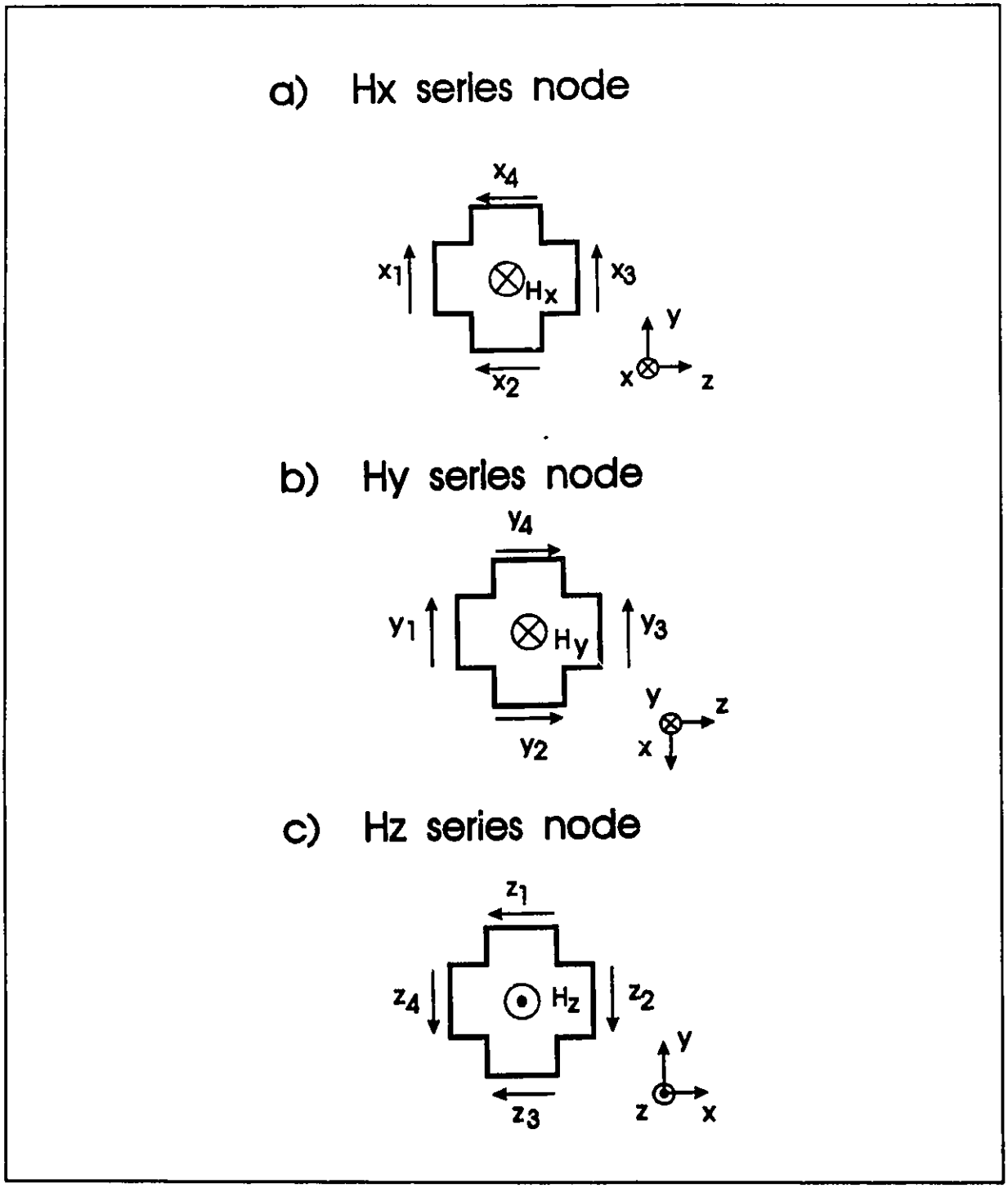

Fig. B-1 Definition of variables used in derivation

with

$$\mathbf{Q} = C_o \begin{pmatrix} 3 & 1 & 1 & -1 \\ 1 & 3 & -1 & 1 \\ 1 & -1 & 3 & 1 \\ -1 & 1 & 1 & 3 \end{pmatrix} \tag{B-7}$$

The relations generated by the three series nodes are then given by

$$\begin{pmatrix} x_1 \\ x_2 \\ x_3 \\ x_4 \end{pmatrix} = \mathbf{Q} \begin{pmatrix} v_y \\ v_z\ T_y^{-1} \\ v_y\ T_z \\ v_z \end{pmatrix} \tag{B-8a}$$

$$\begin{pmatrix} y_1 \\ y_2 \\ y_3 \\ y_4 \end{pmatrix} = \mathbf{Q} \begin{pmatrix} -v_x \\ v_z\ T_x \\ -v_x\ T_z \\ v_z \end{pmatrix} \tag{B-8b}$$

$$\begin{pmatrix} z_1 \\ z_2 \\ z_3 \\ z_4 \end{pmatrix} = \mathbf{Q} \begin{pmatrix} -v_x \\ -v_y\ T_x \\ -v_x\ T_y^{-1} \\ -v_y \end{pmatrix} \tag{B-8c}$$

Finally Eq. B-8 is substituted into Eq. B-1 which results in the eigenvalue equation of Eq. 2-53.

APPENDIX C

EXTRACTION OF WAVEGUIDE S-PARAMETERS FROM TLM SIMULATION

This appendix details the methodology used to evaluate the scattering parameters determined from a TLM analysis of a waveguide discontinuity. Consider a homogeneous waveguide section that contains a localized discontinuity. The scattering parameters of the discontinuity are determined by first measuring the scattering parameters of the complete section of waveguide and then de-embedding the required scattering parameters of the discontinuity. In the laboratory, the scattering parameters of the waveguide section are measured by placing a termination on each end of the waveguide that is matched to the impedance of the TE_{10} mode at the frequency of interest. A TE_{10} mode is excited from one end of the waveguide using an appropriate launcher. Scattering parameters are then determined from a measurement of the field strength at the terminations.

In the TLM method, the S-parameter extraction is very similar. Johns absorbing walls are used as matched terminations. An array of voltage generators, connected between the Johns wall and the TLM mesh at one end of the waveguide, generates an incident impulse appropriately weighted to excite the TE_{10} mode. A DFT of the reflected voltages at the end of the waveguide is calculated to determine the S-parameters as a function of frequency.

There are several problems with this approach. The first is that the incident impulse signal propagates in two directions, towards the discontinuity and into the absorbing Johns wall. Hence, the unit incident impulse has to be

decomposed into a forward and backward propagating signal. Also the reflected signal at each port must be decomposed in terms of the TE_{10} eigenmode field for each frequency. This is not a trivial task as the Johns wall is a frequency dispersive impedance representing the waveguide impedance. This problem can be overcome by using a normalization procedure developed by Eswarappa and Hoefer that is outlined in reference [32]. The second problem is that the impulse response generated excites the TE_{10} mode with some frequencies that are below cutoff. These frequency components never decay with time (at z=0) unless the discontinuity is lossy. Hence there will be truncation errors in the DFT recovery of the S-parameters unless careful windowing is performed. To avoid this problem, the excitation signal must be bandwidth-limited such that frequencies below cutoff are not excited.

A more direct method for S-parameter extraction has been developed which avoids the problems mentioned above. In this appendix we consider the case of extracting the S_{11} parameter of a waveguide discontinuity. This is illustrated in Fig. C-1. The generator, G_1, at the incident port P_1 is matched to the link line impedance Z_o rather than the guide impedance Z_q. G_1 generates a unit amplitude incident impulse that is weighted with respect to the link lines to excite a TE_{10} mode. Hence if a TE_{10} mode impulse is desired into a mesh aperture size of N_x by N_y nodes, the generator attached to port 3 of node i,j,k=0 generates an incident voltage

$$ {}_qV^i_{i,j,0,3} = \sin(\pi(i+\tfrac{1}{2})/N_x) \qquad q = 0 \qquad \text{(C-1)} $$

$$ = 0 \qquad \text{otherwise} $$

Note that the frequency components below the TE_{10} cutoff are reflected back into the matched impedance Z_o and absorbed. It is assumed that the plane pl, in Fig.

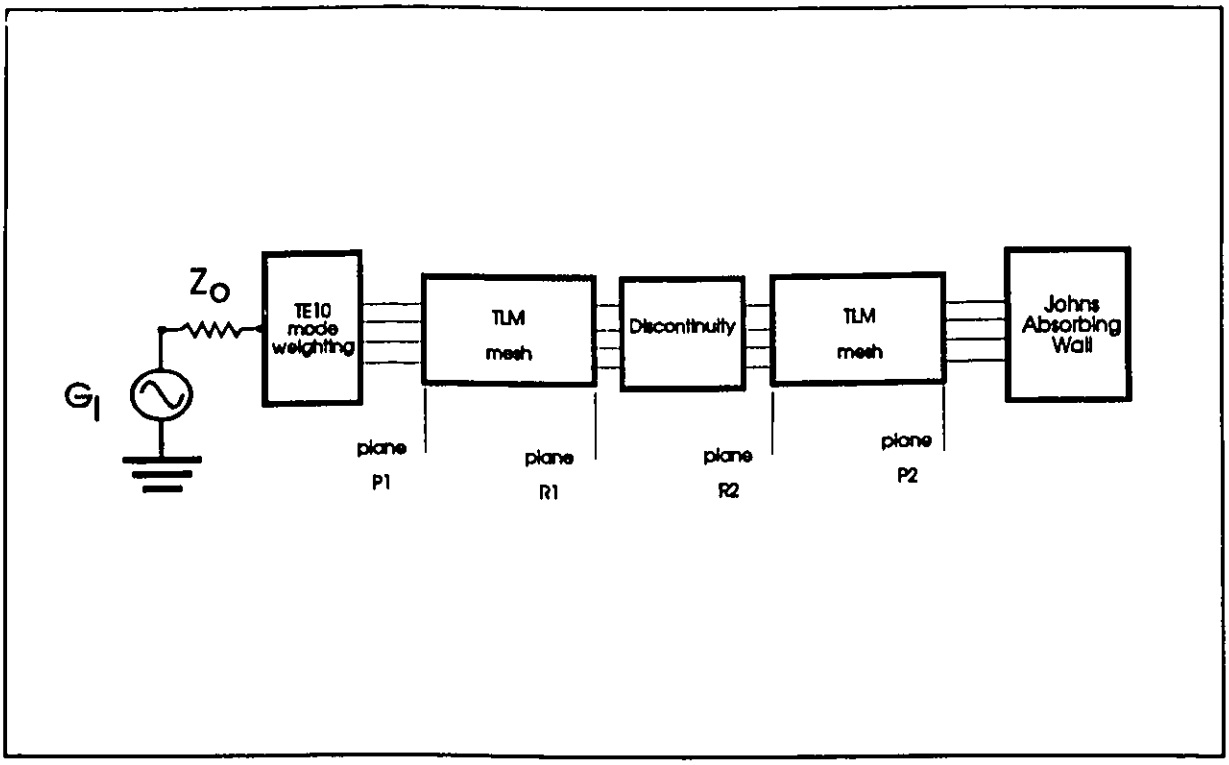

Fig. C-1 Extraction of S_{11} parameter of a waveguide discontinuity simulated by a TLM mesh.

C-1, is far enough away from the discontinuity that evanescent modes do not reach the generator.

Let $S_{11}(f)$ be the S-parameter at the input port P_1. It is given by the DFT of the reflected signal at P_1 as

$$S_{11}(f) = \frac{\sum_{q=0}^{q_{max}} e^{-j2\pi fq\Delta t} \sum_{i=0}^{N_x-1} {}^{q}V^{r}_{i,j,0,3} \sin\left(\frac{\pi(i+\frac{1}{2})}{N_x}\right)}{\sum_{i=0}^{N_x-1} \sin\left(\frac{\pi(i+\frac{1}{2})}{N_x}\right)^2} \qquad \text{(C-2)}$$

Let $\Gamma(f)$ represent the reflection coefficient looking into the waveguide discontinuity from the reference plane R_1 shown in Fig. C-1. The relation

between $\Gamma(f)$ and $S_{11}(f)$ is found from the equivalent signal flow diagram in Fig. C-2 which represents the waveguide problem in Fig. C-1. Here R(f) is given by

$$R(f) = \frac{Z_g(f) - Z_o}{Z_g(f) + Z_o} \qquad \text{(C-3)}$$

Γ_o is the propagation term between the reference plane R_1 and the input port P_1 given by

$$\Gamma_o(f) = e^{-j\, k_z(f)\, d\, N_{rp}} \qquad \text{(C-4)}$$

with N_{rp} as the number of TLM nodes between R_1 and P_1. Note that $k_z(f)$ can be determined from the dispersion equation of the condensed node. $Z_g(f)$ is the impedance of the simulated TE_{10} mode in the rectangular waveguide. It is very close to the analytical expression of

$$Z_g(f) \approx 2\, \frac{k_o}{k_z} \qquad \text{(C-5)}$$

An exact evaluation of $Z_g(f)$ is possible by considering the eigenmode of the TE_{10} mode in the TLM mesh. Unfortunately, this procedure is very lengthy and is therefore not included here.

Using Mason's rule, the expression for $\Gamma(f)$ is derived as:

$$\Gamma(f) = \frac{S_{11}(f) - R(f)}{\Gamma_o(f)^2\,(1 - R(f)^2) - (S_{11}(f) - R(f))\,\Gamma_o(f)^2\,R(f)} \qquad \text{(C-6)}$$

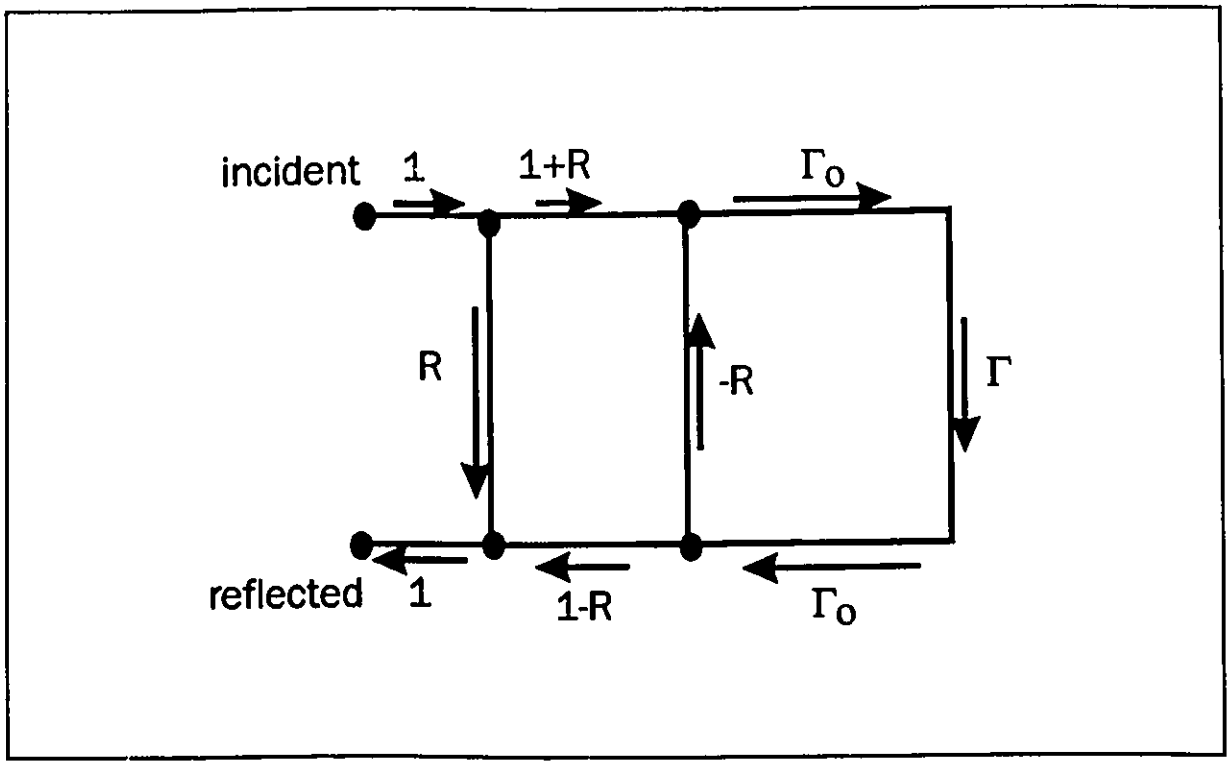

Fig. C-2 Equivalent signal flow diagram of waveguide discontinuity of Fig. C-1

If the discontinuity is lossless and of infinitesimal width, then the equivalent normalized shunt admittance of the discontinuity can be related to Γ by

$$\Gamma = \frac{-Y_B}{\frac{2}{Z_o} + Y_B} \qquad \text{(C-7)}$$